The Pennsylvania State University

The Graduate School

Department of Civil and Environmental Engineering

TOWARD A HYDROLOGIC MODELING SYSTEM

A Dissertation in

Civil Engineering

by

Mukesh Kumar

Submitted in Partial Fulfillment
of the Requirements
for the Degree of

Doctor of Philosophy

August 2009

The dissertation of Mukesh Kumar was reviewed and approved* by the following:

Christopher J. Duffy
Professor of Civil Engineering
Dissertation Advisor
Chair of Committee

Patrick M. Reed
Associate Professor of Civil Engineering

Thorsten Wagener
Associate Professor of Civil Engineering

Padma Raghavan
Professor of Computer Science

Peggy Johnson
Department Head, Civil and Environmental Engineering

* Signatures are on file in the Graduate School

Abstract

Surface water, plant water, soil and groundwater, and the atmosphere are all linked components of the hydrologic continuum. Understanding the interaction between these components and the ability to predict the availability, variability and quality on large scale, requires an accurate and efficient solution strategy. Here we present the underpinnings of a framework referred to as Hydrologic Modeling System (HMS), to couple physics, numerics, data and computation, with the goal to simulate coupled hydrologic process interactions at multiple spatio-temporal scales. The primary component of the framework is a physics-based, spatially distributed, fully coupled, constrained unstructured mesh based Finite-Volume model that simultaneously solves integrated hydrologic processes in heterogeneous, anisotropic domains. The holistic approach developed here, emphasizes the need for efficient simulations through spatially adaptive domain decomposition strategies, use of multi-processor clusters, and seamless and dynamic flow of data between data-management systems and hydrologic models. The modeling framework has been applied from hillslope (10-100m) to catchment (100-1000m) to synoptic scales (>100km) by using different number and approximation of process equations depending on model purpose and computational constraint. Examples will demonstrate how this model provides insight into the influence of drainage from unsaturated zone on delayed water table drawdown, the role of water table position on infiltration and surface runoff, and the interaction of overland flow-groundwater exchanges in relation to the dynamics of infiltrating/exfiltrating surfaces on the hillslopes. Large scale implementation of the model in Little-Juniata Watershed (845 km^2) unfolds a range of multiscale/multiprocess interactions including the influence of local upland topography and stream morphology on spatially distributed, asymmetric right-left bank river-aquifer interactions, and, the role of macropore and topography on ground water recharge magnitude, time scale and spatial distribution. Finally, the computational challenges posed by using such complex model will be addressed, along with an outlook for future efforts along these lines.

Table of Contents

List of Figures

List of Tables

Acknowledgements

Looking back, it is humbling to see the innumerable number of individuals, experiences and ideas that has shaped me and this PhD, during my stay at Penn State. This is my humble attempt to thank many, but not all, who played a vital part directly or indirectly in making this experience a memorable one.

First and foremost I would like to thank my advisor, Prof. Chris Duffy, for being a true friend, philosopher and guide. I thank him for his willingness to listen even when I didn't made sense, for his encouragement when I felt overwhelmed, for his openness to conflicting ideas and criticisms, and for letting me explore new and unknown directions. I thank him for fostering an atmosphere that encouraged independent research and thinking. I thank him for being there to share my personal joys and sorrows in my life. And finally I thank him for providing innumerable opportunities to discuss and share my research with the best in the field, for the financial support during my long stay at Penn State and for many trips to conferences.

Next, I want to thank Dr. Patrick Reed, who challenged me to be the best I can be. I thank him for being a great mentor to me and for his ever useful suggestions regarding my research and my career path.

I am also grateful to Dr. Thorsten Wagener for his advice about numerous issues in my research, especially emphasizing the importance of simplifying large and complex problems. I also thank him for keeping me abreast with the available job opportunities. I would also like to thank Prof. Padma Raghavan for her constructive comments on various aspects of my research. I am thankful to Dr. Doug Miller and Dr. Karen Salvage for the opportunity to work with them, and for their help and tips in writing research articles. I thank Dr. Salvage for teaching me through example how attention to details is an indispensable prerequisite for good science.

In addition to faculty mentors, I have greatly benefited from the help and discussions from fellow students. I thank Mr. Gopal Bhatt for bringing the best out of me in designing algorithms and experiments for error testing. I thank him for all his positive criticisms which made me a better researcher and a person. I also benefited a great deal from my discussions with Dr. Shuangcai Li, particularly about higher-order numerical procedures which later paved the way for development of FIHM.

My stay at Penn State was made memorable by so many of my friends. I particularly cherish the discussions about politics, psychology, spirituality, minority rights, international relations, and philosophy with Sid, Rashi, Ben, Joe, Keith, Mutthu and many more, and thank them for sharing their ideas. I thank Sedmera family, Peter and Yizhong for making me feel at ease when I joined Penn State. I would also like to thank Ajay, Mat, Tanmay, Yong Tang, Gautam, Eva and all the graduate students in the Water Resources Group who helped me along the way and made this journey a lot more fun.

I would like thank my family members (Papa, Mummu and Faazu) for their patience and support. Finally I would like to thank my brother (Rakesh) for his encouragement and his mentoring at every step during my PhD, without whom my graduate studies would not have been possible, and to him I dedicate this thesis.

CHAPTER 1:

Introduction

1.1. Motivation

Sustainable management of water is increasingly recognized as the key to social, economic and environmental development with potential consequences on agriculture, energy demand and supply, transportation, forest fires, flood and droughts, and ecosystem support. Critical to any sustainable water management strategy is our understanding of the circulation of water, and our ability to assess and predict its availability, variability and quality. The need to understand and predict has become even more urgent in impending climate change scenarios which threaten to put increased stress on water resources (Lettenmaier et al. 1999; Milly et al. 2002; Christensen et al. 2004; Milly et al. 2005). However, the characterization and modeling of water cycle processes are extremely challenging due to their closely coupled nature and because of their occurrence in disparate media (ground, land surface, atmosphere and plants) and over vast spatial scales (that can range from a few centimeters for infiltration, to several kilometers for groundwater flow) and time scales (that can extend from a few seconds, typical for evaporative fluxes, to the several years or decades for base flow). As noted by Intergovernmental Panel on Climate Change (IPCC, 2001), we still do not have an adequate understanding and ability to model and predict water cycle processes and the associated feedbacks.

Numerical models have often been used for hypothesis testing and conceptual understanding of hydrologic process interactions, and to predict and project the missing information for management of water resources. They generally fall into three different groups, namely, (1) empirical black box, (2) conceptual, and (3) physics-based models. The first two modeling strategies are parametric in nature (e.g. Stanford watershed model by Crawford and Linsley 1966, HSPF by Bicknell et al. 1993, LASCAM by Viney and Sivapalan 1999, 2001) and require only a modest numbers of parameters to be calibrated for their operation. Despite their simplicity, such models have proven quite successful in simulating hydrograph at the catchment outlet. However the parameters in these models often have ambiguous physical meaning and predicted states obtained are lumped or at outlet locations only. Because of the lack of detailed information of states and fluxes obtained by these models, their use as a management tool within the watershed is limited. Also, these models provide only limited understanding of process interactions. As noted

by Klemes (1986), "for a good mathematical model it is not enough for it to work well. It must work well for the right reasons". Physics-based distributed hydrologic models inherently follow Klemes' philosophy of hydrologic modeling (with varying degree of success) by using parameters which are related directly to the physical characteristics of the catchment (topography, soil, vegetation, and geology) to predict spatially-varying hydrologic states at user defined locations. These models predict distributed hydrologic states to resolve hillslope and other spatial scales within the watershed, and are suited to take advantage of the high resolution remote sensing, radars and other new spatio-temporally distributed observation networks. Clearly, the increase in number of predicted states makes the model both computationally and data intensive as a result of solver numerics and data-handling. The large number of physical parameters incorporated in these models also poses a data management challenge. In order to assimilate the hydrogeologic parameters and forcings with reasonable degree of accuracy, and to simulate non-linear interactions between numerous process states at fine spatio-temporal resolutions, these models need to be computationally efficient, numerically robust, and flexible enough to incorporate new data and processes.

This thesis attempts to enhance our ability to understand and predict the hydrologic process interactions between vegetation, land-surface and subsurface through numerical modeling, by making advancements in a) accurate and efficient representation and seamless incorporation of distributed data in models, b) representation of processes and their interactions, c) higher order numerical discretization of hydrologic processes in models, and d) computational efficiency of model simulations. The coupling of physics, numerics, data and computation contribute to a synergistic framework for large-scale, distributed modeling which we refer to as Hydrologic Modeling System (HMS). The HMS aims to simulate multi-physics, coupled process interactions at multiple scales while striking a balance between fine scale representation of process and data, and computational load. The integrated framework also facilitates data integrity and concurrent data access thus reducing the model setup time and allows rapid prototyping of model simulations in newer settings and scenarios. The HMS will be used to answer important hydrologic science questions such as a) How are regional groundwater recharge, soil moisture, snow melt, and runoff affected by the heterogeneity in

physiography, topography and hydrogeology and by the spatio-temporal variability in climate forcings and antecedent conditions; b) How do preferential pathways (macropores) influence the aquifer recharge and base flow; c) What are the feedbacks between vegetation and groundwater and how does that influence basin runoff; and d) How does groundwater and capillary zone influences surface runoff generation.

1.2. Background and Scope

This thesis comprehensively details a strategy for large scale hydrologic modeling by addressing accuracy and efficiency issues related with data, processes, numerics and computation. Specifically we address the following four issues.

Since fine spatio-temporal resolution and increased process dimension in distributed hydrologic models will have large data requirements, there is a practical need to strike a balance between descriptive detail and computational load for a particular model application. We address this by developing an accurate and efficient geodata representation strategy for distributed hydrologic models.

In order to handle large data sets used and generated by the distributed models, a tool that facilitates efficient data query, storage, transfer and retrieval across data management, visualization, numerical model and decision-support system is needed. We have developed a "shared data model" which facilitates seamless data flow between a numerical model and a geodatabase thus allowing flexible parameter steering, storage efficiency, enhanced accuracy and faster prototyping of model simulations.

Surface water, the vadose zone, and groundwater are linked components of a hydrologic continuum. The coupled processes interact at a variety of spatio-temporal scales influenced in part due to the heterogeneity in topography, climate, land-use and hydrogeology. In order to capture the interaction between different components of a hydrologic continuum, we have developed a flexible and extensible strategy to perform fully-coupled, multi-scale, multi-process simulations.

With increase in spatio-temporal resolution of the model simulation and the number of predicted hydrologic states, distributed models require an extremely large amount of computation time, sometime rendering solution of large problems practically intractable or atleast not suitable for a near real-time prediction. In order to perform high

temporal and spatial resolution simulations in a large problem domain in feasible time, we have developed a parallelized distributed model to take advantage of computing power of massively parallel processors.

Here we briefly introduce the issues and the corresponding solutions that have been addressed in this thesis.

1.2.1. Geodata Representation in Distributed Hydrologic Models

Physically-based, fully-distributed hydrologic models simulate hydrologic state variables in space and time while using information regarding heterogeneity in climate, land use, topography and hydrogeology. Because of the heterogeneity and fine resolution of the observed data, a strategy to accurately represent geodata in models must take into account the associated increase in computational load. Representational accuracy of geodata (topography, land cover, soil, geology, vegetation and climate) on a distributed model grid depends on the resolution of observed data and model grid and the type of discretization strategy (unstructured or structured) which determines its flexibility to conform to data boundaries.

Structured meshes complement the data ingestion process for spatially distributed geologic, topographic and meteorological data that are available as raster maps/images and have been widely used in integrated hydrologic models such as PARFLOW-Surface Flow (Kollet and Maxwell 2006) and MODHMS (Panday and Huyakorn 2004). However, rigidness of the regular grids prevents the resolution of relatively small topological structures without either resorting to a higher spatial resolution or using a nested or adaptive mesh refinement (Blayo and Debreu, 1999). Structured meshes also lack flexibility in fitting complex-shaped domains. No matter how fine the resolution of the regular grid is, linear features which are not aligned in the principal direction of the grid are "aliased". This redefinition of boundaries because of *gridding* at different spatial scales, particularly at places where hydrologic properties undergo a transition like a land cover change from forest to urban or a topographic changeover, significantly affects the modeling of movement of matter and energy (Woo 2004). Structured mesh representations also restricts surface flow directions to 45-degree increments (Tarboton 1997) which can introduce anisotropy in preferred flow direction (Braun and Sambridge

1997). Many of these limitations can be overcome by using a decomposition strategy based on Triangular Irregular Networks (TINs) (Goodrich 1990, Jones et al. 1990, Vivoni et al. 2004, Ivanov et al. 2004) or generalized unstructured meshes (Qu and Duffy 2007). The advantage of an unstructured mesh is that it can provide an "optimal" representation of the domain with the least number of elements while still conforming to limited set of physical and geometric constraints. The unstructured grid leads to a large decrease in the number of nodes/elements with respect to structured meshes (Shewchuk 1996). Also, it allows better representation of line-features such as the stream network, land-use/ land-cover boundaries and watershed boundaries.

In order to unlock the full potential of unstructured mesh decomposition, a flexible domain decomposition strategy for efficient and accurate integration of the physiographic, climatic and hydrographic watershed features have been devised. The approach takes advantage of different GIS feature types while generating high-quality unstructured grids with user-specified geometrical and physical constraints. The framework is able to anchor the efficient capture of spatially distributed and temporally varying hydrologic interactions and also ingest the physical prototypes effectively and accurately from a geodatabase. The proposed decomposition framework is a critical step in implementing high quality, multiscale, multiresolution, temporally adaptive and nested grids with least computational burden. The framework is generic and can be used for any hydrologic models based on unstructured meshes.

1.2.2. Seamless Data Flow Between Geographic Information Systems (GISs) and Hydrologic Models

Distributed physical models require new strategies for data representation, model domain decomposition, a-priori parameterization, and visualization. The Geographic Information System (GIS) has been traditionally used to accomplish these data management functionalities in hydrologic applications. However, the interaction between the data management tools and the physical model are often loosely integrated and nondynamic. This is because a) the data types and formats for the physical model system and the distributed data or parameters may be different (National Research Council 1999), with significant data preprocessing required before they can be shared, b) the management

tools may not be accessible or shared by the GIS and physical model c) the individual systems may be operating system dependent or are driven by proprietary data structures. The impediment to seamless data flow between the two software components has the effect of increasing the model setup time and analysis time of model output results, and also makes it restrictive to perform sophisticated numerical modeling procedures (real time forecasting, sensitivity analysis etc.) that utilize extensive GIS data.

Several efforts, such as the development of water and erosion prediction project (WEPP) interface on GRASS (Engel et al. 1993), BASINS by EPA (Lahlou et al. 1998), SWAT by Luzio et al. (2002) and Watershed Modeling System (WMS, Nelson 1997), have tried to alleviate the aforementioned problems. However, these approaches were basically trying to "couple" a GIS and a process-based hydrologic model for efficient processing, storing, manipulating, and displaying of hydrogeological data. WMS was a major development and different from other attempts in that it was a stand-alone GIS system totally dedicated to hydrologic application. Development of Arc Hydro (Maidment 2002) was another important step in defining an exhaustive data model for a hydrologic system and providing a framework for storing and preprocessing geospatial and temporal data in GIS. The developed data model provided rules for the structure, relationships and operations on data types often used in hydrologic modeling. McKinney and Cai (2002) went a step further in reducing the gap between GIS and models by outlining an object oriented methodology to link GIS and water management models. In the process, they identified the Methods and Objects of the water management models that can be represented as spatial and thematic characteristic in the GIS.

Here we propose a robust integration methodology that facilitates seamless data flow between data and model functionalities thus making the interactions between them fluid and dynamic. The work lays the foundation for fully integrated and extensible, HMS through a shared data model that is designed using an Object Oriented Strategy. The shared data model takes into consideration the data type descriptions, identification of data-classes, relationships and constraints. The shared data model provides a) flexibility of modification and customization b) ease of access of GIS data structure by the hydrologic model c) richness for representing complex user defined spatial relations and data types, and d) standardization easily applicable to new model settings and

modeling goals. The developed data model has been used as a method base for developing a coupled GIS interface to Penn State Integrated Hydrologic Model (PIHM) called PIHMgis

1.2.3. Integrated Distributed Modeling of Coupled Hydrologic Processes

Understanding and predicting of flow on the surface and in the subsurface necessitates recognizing that surface water, plant water, soil and groundwater, and the atmosphere are linked components of a hydrologic continuum. Changes in one affect the other on a variety of spatio-temporal scales influenced in part due to the heterogeneity in topography, climate, land-use and hydrogeology. In order to capture the interaction between different components of a hydrologic continuum and to use this understanding in water management situations, an accurate numerical model is needed. Full coupling of physical processes, natural numerical coupling, and parsimonious but accurate data coupling are three key steps in efficient and accurate simulation of distributed hydrologic states in watersheds. The previous two sections introduced a data-coupling strategy with the numerical model. Here we present a physically-based, spatially distributed hydrologic model that utilizes all the three coupling strategies.

Since Freeze and Harlan (1969) published their blueprint for physically-based distributed models, much progress has been made in the development of first-principle, physics-based models for individual processes of infiltration, evapotranspiration, recharge, groundwater flow, surface runoff, and river flow. Studies by Gottardi and Venutelli (1993) and, Feng and Molz (1997) for overland flow runoff; USACE-UNET (1997), and Strelkoff (1970) for flow in rivers and Huyakorn et al. (1986) and Paniconi and Wood (1993) for modeling saturated–unsaturated flow in the subsurface particularly stand out. Most of the modeling efforts dealing with simulation of individual processes assume that interacting processes are apriorily known, while they ignore the process feedbacks. As a result, these models often have to introduce undue empiricism. Integrated approaches to modeling coupled processes have recently gained momentum by employing varied strategies to link individual processes. Three commonly used strategies for linking coupled processes (Langevin et al., 2005) are:

a) a sequentially coupled approach (also referred as uncoupled approach by Morita and Yen (2000) and as an externally coupled approach by Freeze (1972)), in which the head for one system acts as a general-head boundary for the other system. No feedbacks are considered in this linking strategy. Prime examples in this category are studies by Singh and Bhallamudi (1998) and Bixio et al. (2002) who solved for both surface and subsurface flow noniteratively by setting interficial boundary condition only once during each time step.

(b) a sequentially coupled approach in which the interaction flux is applied as a boundary condition to each model through feedback mechanism (also referred as iterative coupling by Morita and Yen (2000)). This solution methodology is similar to an externally coupled approach where interficial boundary condition obtained from solution of one process is used in solution of the other. However, here the solution state of the second process is used to update the internal boundary condition of the first process within the same time step. The whole process is repeated till the solution state of each process stops changing within a tolerance convergence criteria. Kouznetsov et al. (2007) used this approach to combine the one dimensional hydrodynamic overland flow equation with three dimension Richard's equation in FEMWATER.

(c) a 'fully coupled' or 'fully implicit' approach in which the interacting processes are solved simultaneously. Theoretically, higher level of coupling translates to higher accuracy. Fairbanks et al. (2001) observed that a sequential coupling approach results in numerically weak, inaccurate and unreliable solutions and fully coupled methods were most robust and accurate. New generation of distributed models such as InHM (Vanderkwaak, 1999), WASH123D (Yeh and Huang, 2003), MODHMS (Panday and Huyakorn, 2004) and PARFLOW-Surface Flow (Kollet and Maxwell, 2006) use this approach.

Among the physics-based, distributed, fully-coupled models, MODHMS and PARFLOW-Surface Flow use finite difference methods for numerical solution of hydrologic states while InHM and WASH123D are based on finite element methods. Finite difference based models have some significant advantages in terms of ease of meshing the domain, simple topological structure and ease of parallelization, but the rigidity of the structured grids in conforming to curvilinear geometries and representation

of heterogeneities make it prohibitive to perform accurate large scale simulations. Barrash and Dougherty (1997) and the USEPA (1994) also reported loss of accuracy in predicting hydraulic heads near regions of steep head gradients and boundaries using finite difference models. The inaccuracy can be reduced by performing relatively fine localized discretization in areas of steep head gradient (Leake and Claar, 1999; Mehl and Hill, 2004), however this results in long execution times. Also, the conservation property in the finite difference based models is only satisfied for infinitesimal grid size. An alternate solution strategy is the traditional Galerkin finite element methods which are used to solve diffusion wave equations in WASH123D. These methods ensure continuity in gradient at the discretization boundary but there is no local conservation of mass within each discretized unit element (Di Giammarco et al., 1996). Control volume finite element (CVFE) methods alleviate this problem (InHM is based on CVFE) and are able to conserve mass.

We present a physically-based, spatially distributed hydrologic model (called PIHM) based on the full-coupling of hydrologic processes on unstructured meshes. The model uses a semi-discrete, Finite-Volume approach to define the distributed process equations on discretized unit elements which ensures conservation of the solution property within each discretized element. Some of the processes simulated in the model are interception, snow melt, transpiration, evaporation, overland flow, subsurface flow, river flow, macropore based infiltration and lateral stormflow, as well as flow through and over hydraulic structures such as weirs and dams. An implicit Newton-Krylov based solver that utilizes adaptive time stepping provides a robust and stable solution. An important feature of the PIHM formulation is that its data structure remains isolated and independent from the solver's data structure. This approach allows the user to easily alter the system of equations in the kernel without having to manually change the numerical discretization. Multiple formulations can be activated simply using boolean switches on the right hand side of ODE. This provides the user a unique flexibility in the choice of process equations used in different parts of the model domain, depending on the model purpose or other computational constraints. The implementation of the model has been performed for a mesoscale watershed in central PA (Little-Juniata Watershed, 845 km^2).

Model results are validated by comparison of observed and predicted streamflow and groundwater levels at multiple locations.

The first-order spatial accuracy of process discretizations in PIHM, in addition to the low-dimensional representation of subsurface flow and the assumption of flux being orthogonal to the triangular edges, makes the model efficient leading to its application in large watersheds. However this limits the fine scale prediction of potentiometric head in the subsurface. The piecewise constant head representation within an element in PIHM causes smearing of discontinuities and are particularly inaccurate for simulation in orthotropic and anisotropic media (Pasdunkorale and Turner, 2003). Also, the assumption of orthogonal fluxes across the triangular edges is only ensured by acute angled discretizations in isotropic media only. In order to avoid these limitations, a next-generation fully coupled, second order accurate, upwind cell-centered, constrained unstructured mesh based Finite-Volume model (FIHM) has been developed. This model simultaneously solves unsteady overland/channel (2-D) and subsurface flow (3-D) equations in heterogeneous, anisotropic domains. Physical process representation for surface flow is based on a depth-averaged 2-D diffusive wave approximation of the Saint Venant equations while subsurface flow simulation is based on the complete three-dimensional, variably saturated form of Richards's equation. A higher order scheme for overland flow (Lin et al. 2003; Fiedler and Ramirez, 2000) and subsurface flow (Manzini and Ferraris, 2004) yields improved simulation of states and derived hydraulic conductivity fields both in areas of smooth and steep gradients. Full coupling between overland and vadose zone flow is handled based on the continuity of both head and flux. FIHM model also handles modification of the flow field due to arbitrarily oriented anisotropy of hydrogeologic and physiographic properties. This is particularly unique as majority of existing distributed models that employ structured, body-fitted meshes (ModHMS, Panday and Huyakorn 2004) solve of anisotropy by aligning their coordinate system with the principal directions of the conductivity tensor. However such a methodology is not easy to use in problems with multiple anisotropic materials. Even the finite volume based models are generally not designed to handle both inhomogeneity and anisotropy. As noted by Klemes (1986), a hydrologic model must demonstrate, before it is used operationally, how well it can perform the kind of task for which it is intended.

An exhaustive set of verification experiments has been used to evaluate the FIHM model performance for each individual process and the interactions between them

1.2.4. Distributed Hydrologic Modeling on Parallel Processors

Distributed integrated hydrologic models like PIHM and FIHM, are data and computationally intensive. With the advent of parallel processing architectures, high performance computing (HPC) is a reality and has opened up new opportunities for complex and large scale modeling. HPC offers the ability to compute solutions to problems not possible on desktop machines. It provides the ability to: (i) run models at finer spatio-temporal discretization, and (ii) perform large number of simulations under different conditions. In order to perform a high temporal and spatial resolution run of a large scale hydrologic model in feasible time, parallelized versions of hydrologic model that can run on a cluster of parallel processors must be developed. This translates to running different parts of the same model simulation on a network of large number of processors thereby reducing the time needed to obtain solution.

We present parallelized version of PIHM model (called pPIHM) using MPI (Message Passing Interface, Gropp et al. 1999) for distributed processors. The efficient implementation of the pPIHM is supported by proper partitioning of the model domain to ensure load balance between processors and minimize interprocessor communication. The thesis demonstrates for the first time the use of graph and geometric partitioning algorithms vis-à-vis domain-decomposition topology, hydrologic processes representation and process time-scales in parallelization of a fully-coupled hydrologic model. The thesis also discusses and highlights several hydrologic, architectural and algorithmic issues which need to be incorporated in an efficient domain partitioning for parallel implementation of integrated distributed hydrologic model.

1.3. Organization

The remaining chapters of this dissertation are organized according as our attempts at addressing individual issues discussed in the previous section. The chapters in this thesis are individually published or are in review as stand-alone papers. As such some overlap occurs between this introduction, the chapters and the summary.

- Chapter 2 presents an efficient domain decomposition framework for accurate representation of geodata in distributed hydrologic models
- Chapter 3 presents an object oriented shared data model for GIS and distributed hydrologic models
- Chapter 4 presents the role of physical, numerical and data coupling in a mesoscale watershed model
- Chapter 5 presents a second order accurate, Finite Volume Based, Integrated Hydrologic Modeling (FIHM) framework for simulation of surface and subsurface flow
- Chapter 6 presents a domain partitioning strategy for implementation of large scale integrated hydrologic models on parallel processors
- Cheaper 7 presents the parallelization of fully coupled distributed hydrologic model
- Chapter 8 presents an overall summary of scientific contributions of this dissertation and recommendations for future work.

1.4. References

Barrash, W., and M.E. Dougherty. 1997. Modeling axially symmetric and nonsymmetric flow to a well with MODFLOW, and application to Goddard2 well test, Boise, Idaho. Ground Water; 35(4):602–11.

Beven K. 2002. Towards an alternative blueprint for a physically based digitally simulated hydrologic response modelling system. Hydrological Processes 16: 189–206.

Bicknell, B. R., J. C. Imhoff, J. L. Kittle, A. S. Donigian, and R. C. Johanson, 1993. Hydrolgic Simulation Program - FORTRAN (HSPF): User's Manual for Release 10.0. EPA 600/3-84-066. U.S. Environmental Protection Agency, Environmental Research Laboratory, Athens, GA

Bixio, A.C., G. Gambolati, C. Paniconi, M. Putti, V.M. Shestopalov, V.N. Bublias, A.S. Bohuslavsky, N.B. Kasteltseva, and Y.F. Rudenko. 2002. Modeling groundwater–surface water interactions including eff ects of morphogenetic depressions in the Chernobyl exclusion zone. Environ. Geol. 42:162–177.

Blayo, E., and L. Debreu, 1999. Adaptive mesh refinement for finite difference ocean model: some first experiments. Journal of Physical Oceanography, 29, 6, 1239-1250.

Braun, J., and Sambridge, M., 1997, Modelling landscape evolution on geological time scales: a new method based on irregular spatial discretization. Basin Research, 9, p. 27-52.

Christensen, N. S., A. W. Wood, N. Voisin, D. P. Lettenmaier and R. N. Palmer (2004). The effects of climate change on the hydrology and water resources of the Colorado River basin. Climatic Change, 62(1-3), 337-363.

Crawford NH, Linsley RS., (1966). Digital Simulation in Hydrology: The Stanford Watershed Model IV. Technical Report no. 39, Department of Civil Engineering, Stanford University, Palo Alto, CA.

Di Giamarco, Todini PE, and Lamberti P. A conservative finite elements approach to overland flow: the control volume finite element formulation. J. Hydrol., 175 pp.267-291; 1996

Engel, B. A. et al. (1993): A Spatial Decision Support System for Modeling and Managing Agricultural Non-Point Source Pollution. Environmental Modeling with GIS, Goodchild, M. F. et al. (eds.), New York, Oxford University Press, 231-237.

Fairbanks J, Panday S, Huyakorn PS. Comparisons of linked and fully coupled approaches to simulating conjunctive surface/ subsurface flow and their interactions. In: Seo, Poeter, Zheng, Poeter, editors. MODFLOW 2001 and Other Modeling Odysseys—Conference Proceedings, Golden, CO;p. 356–61; 2001

Feng K, Molz FJ. A 2-D, diffusion-based, wetland flow model. Hydrol., 196: 230-250; 1997

Fiedler, F.R., and J.A. Ramirez. 2000. A numerical method for simulating discontinuous shallow flow over an infiltrating surface, International Journal for Numerical Methods in Fluids, 32(1)

Freeze, R.A. 1972. Role of subsurface fl ow in generating surface runoff : 1. Base flow contribution to channel fl ow. Water Resour. Res. 8:609–623.

Freeze RA, Harlan RL. 1969. Blueprint for a physically-based digitally simulated, hydrologic response model. Journal of Hydrology 9: 237–258

Goodrich, D.C., 1990. Geometric simplification of distributed rainfall-runoff model over a range of basin scales. PhD Dissertation, Tucson, AZ: Department of Hydrology and Water Resources, University of Arizona, 361 pp.

Gottardi G, Venutelli M. A control-volume finite-element model for two-dimensional overland flow. Adv Water Resour ;16:277–84; 1993

Gropp, William; Lusk, Ewing; Skjellum, Anthony. (1999) Using MPI, 2nd Edition: portable Parallel Programming with the Message Passing Interface. MIT Press In Scientific And Engineering Computation Series, Cambridge, MA, USA. 395 pp. ISBN 978-0-262-57132-6

Huyakorn PS, Springer EP, Guvanasen V, Wadsworth TD, A three dimensional finite element model for simulating water flow in variably saturated porous media. Water Resour Res;22(12):1790–808; 1986

IPCC, 2001, Climate Change 2001: Impacts, Adaptation, and Vulnerability. A Contribution of Working Group II to the Third Assessment Report of the Intergovernmental Panel on Climate Change [McCarthy, J.J., O.F. Canziani, N.A. Leary, D.J. Dokken, and K.S.White (eds.)]. Cambridge University Press, Cambridge, United Kingdom and New York, NY, USA, 1032 pp.

Ivanov, V.Y., Vivoni, E.R., Bras, R.L. and Entekhabi, D., 2004. Catchment hydrologic response with a fully-distributed triangulated irregular network model. Water Resources Research, 40

Jones, N.L., Wright, S.G., and Maidment, D.R., 1990. Watershed delineation with triangle based terrain models. Journal of Hydraulic Engineering 116:1232-1251

Kang S.-L., K.J. Davis, 2008. The effects of mesoscale surface heterogeneity on the fair-weather convective atmospheric boundary layer, J. Atmos. Sci., 65, 3197-3213

Klemes V. 1986. Dilettantism in hydrology: transition or destiny? Water Resources Research 22: 177S–188S.

Kollet, S.J., and R.M. Maxwell. 2006. Integrated surface-groundwater flow modeling: A free-surface overland flow boundary condition in a parallel groundwater flow model, Advances in Water Resources, (29)7, 945-958

Kouznetsov, M.Y., R. Roodsari, Y.A. Pachepsky, D.R. Shelton, A.M. Sadeghi, A. Shirmohammadi, and J.L. Starr. 2007. Modeling manure-borne bromide and fecal coliform transport with runoff and infi ltration at a hillslope. J. Environ. Manage. 84:336–346.

Lahlou, M., Shoemaker, L., Choudry, S., Elmer, R., Hu, A., Manguerra, H. and Parker, A., 1998. ‘Better assessment science integrating point and nonpoint sources: BASINS 2.0 User’s Manual’,EPA-823-B-98-006, U.S. Environmental Protection Agency, Office of Water, Washington, DC, USA

Langevin C, Swain E, Wolfert M. Simulation of Integrated Surface-Water/Ground-Water Flow and Salinity for a Coastal Wetland and Adjacent Estuary. Journal of Hydrology 314 (1-4), 212-234; 2005

Lettenmaier, D. P., A. W. Wood, R. N. Palmer, E. F. Wood and E. Z. Stakhiv (1999). Water resources implications of global warming: A US regional perspective. Climatic Change, 43(3), 537-579.

Lin, G.F., J.S. Lai, and W.D. Guo. 2003. Finite-volume component-wise TVD schemes for 2D shallow water equations, Advances in Water Resources, 861-873

Loague, K. and VanderKwaak, J.E., 2004, Physics-based hydrologic response simulation: platinum bridge, 1958 Edsel, or useful tool. Hydrologic Processes, 18, 2949-2956

Luzio. Di, M., Srinivasan, R., Arnold, J.G., and Neitsch, S.L., 2002. Arcview Interface for SWAT2000. User's Guide. U.S. Depart- ment of Agriculture, Agriculture Research Service. Temple, Texas. Available at http://www.brc.tamus.edu/swatt/downloads/ doc/swatav2000.pdf Accessed on March 18, 2008

Maidment, D., 2002. Arc Hydro: GIS for Water Resources. Redlands, CA, ESRI Press

Manzini, G., and S. Ferraris. 2004. Mass-conservative finite volume methods on 2-D unstructured grids for the Richards equation, Advances in Water Resources, 27 1199–1215

Maxwell, R.M., Chow, F.K., Kollet, S.J., The groundwater-land-surface-atmosphere connection: soil moisture effects on the atmospheric boundary layer in fully-coupled simulations, Advances in Water Resources (2007),

Mckinney, D.C., and Cai, X.M., 2002. Linking GIS and water resources management models: an object-oriented method. Environmental Modeling & Software, 17, 413-425

Milly, P. C. D., K. A. Dunne and A. V. Vecchia (2005). Global pattern of trends in streamflow and water availability in a changing climate. Nature, *438*(7066), 347-350.

Milly, P. C. D., R. T. Wetherald, K. A. Dunne and T. L. Delworth (2002). Increasing risk of great floods in a changing climate. Nature, 415(6871), 514-517.

Morita, M., and B.-C. Yen. 2000. Numerical methods for conjunctive two-dimensional surface and three-dimensional sub-surface fl ows. Int. J. Numer. Methods Fluids 32:921–957.

Nelson, E.J., 1997. WMS v5.0 Reference Manual, Environmental Modeling Research Laboratory, Brigham Young University, Provo, Utah, 462 pp.

Panday, S., and P.S. Huyakorn. 2004. A fully coupled physically-based spatially-distributed model for evaluating surface/subsurface flow. Adv Water Resour 27:361–382

Qu, Y., and C. J. Duffy (2007), A semidiscrete finite volume formulation for multiprocess watershed simulation, Water Resour. Res., 43,

Pasdunkorale, J.A., and I. W. Turner. 2003. A Second Order Finite Volume Technique for Simulating Transport in Anisotropic Media. The International Journal of Numerical Methods for Heat and Fluid Flow, Vol. 13(1), pp. 31-56

Paniconi C, Wood EF. A detailed model for simulation of catchment scale subsurface flow processes, Water Resour. Res., 29(6), 1601-1620; 1993

Savenije HHG. 2001. Equifinality, a blessing in disguise? Hydrological Processes 15: 2835–2838.

Singh, V., and S.M. Bhallamudi. 1998. Conjunctive surface–subsurface modeling of overland fl ow. Adv. Water Resour. 21:567–579.

Shewchuk, J.R., 1996. Triangle: Engineering a 2D quality mesh generator and Delaunay Triangulator. In 1st workshop on Applied Computational Geometry, ACM, 124-133

Strelkoff T. Numerical solution of Saint Venant equations. ASCE Proceedings, Journal of Hydraulic Dicision 96: 223-252; 1970

Tarbaton, D.G., 1997, A new method for the determination of flow directions and contributing areas in grid digital elevation models. Water Resources Research, 33, no. 2, p. 309-319.

USACE UNET. One-dimensional unsteady flow through a full network of open channels, User's Manual. US Army Corps of Engineers, Hydrologic Engineering Center, Davis, CA; 1997

US Environmental Protection Agency (USEPA), 1994. A technical guide to ground-water model selection at sites contaminated with radioactive substances. EPA/402/R-94/012, Office of Solid Waste and Emergency Response, US Environmental Protection Agency, Washington, DC.

VanderKwaak, J.E. 1999. Numerical simulation of flow and chemical transport in integrated surface–subsurface hydrologic systems, Doctorate Thesis, Department of Earth Sciences, University of Waterloo, Ontario, Canada

Viney N.R. and Sivapalan M. (1999) A conceptual model of sediment transport: application to the Avon river basin in Western Australia. Hydrological Processes, 13, 727–743.

Viney N.R. and Sivapalan M. (2001) Modelling catchment processes in the Swan-Avon river basin. Hydrological Processes, 15, 2671–2685.

Vivoni E.R., Ivanov, V.Y., Bras, R.L. and Entekhabi, D., 2004. Generation of triangulated irregular networks based on hydrological similarity. Journal of hydrologic engineering, 9, 4. 288-302

Yeh, G.T., and G.B. Huang. 2003. A Numerical Model to Simulate Water Flow in Watershed Systems of 1-D Stream-River Network, 2-D Overland Regime, and 3-D Subsurface Media (WASH123D: Version 1.5), Technical Report. Dept. of Civil and Environmental Engineering, University of Central Florida, Orlando, Florida

Woo, M.K. 2004. Boundary and border considerations in hydrology, Hydrological Processes, 18, 1185-1194

CHAPTER 2:

An efficient domain decomposition framework for accurate representation of geodata in distributed hydrologic models

2.1. Introduction

Distributed models simulate hydrologic states in space and time while using discretized information regarding the distribution and parameters of climate, land use, topography and hydrogeology (Freeze and Harlan 1969). These models have inherent advantages over conventional lumped models particularly because natural heterogeneities control watershed behavior(s) and also help in resolving the feedback processes between state variables (Entekhabi and Eagleson 1989; Pitman et al. 1990). The numerical solution strategies require spatial discretization of the model domain into spatially connected units. For example grid decomposition for land surface models may take advantage of relevant physical subdomains such as hillslopes (Band 1986), a contour (Moore et al. 1988), structured (Panday and Huyakorn 2004) or unstructured grids (Qu and Duffy 2007). In the case of multi-process/multi-scale models, the representation of topography, land cover, soil, geology, vegetation and climate on a distributed model grid must, by necessity, deal with questions of computational efficiency and limits of parameterization. Since our goal is to perform physics based simulations on large watersheds, our strategy is to minimize the resolution of spatial discretization (fewest number of elements to preserve the essential physics) while still capturing the local heterogeneities in parameters and process dynamics. We achieve this by generating conformed Delaunay triangulation by using distributed GIS anchor objects like points, lines and polygons.

2.2. Domain decomposition: Limitations and scope

Geometrically, the quality (shape and size) and type of the discrete elements which make up the model grid determines the accuracy, convergence, memory storage and computational cost of the numerical solution. Physically the decomposed domain must admit a) conformity with the boundary b) connectivity between elements and c) continuity of mass within each terrain element. The use of rectangular grids with uniform topological structure have seen wide use for domain discretization for integrated hydrologic models such as PARFLOW-Surface Flow (Kollet and Maxwell 2006) and MODHMS (Panday and Huyakorn 2004). The inherent simplicity of a structured grid has

the advantage of fast computations for linear/nonlinear systems because of uniformity in the size of neighboring grids and the ease of determining grid's neighbors. Furthermore, the regularity of structured meshes makes it straightforward to parallelize computations. More to the point, it also complements the data ingestion process for spatially distributed geologic, topographic and meteorologic data that are available as raster maps/images. The computational advantage of modeling on structured grids is sometimes offset by the need for very fine spatial discretization in order to capture local heterogeneities and boundary "edges". Rigidness of the regular grids prevents the resolution of relatively small topological structures without either resorting to a higher spatial resolution or using a nested or adaptive mesh refinement (Blayo and Debreu, 1999). Structured meshes also lack flexibility in fitting complex-shaped domains. Techniques have been devised to find appropriate coordinate transformations like conformal mapping and algebraic methods which would lead to better fitting of irregular shapes (Castillo 1991, Thompson 1982). However these methods are complex and introduce errors due to interpolation of derivatives. The "Staircase effect" at the boundaries is observed when no transformation is applied. No matter how fine the resolution of the regular grid is, linear features which

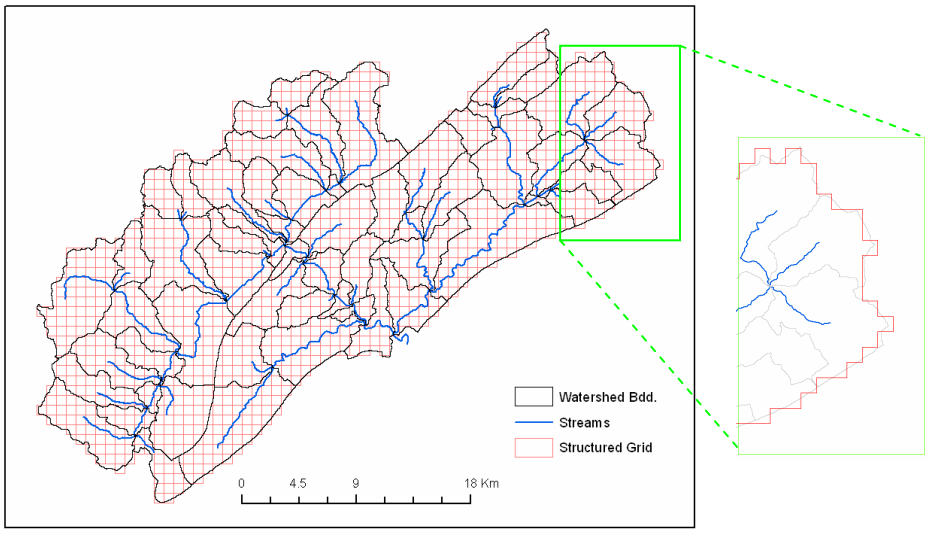

Figure 2.1 Domain decomposition of Little Juniata Watershed using rectangular grid. The "zoomed in" portion of the boundary shows aliasing (stair-case effect) of watershed boundary by structured mesh. Such aliasing can be expected near all kinds of topographic, hydrographic (river, lakes etc.) and physiographic (land use/land cover, soil types etc.) boundaries.

are not aligned in the principal direction of the grid are "aliased". This redefinition of boundaries because of gridding at different spatial scales, particularly at places where hydrologic properties undergo a transition like a land cover change from forest to urban or a topographic changeover, significantly affects the modeling of movement of matter and energy (Woo 2004). Structured mesh representations also restricts surface flow directions to 45-degree increments (Tarboton 1997) which can introduce anisotropy in preferred flow direction (Braun and Sambridge 1997). Finally, regular grids create complications for Nuemann-type boundary conditions as they are forced to align in the two principal orthogonal directions along which the grid is oriented. Figure 2.1 provides an example of the aliased boundary representation for the Little Juniata watershed in central Pennsylvania.

Many of these limitations can be overcome by using a decomposition strategy based on Triangular Irregular Networks (TINs) (Goodrich 1990, Jones *et. al.* 1990, Vivoni *et. al.* 2004, Ivanov *et. al.* 2004) or generalized unstructured meshes (Qu and Duffy 2007). The advantage of an unstructured mesh is that it can provide an "optimal" representation of the domain with the least number of elements while still conforming to limited set of physical and geometric constraints. The unstructured grid leads to a large decrease in the number of nodes/elements with respect to structured meshes (Shewchuk 1996). Also, it allows better representation of line-features such as the stream network, land-use/ land-cover boundaries and watershed boundaries. In order to unlock the full potential of unstructured mesh decomposition, we generate them in a "smart" way by using GIS feature objects. This approach leads to discrete domains that are computationally efficient and which honor the edges and transitions of the important physiographic, geologic, ecologic and hydroclimatic variables. The next section discusses unstructured grid representations for integrated hydrologic modeling.

2.3. Solving multiple processes on an unstructured mesh

There are two approaches to solving systems of hydrologic equations simultaneously. The first is a weakly coupled approach where water and energy exchange between surface water, groundwater, vegetation and atmosphere are solved separately on different

discretized domains while sharing interaction flux as individual boundary conditions. The physical interaction in this case is weakly coupled in that the communication between processes is intermittent and only occurs as necessary to satisfy conservation or efficiency constraints. The synchronization of communication is performed by controller software. Since the decomposition framework for each individual physical process is separate, data assignment, topology definitions, data geo-registration and flux exchange between different physical components of the models is an error prone and computationally intensive approach. Weakly coupled models are also susceptible to convergence problems (Abbot et. al. 1986) and unreliable solutions (Fairbanks et. al. 2001). The second strategy can be referred as "full" volume coupling, where all the physical process equations are solved simultaneously on each element distributed across the domain. For the purposes of this paper, there are important advantages to the volume-coupling approach in that the approach offers a consistent and uniform assignment and registration of geo-data for all the physical model equations and for all discrete elements in the domain. The Penn State Integrated Hydrologic Model (PIHM, Kumar et. al. 2008, Qu and Duffy 2007) uses the latter approach and is briefly described next.

PIHM is a semi-discrete finite volume method (FVM) based numerical model. It solves ordinary differential equations (ODE) corresponding to all the interacting hydrologic processes on each discretized watershed element. PIHM uses implicit Newton-Krylov integrator available in the CVODE (Cohen and Hindmarsh 1994) to solve for state variables at each time step. The discretized control volume elements used in PIHM are either triangular or linear in shape as shown in Figure 2.2. Triangular land surface elements are projected downwards to the bedrock or regolith to form a prismatic element in 3D. Linear elements represent rivers and are projected downwards to the river bed. The model is designed to capture “dynamics” in multiple processes while maintaining the conservation of mass at all cells, as guaranteed by the finite volume formulation. The finite volume formulation also has the ability to handle discontinuous solutions (Leveque 2002). The conservation laws that are conveniently derived from the physical relationships approximate the average state of the process variable over the kernel volume.

In order to perform accurate and efficient simulations, domain decomposition quality should be considered as important as the numerical scheme itself. Mesh size, shape and the ability to capture graded and/or sharp spatial changes depending on the time scale of the interacting hydrologic processes, spatial gradient of the state variables

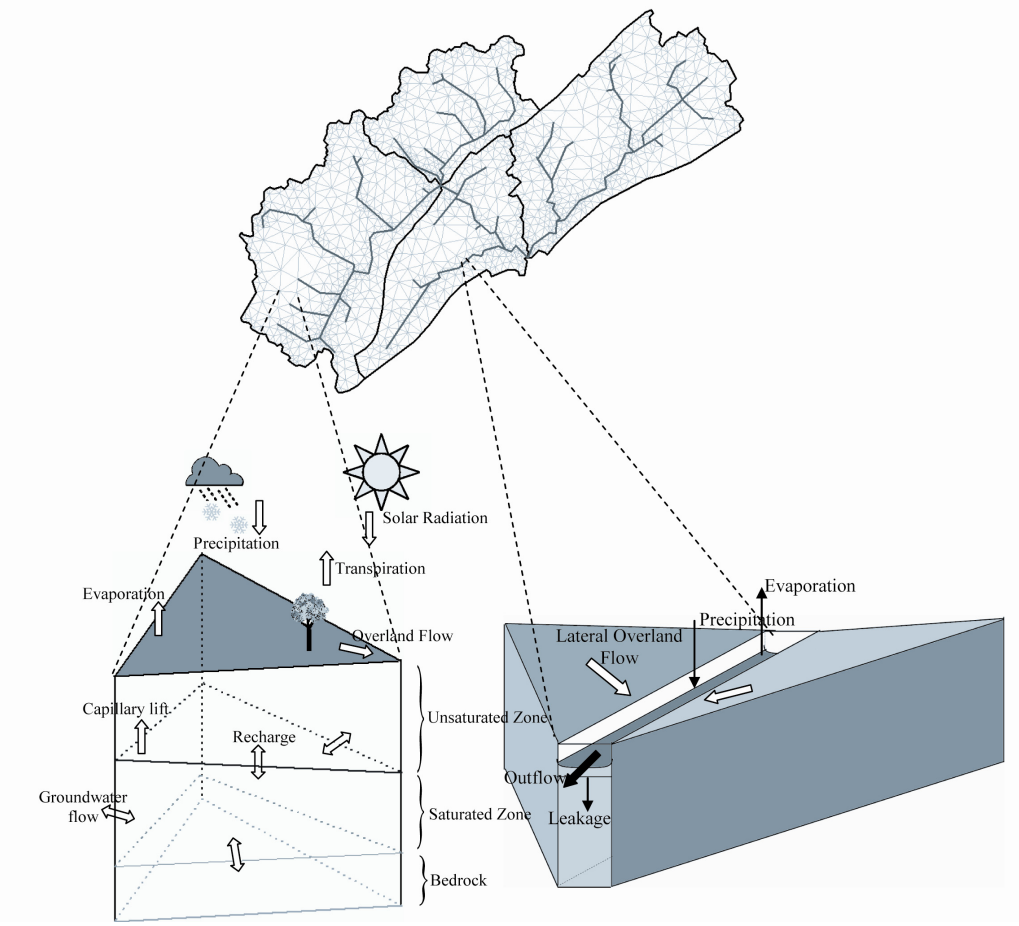

Figure 2.2 All the interacting hydrologic processes in PIHM are defined on prismatic watershed elements or linear river elements. ODEs corresponding to each process from all across the model domain are solved together to predict state variables at next time step.

and the heterogeneity in model parameter distribution determines the stability, convergence and accuracy of the solution. PIHM uses a smart unstructured mesh decomposition that is generated using GIS feature objects to enhance topographic and hydrographic representations, which are discussed in the next section.

2.4. Unstructured mesh generation and GIS objects

Although theoretical and computational aspects of unstructured meshes have been widely documented in computational fluid dynamics literature (Weatherill 1998), limited efforts have been made to generate them using GIS feature-objects for hydrologic modeling applications. This is in part due to the limited use of unstructured meshes in hydrologic modeling, which have been restricted to TINs only (Ivanov *et. al.* 2004), and also because of the disconnect between data structures of the GIS feature objects and geometric objects used in computational geometry applications. Most of the unstructured meshing tools (e.g. Henry and Walters 1993 and Shewchuk 1997) use points or planar straight line graphs (PSLGs) to generate Delaunay triangulations. This necessitates representation of existing GIS feature objects such as points, lines, polygons, junctions and edges as either points or PSLGs only. A PSLG is a set of vertices and segments that satisfies two constraints – a) PSLG must have two vertices that serve as endpoints b) segments in a PSLG are permitted to intersect only at their endpoints. By reprocessing we can essentially reduce all the different feature objects to either a node or a line, making them suitable for use in traditional unstructured meshing tools.

2.4.1. Reprocessing of GIS objects

Data structure of points and junctions can have a representation similar to nodes when both are defined with an identifier; a coordinate location and a corresponding attribute. Edges and Polyline features in GIS have data structures similar to PSLGs when defined by an identifier, number of segments in each compound object, and a start and end node identifier for each segment. Edge features also carry additional topology information. A polygon feature can be viewed as a collection of chained polylines that form a closed boundary around individual areas having no gaps or overlaps (Nyerges 1993). Figure 2.3 shows the data structure of each object type. A GIS representation of a natural watershed

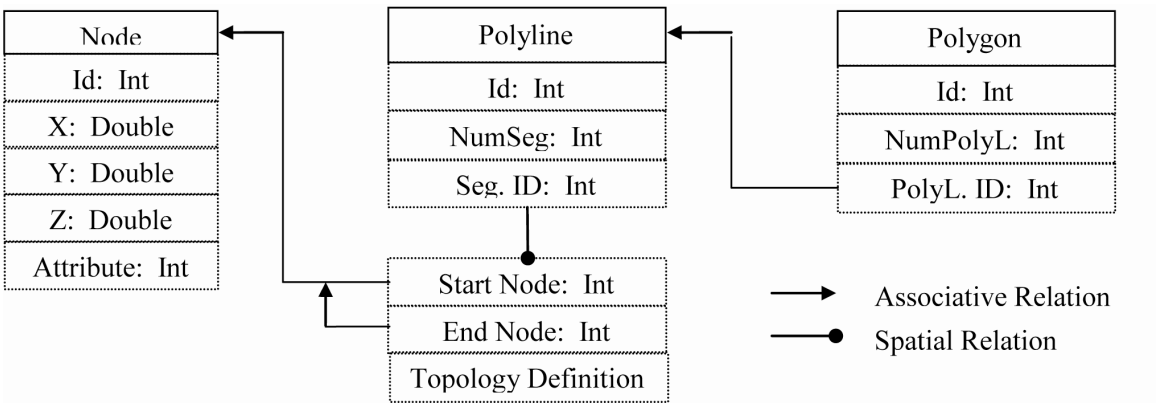

Figure 2.3 Data structure of Node, Polyline and Polygon feature objects. NumSeg ≡Number of line segments in a polyline. Seg. ID ≡ Line segment ID. NumPolyL ≡Number of Polylines. PolyL. ID ≡ Polyline ID.

is a complex multi-polygon feature composed of subshed boundaries (shown in Figure 2.2), lakes, wetlands and river reaches. For application to unstructured meshing tools for watershed modeling, multi-polygon features need to be further broken down into

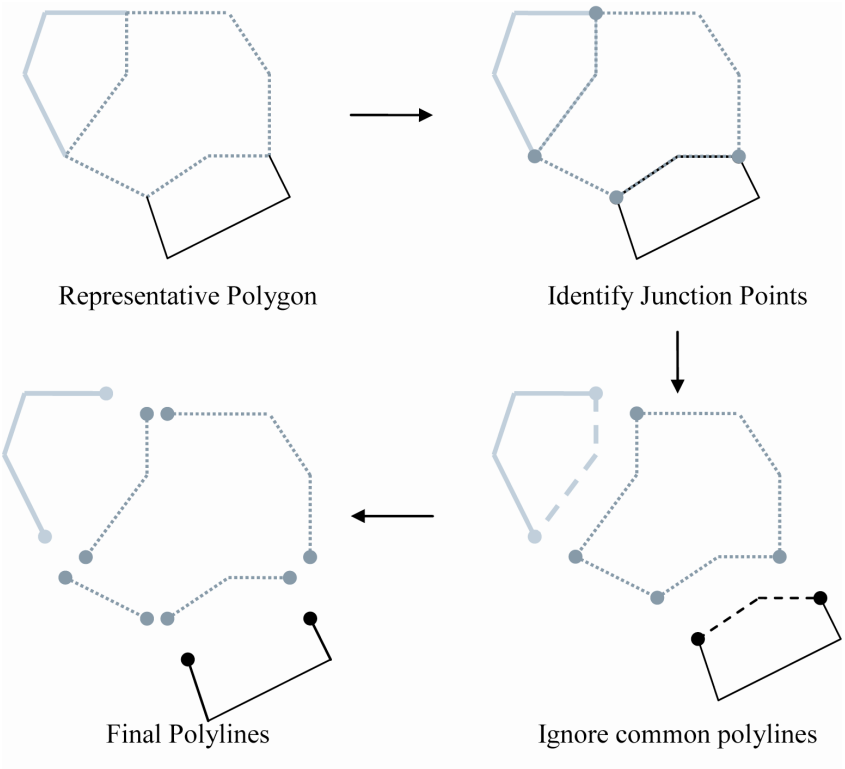

Figure 2.4 Intermediate steps in polygon to polyline simplification.

simplified polyline features. This is accomplished by disintegrating each polygon feature into polylines at junction (intersection) points or at the entry node of a polygon. The

process involves a sequence of four steps- a) Identify polygons that share edges b) Identify the junction nodes of sharing polygons c) Store polyline segments between the two junction nodes or between a junction and an end/start node d) Discard duplicate polyline obtained from either one of the sharing polygons. Identifying the total number of polygons as totPolygon, the pseudocode for transforming multi-polygon into polylines is shown below:

PolygonToPolyline():

```
For i = 0 to totPolygon {
        For j = 0 to (i-1)th Polygon {
                If ((MBD of ith Polygon) ⋂ (MBD of jth Polygon)) ≠ NULL {
                        IdentifyJunctionPoints()
                        Disintegrate() Polygon to PolyLines at junction point(s) and at id = 0
                        Delete() shared polyline from jth Polygon
                }
        }
}
```

Appendix:

If ((MBD of $\mathbf{i}^{th}$ Polygon) ⋂ (MBD of $\mathbf{j}^{th}$ Polygon)) ≠ NULL

➔ Intersection Area ≠ 0

➔ Polygon **i** shares junction(s) with Polygon **j**

IdentifyJunctionPoints():

```
For k = 0 to numPts_1 in IntersectionArea of Polygon 1 {
        For m = 0 to numPts_2 in IntersectionArea of Polygon 2 {
                If (kth Pt1 = mth Pt2) { /* These points are shared by two
intersecting/partially overlapping polygons */
                        /* Following conditions identify a junction node from the shared
nodes */
                        If ((((k-1)th Pt1 = (m-1)th Pt2) AND ((k+1)th Pt1 ≠ (m+1)th Pt2)) OR
                           (((k-1)th Pt1 = (m+1)th Pt2) AND ((k+1)th Pt1 ≠ (m-1)th Pt2)) OR
                           (((k+1)th Pt1 = (m+1)th Pt2) AND ((k-1)th Pt1 ≠ (m-1)th Pt2)) OR
                           (((k+1)th Pt1 = (m-1)th Pt2) AND ((k-1)th Pt1 ≠ (m+1)th Pt2))) {
                                kth Pt1 and mth Pt2 are Junction Points
                        }
                }
        }
```

Legends:

numPts_*:	Number of points of Polygon * in the Intersection Area
Pt*:	Nodal points belonging to polygon *
MBD:	Minimum Bounding Rectangle

A schematic application of the algorithm on a representative multi-polygon feature is shown in a series of steps in Figure 2.4. The algorithm has been incorporated in the implementation of PIHMgis (www.pihm.psu.edu/pihmgis/).

With all GIS feature objects being reduced to a point or a PSLG, a domain decomposition tool like TRIANGLE (Shewchuk 1997) can be used for unstructured mesh decomposition. However the raw polylines and the ones obtained from reprocessing of GIS polygons generally have segment lengths that are very small compared to the

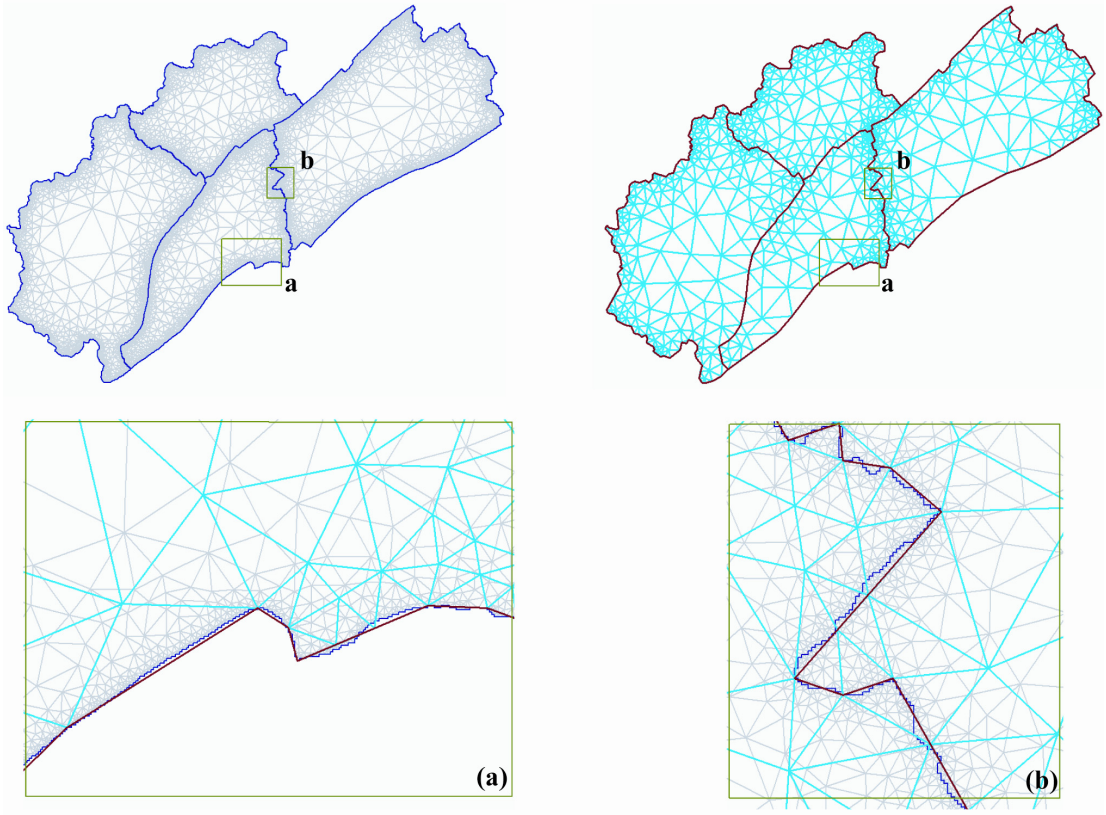

Figure 2.5 Bottom left and right figures show unstructured mesh decomposition of Little Juniata Watershed before and after reconditioning of polyline. Bottom two figures show the zoomed-in fused image of triangulations at two different locations in the watershed. Note the excessive high concentration of triangles formed in the "un-conditioned" case. Polyline reconditioning removes aliasing in the boundaries by removing nodes at unwanted locations.

dynamical scales of interest in the hydrologic model. The smaller segment lengths are an artifact of DEM-processing based watershed delineation algorithms that are available in ArcHydro (Maidment 2002) and TauDEM tool (Tarboton and Ames 2001). Segments obtained from DEM processing have their lengths determined by the resolution of the DEM used for watershed delineation. Digitized watershed polygon boundaries may be composed of segments with smaller lengths than are needed to efficiently represent process dynamics. Smaller segment lengths translate to generation of unnecessarily small triangles in the vicinity of polylines (as shown in Figure 2.5) thus also resulting in an excessive number of mesh elements in the model domain. This places an impractical time-step restriction on the model to maintain numerical accuracy and stability (e.g. the Courant–Friedrichs–Lewy (CFL) condition in explicit time-stepping methods, Courant et al. 1928). In order to produce high-quality meshes while still maintaining the fidelity of the internal and external polyline boundaries, reconditioning of polyline needs to be performed.

2.4.2. Polyline reconditioning

Reconditioning of polyline translates to a simplification of the line boundary by removing small fluctuations or extraneous bends while preserving the essential shape. The approximation error here is controlled by setting a maximum-distance-from-vertex to the approximated polyline criteria. Simplification of polyline is performed based on the Douglas and Peucker (DP) algorithm (1973). The first approximation of the polyline is a line segment connecting the first and last vertices of the polyline. Recursively, the maximum normal departure of each segment of the approximation to the vertices in the original polyline segment is calculated. If the distance from the farthest vertex to this approximate segment is larger than some specified tolerance, then the vertex is added to the approximating polyline. The algorithm terminates when all vertices in the original polyline are within a specified tolerance for distance. Sequential execution of the algorithm on a representative polyline is shown in Figure 2.6. Pseudocode of the algorithm is shown below:

SimplifyLine():

Read points in polyline from **0** to **n**: Pts[node_0, node_1,……..node_n]
/* Recursive simplification. Starts with selection of end points of a polyline */
Simplify (Pts [], tolerance, **0**, **n**)
Connect all MARKEDnode to get Simplified Line

Simplify (Pts [], tolerance, **i**, **j**) :

```
/* Find the vertex in original polyline that is farthest from approximate segment */
If (j+1 > k) {
        MAXdistance =0
        For index = i+1 to j-1 {
                Find distance() of node_index from line segment (node_i ↔ node_j)
                        If (distance() > MAXdistance) {
                                MAXdistance = distance()
                                MARKnode = index
                        }
        }
/* Use the MARKEDnode (that is farthest from approximate segment) to anchor another
set of approximation */
        If (MAXdistance > tolerance) {
                MARKEDnode = MARKnode
                Simplify(Pts[], tolerance, i, index)
                Simplify(Pts[], tolerance, index, j)
        }
}
```

/* Distance calculation between node_index and segment(node_i ↔ node_j) */
/* node_index = (x3, y3); node_i = (x1, y1); node_j = (x2,y2) */

distance():

$$m = \frac{(x3 - x1) * (x2 - x1) + (y3 - y1 * (y2 - y1)}{\|node\_i - node\_j\|^2}$$

$$\text{Distance} = \sqrt{(x3 - (x1 + m(x2 - x1))^2 + (y3 - (y1 + m(y2 - y1))^2}$$

Figure 2.5 shows how polyline reconditioning results in a reduction in the number of triangles formed particularly near the boundaries. The algorithm has been incorporated in the implementation of PIHMgis (www.pihm.psu.edu/pihmgis/).

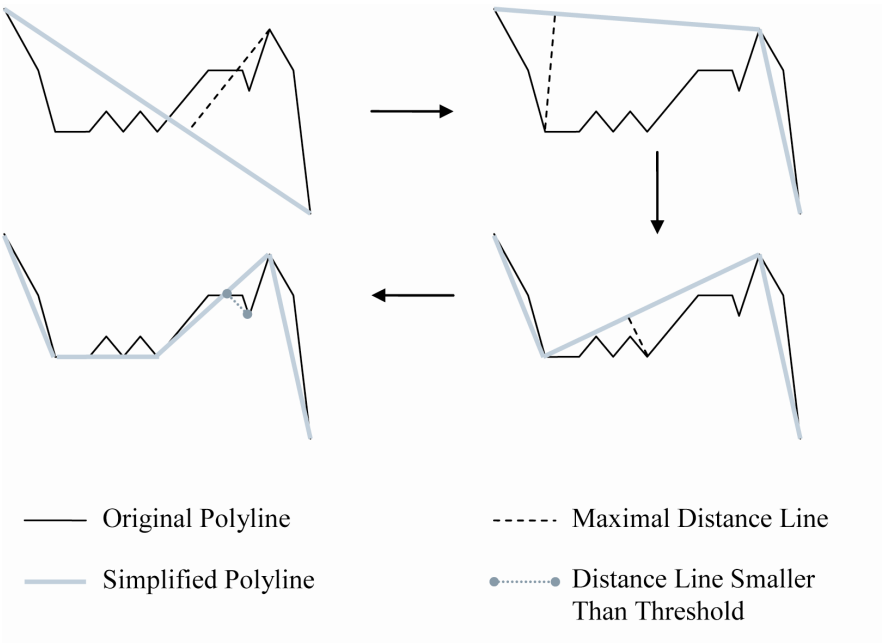

Figure 2.6 Intermediate steps in polyline simplification using Douglas-Peucker algorithm

2.4.3. Delaunay Triangulation based mesh generation

By using Very Important Points (VIPs), junctions, observation station nodes, and the boundary PSLGs as constraints, unstructured meshes that satisfy an "empty circle" condition are generated. Such unstructured meshes are called Delaunay triangles. We note that an "empty circle" condition means that the circumcircles of the triangles does not enclose the vertices of any other triangles in the mesh. Delaunay triangulation also satisfies "max-min angle optimality" condition (Lawson 1977). This optimality criteria essentially ensures a high quality triangulation i.e. triangles created have a circumradius-to-shortest edge ratio (say *M*) as small as possible (Miller *et. al.* 1995). This means that the generated triangles are balanced and not skewed. VIPs that are used as constraints during triangulation are obtained by the implementation of VIP algorithm of Chen and Guevara (1987) or Fowler and Little (1979) on a DEM. External boundary polyline which can be either concave or convex, acts as a spatial limit-constraint in decomposition, beyond which no triangles are generated. The tolerance criteria in polyline reconditioning and VIP algorithms determine the degree of approximation of vector boundaries and raster DEM respectively. Smaller tolerance criteria results in tighter approximations but it also increases the number of unstructured meshes. Figure

2.7 shows the generation of higher resolution meshes with a decrease in polyline tolerance criteria and increase in number of VIP nodes. For all unstructured mesh decomposition

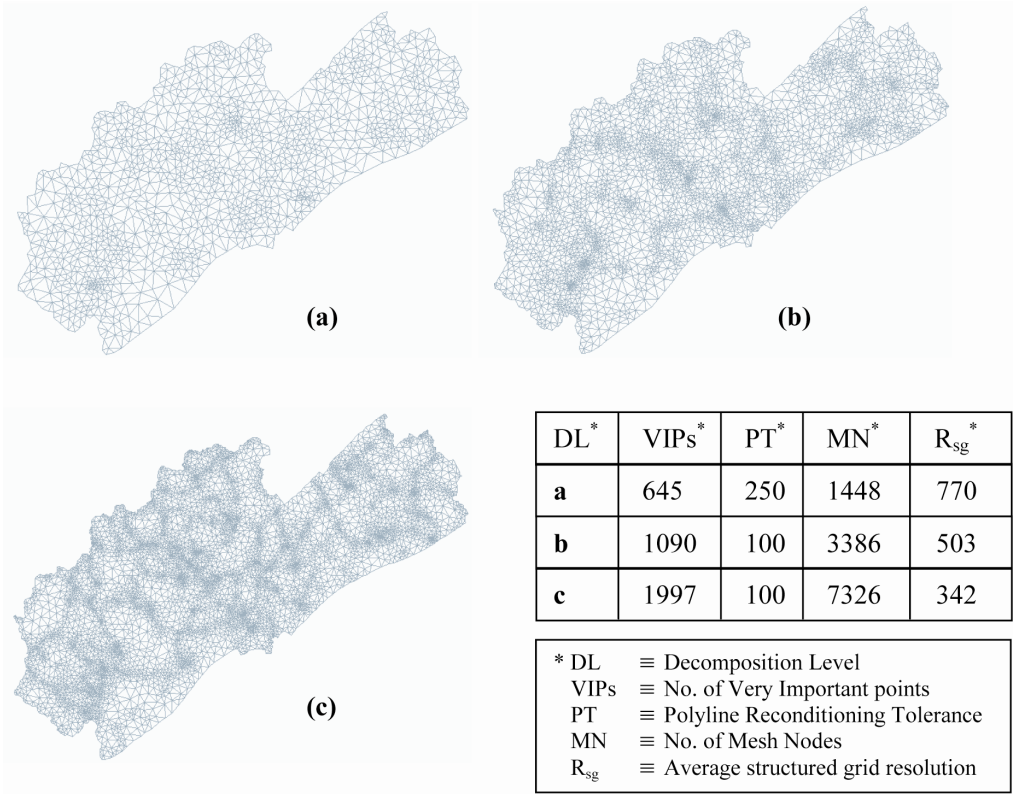

DL*	VIPs*	PT*	MN*	R_{sg}*
a	645	250	1448	770
b	1090	100	3386	503
c	1997	100	7326	342

* DL ≡ Decomposition Level
VIPs ≡ No. of Very Important points
PT ≡ Polyline Reconditioning Tolerance
MN ≡ No. of Mesh Nodes
R_{sg} ≡ Average structured grid resolution

Figure 2.7 The number of mesh elements increases with increasing number of VIPs inserted during Delaunay triangulation and the decreasing tolerance magnitude used in polyline reconditioning of boundaries.

resolutions, triangulations outperform their structured mesh counterparts with the same average resolution in terms of both efficiency and accuracy. Figure 2.8(a) shows the average root-mean-square error (RMSE) in representation of DEM and its slope by a structured grid decomposition of the watershed relative to an unstructured mesh. RMSE is calculated by evaluating the difference in elevation/slopes for both structured and unstructured grids w.r.t original high resolution DEM. Three decomposition levels for unstructured meshes used in calculation of the error statistics correspond to the decompositions shown in Figure 2.7. The average structured grid resolution (R_{sg}) is calculated by

$$R_{sg} = \sqrt{\frac{A}{N_{umn}}} \tag{2.1}$$

where A is the area of the watershed and N_{umn} is the number of nodes in the unstructured mesh. By this simple measure, unstructured meshes outperform structured meshes at all resolutions and for all criteria considered. Figure 2.8(b) shows the average "vector error" per unit length of original polyline boundary in capturing its tortuousities by structured and unstructured grids respectively. Vector Error is calculated by

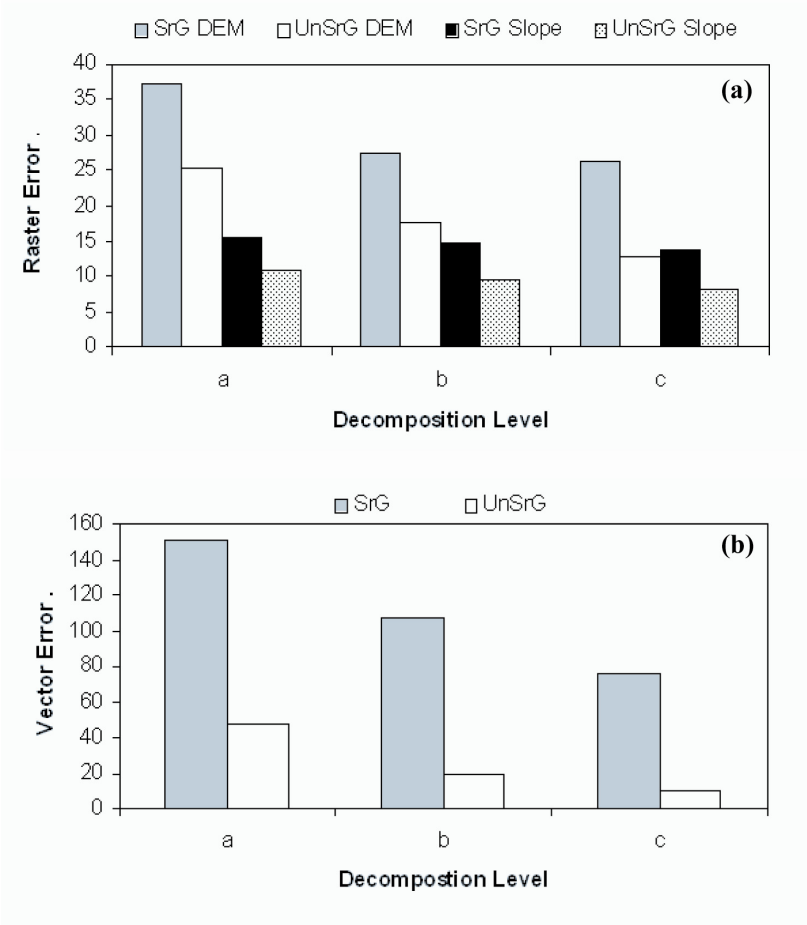

Figure 2.8 (a) Root mean square error in representation of DEM and Slope at three levels of mesh decomposition. Note, Decomposition Level –a,b and c- are same as those shown in Figure 2.7. Structured grids based decomposition leads to larger error in both DEM and Slope representation than Unstructured grids. (b) Root mean square error in representation of polyline per unit length of polyline. At all decomposition levels, unstructured grids agree to the boundaries better than structured grids. Note: SrG ≡ Structured Grid Decomposition, UnSrG ≡ UnStructured Grid Decomposition

calculating the area of the enclosed polygon bounded by original polyline and the corresponding boundary polyline representation used in structure or unstructured meshes. Again unstructured meshes show better performance for the representation of boundary heterogeneities. Obviously with increasing resolution of either type of grids, there is a

reduction in the error magnitude. We note that a standard Delaunay triangulation is not sufficiently suited for hydrologic modeling as it does not ensures generation of "quality" triangles and also does not respect the internal boundary constraints.

2.5. Model and Data Constraints on Decomposition

Depending on the numerical formulation of the physical equations, local topographic gradients and physiographic heterogeneity, generation of unstructured meshes can be customized to enhance representational accuracy and to capture different time scales of process interaction. Customization criteria are generally based on constraints posed by hydrologic model design and data heterogeneity.

2.5.1. Model constraints

Many of the unstructured mesh based models like PIHM (Kumar *et. al.* 2008, Qu and Duffy 2007) and RSM (Lal *et. al.* 2003) assume that the flux across the triangle edges is always orthogonal. This assumption simplifies the numerical formulation of process equations and also saves extra computation in defining the directional components of the fluxes. The "orthogonal" condition is ensured by considering a circum-center (instead of centroid) as the representative location of triangular elements. We note that the line joining the circumcenter of neighboring triangles will always be perpendicular to the common side shared by the triangles. Triangulations generated based on a circumcenter formulation also aids diagonal dominance (Baker *et. al.* 1988) and faster convergence of

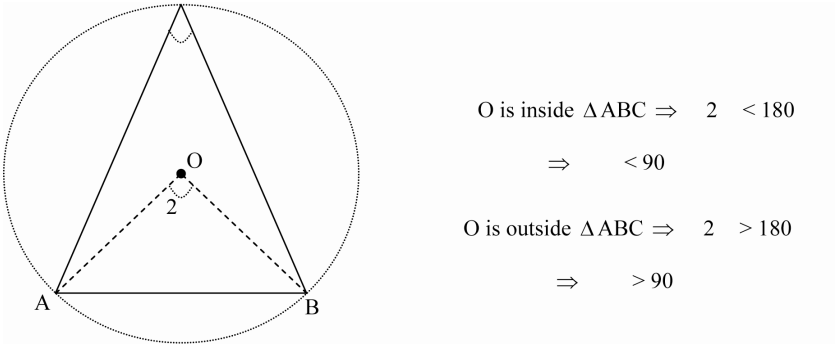

Figure 2.9 Circumcenter O of ΔABC will lie inside its boundaries if and only if the triangle is acute angled i.e. $\alpha < 90$.

the numerical method (Vavasis 1993). However, as shown in Figure 2.9, the circum-center of obtuse angled triangles can sometimes fall outside the triangle. To avoid this condition requires a constraint on the triangle shape that all the angles have to be acute. It is evident from Figure 2.10 that the upper bound on the ratio *M* (circumcenter-to-shortest triangle edge) ensures that the lower bound on the smallest angle of the triangle is $Sin^{-1}(\frac{1}{2M})$ and vice versa (Shewchuck 1996). The lower bound on the smallest angle in turn bounds the largest angle of the triangle also i.e. if the smallest angle is θ then the largest angle can not be larger than 180-2θ. This implies that by manipulating the value of *M*, we can

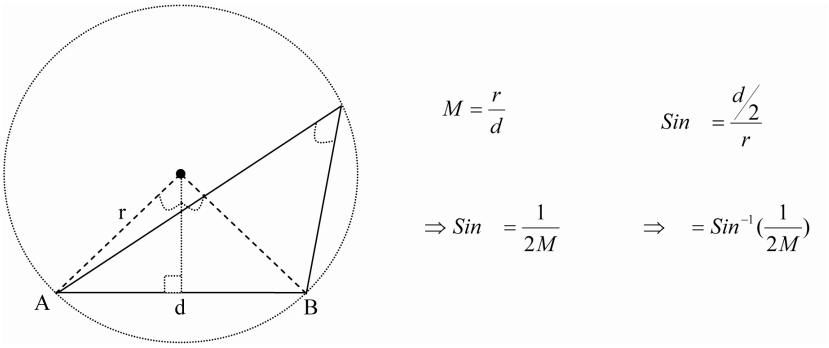

Figure 2.10 The upper bound on *M* (ratio of circumradius to smallest triangular edge) is controlled inversely by an angle α that is subtended by the smallest side AB of the triangular element on the opposite vertex.

have delaunay triangles with its largest angle bounded. Ruppert's Delaunay refinement algorithm (Ruppert 1995) employs a bound of $M = \sqrt{2}$ which means the angles of the triangles range between 20.7^o and 138.6^o while Chew's Delaunay refinement algorithm (Chew 1993) employs a bound of $M = 1$ which means the angles range between 30^o and 120^o.

Another model constraint desirable for unstructured mesh generation is size. Maximum allowable size of the triangles determines the total number of discretized elements and hence the computational load and memory storage requirements for a simulation. Furthermore, meshes are expected to have the ability to grade from small to large elements over a relatively short distance. A larger value of *M* translates to sharp gradation in triangle size. A Delaunay triangulation algorithm proposed by Bern *et al.* (

1994), Baker *et al.* (1988) and Hitschfeld and Rivara (2002) generates non-obtuse triangles only, perfect for use in circumcenter based model formulations. Nonetheless, these algorithms have limited flexibility in terms of controlling the upper bound on the number of nodes in triangulation, the implementation of VIPs and PSLGs as internal boundaries and also in terms of spatial gradation in triangle size. The user must settle for a tradeoff between the number of elements in the watershed and the number of triangles that violate the non-obtuse criterion. Ruppert's algorithm (Ruppert 1995) generates nicely graded and optimal-size triangles while relaxing the non-obtuse triangle criteria. This algorithm produces a mesh whose size (number of elements) is at most a constant factor larger than the size of the smallest possible mesh that meets the same angle bound (Shewchuk 1997). For the relatively small percentage of triangles that violate the non-obtuse criterion, the centroid is assumed to be the representative of triangular element.

2.5.2. Data constraints

Thematic spatial data that relate hydrographic and hydrogeologic parameters (e.g. soil maps, stream cross-sections and wells/sinks) (Peuquet 1988), can be used as constraints on the generation of unstructured meshes. These data sets can be irregular or regular sample points, contours, polygons, grid cells and triangular nets. All these types of data sets can be handled as one of the three kinds of constraining layers (Bern and Eppstein 1992) in domain decomposition as discussed earlier:

2.5.2.1. Internal p*olygons/polylines*

Reprocessed internal polygons and polylines can serve as an internal boundary for triangulation which essentially means that they can support triangulation on either side of boundary. The triangulation generated while taking into account the polyline PSLGs as constraining boundaries is called a constrained Delaunay triangulation (CDT). Internal boundaries pose an extra constraint for Delaunay triangles as their interior can not intersect a boundary segment and their circumcircles should not encloses any vertex of the PSLG that is *visible* from the interior of the triangle (Shewchuk 1996). Two points are

said to be visible to each other when no PSLG lies between them. CDT has been also used by Vivoni *et al.* (2005) while using landscape indices as the PSLG. However, constrained Delaunay leaves some of the triangular elements adjacent to the PSLG to be non-delaunay. By the addition of extra Steiner points on the PSLGs, such triangles are transformed to follow a conformed Delaunay Triangulation property while still respecting the shape of the domain as well as the PSLG.

2.5.2.1.1. Typical internal polygons: Thematic classes and hydrodynamic descriptors. Examples of internal polygon boundaries are thematic classes like soil types

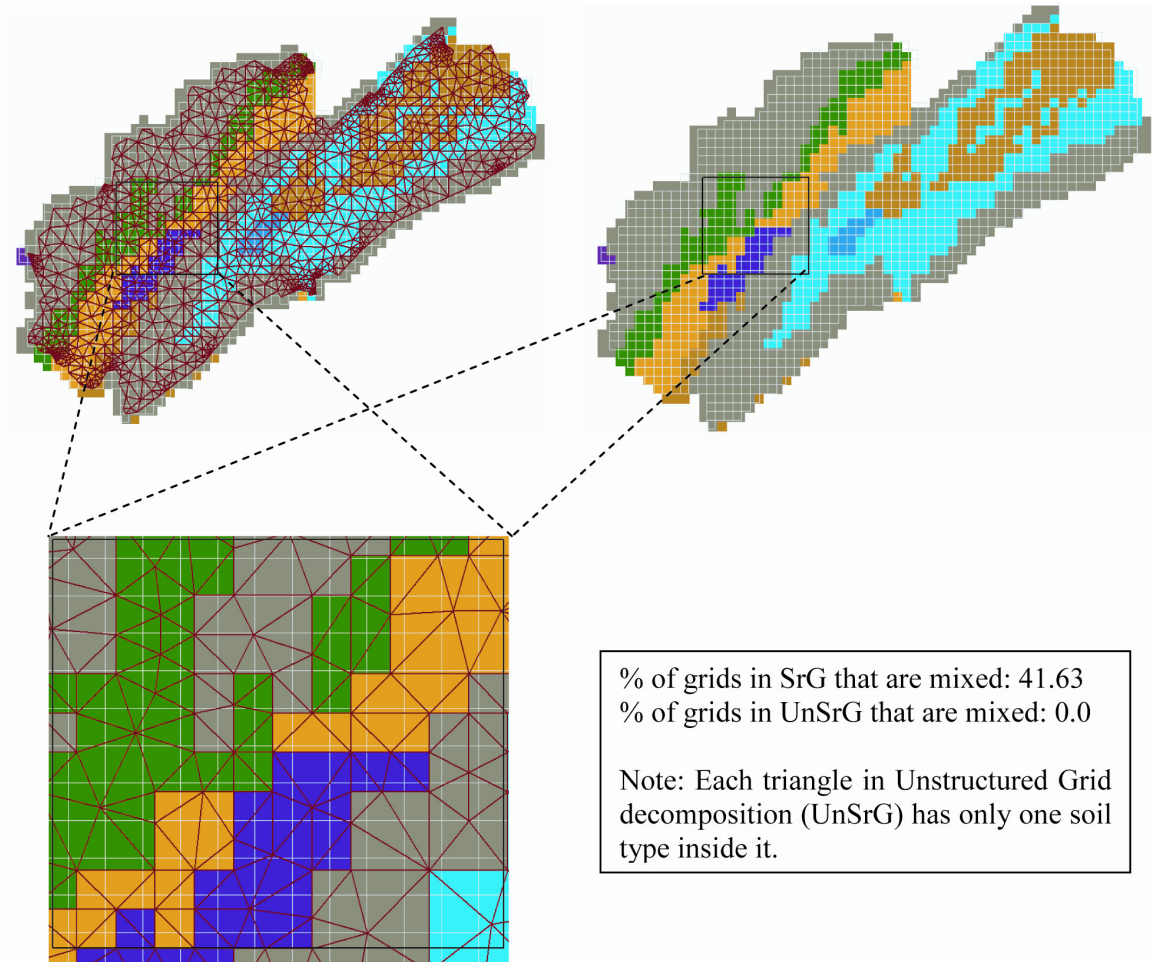

Figure 2.11 Top left unstructured mesh decomposition (UnSrG) is generated based on thematic class (soil type) boundary as constraint. Top right structured mesh (SrG) decomposition has same spatial resolution as the grid on left. Colored grid in the background of both the decompositions is a soil type map. The zoomed-in image shows that SrG (in light grey) have multiple soil classes within them. UnSrG edges (in red or dark grey (in black and white)) overlap soil class edges thus resulting in a "one soil class assignment" to each triangle

and land use/land cover types or hydrodynamic descriptors like subshed boundaries and hypsometry.

The unique advantage of using thematic classes as constraints in decomposition is that the resulting model grid contains a single class. This leads to non-introduction of any additional data uncertainty arising from subgrid variability of themes within a model grid. Figure 2.11 highlights this concept, where an unstructured mesh generated using soil theme as a constraint leads to decomposition where each triangle has a single soil type. For structured grid decomposition with the same average resolution as the unstructured mesh, we observe that 41.63 % percent of the grids have mixed themes. Generating grids that do not follow edges of thematic classes (as shown in the case of structured grids) introduces uncertainty in parameterization and its effect is widely documented in hydrologic modeling literature (Beven 1995, Yu 2000).

Hydrodynamic descriptors can be thought of as topographic controls, such as subshed boundaries and hypsometry that influence the movement of water through the landscape (Winter 2001). Implementing hydrodynamic descriptors as constraints in domain decomposition (as shown in Figure 2.5) has several advantages in modeling:

1) Precise evaluation of the magnitude of groundwater flux exchanges across the subshed boundaries. Since the subshed topographic boundaries are fixed (and so are the mesh edges that are anchored to these boundaries), seasonal shifts in the ground water divide and flux with respect to the subshed boundaries can be tracked.

2) The specified no-flux condition on surface water flow across the subshed boundaries reduces computation load.

3) It is evident from Figure 2.5 that the triangular elements along the boundaries are smaller than internal elements. The subshed boundaries also represent relatively higher regions in the watershed where the hydrologic gradient can be expected to be high. Large gradients in elevation directly affect changes in temperature, wind, precipitation and vegetation. In order to capture these changes, relatively smaller sized meshing is needed. The approach to triangulation of subshed boundaries outlined above helps to achieve this.

4) This approach also provides a multi-scale framework of modeling the basin at watershed and subshed scales simultaneously.

Another hydrodynamic descriptor is hypsometry. Shun and Duffy, 1998 observed that a simple three-region hypsometric classification of watershed area into upland, lowland and middle elevation intervals could capture important elevation changes in precipitation-temperature-runoff. The uplands generally act as recharge zones, intermediate elevations as translational zones and lower regions as discharge zones. Hypsometry, or area – altitude relationship, relates horizontal cross- sectional area of a drainage basin to the relative elevation above base level (Strahler 1952). Strahler (1958) interpreted regions with low hypsometric values as eroded landscapes and high values as young landscapes with low erosion. This means that polygons corresponding to the three hypsometric divisions can be assigned unique attributes according to their characteristic time scales of groundwater flow or geomorphic evolution. Separating boundaries can be treated as contours. Figure 2.12 shows the hypsometric curve for Little Juniata Watershed. The three hypsometric divisions are obtained using the Jenks's optimal classification strategy (Coulson 1987 and Jenks 1977). With this method, intra-class variance of elevation values is minimized and the differences between classes are maximized resulting in better representation of groupings and patterns inherent in the dataset. As is evident from Figure 2.12 regions in the basin that are relatively flat have larger triangular elements whereas the mountainous regions are discretized into small elements.

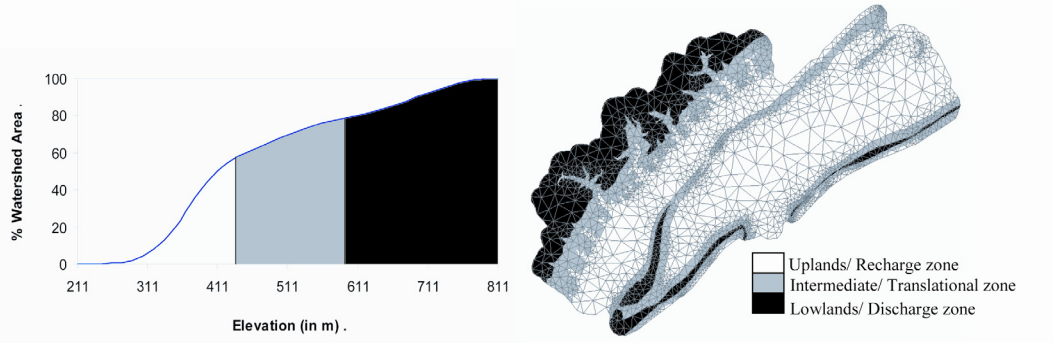

Figure 2.12 Left figure shows the elevation hypsometric curve of Little Juniata Watershed. Delaunay Triangulation of Little Juniata Watershed while using hypsometric division as a constraint. Expectedly in regions of higher topographic extremes/gradient, concentration of meshes is higher. Note the formation of smaller triangles besides the streams. Similar divisional constraints can be used for vegetation and climate regimes

Traditional slope preserving meshes that retain high nodal density in regions of high terrain variability (Lee 1991) are generated when the constraints are derived from elevation.

2.5.2.1.2. Typical internal PSLGs: River network. An important example of constraining PSLGs used in domain decomposition is a river network. A higher concentration of triangles generated along the river network (see Figure 2.2) reflects the relatively faster hydrodynamics of riparian regions. Accurate assessment of flooded areas that get inundated with slight increase in river head can be performed when smaller triangles are generated in the vicinity of the river network. This facilitates flood-plain and flood inundation zone mapping.

We note that with the increasing number of internal boundary constraints, the number of mesh elements increases. This implies that a tradeoff exists between accuracy of representation of watershed properties (which is gained through the use of internal boundary constraints) and computational load. While the choice of any of these constraints is optional, any decision to insert an internal boundary must take into account the tradeoff between accuracy and computational load. Assuming that there is no uncertainty associated with the location of internal boundary itself, quantification of accuracy gained after the use of an internal boundary can be done at - a) "pre-modeling" stage, where accuracy in representation of a watershed property on decomposed domain is assessed, and b) "post-modeling" stage, where accuracy in representation of modeled physical states such as evapotranspiration, spatial distribution of snow etc. are assessed. For particular boundary types (like soil and vegetation), the uncertainty associated with their position and degree of transition can be significant. In such situations, representational accuracy calculations must be weighted by the inherent positional uncertainty. The error posed by such uncertainty can be limited to a certain extent by using a buffer region (and the boundary) on the either side of the boundary as constraints. Buffer constraint will lead to generation of smaller mesh elements on the either side of the boundary until some specified width quantified by "position/transition-uncertainty". In such cases, mixed transition properties can be specified to the cells inside the buffer while using “hard” categorical properties outside of it.

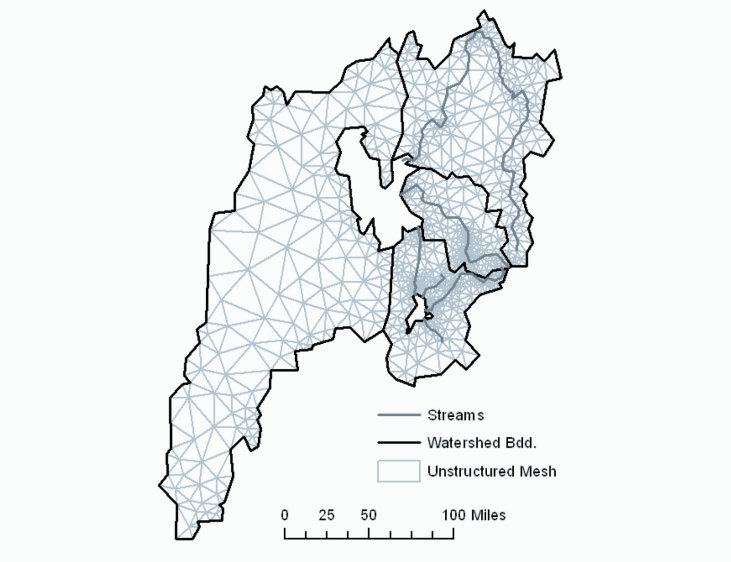

Figure 2.13 Domain decomposition of Great Salt Lake Basin. Note that no triangles are created inside the lake.

2.5.2.2. Holes

The data structure of a hole is exactly that of a polygon. But there is a constraint on the operation. Holes are regions inside the basin boundary or other polygons that act as an external boundary and so are not triangulated. One example of a hole is a lake. Figure 2.13 shows the Great Salt Lake and Utah Lake within Great Salt Lake basin regions. Assuming the height of water in the lake is same everywhere within its boundary, the lake can be considered as a single control volume entity for modeling. This of course saves computational load where the assumption is valid. For a model scenario of increasing lake levels from a minimum pool, the adjacent elements will be submerged. However, because of the relatively small triangles adjacent to the boundary, a more accurate depiction of temporal changes in spatial extent of lake boundary and inundated areas can be performed.

2.5.2.3. Points

Constraining points along with the Steiner points act as vertices for triangulation. A Steiner point is a node that is inserted in a line to divide it into smaller segments. It is not

a part of the original set of constraining points and is generated only during triangulation. A typical constraining point can be the stage observation stations at hydraulic control

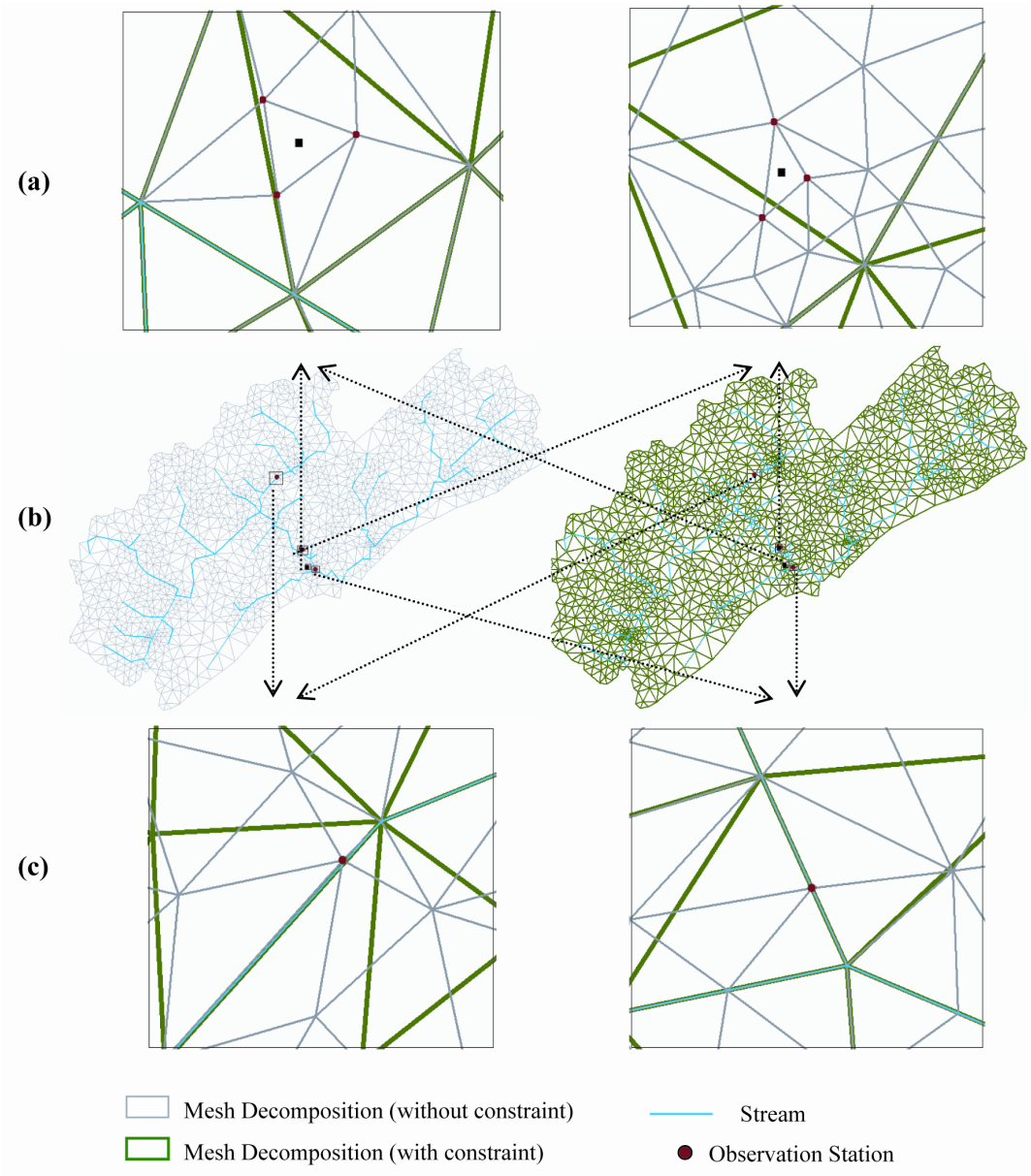

Figure 2.14 (a) Zoom-in of mesh decomposition with and without using groundwater observation stations as constraints for two locations inside the watershed (b) Mesh decomposition with (right side, green) and without (left side, grey) using observation stations as constraints (c) Zoom-in of mesh decomposition with and without using stage observation stations as constraints for two locations on Little Juniata River. We note that in constrained decomposition, triangulations are generated such that the observation stations lie directly on the mesh nodes

structures like weirs, gates, pumps etc or ground water measuring stations. Modeled results of state variables at these constraining points can be compared directly to the

observed values. This reduces any uncertainty in comparison of model results to observation as it happens in most cases where observation stations are not exactly the modeled locations. Figure 2.14 shows mesh decomposition for two cases, one with observation stations as constraint and the other without it. We note that the observation station on the river, as well as in the watershed is left to dangle somewhere in the middle of the discretized element in the unconstrained decomposition case. For comparison with stage or groundwater level obtained from the model in such cases will need interpolation of modeled results to observation locations. On the other hand in a constrained decomposition case, observation stations can also act as a node for triangulation resulting in simulation of state variables exactly at the modeled locations. To put it simply, modeled location and observation locations are the same in the constrained decomposition case. In the future, constrained domain decomposition based on the sensor-networks locations should facilitate direct assimilation of observed data into the model (Reed et. al. 2006)

2.6. Advances in hydrologic modeling

Using the constrained decompositions discussed earlier, integrated modeling of hydrologic processes in Little Juniata Watershed (shown in Figure 2.2) is performed. For detailed model related information, readers are referred to Kumar *et al.* 2008. The model generates a large amount of spatio-temporal data of each hydrologic state such as interception storage, snow depth, overland flow, ground water depth, soil moisture, river flow and evapotranspiration. Figure 2.15 shows a representative spatial distribution of modeled evapo-transpiration at two snapshots in time. We also show the spatial distribution of average river streamflow, percentage of time different sections of the river is gaining and finally the streamflow time series at four separate locations in the watershed. These are few of the spatio-temporal predictions obtained from model

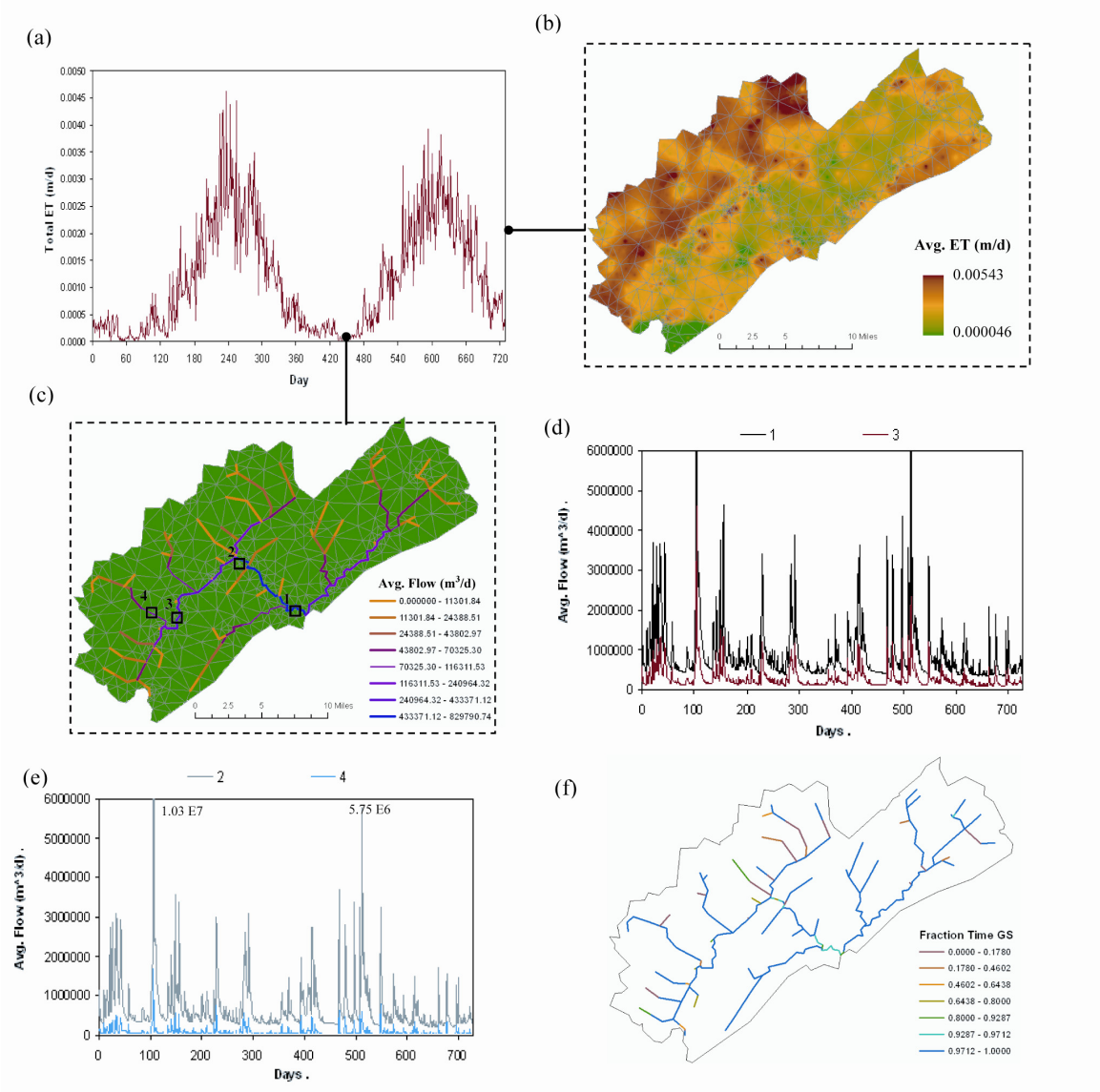

Figure 2.15 (a) shows the average evapo-transpiration (ET) time series for the Little Juniata watershed for two year period. Snapshots for spatial distribution of ET during the maximum and minimum extremes are shown in (b) and (c) respectively. Since we have used same color range to represent both extremes, ET appears to be uniform everywhere (though that is not the case) during winter as the values are quite small. (d) and (e) shows the streamflow hydrograph at four locations in the stream network. (f) shows the percentage of time each stream segment gains water from the aquifer. We note that all the results shown above are for a simulation period of 2 years ranging from Nov, 1983 to Oct. 1985

simulation. The model results shown in Figure 2.15 are from a static decomposition of the watershed. A higher resolution modeling with least additional computational burden can be performed by a) selective "zooming" in an area of interest while leaving discretization in rest of the watershed to be coarse, and b) adaptively changing the grid

resolutions in different parts of the watershed depending on the spatial rate of change of a physical state in a localized region.

Such advanced modeling is facilitated by the flexibility in generation of multi-resolution nested and adaptive (refinement/derefinement) unstructured meshes while using different constraints.

2.6.1. Nested triangulation

Nested models are already common in other fields of science, (e.g. fluid dynamics: Carey *et al.* 2003, geology: Gautier *et. al* 1999; and climatology: Loaiciga *et al.* 1996). In

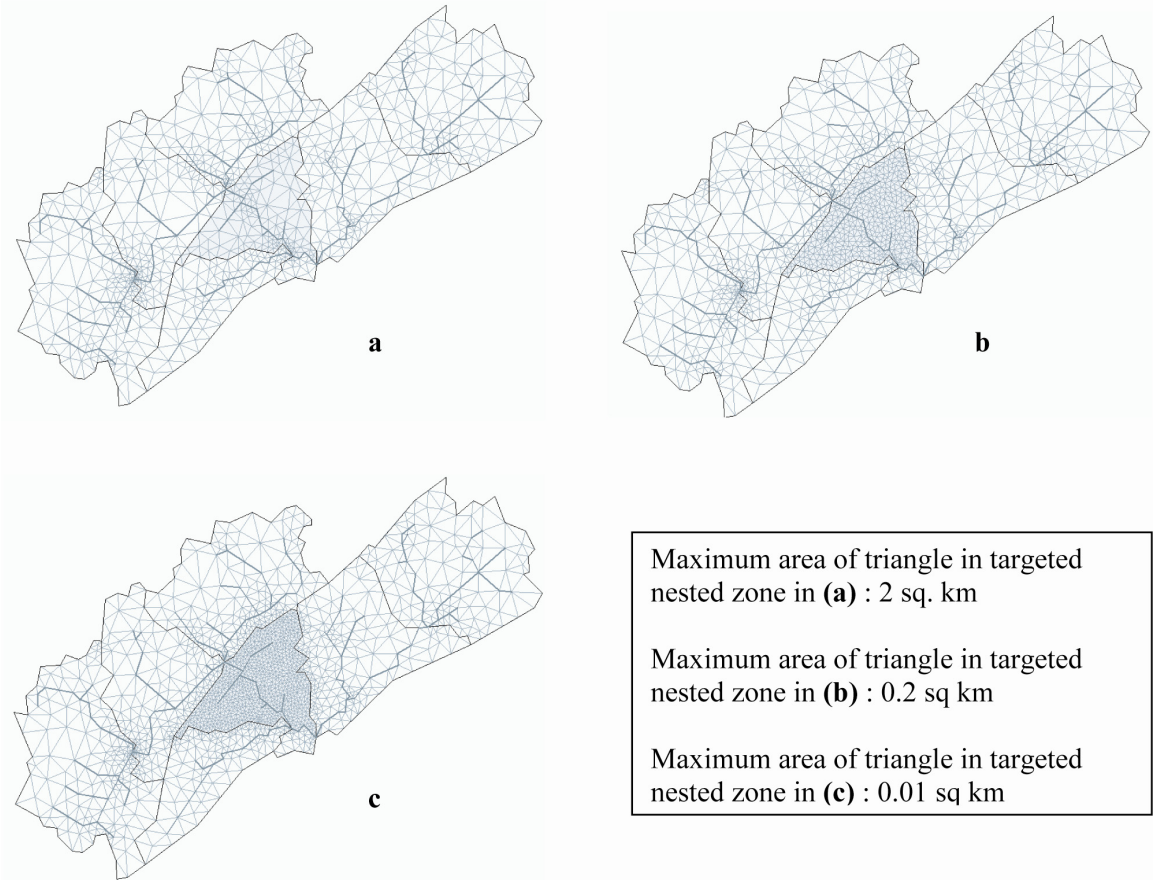

Figure 2.16 Nested Mesh decomposition of Little Juniata Watershed while using subsheds as internal boundary. For computational efficiency a localized region of the basin (around main stem of Little Juniata River, shaded in the figure) can be discretized to higher spatial resolution elements while leaving rest of the basin at coarser resolution. Under a single framework, mesoscale to microscale modeling can be performed.

hydrologic modeling, development of nested models is still in its infancy stage (Grayson and Blöschl 2001). The basic principle behind this strategy is triangulation of the domain

of interest into large elements combined with locally refined or nested grids where higher resolution is necessary. The main advantage of the approach is seamless assimilation of spatially varied forcings, parameters or the constitutive relationships in different regions of the basin. This nested-grid configuration makes it possible to combine realistic large-scale simulations with mesoscale forecasts for selected regions. Figure 2.16 shows that triangles generated in a subshed around the main stem of Little Juniata River are much smaller than the rest of the basin. This local high-resolution representation of parameters and processes minimizes computation. Nested triangulations will have applications for:

1) integrated hydrologic studies in larger basins which have high resolution data-support in one of its subwatersheds. The subwatershed in this case can be decomposed at relatively higher resolution than the rest of the basin to take maximum advantage of the high resolution observed data while still maintaining all boundary conditions and conservation rules.

2) studies which focus on understanding scaling issues and comparison of scaling effects across the basin.

3) the implementation of new physical processes in watershed and river basin studies which are relatively more computationally intensive. One example might be physics - based snows melt modeling. Modeling snow-melt is quite critical in mountainous basins as it directly affects flooding, contaminant transport, water supply recharge and erosion (Walter *et. al.* 2005). Snow-melt modeling generally falls in two categories: *temperature-index* models that assume an empirical relationship between air temperature and melt rates and *energy- balance* models that quantifies the melt amount by solving energy balance equations. The most common justification for temperature index snowmelt models is the need for a reduced number of input variables, and also the model and computational simplicity. Several researchers (Ambroise et al. 1996, Fontaine et al. 2002) have derived acceptable results from temperature index models. Nevertheless, because of the incorporation of energy interaction between topography, wind and radiation, an energy-balance model is better placed in simulation of spatial heterogeneity in snow accumulation and redistribution (Winstral and Marks 2002). Since, energy based models like SNOBAL (Marks et al. 1998) run at shorter time intervals, need a high resolution DEM and forcing data as its support and solves a large number of state

variables; they can only be run over a small watershed with present computational constraints or run in an offline weakly coupled mode. So an energy based modeling can be performed in the high resolution nested watershed while temperature-index modeling approach can be used for rest of the watershed.

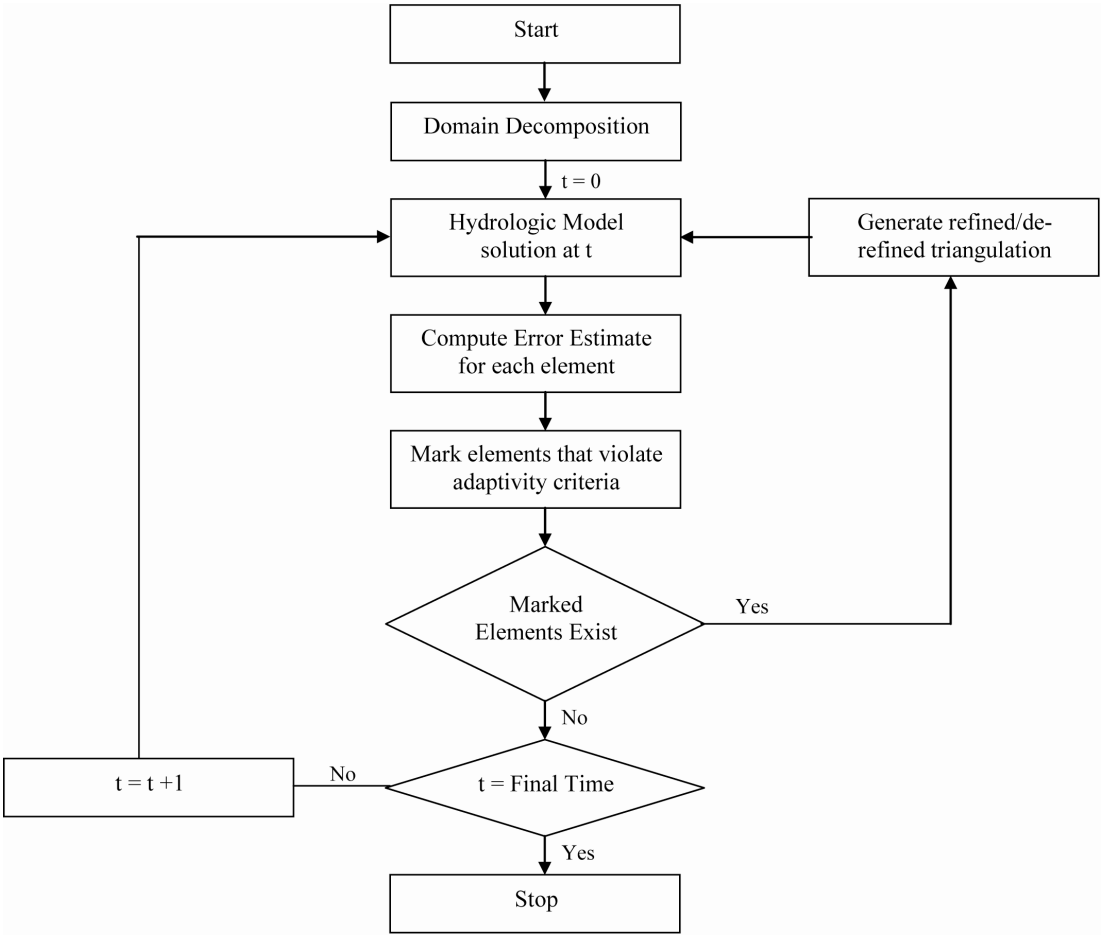

Figure 2.17 Flow chart depicting the dynamically adaptive refinement/de-refinement algorithm for hydrologic modeling. Depending on the hydrodynamics, a particular region can be refined to finer or coarse triangular elements in order to capture the hydrologic process accurately

4) watersheds susceptible to large and frequent floods in limited areas but where the runoff is generated in upland non-flooding areas. Higher resolution discretization in a watershed will lead to accurate mapping of areas which will get flooded with given increase in stream-stage level (Shamsi 2002).

5) understanding the relation of groundwater flow dynamics within a subshed to the rest of the basin. Subshed topographic boundaries are simply a surface descriptor and as noted by Brachet 2005, the groundwater flow divide can change seasonally affecting the water

flux in and out of the watershed. With a nested modeling approach, movement of ground water divide can be mapped with acceptable precision.

Clearly the nested triangulation strategy has implications for studying the scaling behavior and scale transitions with a river basin.

2.6.2. Adaptive refinement/derefinement of triangulation

The triangulation and domain representation discussed above, is spatially adaptive in the sense that the resolution of the elements are not uniform. The resolution and distribution of triangles depends on the constraining layers, the tolerance in VIP generation and the polyline reconditioning algorithms, and the boundary heterogeneities. Clearly, widely varying spatial and temporal scales, in addition to the nonlinearity of the dynamical system can raise interesting and challenging modeling problems. In many applications, because of the particular dynamics of the problem, meshes may need to be further (de)refined locally after initial computation. An example is when the computed solution is rapidly varying in time within small areas of the domain while the solution is relatively slow in other parts. Solving such a problem more efficiently and accurately requires a solution-adaptive triangulation strategy. This is a necessity for resolving coupled physics with different time scales which is encountered in hydrologic models. Solution adaptation can save several orders of magnitude in computational load by avoiding under-resolving high-gradient regions in the problem, or conversely, over resolving low gradient regions at the expense of more critical regions. While this strategy can prove problematic within finite difference and finite element analyses, finite volume methods, particularly those based on a triangular mesh system, lend themselves quite naturally to automatic adaptive refinement/de-refinement procedures (Sleigh et. al. 1995).

Dynamically adaptive grid approaches have long been used in astrophysical, aeronautical and other areas of computational fluid dynamics problems (Berger and Oliger 1984, Berger and Colella 1989). Zhao *et al.* (1994) used a Riemann solver approach to calculate fluxes on unstructured, mixed quadrilateral-triangular grid system in river and flood plain. Sleigh *et* al. (1998) used adaptive refinement/de-refinement for computational efficiency while predicting flow in river and estuaries using unstructured

finite volume algorithm. For a finite volume integrated hydrologic model like PIHM, adaptive refinement can be carried out in the regions where intermittent dynamics occurs. An example is an ephemeral channel. Since the channel is dry for most part of the year, there is no need to have an *a priori* high-resolution grid. Depending on the status of the channel network, the dynamics will trigger adaptive refinement/de-refinement. Other situations include hortonian runoff, convective precipitation in a part of basin and sudden increase in river stage due to dam break or flash floods. In each case adaptive refinement/de-refinement of existing triangulations will save on the computation load. Figure 2.17 shows the flow diagram depicting the refinement/de-refinement procedure. Refinement is performed by inserting carefully placed vertices until the triangular element meets constraints on element quality and size which is decided *a priori*. Inserting a vertex to improve elements that don't satisfy the refinement criterion in one part of a mesh will not unnecessarily perturb a distant part of the mesh that has no "bad" elements. That is, insertion of a vertex is a local operation, and hence is inexpensive except in unusual cases. The refinement/de-refinement criterion is generally based on metrics that

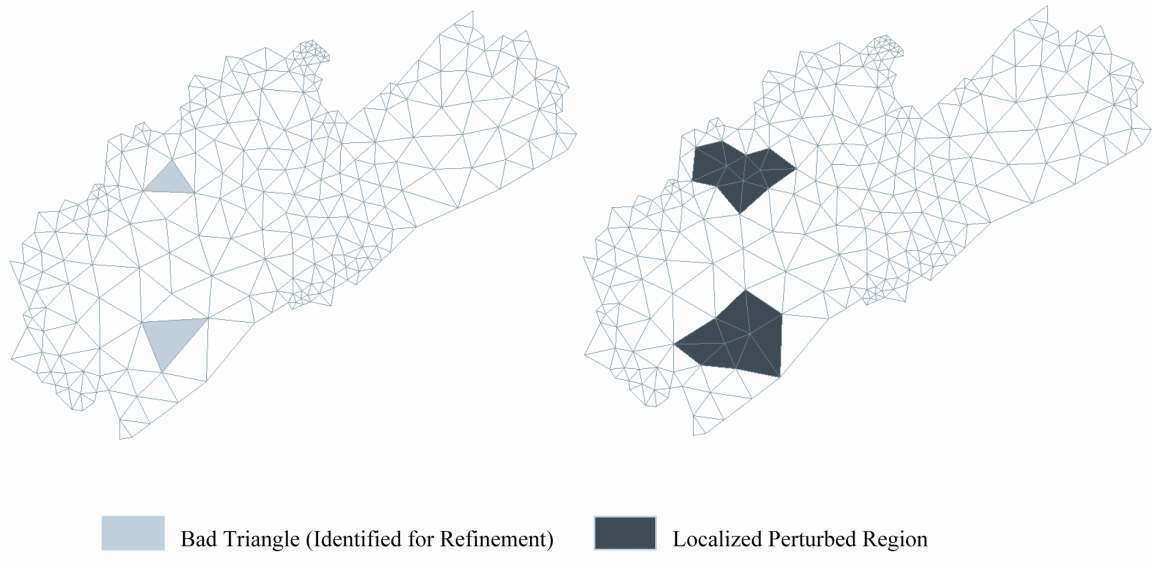

Figure 2.18 Coarse-scale unstructured mesh decomposition of Little Juniata Watershed (Left). At any time *t* during simulation, two triangles (light grey) are marked as Bad Elements depending on spatial gradient estimate of a state variable and are identified for refinement. Decomposition on the right shows insertion of a node inside the marked elements and the resulting perturbed region. Note the formation of new triangles and the triangulated area that gets perturbed is very small relative to the whole watershed. Triangles in the unperturbed region remain same

quantify a sudden change in magnitude of a state variable over a localized area or time. Figure 2.18 shows refinement of two marked triangles in different parts of domain. It is obvious from the figure that the original triangulation is affected locally only.

2.7. Conclusion

A strategy for unstructured mesh decomposition is proposed which captures the phenomenological and hydrologic complexity of the watershed while minimizing the equations to be solved. The framework provides a tight coupling between geo-data and the processes that are modeled on it. The strategy seamlessly incorporates computational geometry based algorithms to process GIS feature objects for discretization for model domain. The framework incorporates the constraints posed by hydrologic process dynamics, numerical solver, data heterogeneity and computational load. It outperforms structured grids based representations in terms of accurate representation of raster and vector layers. Polygon reprocessing and polyline reconditioning algorithms facilitate the use of available GIS feature objects in domain decomposition. Flexibility of the framework in terms of model implementation, model development, data and process constraints, and elevation-derived-VIPs, provides added advantages when compared to traditional TINs. Rapid prototyping of meshes which better reflect the constraints of the problem under consideration can be obtained. The problem constraints that are addressed include: the computational burden, the need for reduction in uncertainty of state variables, the accurate specification of boundary conditions, the application of multiscale or nested models, and the need for dynamically adaptive refinement/de-refinement.

In summary, the “support-based” domain decomposition and unstructured grid framework provides a close linkage between geo-scientific data and complex numerical models. The strategy extends the GIS based algorithms to be used in distributed numerical modeling setting. The framework is generic and can be implemented for linking other numerical process models of mass, momentum and energy to their respective geodatabases.

2.8. References

ABBOT, M.B., BATHURST, J.C., CUNGE, J.A., O'CONNELL, P.E. and RASMUSSEN, J. 1986, An Introduction to the European Hydrological System – Systeme Hydrologique Europeen, "SHE", 2 : History and Philosophy of a Physically-based, Distributed Modelling System. *Journal of Hydrology*, 87, 61-77

AMBROISE, B., FREER, J., BEVEN, K.J., 1996. Application of a generalised TOPMODEL to the small Ringelbach catchment, Vosges, France. *Water Resources Research*, 32, 2147–2159.

BAKER B.S., GROSSE E., and RAFFERTY, C.S., 1988. Nonobtuse triangulation of polygons. *Discrete and Computational Geometry*, 3, 147-168.

BAND, L. E., 1986. Topographic partition of watersheds with digital elevation models. *Water Resources Research*, 23(1), 15–24.

BERGER, M. J., and COLELLA, P., 1989. Local adaptive mesh refinement for shock hydrodynamics. *Journal of Computational Physics*, *82* (1), 64–84.

BERGER, M., and OLIGER, J., 1984. Adaptive mesh refinement for hyperbolic partial differential equations. *Journal of Computational Physics*, 53 , 484–512.

BERN, M.W., EPPSTEIN, D., 1992. Mesh Generation and Optimal Triangulation, *Computing in Euclidean Geometry: Lecture notes on computing, World Scientific*, 23-90.

BERN, M., MITCHELL, S., and RUPPERT, J., 1994. Linear-size nonobtuse triangulation of polygons. In *Proceedings of 10th ACM Symposium on Computational Geometry*, 221-230.

BEVEN K.J., 1995. Linking Parameters Across Scales: Subgrid Parameterizations and Scale Dependent Hydrological Models. *Scale Issues in Hydrological Modelling*, Kalma, J.D., Sivapalan M. (eds); Wiley: Chichester, pp. 263-281.

BLAYO, E., and L. DEBREU, 1999. Adaptive mesh refinement for finite difference ocean model: some first experiments. *Journal of Physical Oceanography*, 29, 6, 1239-1250.

BRAUN, J., and SAMBRIDGE, M., 1997, Modelling landscape evolution on geological time scales: a new method based on irregular spatial discretization. *Basin Research*, 9, p. 27-52.

CAREY, G., KIRK B. and LIPNIKOV, K, 2003. Nested grid iteration for incompressible viscous flow and transport. *International Journal of Computational Fluid Dynamics*, 17(4):253-262

CASTILLO, J.E. (Eds.), 1999. Mathematical Aspects of Numerical Grid Generation. SIAM, Philadelphia.

CHEW, L.P., 1993. Guaranteed-Quality Mesh Generation for Curved Surfaces. In *Proceedings of the Ninth Annual Symposium on Computational Geometry* (San Diego, California), pages 274–280. Association for Computing Machinery

COULSON, M.R.C., 1987, In the matter of class intervals for choropleth maps: With particular reference to the work of George F. Jenks: *Cartographica*, 24, p. 16-39

COURANT, R., FRIEDRICHS, K.O., LEWY, H., 1928. Uber die partiellen differenzgleichungen der mathematischen physic (on the partial difference equations of mathematical physics). *Mathematische Annalen* 100, 32–74.

DOUGLAS, D., PEUCKER, T., 1973. Algorithms for the reduction of the number of points required to represent a digitized line or its caricature. *The Canadian Cartographer* 10, 112–122.

ENTEKHABI, D., and EAGLESON, P.S., 1989. Land surface hydrology parameterization for atmospheric general circulation model including subgrid scale spatial variability. *Journal of Climate*, 2, 816-831.

FAIRBANKS, J., PANDAY, S., and HUYAKORN, P.S., 2001. Comparisons of linked and fully coupled approaches to simulating conjunctive surface/ subsurface flow and their interactions. In Seo, Poeter, Zheng, Poeter, (Eds). MODFLOW 2001 and Other Modeling Odysseys— Conference Proceedings, Golden, CO;p. 356–61

FONTAINE, T.A., CRUICKSHANK, T.S., ARNOLD, J.G., HOTCHKISS, R.H., 2002. Development of a snowfall-snowmelt routine for mountainous terrain for the soil water assessment tool (SWAT). *Journal of Hydrology* 262, 209–223.

GAUTIER, Y, BLUNT, M.J., CHRISTIE, M.A., 1999. Nested gridding and streamline based simulation for fast reservoir performance prediction. *Computational Geosciences* 3:295-320

GOODRICH, D.C., 1990. Geometric simplification of distributed rainfall-runoff model over a range of basin scales. PhD Dissertation, Tucson, AZ: Department of Hydrology and Water Resources, University of Arizona, 361 pp.

HENRY, R.F., WALTERS, R.A., 1993. Geometrically based, automatic generator for irregular triangular networks. *Communications in Numerical Methods in Engineering* 9 (7), 555–566.

GRAYSON, R. and BLÖSCHL, G. 2001. *Spatial patterns in catchment hydrology*. Cambridge University Press.

IVANOV, V.Y., VIVONI, E.R., BRAS, R.L. and ENTEKHABI, D., 2004. Catchment hydrologic response with a fully-distributed triangulated irregular network model. *Water Resources Research*, 40.

HITSCHFELD, N., RIVARA, M.C, 2002, Automatic construction of non-obtuse boundary and/or interface delaunay triangulations for control volume methods, *International Journal of Numerical Methods in Engineering*, 55,803-816.

JENKS, G.F. 1977. Optimal data classification for choropleth maps. Occasional paper No. 2, Department of geography, University of Kansas, Lawrence.

JONES, N.L., WRIGHT, S.G., and MAIDMENT, D.R., 1990. Watershed delineation with triangle based terrain models. *Journal of Hydraulic Engineering* 116:1232-1251

KUMAR, M., BHATT, G. and DUFFY, C., 2008. Role of process and data coupling in Mesoscale Watershed Model, *Advances in Water Resources* (in review)

KOLLET, S. J., and MAXWELL, R. M., 2006, Integrated surface-groundwater flow modeling: A free-surface overland flow boundary condition in a parallel groundwater flow model, *Advances in Water Resources*, (29)7, 945-958

LEE, J., 1991. Comparison of existing methods for building triangular irregular network models of terrain from grid digital elevation models. *International Journal of Geographical Information Systems*, 5(3), pp. 267–285.

LOAICIGA, H.A., VALDES, J.B., VOGEL, R., GARVEY, J., SCHWARZ, H., 1996. Global warming and the hydrologic cycle. *Journal of Hydrology* 174:83-127

MAIDMENT, D.R. (Ed.), 2002, Arc Hydro: GIS for Water Resources (Redlands, CA: ESRI Press, 2002).

MARKS, D., KIMBALL, J., TINGEY, D., LINK, T., 1998. The sensitivity of snowmelt processes to climate conditions and forest cover during rain-on-snow: A study of the 1996 Pacific Northwest flood. *Hydrological Processes* 12: 1569-1587.

MILLER, G.L., TALMOR, D., TENG, S.H., and WALKINGTON, N., 1995. A Delaunay Based Numerical Method for Three Dimensions: Generation, Formulation, and Partition. In *Proceedings of the Twenty- Seventh Annual ACM Symposium on the Theory of Computing* (Las Vegas, Nevada), pages 683–692.

MOORE I. D., O'LOUGHLIN, E.M., BURCH. A., 1988. Contour-based topographic model for hydrological and ecological applications, *Earth Surface Processes Landforms*,13,305-320.

NYERGES, T.L., 1993. Understanding the scope of GIS: Its relationship to environmental modeling. In *Environmental Modeling with GIS*, Goodchild, M.F., Parks, B.O. and Steyaert, T. (Eds.), New York: Oxford University Press, pp. 75-93.

PANDAY, S., and P.S. HUYAKORN, 2004. A fully coupled physically-based spatially-distributed model for evaluating surface/subsurface flow, *Advances in Water Resources*, 27, 361-382.

PEUQUET, D.J., 1988, Representations of geographic space: Towards a conceptual synthesis. *Annals of the Association of American Geographers*, 78, pp. 375-394.

PITMAN, A.J., HENDERSON-SELLERS, A., and YANG, Z.L., 1990. Sensitivity of regional climates to localised precipitation in global models. *Nature*, 346, 734-737.

REED, P. M., BROOKS, R. B., DAVIS, K. J., DEWALLE, D. R., DRESSLER, K. A., DUFFY, C. J., LIN, H., MILLER, D. A., NAJJAR, R. G., SALVAGE, K. M., WAGENER, T., and YARNAL, B., 2006. "Bridging River Basin Scales and Processes to Assess Human-Climate Impacts and the Terrestrial Hydrologic System." Part of CUAHSI/NSF Hydrologic 4 Vision Series, *Water Resources Research*, 42.

RUPPERT, J. 1995. A Delaunay Refinement Algorithm for Quality 2-Dimensional Mesh Generation. *Journal of Algorithms*, 18(3):548–585.

SHUN.T., and DUFFY, C.J.,1998. Low-frequency oscillations in precipitation, temperature, and runoff on a west facing mountain front: A hydrogeologic interpretation, *Water Resources Research*.,35,191-201

STRAHLER, A.N., 1952. Hypsometric (area-altitude) analysis of erosional topography. *Geological Society of America Bulletin*, 64:165-176.

STRAHLER, A.N., 1958. Dimensional analysis applied to fluvially eroded landforms, *Geological Society of America Bulletin*, 69, 279-300.

SHAMSI, S.U., 2002, GIS applications in floodplain management, In *ESRI GIS user conference*, Tel Aviv.

SHEWCHUK, J.R., 1997. Delaunay refinement mesh generation, PhD Thesis, Carnegie Mellon University.

SHEWCHUK, J.R., 1996. Triangle: Engineering a 2D quality mesh generator and Delaunay Triangulator. In *1st workshop on Applied Computational Geometry*, ACM, 124-133.

SLEIGH, P. A., GASKELL, P. H., BERZINS, M., WARE, J. L. and Wright, N. G., 1995. A reliable and accurate technique for the modelling of practically occuring open channel flow. In *Proceedings of the Ninth International Conference on Numerical Methods in Laminar and Turbulent Flow*, 881-892.

SLEIGH, P. A., GASKELL, P. H., BERZINS, M., WARE, J. L. and Wright, N. G., 1998. An unstructured finite volume algorithm for predicting flow in rivers and estuaries. *Computer and Fluids*, Vol. 27, 4, 479-508.

TARBOTON, D.G., 1997, A new method for the determination of flow directions and contributing areas in grid digital elevation models. *Water Resources Research*, 33, no. 2, p. 309-319.

TARBOTON, D. G., and D. AMES. 2001. Terrain Analysis Using Digital Elevation Models. In *Forest Service 2001 Geospatial Conference*, Salt Lake City.

THOMPSON, J.F., (Eds.), 1982. *Numerical Grid Generation*. North-Holland

VAVASIS, S.A., 1993. Stable finite elements for problems with wild coefficients. Tech. Report TR93-1364, Dept. of Comp. Science, Cornell University.

VIVONI E.R., IVANOV, V.Y., BRAS, R.L. and ENTEKHABI, D., 2004. Generation of triangulated irregular networks based on hydrological similarity. *Journal of hydrologic engineering*, 9, 4. 288-302.

VIVONI, E.R., TELES, V., IVANOV, V.Y, BRAS, R.L., and ENTEKHABI, D., 2005. Embedding landscape processes into triangulated terrain models. *International Journal of Geographical Information science*, Vol. 0, No. 0, 1-29.

WALTER, M.T, BROOKS, E.S., MCKOOL, D.K., KING, L.G., MOLNAU, M., and BOLL.J., 2005. Process based snowmelt modeling: does it require more input data than temperature-index modeling? *Journal of Hydrology*, 65-75.

WEATHERILL, N. P., 1998, Introduction to Unstructured Grids in Handbook of Grid Generation, Thompson, J. F., Soni, B. K., and Weatherill, N. P. (Eds.), CRC Press.

WINSTRAL, A. and MARKS, D. 2002. Simulating wind fields and snow redistribution using terrain- based parameters to model snow accumulation and melt over a semi-arid mountain catchment, *Hydrologic Processes*, 16, 3585-3603.

WINTER, T.C., 2001, The concept of hydrologic landscapes. *Journal of the American Water Resources Association*, 37, p. 335-349.

WOO., M.K, 2004. Boundary and border considerations in hydrology, *Hydrological Processes*, 18, 1185-1194.

YU, Z., 2000. Assessing the response of subgrid hydrologic processes to atmospheric forcing with a hydrologic model system. *Global Planet Change*, 25, pp. 1–17

ZHAO, D.H., SHEN, H.W., TABIOS, G.Q., LAI, J.S. and TAN, W.Y., 1994. Finite-volume Two-dimensional Unsteady-flow Model for River Basins, *Journal of Hydraulic Engineering*, 120(7), 863–883.

CHAPTER 3:

An Object Oriented Shared Data Model for GIS and Distributed Hydrologic Models

3.1. Introduction

Physics-based distributed hydrologic models (DHMs) simulate hydrologic state variables in space and time while using information regarding heterogeneity in climate, land use, topography and hydrogeology (Freeze and Harland 1969; Kollet and Maxwell 2006). Because of the large number of physical parameters incorporated in the model, intensive data development and assignment is needed for accurate and efficient model simulations. A Geographic Information System (GIS) has the ability to handle both spatial and non-spatial data, and to perform data management and analysis. However it lacks the sophisticated analytical and modeling capabilities (Maidment 1993; Wilson 1996; Abel *et. al.* 1994 and Kopp 1996). On the other hand from the physical model perspective, they generally lack data organization and development functionalities. Moreover, the data structure they are based on does not facilitate close linkage to the GIS and decision support system (DSS) (National Research Council 1999). This increases the model setup time, hinders analysis of model output results, compounds data isolation, reduces data integrity and limits concurrent access of data because of broken data flow between the data, physical model, and decision support systems. The problem is acute when dynamic interaction is required during the model simulation. A need for restructuring of individual GIS and physical-modeling systems provides the motivation for this paper.

One important effort in bridging the gap between hydrologic model and GIS is due to Smith and Maidment (1995), who developed a Hydrologic Data Development System (HDDS) based on ARC/INFO. Other instances of development of interfaces for modeling are water and erosion prediction project (WEPP) interface on GRASS (Engel *et al.* 1993), an interface between ArcInfo and HEC modeling system (Hellweger and Maidment 1999), BASINS by EPA (Lahlou *et al.* 1998), SWAT by Luzio *et al.*(2002) , inland waterway contaminant spills modeling interface (Martin *et al.* 2004) and Watershed Modeling System (WMS, Nelson 1997). An overview of attempts to develop hydrologic models inside GIS is reviewed by Wilson (1999). We note that all the above approaches were basically trying to “couple” a GIS and a process-based hydrologic model for efficient processing, storing, manipulating, and displaying of hydrogeological data. WMS was a major development and different from other attempts in that it was a

stand-alone GIS system totally dedicated to hydrologic application. Development of Arc Hydro (Maidment 2002) was another important step in defining an exhaustive data model for a hydrologic system and providing a framework for storing and preprocessing geospatial and temporal data in GIS. The developed data model provided rules for the structure, relationships and operations on data types often used in hydrologic modeling. McKinney and Cai (2002) went a step further in reducing the gap between GIS and models by outlining an object oriented methodology to link GIS and water management models. In the process, they identified the Methods and Objects of the water management models that can be represented as spatial and thematic characteristic in the GIS.

In this paper we propose a robust integration methodology that facilitates seamless data flow between data and model functionalities thus making the interactions between them fluid and dynamic. The objective of this work is to lay the foundation for fully integrated and extensible, GIS-DHM system through a shared data model that can support both of them. The shared data model provides a) flexibility of modification and customization b) ease of access of GIS data structure by the hydrologic model c) richness for representing complex user defined spatial relations and data types, and d) standardization easily applicable to new model settings and modeling goals. The data model has been developed using state of the art computer programming concepts of object oriented programming (OOP). We also discuss in detail the intermediate steps of designing the shared data model from a GIS data model. The emphasis in this exercise is elucidating program design, not the coding details. The resulting data model supports a coupled framework that serves as a GIS interface to Pennstate Integrated Hydrologic Model (PIHM) and is called PIHMgis. PIHMgis is developed on the QGIS open source framework. The strategy presented here shows that the concepts and capabilities unique to the coupling approach can easily be implemented in other GISs and DHMs. An example of the integrated software proposed here has been developed using object oriented programming languages like Qt and C++ and is open source (http://sourceforge.net/projects/pihmgis/).

Table 3.1 Characteristics of different levels of integration between a GIS and a hydrologic model

Characteristics	Coupling Level		
	Loose	Tight Integration	Embedding
Shared User Interface	×	√	√
Shared data and method base	×	√	√
Intra-simulation Model Modification	×	×	√
Intra-simulation Query and Control	×	×	√
Above translates to →	• Distinct GIS and Hydrologic Modeling packages with individual interfaces • Information sharing through file exchange which can be tedious and error prone • Underlying advantage is: different packages facilitate independent development	• Data exchange is automatic • Merges different tools in a single powerful system • Avoids inconsistency and data loss originating from redundancy and heterogeneity of method base	• Steerable numerical simulation in terms possibility of changes in parameter or processes while running • Significantly complex programming and data management • Changes to the code are not easy because of its monolithic structure.

3.2. Integration methodology

Efforts to couple GIS with hydrological models (see Table 3.1) generally follows either a loose, tight, or embedded coupling (Nyerges 1993; Goodchild 1992) strategy. Watkins *et al.*, (1996) and Paniconi *et al.*,(1999) have discussed in detail the relative advantages and disadvantages of coupling in terms of watershed decomposition, sensitivity and uncertainty analysis, parameter estimation and representation of the watershed. Loose coupling is prone to data inconsistency, information loss and redundancy, leading to increased model setup time. At the same time, loosely coupled approaches are much simpler to design and program. At the other extreme, embedded coupling can leave the code inertial to change because of its large and complex structure (Goodchild 1992; Fedra 1996). Nonetheless embedded coupling provides the dynamic ability to visualize

and suspend ongoing simulations, query intermediate results, investigate key spatial/temporal relations, and even modify the underlying hydrologic model parameters (Bennett 1997).

From our point of view both tight and embedded coupling strategies offer the necessary degree of sharing between GIS and hydrologic model for efficient data query, storage, transfer and retrieval. We also note (from Table 3.1) that both coupling strategies underscore the existence of a shared data model in their implementation. Clearly, the integration of GIS tools and simulation models should first address the conceptual need of a shared data model that is implemented on top of a common data and method base. In order to design such a shared data model, we follow a four-step approach. First we carry out identification and classification of the various data types that form the hydrologic system (section 3). Then we design the object oriented data model for the data types identified in the previous step (section 4). In the third step, we study the hydrologic model structure in terms of its data needs and adjacency relationships (section 5). Finally, re-representation of the GIS-data data model classes to conform to the distributed hydrologic model data structure is carried out (section 6). Next we discuss in detail the design steps of the shared data model.

3.3. Conceptual classification of raw hydrologic data

A hydrologic model domain encompasses a wide range of hydraulic, hydrologic, climatic and geologic data including topography, rivers, soil, geology, vegetation, land use, weather, observation wells and fractures. A conceptual classification of raw hydrologic data needs to incorporate data of different origins, representation types and scales.

Figure 3.1 illustrates a hierarchical categorization of real data typically required in hydrologic models. The design is intended to incorporate spatially heterogeneous thematic data types along with associated time series data, derived data and attributes. The data types can be defined as field-based and object-based (Goodchild 1992). Field based data define a spatial (or temporal) framework consisting of a set of locations related to each other by (temporal) distance, direction and contiguity (Galton 2001). Object based data are collection of individual entities that are characterized by geometry,

topology and non-spatial attribute values (Heuvelink 1998). Spatial information to these entities is explicitly defined either as attributes or as a function of location that is inherent in a point, a line or a polygon. We note that this kind of distinction in GIS features has been traditionally associated with raster and vector data only. However, here we extend the concept of field-data by considering it as a "continuous concept" whose unitary element exists either in space or time with respective entity information attached to it. For example, a unit element of any tessellation, like a grid or a TIN (triangular regular network) has an associated value that defines a property/characteristic magnitude/value anywhere within the field boundary. Similarly for a time series, there is a value attached to any instant in the time series.

Figure 3.1 shows further sub-classification of "field" and "object" data types that are relevant to hydrologic modeling. An object consists of points, line and polygons. The fundamental scope of the object sub-data types has been extended, in order to incorporate complex features (made up of multiple simple features) and the dynamic nature of observer and observables. We classify Points as Static and Floating depending on their primary existence in space or time. For example, a static point can be identified by a location at which a time series data such as wind speed is being observed. On the other hand, an example of a Floating point can be a volunteer in a soil moisture measurement field campaign who goes around the field taking soil moisture samples at different locations. In the former case, the observer is fixed in space and is observing state in time while in the latter case a continuous time clock is fixed to the observer while he/she moves around and takes sporadic samples at different locations. Static points have been further subcategorized into Isotropic and Anisotropic points. Anisotropic points are locations whose entity attributes needs information regarding direction and magnitude and possibly magnitude changing with direction (e.g. a 2nd rank tensor). An example of an anisotropic property representation at a point is hydraulic conductivity (Freeze and Cherry 1979). Line objects have been sub-categorized into standard 2D and a 3D line. 3D polylines are made up of line segments that exist in three dimensions. For example, an underground pipe network for drainage/waste removals etc. which can change directions/planes in 3D at junctions. Polygon objects have been subcategorized into Static and Floating polygons. Floating polygons are bounded regions whose areas changes in

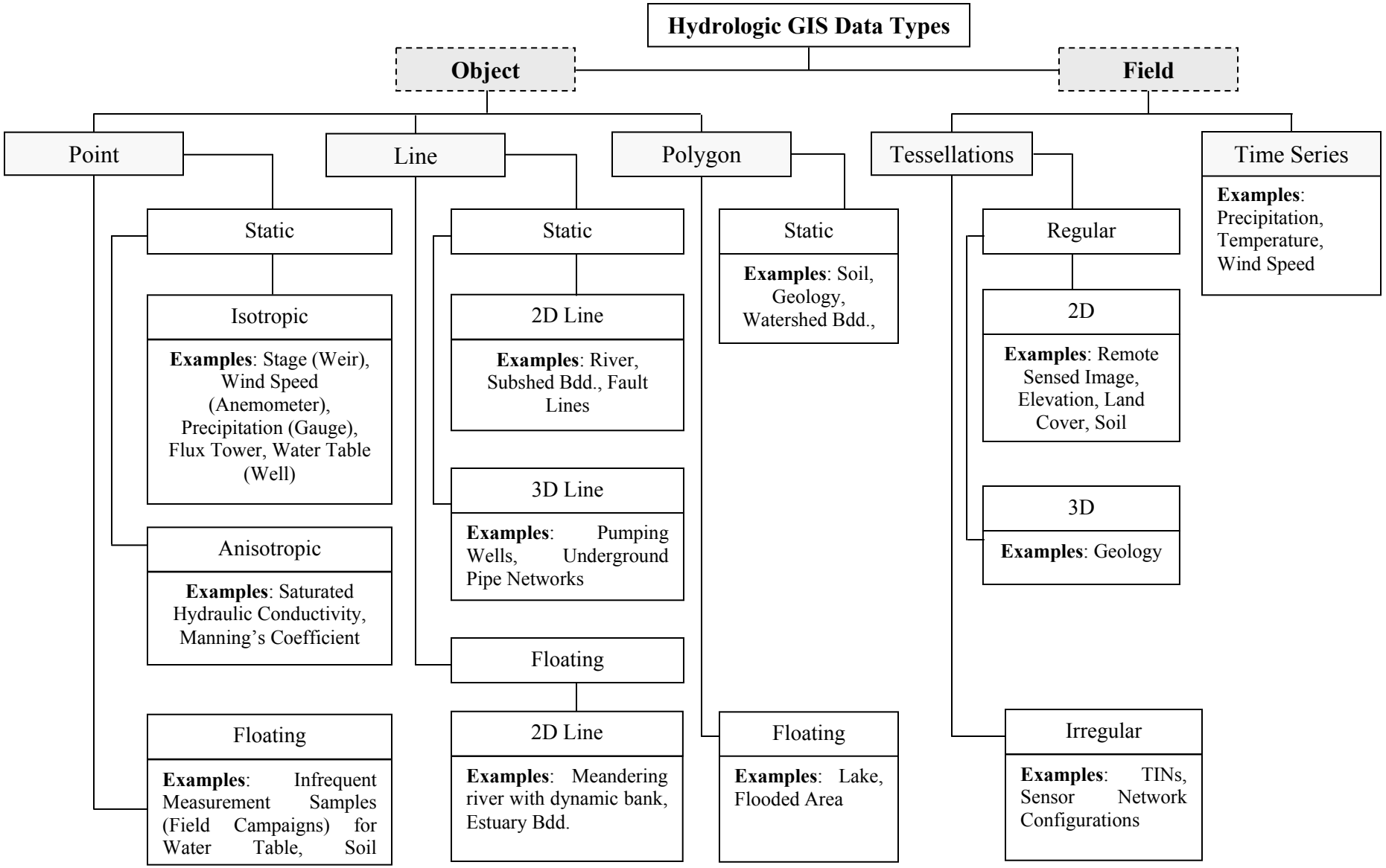

Figure 3.1 Conceptual classification of existing GIS data types relevant to hydrologic modeling

time such as a flooded region or a lake. Field objects have been sub-classified into Tessellations (spatial) and Time series (temporal) components. Unitary elements of tessellations define units of spaces with entity information attached to it.

The conceptual representation discussed above is generic and acts as a template that can be populated by new data. Next we try to formally represent the data types in classes and identify their attributes and their relationships with other classes.

3.4. Hydrologic Data Model Design

A hydrologic data model is a formal representation of the real world that provides a standard structure for storage, sharing and exchange of data independent of the software environment and programming languages. It provides a simplified abstraction of reality by a) isolating real world hydrologic objects into independent classes, b) removing redundant class objects, c) defining relationships between independent classes, and d) defining integrity constraints on them.

The design of a hydrologic data model is performed keeping in mind the range of required data types and their relationships among themselves (Wright *et al.* 2007). Some data, such as elevation and soil properties, vary continuously in space while others like observed streamflow vary continuously in time. The representation of data also changes depending on the scale of interest. On a coarse scale the stream channel can be represented as a one dimensional curvilinear object, on a finer scale it can be considered as a three dimensional topographic section with width, depth and length. For longer time scales such as climate change or landscape evolution studies, the stream channel representation will also need a time identifier in addition to width, depth and length attributes. These are necessary in order to track the changes in shape over time due to erosion/deposition on the river bed or banks. This means that the designed data model a) must have the *flexibility* to incorporate different representations of the same object at different scales, b) should be *extensible* with a potential to incrementally enrich it with new data types and construct complex objects, and c) should be *robust*, and *adaptable* to changing hydrologic conditions by using different instances of a single object (reusability). Maximum information, minimum data redundancy, reduction of storage

capacity, and optimum retrievability of data for analysis are the desired objectives in design process. All these characteristics are sufficed by designing the data model using object oriented concepts of inheritance, polymorphism and encapsulation.

3.4.1. Object Oriented Design principles

An object-oriented data modeling strategy provides a formal definition of objects, its attributes, behaviors, and operations that can be performed on it (Alonso and Abbadi 1993; Raper and Livingston 1995; Milne *et al.* 1993).

3.4.1.1. Classes, Methods and Relationships

Each data model Object is essentially an instance of a Class. Classes are object oriented constructs which group objects that share the same set of attributes and methods. Methods are the functions that define the interaction of objects to the outside world. While every object in a class shares some of the same set of attributes and methods, they may have additional properties attached to them. In addition to a description for objects, its attributes and behaviors, a data model also explains the relationship between classes. An example of a class can be a Line feature and one of its instances might be a river. Attribute fields of the river line are an integer identifier, number of line segments and start and end points of each segment. Calculation of total flow volume by using the river dimension attributes will be an example of Method for the river object. In order to account for flow and interactions between each river segment and the watershed, and also to streamline query and storage, definition of (topological) relationships between classes is needed. The three main relationships between classes that have been implemented in the design of the hydrologic data model are Generalization, Association and Aggregation.

A generalization relationship between any two classes means that one of the classes (Child class) is derived from the other (Base class). This relationship is inherent to object-oriented modeling through the “inheritance” mechanism. The subclasses of a base class share many properties between themselves while separating from each other on the basis of new “identity” properties. This relationship markedly simplifies and clarifies

the data model and minimizes redundancy in definitions, access and storage. Generalization is denoted by a solid line with a closed arrowhead pointing to the super class.

Association shows the relationship between instances of classes. It is the most common form of relationship and can connect classes both in time and in space. An association linkage can either be a bi-directional association, which means that both of the connecting classes are aware of the relationship with each other or a unidirectional association where only one of the classes knows about the relationship. One other type of association that has been implemented in the developed data model is Reflexive association. This linkage represents the association of the class to itself. This means that another instance of class is associated to the present one.

Aggregation relationships explain the interaction of individual parts/components (simple objects) to a complex object.

The formal static structural representation of classes, its attributes and relationship is done using a Unified Modeling Language (UML) Class Diagrams.

3.4.1.2. UML Representation

UML is a standardized specification language for visualizing, constructing and documenting an abstract model of a software system. It provides a programming-language independent view of the structure and behavior of classes. The two primary components of UML are the Meta-Model and Notation (Martin, 2002). Meta-Model is self-description of the UML objects, attributes, methods and relationships in UML thus providing a standard framework for transfer of object models among different Computer Aided Software Engineering (CASE) tools through XML Metadata Interchange (XMI) format. We note that ArcGIS supports a range of CASE tools which can be used to translate data models generated in XMI template into empty geodatabases (Wright *et al.* 2007). These geodatabases can be populated by users for hydrologic data storage. Notation is a full bodied representation of a) static structure of the system using object classes and relationships; and b) dynamic behavior of the system using collaborations between objects and transformation operations.

The static structure of the data model is shown using Class Diagrams. Class diagrams are composed of classes, attributes, operations, and relationships among classes. The fundamental unit of a Class Diagram is a class icon which is shown in Figure 3.2(a). The topmost compartment contains the name of the class, the middle contains a list of

Class
Attribute Name [multiplicity]: Type = Initial value {Property String}
Operation (Attribute: Type): Return Type {Property String}

(a)

Multiplicity Notation	**Explanation**
1	One Instance
0..1	0 or 1 instance
0..* or *	0 or more instances
0..n	0 to n instances

(b)

Figure 3.2 (a) Three compartment structure of Class icons. Options listed inside curly or large brackets are optional. (b) Cardinality/Multiplicity notation of relationships in a Class Diagram

attributes, and the bottom compartment contains a list of operations. We note that attribute-name is followed by the attribute-type identifier separated by a colon. Similarly in the third compartment, return type of operations follows the operation itself. Each operation uses the arguments that sit inside the parenthesis. The descriptions in the bottom two compartments are optional. Relationships in UML class diagrams are denoted by lines connecting the participating classes. Generalization relationships are represented by line drawn from a Child class to a Base class with a white, solid arrow at the end. Uni-directional Associations are represented by single ended arrowheads where the class from which the arrow initiates is the class which has knowledge of the relationship. The Aggregation relationship is denoted by a white diamond (for the aggregate class) on one end of the link and arrow (for the "part" class) on the other. Relationships also include an optional notation at each end of the link to indicate the multiplicity of instances. Common notations of Multiplicity are shown in Figure 3.2(b).We now present the hydrologic data model structure in UML. Definitions of relevant abbreviated symbols are given in Appendix I.

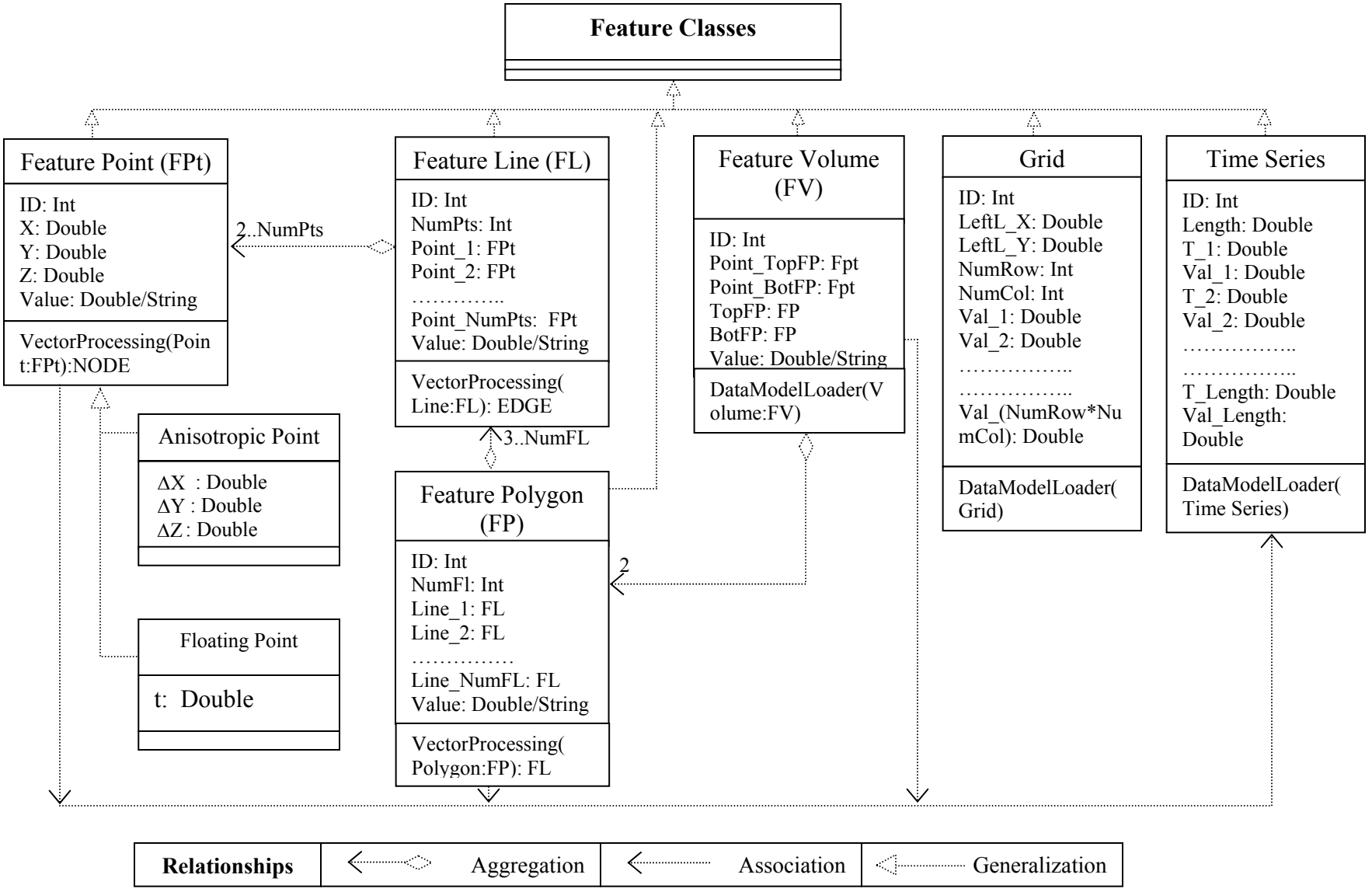

Figure 3.3 GIS data model class diagram design for hydrologic data in UML 2.0. Note the type and cardinality of relationships between various classes (details in Section 4.2). The operators in the bottom compartment for each individual class are used in transformation of GIS data model into a shared data model structure that is valid on hydrologic model grids.

3.4.2. Hydrologic Data Model Class Diagram

The hydrologic data model provides primitives to model the geometry and topology of the hydrologic data by providing support for class definitions and spatial relationships. The data types have been classified into six primary classes: Feature point, Feature Line, Feature Polygon, Feature Volume, Grid and Time series. The instance objects of each of these classes can be seen in the conceptual diagram of the data model in Figure 3.1. A Point class is completely defined by its location and attributes value. Figure 3.3 shows that Anisotropic and Floating points are a child class of the Feature Point. This means that they inherit the properties of Point class and have additional properties that identify them. Line class is basically a collection of line segments that joins Nodes (points). The multiplicity/cardinality of the aggregation relationship of points to a line class varies from 2 to NumPts. Similarly, Line class aggregates to form Polygons. A Polygon must have atleast 3 lines. Polygons aggregate to form a Feature Volume. 3-D Feature Volumes are an aggregation of two Polygons. Figure 3.4 explains the design of first four feature objects. We note that all the features have an existence in 3-D. This is particularly important for accurate characterization of hydrologic data like watershed boundaries, subsurface properties or even measurement stations in or above the ground which have existence in 3D (e.g. met-towers). The aggregation relationships shows how traditional 2D simple objects like points and lines can be used to make a composite higher dimension complex feature. One such example is description of underground water pipe network which is basically a collection of straight pipes that zigzags through the subsurface in various planes. We note that directionality (clockwise or counterclockwise) of feature line sequence or of connections between polygons is inherently defined by the definition of a Feature Polygon and Feature Volume respectively. Figure 3.3 also shows details of a Time series data class which is related to the feature objects through unidirectional association.

The developed hydrologic data model acts as a transitional formal representation that bridges the gap between the raw data types and their seamless assimilation in hydrologic applications. Independently, the data model serves as a template to store and organize raw hydrologic data in GIS. For the data model to be used seamlessly in

hydrologic modeling, hydrologic modeling, the data structure and relationships needs to be modified such that it supports representation of data and relationships on a hydrologic model grid.

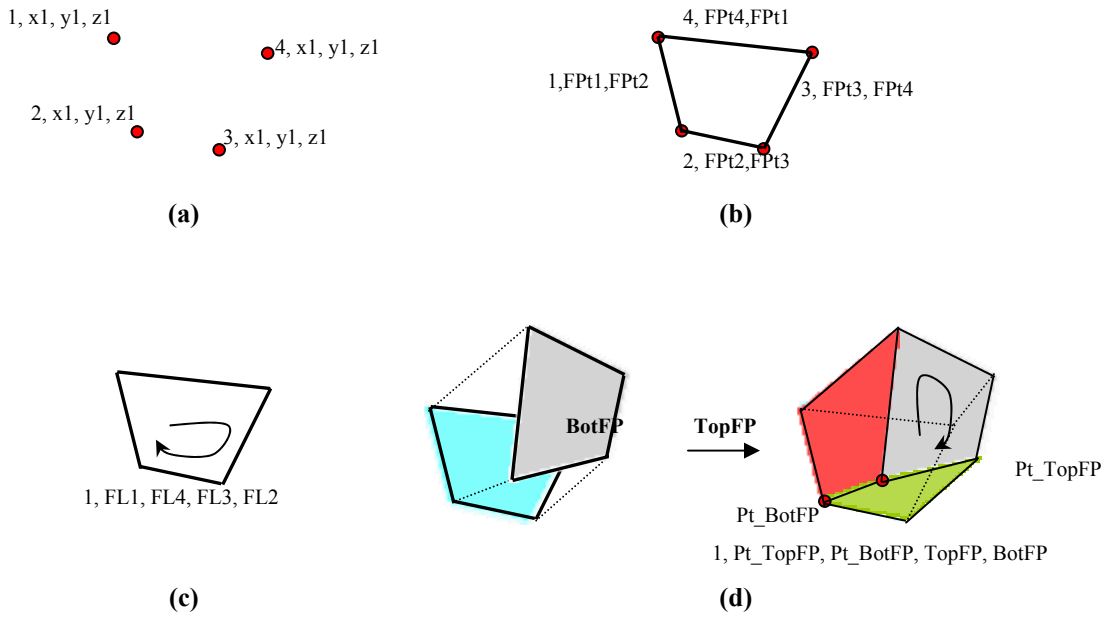

Figure 3.4 Feature object designs for a) Point b) Polyline c) Polygon and d) Volume. Note the implicitness of the "sequence of constructs" in Feature Polygon and Feature Volume design. (c) shows that edge polylines of the polygon are always listed in clockwise direction. Similarly, definition of a 3D feature necessities pivot point and boundary polygons in a particular sequence. Note that the identification of one point from both top and bottom polygon in design of Feature Volume is done in order to pivot the connection sequence of the nodes of the two polygons which results in a 3D feature

The eventual goal of course is to have a shared data model that can fully describe the hydrologic GIS data objects (shown in Figure 3.3) as well as their representational complement in the hydrologic model.

3.5. Hydrologic Model Structure: Process Representation and Adjacency Relationships

The conceptualization of process interactions and the shape and adjacency property of unit elements in the model grid, control the design of the hydrologic model data structure. Here we highlight the data and topologic needs of the hydrologic model data structure

vis-à-vis a finite volume based Penn State Integrated Hydrologic Model (PIHM, Kumar *et. al.* 2008a; Qu and Duffy 2007). We reiterate that all the steps taken are generic and can be used as a template in other GIS-hydrologic model coupling efforts that are based on different mesh decomposition strategies (e.g. structured meshes for finite difference models). Next we highlight how the representation of physical processes and discretization of the model domain influences the hydrologic model data structure.

Table 3.2 Differential equations of hydrologic processes on a model kernel

Process	Governing equation/ model	Original governing equations	Semi-discrete form ODEs
Channel Flow	St. Venant Equation (1D)	$\frac{\partial h}{\partial t}+\frac{\partial(uh)}{\partial x}=q$	$\left(\frac{d\varsigma}{dt}=P+\sum_{j=1}^{3}Q_{gc}+\sum_{j=1}^{2}Q_{oc}+Q_{in}-Q_{out}-E_c\right)_i$
Overland Flow	St. Venant Equation (2D)	$\frac{\partial h}{\partial t}+\frac{\partial(uh)}{\partial x}+\frac{\partial(vh)}{\partial y}=q$	$\left(\frac{dh}{\partial t}=(1-veg)P+P_t-I \quad -E_o-Q_{oc}+\sum_{j=1}^{3}Q_s^{ij}\right)_i$
Unsaturated Flow	Richards Equation	$C(\psi)\frac{\partial\psi}{\partial t}=\nabla\cdot(K(\psi)\nabla(\psi+$	$\left(\frac{d\xi}{dt}=I-q^0-ET_g\right)_i$
Groundwater Flow	Richards Equation	$C(\psi)\frac{\partial\psi}{\partial t}=\nabla\cdot(K(\psi)\nabla(\psi+$	$\left(\frac{d\zeta}{dt}=q^0+\sum_{j=1}^{3}Q_g^{ij}-Q_l+Q_{gc}\right)_i$
Interception	Bucket Model	$\frac{dS_I}{dt}=P-E_I-P_o$	$\left(\frac{dS_I}{dt}=veg(P-E_I-P_t)\right)_i$
Snow melt	Temperature Index Model	$\frac{dS_{snow}}{dt}=P-E_{snow}-\Delta w$	$\left(\frac{dS_{snow}}{dt}=P-E_{snow}-\Delta w\right)_i$

3.5.1. Physical process interaction

PIHM is a finite volume based integrated hydrologic model. It simulates multiple physical states on discretized elements (also called model kernel) of a watershed domain. The governing equations on each model kernel are defined using an ordinary or partial differential equation (ODE or PDE). By using the Method of Lines approach, PDEs are converted to ODEs (Leveque 1994). The resulting system of ODEs is assembled and

Table 3.3 Data requirements for calculation of physical states on a model kernel at any simulation time

Process	Data Support
Channel Flow	Head in adjacent triangular elements, Head in river segment downstream and upstream, Initial head value at the start of simulation, Precipitation, Evaporation, Manning's coefficient, Coefficient of discharge for weir flow across river bank, Elevation of end nodes of river segment, Leakage coefficient, Subsurface flow head in adjacent triangles, boundary conditions Note: Head → Overland Flow (unless specified otherwise)
Overland Flow	Head in neighboring elements, Head in river segment (if river is neighbor to the prismatic cell), Initial head value, Net Precipitation, Evapotraspiration, Elevation of nodes of triangular element, boundary conditions Note: Head → Overland Flow
Unsaturated Flow	Capillary flow, Initial head value, subsurface flow head, Infiltration, hydraulic conductivity, evapotranspiration, root uptake, soil porosity, Van genuchten soil parameters, boundary conditions Note: Head → Unsaturated Flow
Groundwater Flow	Head in adjacent triangles, Initial Head value, capillary flow, hydraulic conductivity of the elements and its neighbors, Bedrock depth, soil porosity, Van genuchten soil parameters, boundary conditions Note: Head → Groundwater Flow
Interception	Interception storage capacity, Precipitation, LAI, Evapotranspiration, initial interception
Snow melt	Initial snow depth, initial snow density, initial snow surface layer temperature, initial average snow cover temperature, average snow liquid water content, net solar radiation, incoming thermal radiation, air temperature, vapor pressure, wind speed, soil temperature, precipitation
Infiltration	Overland flow head, unsaturated soil moisture, hydraulic conductivity, porosity, macropore, precipitation rate, maximum infiltration capacity
Evapotranspiration	Wind speed, Humidity, Net radiation, soil heat flux, vapor pressure deficit, mean air density, Interception storage capacity, LAI, soil saturation, atmospheric resistance, stomatal resistance, vegetation fraction, unsaturated zone saturation

solved simultaneously using a stiff ODE solver known as CVODE (Cohen and Hindmarsh 1994). Table 3.2 lists the ODEs defined on a model kernel. In Table 3.2, $P, P_t, I, E_I, E_o, E_{snow}, ET_g, E_c$ are precipitation, throughflow, infiltration, and evaporation from interception, overland flow, snow, unsaturated zone and channel respectively. Q_s^{ij} and Q_g^{ij} is the lateral overland flow and groundwater flow from element i to its neighbor j. Q_{oc} and Q_{gc} describes interaction between overland flow and channel, and groundwater and channel respectively. q^0 is internal recharge flux between unsaturated and saturated zone. Q_l is vertical leakage through an underlying

confining bed. Q_{in} and Q_{out} are flow in and out of a channel section. Δw is snow melting rate and veg is the areal vegetation fraction in a control volume.

We note that the ODEs defining rate of change of overland and ground water flow depth (Table 3.2) depend on the head in adjacent kernels. Similarly, channel head is dependent on lateral fluxes from upstream and downstream channel sections, and the watershed. This means that a design of the hydrologic model data structure must incorporate the topologic relationship between neighboring unit elements. In addition to these relationships, Table 3.3 also lists the data requirements for calculation of each physical state on every model kernel at any time. An inclusive hydrologic model data structure will account for all the data requirements at all times.

The hydrologic model data structure is also influenced by the shape and adjacency of unit elements, which are in turn defined by the choice of domain decomposition (structured and unstructured) and numerical solution strategy (finite element, difference or volume) employed in modeling.

3.5.2. Domain Decomposition

The process of discretizing the watershed into adjoining physical subdomains based on hillslopes (Band 1989), contours (Moore *et al.* 1988), structured or unstructured grids, is called domain decomposition. Distributed hydrologic models solve physical states on the decomposed elements of a watershed using finite difference, finite volume, and finite element methods. As mentioned previously, PIHM uses unstructured meshes to decompose the domain. The individual unit control volume elements are either prismatic (for watershed elements) or trapezoidal/cuboidal (for river elements). The basic constructs of these shapes are Nodes (vertices of the triangles) and Edges (boundaries of the triangles). The number of boundary faces through which flux exchange takes place is equal to 5 and 6 for prismatic and river elements respectively (shown in Figure 3.5). If a model uses structured grids to decompose the domain, then the number of faces across

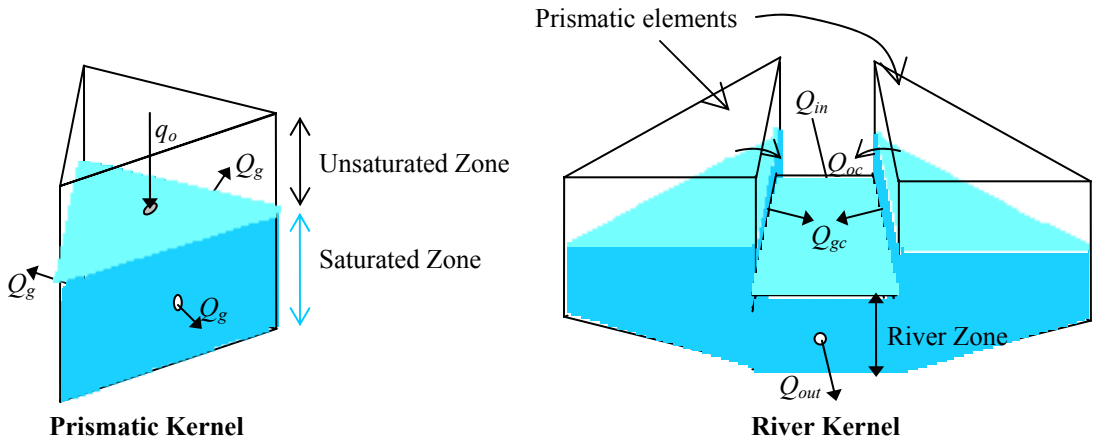

Figure 3.5 Prismatic and River Kernel in PIHM. The number of interaction fluxes between neighbors is equal to 5 for the prismatic kernel and 6 for the river kernel.

which flux exchange can potentially take place in 3D will be equal to 6. So the shapes of the unit element also determine how the relationships between neighboring elements need to be represented in a hydrologic model data structure. We note that the unstructured mesh decomposition poses additional challenges in the design of hydrologic model data structure, particularly in terms of definition of topological relationships, than structured grids where the neighbors are implicitly characterized by the decomposition itself.

With the object oriented hydrologic data model in place (section 4) and the spatial relationships and parameter definitions for the hydrologic model identified (in this section), the last step in shared data model design is to represent the hydrologic GIS data types and the hydrologic model structure using the same feature classes thus providing an automatic connection between GIS and the hydrologic model. The next section discusses the design of this shared data model

3.6. Shared Data Model Design

The shared data model captures the spatial structure of hydrographic features and temporal objects by identifying six classes: Node, Element, Channel, Soil, Land Cover and Time Series (shown in Figure 3.6). These classes are representational complements of the six GIS data model classes (see Figure 3.3) and can be obtained by applying

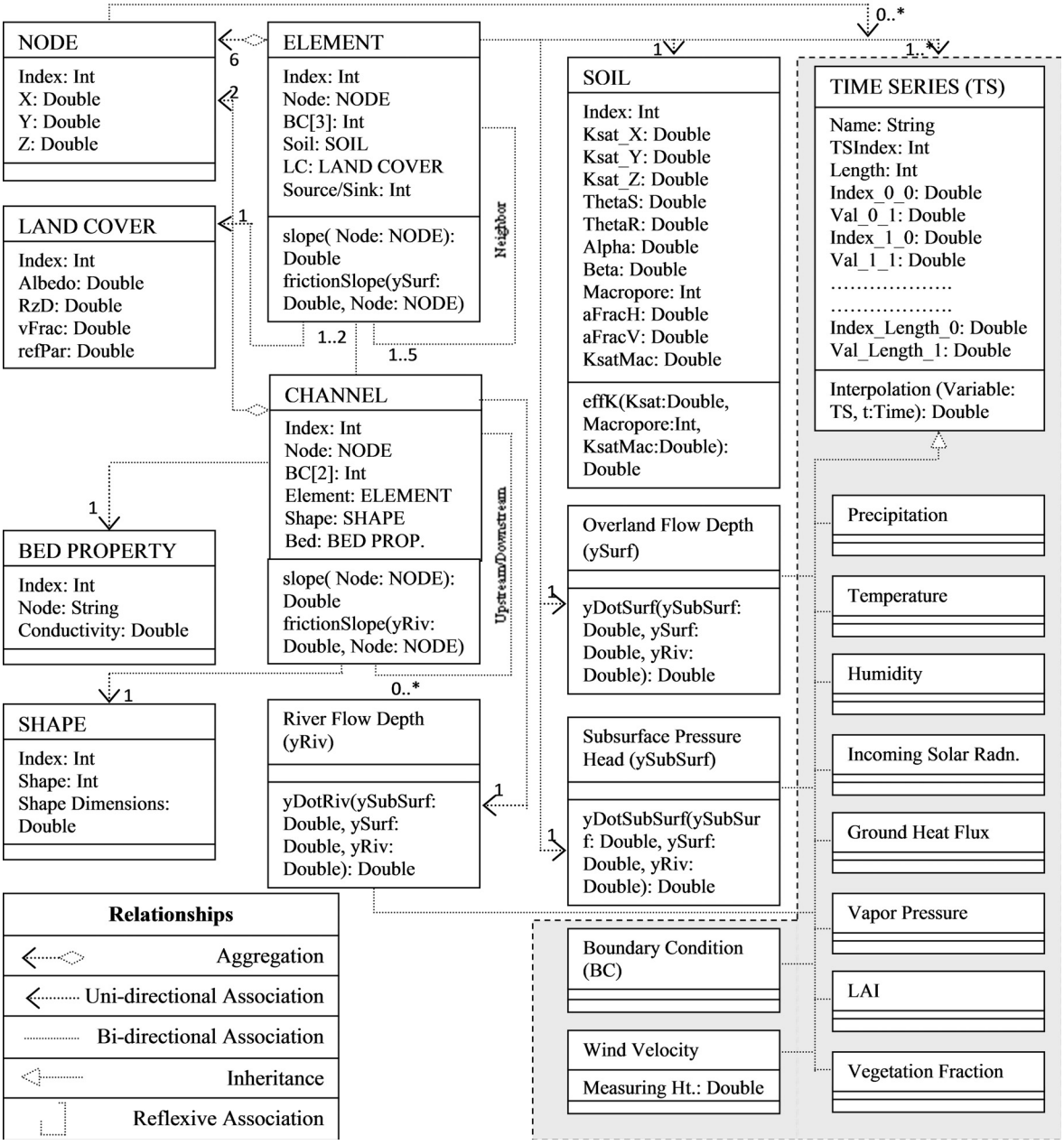

Figure 3.6 Shared data model class diagram design for GIS-Hydrologic Model coupling in UML 2.0. Note the type and cardinality of relationships between various classes (details in section 3.6).

appropriate transformations or redefinitions. The relevant geometric, spatial and topological transformations performed on GIS data types are shown in Figure 3.7. By generating mesh decomposition using points and lines as constraints (more details in Kumar *et. al.* 2009), nodes of the triangles automatically act as the Feature Points and Edges of the triangles act as Feature Lines. Properties and attributes of boundaries of the

Feature Polygon are assigned to the Element edges after converting the polygons to polyline and then to lines. Attributes of the Feature polygons and Feature Volumes are

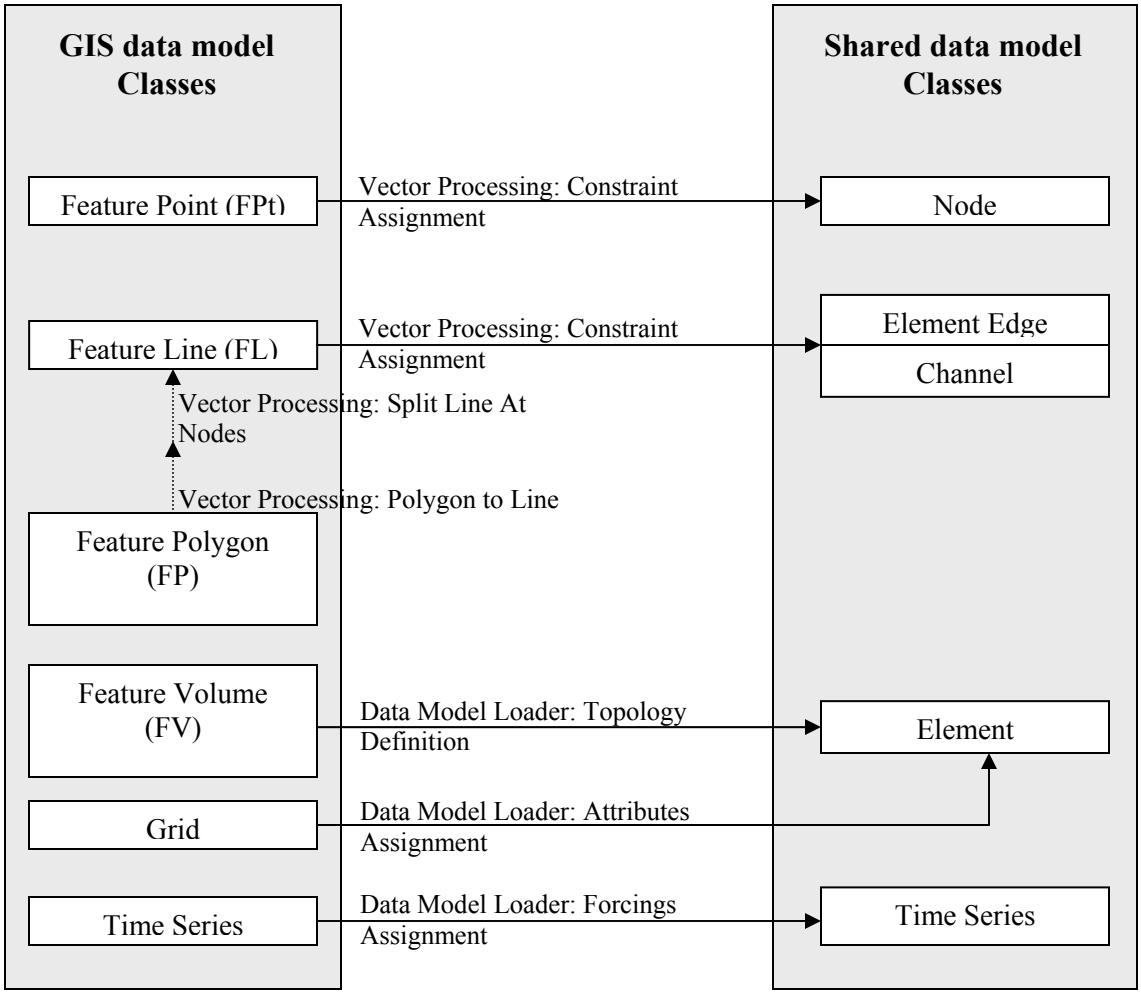

Figure 3.7 Class Re-Representation diagram showing the transformation of a GIS based data model classes into Classes identified in Shared Data Model design. The arrows originate from each individual GIS data model class and end in the corresponding complement shared data model class. Operators/Functions that perform this transformation are shown along the arrows. Dotted arrows represent intermediate transformation operations.

geographically registered to the triangular elements. We note that all the re-representation of hydrologic GIS data types are "loss-less" mappings implying that they reversible. By aggregating Element Edge, Channel or Elements based on its attribute properties, we can revert back from Shared Data model class to original GIS data objects. The operators used in re-representation of classes are shown over the lines connecting the source and result class in Figure 3.7. These operators are also listed as Methods (in the bottom-most

compartment) in the GIS data model class diagrams (see Figure 3.3). Names of each of these operators are self-explanatory for their functions. We note that the dotted line in the transformation diagram indicates the intermediate results.

Figure 3.6 also shows the Aggregation, Uni-directional Association, Reflexive Association and Generalization relationships supported in the shared data model. An Element class represents a discretized triangular element in 2D and a prismatic element in 3D and is defined by six nodal locations listed in a clockwise direction at two levels. The prismatic element has five neighbors- three on the sides and one at the top and bottom. We note that neighbors of an element also belong to an Element class and this recursive relationship is captured by Reflexive association. The cardinality of this relationship is 1 to 5 which means that there has to be at least one neighboring element to an Element object. A maximum cardinality of 5 denotes that a 3D element can have a total of 3 lateral and 2 vertical neighbors. A Channel class is defined by the two end nodes and neighboring elements on the either side of channel. Each channel segment is also composed of an upstream and downstream channel segment which is captured by a Reflexive association. We note that the multiplicity of this relationship varies from 0 to any integer value. This means that a channel segment can stand alone in the watershed with no upstream or downstream channels. A Channel is also Bi-directionally associated with an Element with a multiplicity of 1 to 2. This translates to existence of atleast one neighboring triangular element to a channel segment. Bi-directionality ensures that both Element and Channel is aware of this topological relationship. These relations are fundamentally important for spatial integrity of the hydrologic modeling framework. Each Element class is also associated with Soil, Land Cover and Time Series class. This ensures clean and efficient assignment of properties to each Element. Similarly the Channel is associated to Bed Property and Shape classes. Soil Class contains several attribute fields such as Hydraulic conductivities and van-Genuchten equation soil retention parameters (van Genuchten 1980). Attributes of Land cover class are root zone depth, albedo and photosynthetically active radiation from each land cover type. We note that Precipitation, Temperature, Humidity, Incoming Solar Radiation, Ground Heat Flux, Vapor Pressure, LAI, Vegetation Fraction, Wind Velocity, Time dependent boundary conditions and the observed and simulated state variables are all instances or child

objects to the Time Series Class. Name of the operators shown in Figure 3.5 is self-explanatory of their functions. These operators are concerned with derivation of geometric properties of triangular elements and channels or with the calculation of rate of change of state variables with time. Definitions of various functions are given in Appendix I.

The shared data model design is tested in the development of a coupled GIS-hydrologic modeling system. The integrated software is an open-source, and platform independent, extensible and "tightly-coupled" integrated GIS interface to Penn State Integrated Hydrologic Model (PIHM) and is referred as PIHMgis.

3.7. PIHMgis

PIHMgis is an integrated and extensible GIS system with data management, analysis, data modeling, unstructured mesh generation, visualization and distributed PIHM modeling capabilities. The underlying philosophy of this integrated system is a shared geo-data model between GIS and PIHM that was developed in the previous sections. The shared data model makes it possible to handle the complexity of the representation structures, data types, model simulations and analysis of results. The graphic interface component of PIHMgis has been written in Qt and C++ which supports object oriented class structures in programming. PIHMgis sits on an open source Qgis engine (www.qgis.org) and has been integrated as pluggable software. The interface and the source code can be downloaded from http://www.pihm.psu.edu/pihmgis_downloads.html.

The architectural framework of the interface is shown in Figure 3.8. Directionality of the arrows indicates the possible flow of output from one Method to another. The flow

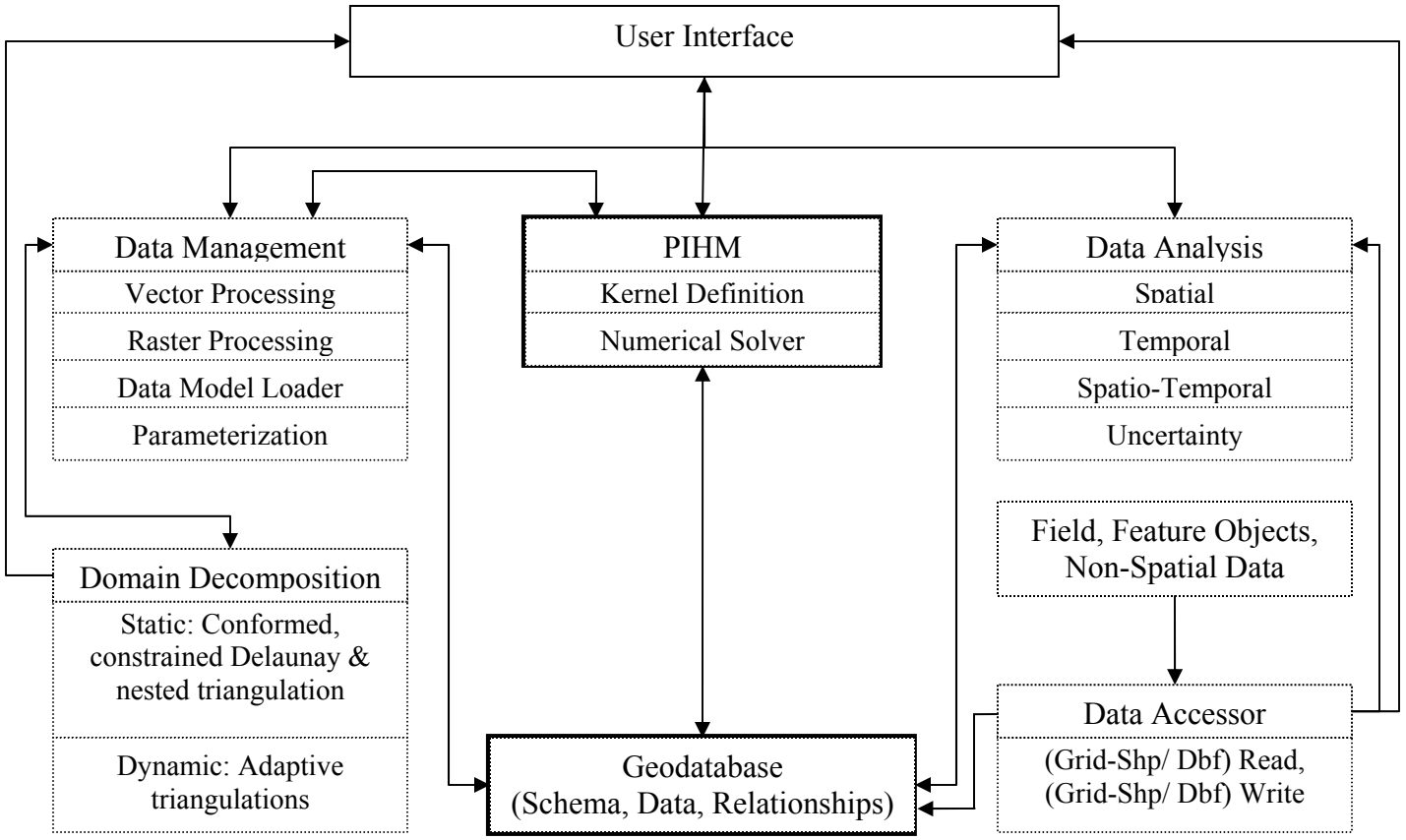

Figure 3.8 Architectural framework of PIHMgis. Directionality of the arrows indicates the possible flow of output from one module to another.

of actions between different class objects in PIHMgis can be shown using an object oriented UML collaboration diagram (see Figure 3.9). These diagrams represent both the static and the dynamic behavior of the system by representing collaboration (simple associations) between objects and mapping the sequence of messages they share between them. The rectangles in the diagram enclose the class and its instance (separated by a colon), and the links between rectangles represent the collaborations (communications) between classes. The chronological labeling of the messages between class objects describes the sequence in which actions are executed. The first communication initiated by the integrated system is from the object from where message 1.0 is released. In order to track the messages/actions that are hierarchically associated with a parent object, a nested numbering of messages is performed. Figure 3.9 shows that a full hydrologic modeling exercise can be carried out in PIHMgis by directly acting upon the raw data types represented in the shared data model, merely by launching a sequence of messages (commands). Starting with digital elevation model raster data, which is an instance of Grid class, Raster processing operations result in delineation of watersheds, definition of streams and extraction of Very Important Points (VIPs). A Vector processing tool with polyline reconditioning algorithms simplifies and splits watershed boundaries and channel segments. Thereafter, vector merging of all the available features layers is performed to create a spatial support for generating constrained domain decomposition. Details about the need of vector processing steps and how they aid flexible domain decompositions are in Kumar *et al.* (2008b). Once domain decomposition has been performed, topology definitions and field assignment of properties, and initialization of state variable on each model kernel is performed. Numerical solver module formalizes all the ODEs in each model kernel in the form of $y' = f(y)$ and then solves the system iteratively. Output results in the form of spatial and time series plots are displayed in the Visualization toolkit integrated in PIHMgis. Details about all the operator functions in the PIHMgis toolkits are discussed in Bhatt *et al.* (2008).

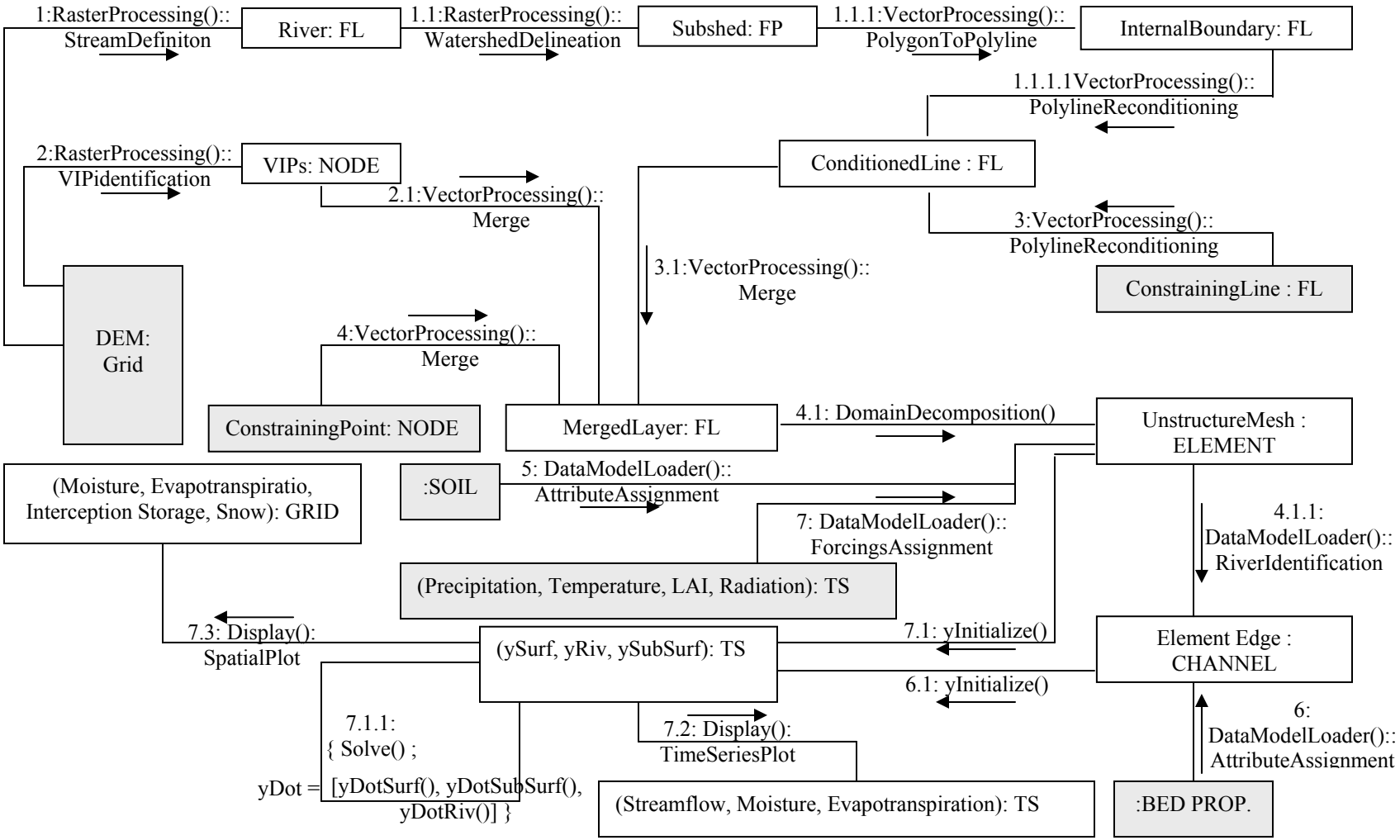

Figure 3.9 Collaboration diagram showing the dynamic activity sequence of classes in PIHMgis. The rectangles denote the class instance, the directionality of arrows denotes the flow of action and nested numbering keeps track of the sequence of operations in a global framework. An example of a hierarchical nesting sequence is 1→ 1.1 → 1.1.1. Shaded boxes denote the independent initiation (trigger) of operations.

3.8. Advantages of Shared Data Model for GIS-Hydrologic Model coupling

A shared data base, relationships and schemas between GIS and the hydrologic model reduces model setup time, enhances data integrity and streamlines model simulations. As a result, the integrated system simulates the model states accurately and efficiently, steers simulations and conveniently manages, analyzes and displays data used and produced by the model. The unique advantages of coupling based on a shared data model development are discussed next.

3.8.1. Enhanced accuracy

As mentioned in Section 6, the hydrologic model grids supported by the shared data model are generated by using GIS points, polyline and polygons as constraints. The unique advantage of using GIS objects as constraints for decomposition is that the resulting model grid can be designed to follow the edges of a single property type (such as Soil, Land Cover, geology, vegetation etc.). This maintains data integrity and limits introduction of additional data uncertainty arising from statistical averaging of multiple class themes within a model grid. Figure 3.10 highlights this concept, where an unstructured mesh generated using soil theme as a constraint leads to decomposition where each triangle has a single soil type. For structured grid decomposition with the same average resolution as the unstructured mesh, we observe that 41.63 % percent of the grids have mixed themes. Generating grids that do not follow edges of thematic classes (as shown in the case of structured grids) introduces uncertainty. Similarly if observation stations (point objects) are used as a constraint in decomposition, hydrologic states can be predicted exactly at the observation stations. The georeferential integrity inherent in the shared data model minimizes any errors during comparison of observed and predicted states which creep in due to interpolation of prediction variables to the observation locations.

3.8.2. Storage efficiency

In any watershed model, there are a limited number of parameters and forcing types (e.g. soil, land cover, precipitation etc.) which are needed to define each hydrologic property over the domain. This translates to storage efficiency at two levels in a shared data model approach. First, the efficiency is gained through storage of (soil or forcing) properties as relational objects which also ensures that these properties are accessible to both the GIS and the hydrologic model. For example, instead of storing all the nine soil attribute parameters (floating type numbers) as separate grids, we are able to store them as a single layer of soil types (an integer attribute of Element Class) with associative relations defined for all the nine attributes of Soil Class. The compression is even more significant in storage of forcing time series such as of Precipitation, Ppt and Temperature, T. Rather than storing the forcing grid at numerous time steps (e.g. satellite images of time series variables like temperature), the precipitation-type attribute for each element class is associated with a precipitation magnitude within a Time Series class. The associative relationships limit data redundancy by avoiding use of multiple sets of similar data. Significant storage efficiency is also gained due to the description of the data on constrained Delaunay triangulations.

3.8.3. Model setup, Real-time visualization and Decision support

The simple, compact and procedural structure of PIHMgis (see Figure 3.9) streamlines the process of organizing the data for model simulations. PIHMgis allows the user to perform semi-automated preliminary model simulations with minimum user input. The ease of use of the coupled system can be judged from the fact that graduate students with no prior knowledge of modeling (in an introductory groundwater modeling class) are able to perform uncalibrated simulations after two training lectures.

The architectural framework of PIHMgis in Figure 3.8 shows that the outputs from the model simulations continually update the geodatabase of the shared data model. This means that any selected number of state variables or fluxes can be plotted at any location while the simulation proceeds. This is particularly useful in assessing whether the simulation results are physically realistic, and gives an opportunity to adjust model or make management decisions in real time. A typical real time plot is shown in Figure 3.10.

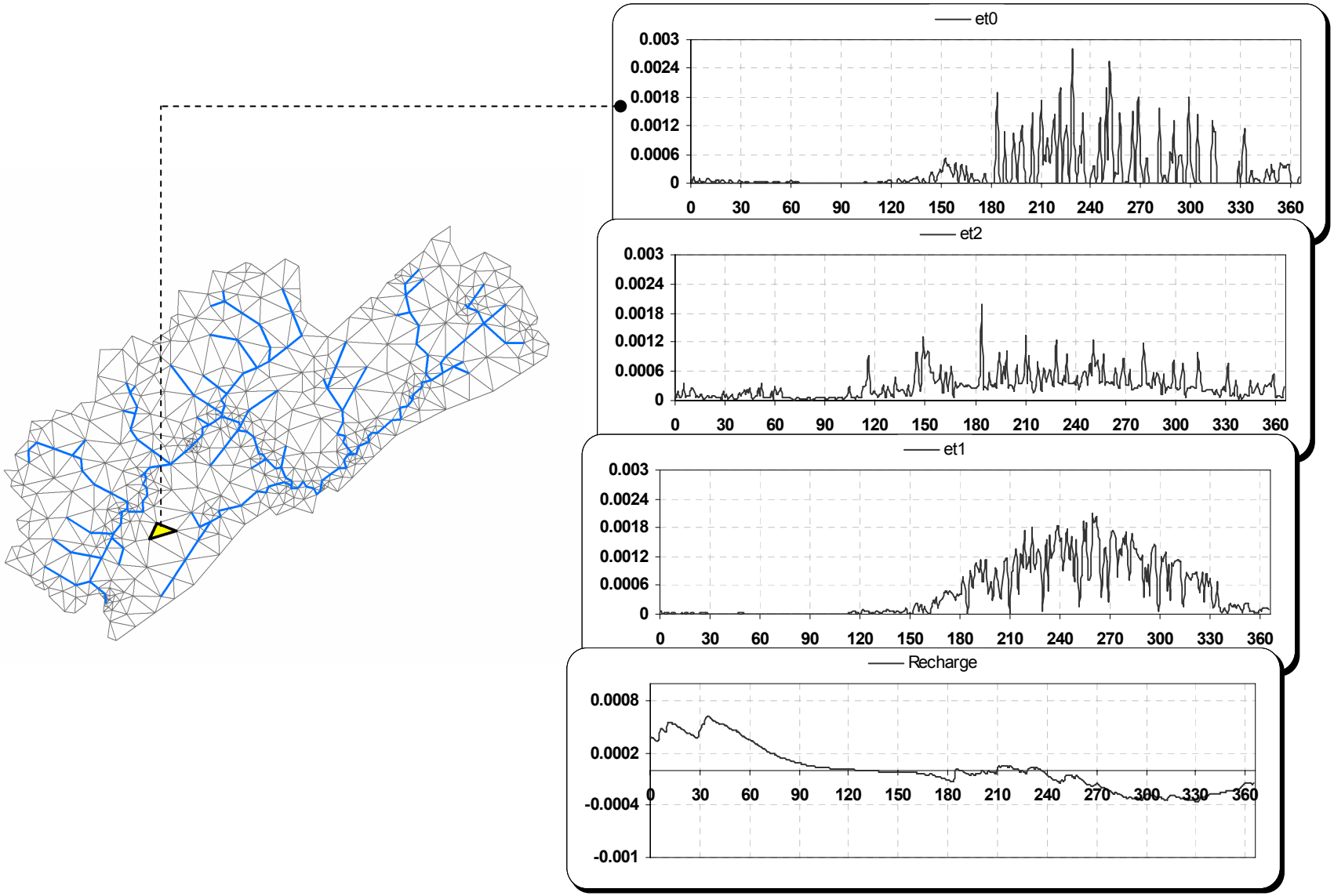

Figure 3.10 Plots of vertical fluxes (et0 ≡ Evaporation from canopy, et1 ≡ Transpiration, et2 ≡ Evaporation from ground, Recharge ≡ Recharge to ground water) at the shaded element after 366 days of simulation in Little Juniata Watershed.

The figure illustrates all vertical fluxes at a selected element (shaded in Figure 3.10) for 366 days of simulation in Little Juniata Watershed. We can immediately see that recharge to groundwater is positive in winter months (from November to January ranging from 0 to 90 days), becomes negative in summer (from July to September ranging from 240 to 330 days), and varies inversely to the total evapotranspiration. During summer, larger evapotranspiration leads to creation of negative matric potential in unsaturated zone. This translates to a negative recharge situation where water moves across the capillary fringe from the saturated to the unsaturated zone. Real time visualization also serves as an "early warning" system to track errors in simulation arising from wrong/bad data input or numerical "blow-up". During the simulation the user can search for the appearance of non-physical states in real time and immediately detect problems in the solution.

3.8.4. Parameter steering

Distributed hydrologic model calibration and sensitivity analysis of parameters requires performing multiple model simulations. Since a shared data model stores GIS data in a hydrologic model grid structure, the coupled GIS-model system provides unique flexibility in modifying parameters or forcing values in any selected portion of the watershed. For example, if it is found during calibration that the leaf area index (LAI) for a particular land cover type is resulting in underprediction of interception storage, the shared data model can efficiently query all Elements of that particular land cover type and perform the required parameter nudging. For traditional approaches with an isolated data-model and data-structures, changes in parameters (such as LAI) in a particular region would require GIS processing on the raw data and generation of new input files. In summary, a streamlined data structure and relationship definitions of a shared data model result in an efficient, integrated and automated steering of parameters

3.9. Conclusions

This paper presents the design and details of a shared data model which can support coupling of GIS with a hydrologic model. The conceptualization and characterization of

this coupling strategy can be used with other physically distributed models and can be extended to management, visualization and decision support tools (e.g. ecological models). The data model is rich yet flexible in terms of its extensibility and simplicity. The data model incorporates representation of wide range of data types varying from static and floating points to 3D feature line and volume objects. The object oriented strategy streamlines the design of the data model and clarifies the relationships between classes. UML class and collaboration diagrams have been developed to show the standardized static and dynamic structure of classes, their operations and activity in the larger software framework. It also provides a clear modular sequencing of operations in the coupled software. Object oriented data model design leads to seamless assimilation of the classes and their relationships directly in object oriented software development. The shared data model is successfully used to develop a prototype open-source, platform independent coupled modeling system referred to as PIHMgis. The shared data model concept creates a process for modeling that improves data flow, model parameter development, parameter steering, efficient grid design and allows real time visualization and decision support.

3.10. References

ABEL, D.J. and KILBY, P.J., 1994, The systems integration problem. *International Journal of Geographical Information Systems Journal of Hydrology*, 87, 61-77

ALONSO, G. and EL ABBADI, A., 1994, GOOSE: Geographic Object Oriented Support Environment. In Proceedings of *ACM/ISCA Workshop on Advances in Geographic Information Systems*, pp. 38-43

BAND, L. E., 1986, Topographic partition of watersheds with digital elevation models, *Water Resources Research*, 23(1), 15–24.

BENNETT, D. A., 1997. A framework for the integration of geographical information systems and model base management, *International Journal of Geographical Information Science*, 11(4): 337–357.

BHATT, G., KUMAR, M. AND DUFFY, C.J., 2008. Bridging the gap between geohydrologic data and distributed hydrologic modeling. In Proceedings of *International Congress on Environmental Modeling and Software*, (accepted).

COHEN, S.D. and HINDMARSH, A.C.,1994. CVODE User Guide, LLNL Technical report *UCRL-MA-118618.*

FEDRA, K., 1996. Distributed Models and Embedded GIS: Strategies and Case Studies of Integration.' In: Goodchild, M.F., Steyart, L.Y., Parks, B.O., Johnston, C., Maidment, D., Crane, M. and Glendinning, S. [eds], *GIS and Environmental*

Modeling: Progress and Research Issues, GIS World Books, Fort Collins, CO., pp.413–417

FREEZE, R.A., AND CHERRY, J.A., 1979. *Groundwater*, Prentice Hall: Englewood Cliffs, NJ., pp. 29.

FREEZE, R. A., and HARLAN, R. L., 1969. Blueprint for a physically-based digitally simulated, hydrologic response model, *Journal of Hydrology*, 9, 237– 258

GALTON, A., 2001. Space, Time, and the Representation of Geographical Reality,*Topoi* 20: 173-187.

GOODCHILD, M.F., 1992. Geographical information science. *International Journal of Geographical Information Systems* 6(1): 31-45.

HELLWEGER, F. L., and MAIDMENT, D. R., 1999. Definition and Connection of Hydrologic Elements Using Geographic Data. *Journal of Hydrologic Engineering*. 4(1), 10-18

HEUVELINK 1998. *Error propagation in environmental modelling with GIS*. Taylor and Francis, London, UK

KOPP, S. M., 1996. Linking GIS and hydrological models: where have we been, where are we going? In *HydroGIS 96: Application of Geographic Information Systems in Hydrology and Water Resources* (ed. by K. Kovar & H. P. Nachtenebel) 13-21. IAHS Publ. no. 235

KOLLET, S. J., and MAXWELL, R. M., 2006. Integrated surface-groundwater flow modeling: A free-surface overland flow boundary condition in a parallel groundwater flow model, *Advances in Water Resources*, (29)7, 945-958

KUMAR, M., BHATT, G. and DUFFY, C., 2009a. The Role of Physical, Numerical and Data Coupling in a Mesoscale Watershed Model, *Advances and Water Resrouces*.(submitted)

KUMAR, M., BHATT, G. and DUFFY, C., 2009. Efficient domain decomposition framework for accurate representation of geodata on watershed model grid, *International Journal of Geographical Information Science*, v23.

LAHLOU, M., SHOEMAKER, L., CHOUDRY, S., ELMER, R., HU, A., MANGUERRA, H. and PARKER, A., 1998. 'Better assessment science integrating point and nonpoint sources: *BASINS 2.0 User's Manual',EPA-823-B-98-006*, U.S. Environmental Protection Agency, Office of Water, Washington, DC, USA

LUZIO. DI, M., SRINIVASAN, R., ARNOLD, J.G., and NEITSCH, S.L., 2002. Arcview Interface for SWAT2000. User's Guide. U.S. Depart- ment of Agriculture, Agriculture Research Service. Temple, Texas. Available at http://www.brc.tamus.edu/swatt/downloads/ doc/swatav2000.pdf Accessed on March 18, 2008

MAIDMENT, D., 1993. Developing a spatially distributed unit hydrograph by using GIS. In Proceedings of *Applications of GIS in hydrology and water resources* (edited by Kovar, K. and Nachtenebel, H.), Vienna. IAHS publ. no. 211. 181-192.

MAIDMENT, D., 2002. *Arc Hydro: GIS for Water Resources*. Redlands, CA, ESRI Press

MARTIN, R., 2002. *Agile Software Development, Principles, Patterns, and Practices*. Prentice Hall.

MARTIN, P.H., LEBOEUF, E.J., DOBBINS, J.P., DANIEL, E.B., and ABKOWITZ, M.D., 2004. Development of a GIS-Based Spill Management Information System. *Journal of Hazardous Materials*, B112:239-252.

MCKINNEY, D.C., and CAI, X.M., 2002. Linking GIS and water resources management models: an object-oriented method. *Environmental Modeling & Software*, 17, 413-425.

MILNE, P., MILTON, S., and SMITH, J., 1993. Geographical Object-oriented Databases: a Case Study. *International Journal of Geographical Information Systems*, 7:39-56.

MOORE I. D. , O'LOUGHLIN, E. M., and BURCH. A., 1988. Contour-based topographic model for hydrological and ecological applications, *Earth Surface Processes Landforms*,13,305-320.

NATIONAL RESEARCH COUNCIL ,1999. New Strategies for America's Watersheds. Washington DC, National Academy Press

NELSON, E.J., 1997. *WMS v5.0 Reference Manual*, Environmental Modeling Research Laboratory, Brigham Young University, Provo, Utah, 462 pp.

NYERGES, T. L.1993. Understanding the scope of GIS: It's relation to environmental modeling. In M. F. Goodchild, B. O. Parks, & L. T. Steyaert, eds. *Environmental Modeling with GIS*. Oxford University Press.

PANICONI, C., KLEINFELDT, S., DECKMYN, J., and GIACOMELLI, A., 1999. Integrating GIS and data visualization tools for distributed hydrologic modelling. *Transactions in GIS*. 3(2), 97-118.

QU, Y., and DUFFY, C. J., 2007, A semidiscrete finite volume formulation for multiprocess watershed simulation, *Water Resources Research*, 43

RAPER, J.F. and LIVINGSTONE, D.,1995. Development of a Geomorphological Spatial Model Using Object-oriented Design. *International Journal of Geographical Information Systems*, 9(4):359-383.

SMITH, P. N., and MAIDMENT, D. R., 1995. Hydrologic Data Development System, *CRWR Online Report 95-1*, Center for Research in Water Resource, The University of Texas at Austin, Austin, TX.

VAN GENUCHTEN, 1980. A closed-form equation for predicting hydraulic conductivity of unsaturated soils, *Soil Sciences Society of America Journal*, 44:892-898

WATKINS, D. W., MCKINNEY, D. C., MAIDMENT, D. R., and LIN, M., 1996. Use of geographic information systems in ground-water flow modeling. *Journal of Water Resources Planning and Management*, ASCE, 122(2), 88–96

WILSON, J.P., INSKEEP, W. P., WRAITH, J. M., and SNYDER, R. D., 1996. GIS-based solute transport modeling applications: Scale effects of soil and climate data input. *Journal of Environmental Quality* 25: 445-53

WILSON, J. P., 1999. Current and future trends in the development of integrated methodologies for assessing non-point source pollutants. In D L Corwin, K Loague, and T W Ellsworth (eds) *Assessment of Non-Point Source Pollution in the Vadose Zone*. Washington DC, American Geophysical Union: 343-61

WRIGHT, D.J., BLONGEWICZ, M.J., HALPIN, P.N. and BREMAN, J., 2007. *Arc Marine: GIS for a Blue Planet*, Redlands, CA: ESRI Press, 202 pp

3.11 Appendix I

List of Symbols

aFracH:	aerial fraction of macropore in horizontal soil section
aFracV:	aerial fraction of macropore in vertical soil section
Albedo:	albedo (reflective fraction) of a land cover type
Alpha:	van-Genuchten scaling parameter
Beta:	van-Genuchten relaxation parameter
BotFP:	Bottom Feature Polygon
Ksat_X:	Horizontal saturated conductivity in X-direction
Ksat_Y:	Horizontal saturated conductivity in Y-direction
Ksat_Z:	Vertical saturated conductivity in Z-direction
KsatMac:	Saturated Macropore conductivity
LC:	Land Cover
LeftL_X:	Lower Left x-coordinate location
LeftL_Y:	Lower Left y-coordinate location
NumCol:	Number of Columns in Grids
NumFl:	Number of Feature Lines in a Polygon
NumPts:	Number of points in a Feature Line
NumRow:	Number of Rows in Grids
t:	Time
Point_TopFP:	Pivot point in Top polygon boundary of Feature Volume
Point_BotFP:	Pivot point in Bottom polygon boundary of Feature Volume
Ppt.:	Precipitation Time series
refPar:	reference incoming solar flux for photosynthetically active canopy
RH:	Relative Humidity Time series
RzD:	Rootzone Depth
Theta_S:	Maximum porosity
Theta_R:	Residual porosity
TopFP:	Top Feature Polygon
Val_(NumRow*NumCol):	Field value at grid location (NumRow, NumCol)
vFrac:	Vegetation Fraction
VP:	Vapor Pressure Time Series
ySurf:	Overland Flow Depth
yRiv:	River stage
ySubSurf:	Moisture head

List of Functions

areaChannel():	Function to calculate cross-section area of the channel element
areaElement():	Function to calculate surficial area of the prismatic element
effK():	Effective conductivity of the subsurface

frictionSlope(): Function to calculate friction slope
Interpoaltion(): Function to interpolate value of a time series at any time using the parsimonious information in Time Series data structure
yDotRiv(): Function to calculate rate of change of river stage
yDotSurf(): Function to calculate rate of change of overland flow depth
yDotSubSurf(): Function to calculate rate of change of moisture head

CHAPTER 4:

The Role of Physical, Numerical and Data Coupling in a Mesoscale Watershed Model

4.1. Introduction

Surface water, plant water, soil and groundwater, and the atmosphere are linked components of a hydrologic continuum. Changes in one affect the other on a variety of spatio-temporal scales. These interactions are influenced by the different components of the "hydrogeologic environment" (Tóth 1970; Jenny 1994) such as vegetation, topography, geology and climate. Clearly, vegetation influences the distribution and rates of water due to a wide range of processes, including interception, stemflow and transpiration (Bosch and Hewlett 1982; Hornbeck et al. 1970) and also contributes to formation of root holes which serve as flow ducts for macroporous infiltration and stormflow (Whipkey and Kirkby 1978) particularly in forested catchments. By considering five watersheds with topography and geology varying from glacial, coastal, wetland, karst and riverine, and climate varying from semi-arid to humid, Winter (1978) observed that local physiographic controls significantly influence the magnitude and direction of interaction between surface and ground water. Sometimes the interactions also modify or interact with the macro-scale hydrogeologic environment resulting in formation of wetlands (Herdendorf 2004), river meanders (Perillo 2005) and floodplains (Nanson 1980).

On the computational side, numerical modeling efforts which focus on simulating individual processes have made significant progress in recent years. Studies by Gottardi and Venutelli (1993) and, Feng and Molz (1997) for overland flow runoff; USACE-UNET (1997), and Strelkoff (1970) for flow in rivers and Huyakorn et al. (1986) and Paniconi and Wood (1993) for modeling saturated–unsaturated flow in the subsurface provide good examples. More recently, distributed and fully coupled approaches to watershed/river basin simulation have become a major research effort. Perkins and Koussis (1996), Govindraju and Kavvas (1991) are examples of coupled surface-subsurface flow by considering the land surface as a boundary through which a flux exchange takes place. In these papers, it was observed that coordinating the interaction between coupled models at artificial internal boundaries posed a severe numerical challenge for transient system responses. Similar observations were also made by Brown (1995) who experienced numerical difficulty in partitioning of rainfall between the

microporous soil matrix and macropores, and Refsgaard and Storm (1996) who reported problem in convergence in MikeSHE (Abbot et al. 1986) because of the need for synchronization of time steps for different flow components. According to Fairbanks et al. (2001), attempts at coupling hydrologic processes where each of the flow processes are simulated separately, using independent time steps and a mixture of explicit and implicit techniques results in numerically weak, inaccurate and unreliable solutions. Of the three established coupling methods (Langevin et al., 2005) viz. a) a sequentially coupled approach in which the head for one system acts as a general-head boundary for the other system (b) a sequentially coupled approach in which the interaction flux is applied as a boundary condition to each model and (c) a 'fully coupled' or 'fully implicit' approach, the last one was found to be most robust and accurate (Fairbanks et al. 2001). The fully coupled solution also outperforms linked/iteratively coupled methods in terms of computational efficiency for highly interactive systems.

Apart from considering multiple processes and full numerical coupling, another important problem for hydrologic simulation involves striking a balance between grid size or process resolution and the scale of computation (Kumar et al. 2009). Models based on structured grids are limited in terms of ingesting fine physiographic details particularly of linear features like rivers and watershed boundaries. This is due to the rigidness of a structured grid in terms of its shape, regularity and orientation in two principal directions only. Terrain and hydrographic features that are not oriented along any of the axes of rectangular grids are difficult to resolve without resorting to high spatial resolution discretization of the entire model domain or performing localized adaptive mesh refinement (Blayo and Debreu 1999). Vivoni et al. (2004), Kumar et. al. (2009), and Qu and Duffy (2007) have discussed the advantages of using Triangular Irregular Networks (TINs) and unstructured meshes over structured grids in terms of computational efficiency, flexibility and accuracy for hydrologic modeling. Among the new generation of physically based distributed hydrologic models such as InHM (VanderKwaak 1999), MIKE SHE (Graham and Refsgaard 2001), MODHMS (Panday and Huyakorn 2004), PARFLOW-Surface Flow (Kollet and Maxwell 2006) and WASH123D (Yeh and Huang 2003), InHM and WASH123D use finite element methodology to solve for states on unstructured grids.

This paper details the physical, numerical and data coupling framework of the Penn State Integrated Hydrologic Model (PIHM). All coupled hydrologic processes (evaporation, interception, snow-melt, overland flow, river flow, subsurface flow and macropore flow) are solved using a fully coupled numerical strategy on unstructured meshes. Spatial adaptivity of unstructured grids and temporal adaptivity of the numerical solver helps to resolve the full range of scales of process interactions over a simulation period. The model application is performed for a 2 year period in the Little Juniata watershed with area of 845 km^2.

4.2. Data Coupling: An Integrated Framework

A data model is a useful way to incorporate a large number of physical data layers into the modeling framework, including topology definitions. Here we use a flexible "shared" data-model to enhance the access of raw GIS data structures directly by the hydrologic model, thus reducing the model setup time, and facilitating data integrity and concurrent data access (Kumar et al. 2008). The integration framework uses the data-model to define relationships between different data types and their relation to the physical model environment (discretized hydrologic domain). The framework supports all scales of hydrologic interactions by using adaptively constructed grids to capture the heterogeneity in the domain physical properties and processes. The decomposition grids are constrained Delaunay triangulations which facilitate efficient ingestion of different physical parameter fields, simply and accurately from a geodatabase. Some common constraints used during grid generation involve point constraints such as stream gage locations, weirs, VIPs (i.e.. Very Important Points after Chen and Guevara (Chen and Guevara 1987)), groundwater well locations, and line constraints such as subwatershed boundaries, land cover, and soil type. The advantage of point and line constraints is in reducing errors due to interpolation or geo-referencing of modeled data to observations. For example, Figure 4.1 shows a domain decomposition of Little Juniata Watershed with and without constraints. The decomposition shown on left does not include observation

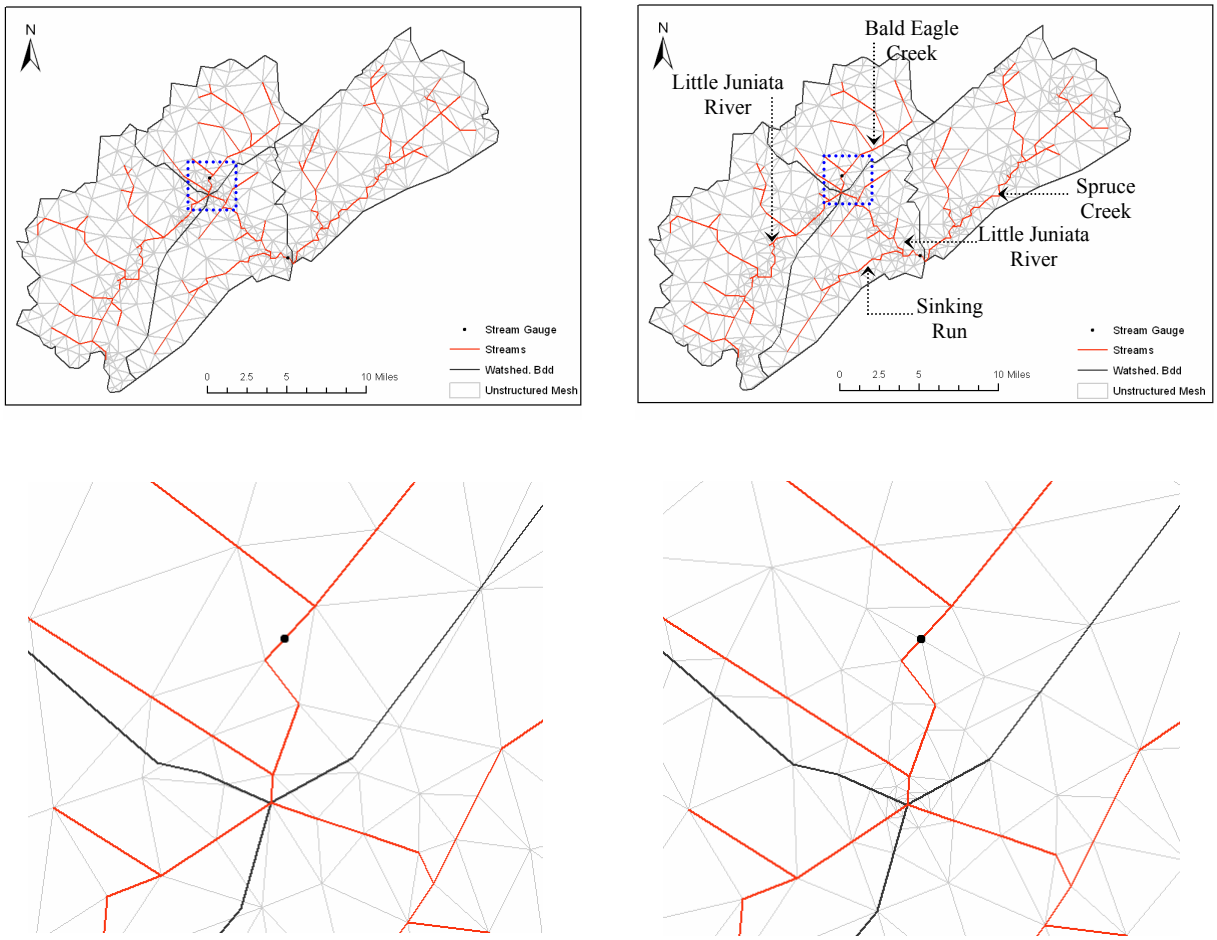

Figure 4.1 Unstructured domain decomposition of Little Juniata Watershed generated with (right) and without (left) the use of subwatershed boundaries and streamflow observation station as constraints. Note that in decomposition with the constraints, the observation station acts as a node of the river discretization element (right). The modeled flux location will be exactly at the gauge location thus appropriately accounting for the exact contributing area. Also the mesh boundary coincides with subwatershed boundaries (right) thus preserving necessary surface water flow directions.

stations as constraints, while the decomposition on the right does. This means that hydrologic states will be predicted exactly at the observation stations in the second case. Decomposition based on a line constraint also limits model parameterization errors. A parameter such as land cover or soil type can be used as a boundary or edge, defined by the sides of triangular elements. This ensures that a single land-cover/soil class exists within an unstructured mesh element thus limiting introduction of any additional uncertainty because of statistical averaging of multiple class types within an element (Kumar et al. 2009). For unconstrained situations, say when land-cover or soil classes are not used as a constraint, a mean parameter or statistic can be specified. Local boundary constraints during decomposition can be used to specify regions with smaller

mesh size, where faster hydrodynamics, steeper topography, or atmospheric forcing effects are expected. Similarly, meshes generated along the river can be designed to better capture the riparian dynamics and flood plain inundation. Apart from its advantage of computational efficiency and spatial adaptivity, unstructured meshes can be tailored to the complex geometries and physics of a given problem (Kumar et al. 2009). Algorithms for generating unstructured meshes using GIS feature objects and the advantages of resulting triangulations are discussed in Kumar et al. (2009).

Once the decomposition has been performed, soil, vegetation and hydrogeologic data are assigned to each element in the mesh. In many cases, the data must be viewed, queried, analyzed or sometimes even reused while the simulation proceeds. Traditionally this step has been addressed using existing GIS tools and feeder data access interfaces. Here we have used the tightly coupled integrated framework called PIHMgis to manage, analyze, visualize and to define relationships between hydrographic units and their physical properties. Details of the GIS-PIHM integration (PIHMgis) can be found in Bhatt et al. (2008).

4.3. Physical Coupling: Semi-Discretized Process Equations

PIHM uses a semi-discrete finite volume formulation for coupled hydrologic processes (Qu and Duffy 2007). A generalized partial differential equation (PDE) of flow of a conservative scalar variable ψ in the hydrologic system is universally expressed as

$$\frac{\partial \psi}{\partial t} = \nabla(\psi U) + \nabla(\Gamma grad\, \psi) + S_{\psi} \tag{4.1}$$

or the rate of change in ψ = (Convective Flux) + (Diffusive Flux) + (Source/Sink),

where U is the velocity vector, Γ is conductivity and S_{ψ} is rate of increase/decrease in ψ due to sources/sinks. The process defining PDEs are then locally reduced to ordinary differential equations (ODEs) by integration on a spatial unit element. The PDEs are integrated over an arbitrary three dimensional control volume, V_i in the model domain as

$$\int_{V_i} \frac{\partial \psi}{\partial t} dV = \int_{V_i} \nabla(\psi U) dV + \int_{V_i} \nabla(\Gamma grad\, \psi) dV + \int_{V_i} S_{\psi} dV \tag{4.2}$$

By applying Gauss's theorem on the convective and diffusive term on the right hand side of the Eq. (4.1), we obtain

$$\frac{\partial}{\partial t}\int_{V_i}\psi dV = \int_{A_{ij}} N.(\psi U)dA + \int_{A_{ij}} N.(\Gamma grad\,\psi)dA + \int_{V_i} S_\psi dV \qquad (4.3)$$

where N is the normal vector to the surface j of the control volume V_i. As mentioned in the previous section, PIHM discretizes the watershed domain into unstructured elements (prismatic in 3D) and the river into linear elements (rectangular/trapezoidal in 3D), as shown in Figure 4.2. This translates into the number of boundary faces j = 5 for prismatic elements and j = 6 for river elements. For notational simplicity, we represent convective flux (ψU) as $\vec{C}_f$ and separate diffusive flux ($\Gamma grad\,\psi$) into vertical ($\vec{G}$) and horizontal fluxes ($\vec{F}$) respectively. This reduces Eq. (4.3) into

$$\frac{\partial}{\partial t}\int_{V_i}\psi dV = \int_{A_{ij}} N.(\vec{C}_f)dA + \int_{A_{ij}} N.(\vec{G}+\vec{F})dA + \int_{V_i} S_\psi dV \qquad (4.4)$$

By integrating the individual terms in Eq. (4.4) and approximating the governing equation by its diffusive equivalents only (in this case by setting $\vec{C}_f = 0$), we obtain a generic semi-discrete form of ODE that defines all the hydrologic processes incorporated in the finite volume of the model as

$$A_i \frac{d\overline{\psi}}{dt} = \sum_j N.\vec{G}A_{ij} + \sum_k N.\vec{F}A_{ik} + \overline{S}_\psi V_i \qquad (4.5)$$

where $\overline{\psi}$ (L) is the average volumetric conservative scalar per unit planimetric control volume area A_i and $\overline{S}_\psi$ is the average source/sink rate per unit control volume. Every prismatic volume (kernel) is a stack of 5 control volumes (Figure 4.2). Eq. (4.5) represents the state variables coupled through vertical flux ($\vec{G}$) and lateral horizontal flux ($\vec{F}$) terms. Similarly a river or channel kernel consists of 2 control volumes as shown in Figure 4.2. Table 4.1 lists the vertical and horizontal flux terms associated with each state and identifies the coupled flux interactions between neighboring control volumes (both in

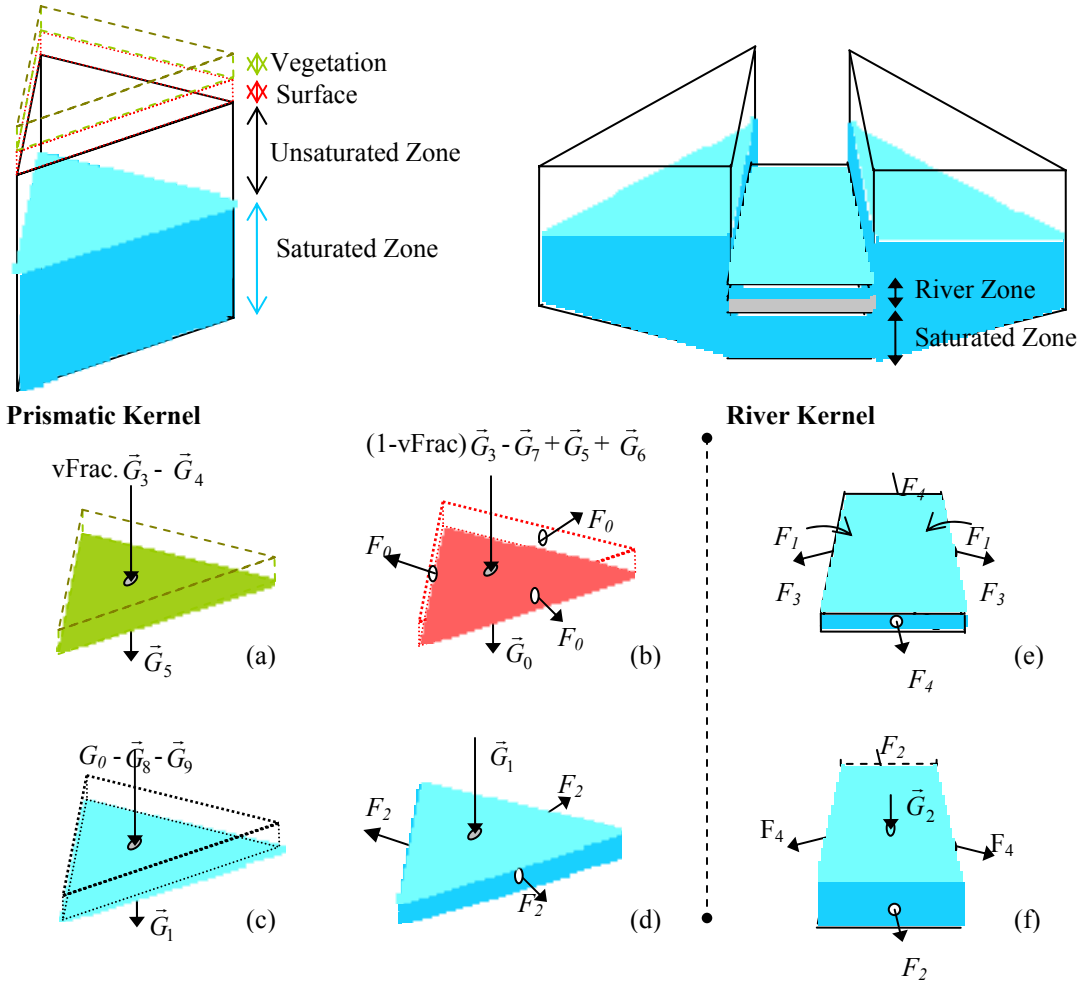

Figure 4.2 Prismatic (top left) and linear River (top right) kernels constitute a model domain. We note that each linear river kernel is sandwiched between neighboring watershed prismatic kernel elements. A kernel is a stack of control volumes corresponding to different states. Process interactions across the control volumes faces (listed in Table 4.1) are also shown. Sub-paneled graphics correspond to control volumes for a) Vegetation b) Overland Flow c) Unsaturated Zone d) Saturated Zone e) River flow and f) Groundwater flow below river bed.

vertical and in horizontal) through a process coupling function $f[]$. Individual vertical, horizontal and source/sink flux terms listed in Table 4.1 can be directly replaced in Eq. (4.5) to evaluate the respective state equations. The coupling function $f[]$ defined in Table 4.1 shows that the coupling between processes such as interception-snow, interception-unsaturated zone is "one-way" only, while interactions between unsaturated-saturated and river-saturated zone are "two-way". Explanations of the symbols not

Table 4.1 Definition of coupling function and the lateral and vertical fluxes across the faces of a control volume. i and j are indices of neighboring control volumes and $\| \ \|$ denotes conditional terms which exist only for the grids that are neighbor of a river element. Explanation of symbols is in Appendix I in Section 4.10

Prismatic Element					
Control Volume	$\overline{\psi}$ (State)	$\vec{G}$ (Vertical Flux)	$\vec{F}$ (Horizontal Flux)	$\overline{S}_{\psi}$ (Source/ Sink)	$f[]$ (Coupling Flux Function)
Interception	ψ_0	$\vec{G}_3 - \vec{G}_4 - \vec{G}_5$	--	--	$\vec{G}_5 \equiv \mathrm{f}[\psi_0]$
Snow	ψ_1	$\vec{G}_3 - \vec{G}_6$	--	--	$\vec{G}_6 \equiv \mathrm{f}[\psi_1]$
Surface Flow	ψ_2	$\vec{G}_3 - \vec{G}_0 - \vec{G}_7 + \vec{G}_5 + \vec{G}_6$	$\vec{F}_0 + \|\vec{F}_l\|$	--	$\vec{F}_0 \equiv \mathrm{f}[\psi_{2i}, \psi_{2j}], \vec{G}_0 \equiv \mathrm{f}[\psi_2, \psi_3]$ $\vec{G}_5 \equiv \mathrm{f}[\psi_0], \vec{G}_6 \equiv \mathrm{f}[\psi_1], \|\vec{F}_l\| \equiv \mathrm{f}[\psi_5, \psi_2]$
Unsaturated Zone	ψ_3	$\vec{G}_0 - \vec{G}_1 - \vec{G}_8 - \vec{G}_9$	--	--	$\vec{G}_0 \equiv \mathrm{f}[\psi_2, \psi_3], \vec{G}_1 \equiv \mathrm{f}[\psi_3, \psi_4]$ $\vec{G}_8 \equiv \mathrm{f}[\psi_3], \vec{G}_9 \equiv \mathrm{f}[\psi_3, \psi_0]$
Saturated Zone	ψ_4	$\vec{G}_1$	$\vec{F}_2 + \|\vec{F}_3\| + \|\vec{F}_4\|$	$-S_1$	$\vec{G}_1 \equiv \mathrm{f}[\psi_3, \psi_4], \vec{F}_2 \equiv \mathrm{f}[\psi_{4i}, \psi_{4j}]$ $\|\vec{F}_3\| \equiv \mathrm{f}[\psi_5, \psi_4], \|\vec{F}_4\| \equiv \mathrm{f}[\psi_6, \psi_4)]$
Linear Element					
Channel zone	ψ_5	$\vec{G}_3 - \vec{G}_2 - \vec{G}_7$	$\|\vec{F}_3\| + \vec{F}_5 + \|\vec{F}_l\|$	--	$\vec{G}_2 \equiv \mathrm{f}[\psi_5, \psi_6], \vec{F}_5 \equiv \mathrm{f}[\psi_{5i}, \psi_{5j}]$ $\|\vec{F}_l\| \equiv \mathrm{f}[\psi_5, \psi_2], \|\vec{F}_3\| \equiv \mathrm{f}[\psi_5, \psi_4]$
Sub-Channel Zone	ψ_6	$\vec{G}_2$	$\|\vec{F}_4\|$	--	$\|\vec{F}_4\| \equiv \mathrm{f}[\psi_6, \psi_4], \vec{G}_2 \equiv \mathrm{f}[\psi_5, \psi_6]$

described in the text can be referred to in Appendix I (section 4.10). Details of the vertical, horizontal and source/sink flux term calculations listed in Table 4.1 are discussed next.

4.3.1. Throughfall Drainage

The rate of throughfall drainage ($\vec{G}_5$) depends on the interception storage depth (ψ_0) by

$$\begin{aligned} \vec{G}_5 &= k \exp[b(\psi_0 / \psi_{0\max})] \text{ for } 0 \le \psi_0 < \psi_{0\max} \\ &= k \exp[b] \text{ for } 0 < \psi_{0\max} \le \psi_0 \end{aligned} \quad (4.6a)$$

where $\psi_{0\max}$ is the canopy water storage capacity (L)

The drainage parameter b (dimensionless) and k (LT^{-1}) are based on Rutter and Morton (1977), who suggested b ranging from 3.0 to 4.6, and k = 3.91 x $10^{-5}\psi_0$ (in mm/min). $\psi_{0\max}$ depends on LAI as

$$\psi_{0\max} = K_L \text{ x } LAI \quad (4.6b)$$

where K_L is assumed to be 0.2 mm (Dickinson 1984). We note that the calculations performed above are "physically based" only in weak sense as they do not take into account the complex canopy architecture and so will be accurate for limited ranges of vegetation types and spatial scales. The ODE defining the changes in the depth of the water stored in the canopy is described by

$$\frac{d\psi_0}{dt} = (\vec{G}_3 - \vec{G}_4 - \vec{G}_5) \quad (4.6)$$

where $\vec{G}_3$ is $vFrac*(1-f_s)$ times the precipitation rate (LT^{-1}), $\vec{G}_4$ is evaporation from canopy storage (LT^{-1}), $vFrac$ is fractional areal vegetation cover in a control volume and f_s is snow fraction.

4.3.2. Evapotranspiration

Total evapotranspiration (ET) is the sum of evaporation (Shuttleworth 1993) from the upper soil layer ($\vec{G}_8$), from overland flow ($\vec{G}_7$), from evaporation of interception ($\vec{G}_4$), and transpiration ($\vec{G}_9$). Total evapotranspiration is expressed as

$$\mathrm{ET} = \vec{G}_4 + \vec{G}_7 + \vec{G}_8 + \vec{G}_9 \tag{4.7}$$

The vertical flux components in Eq. (4.7) are calculated as follows:

$$\vec{G}_7 = (1 - vFrac)\frac{Q^*\Delta + (\rho C_{pa}/r_a)(e_{sz} - e_z)}{\Delta + \gamma} \tag{4.7a}$$

$$\vec{G}_8 = \beta_s \vec{G}_7 \tag{4.7b}$$

$$\beta_s = \begin{cases} 0.5(1 - Cos[\pi(\dfrac{\theta_g}{\theta_{fl}})]) & \theta_g \le \theta_{fl} \\ 1 & \theta_g > \theta_{fl} \end{cases}$$

where $\theta_{fl} = 0.75\theta_{sat}$ is the field capacity, θ_{sat} is saturated moisture content, θ_g is moisture content of the top soil layer and β_s describes the influence of the top soil layer saturation on evaporation from ground (Schmidt et al. 2005). We note that saturation of the top soil layer is related to ψ_3 though van-Genuchten relationship (Eq. 4.11a). Evaporation from the wet canopy is calculated by

$$\vec{G}_4 = vFrac\frac{Q^*\Delta + (\rho C_{pa}/r_a)(e_{sz} - e_z)}{\Delta + \gamma}\delta_r \qquad \delta_r = (\frac{\psi_0}{\psi_{0\max}})^{\frac{2}{3}} \tag{4.7c}$$

where δ_r is the area fraction of the wet canopy as calculated in Deardorff (1978). Sub-linear dependence of δ_r on the ratio of ψ_0 to $\psi_{0\max}$ captures the increasing rate of evaporation of canopy water as the fraction of leaf area containing water decreases. Vegetation also influences ground-water by extraction of soil water by transpiration thus decreasing the amount of percolating water that reaches the saturated zone and increasing the capillary rise. Based on the formulation of (Blondin 1991), transpiration is independently calculated by

$$\vec{G}_9 = vFrac\frac{Q^*\Delta + (\rho C_{pa}/r_a)(e_{sz} - e_z)}{\Delta + \gamma(1 + \dfrac{r_s}{r_a})}(1 - \delta_r) \tag{4.7d}$$

The bulk stomata resistance, r_s (TL^{-1}) of the canopy due to specific humidity gradient between leaves and overlying air depends largely on the minimum resistance, the available solar energy, the availability of water in the root zone and the air temperature (Jarvis 1976). In PIHM, r_s is obtained based on Dickinson (1984) as

$$r_s = \frac{r_{\min}\alpha_r\beta_s}{LAI\,\eta_s{}^4} \qquad \text{where } \alpha_r = \frac{1+f_r}{1+r_{\min}/r_{\max}} \text{ and } f_r = \frac{1.1R_{sc}}{R_s{}^{ref}\,LAI} \tag{4.7e}$$

where R_{sc} (MT^{-3}) is estimated by Beer's law as

$$R_{sc} = R_s(1-\exp(-\alpha LAI)) \tag{4.7f}$$

and $R_s{}^{ref}$ (MT^{-3}) is assumed as 30 Wm^{-2} for trees and 100 Wm^{-2} for grassland and crops (Bougeault 1991). β_s is the saturation in the active soil layer (Eq. 4.7b) for agricultural and pasture land and in the transmission zone for forest, controlled by root depth of each vegetation type. η_s accounts for the reduced activity of plants when the air temperature is very high or very low and is calculated according to

$$\eta_s = 1-0.0016(298.0-T_a)^2 \tag{4.7g}$$

$r_{\max}$, maximum stomata resistance is set uniformly to 5000sm^{-1}. $r_{\min}$ is minimum stomata resistance. For the simulation performed here, $r_{\min}$ is obtained from the vegetation parameters used in LDAS as available on http://ldas.gsfc.nasa.gov/LDAS8th/EROSveg2/LDASvegetation2.shtml.

4.3.3. Snow Melt

The basic snow melt ($\vec{G}_6$) flux is based on a temperature index model equation represented by

$$\vec{G}_6 = C_s(T_a - T_b) \tag{4.8a}$$

The melt rate coefficient C_s typically varies between 1.8 to 3.7 mm/^{o}C. Air temperature is used to partition snow and rain (USACE 1956) according to

$$f_s \quad = 1.0 \qquad T_a < T_s$$

$$= \frac{T_r - T_a}{T_r - T_s} \qquad T_s \le T_a \le T_r \tag{4.8b}$$

$$= 0 \qquad T_a > T_r$$

where T_r (=1^{o}C) is the air temperature above which all precipitation is assumed to fall as rain, and T_s (=-3^{o}C) is the air temperature below which all precipitation is assumed to fall as snow. The semi-discrete ODE representation of snow accumulation/melt is represented by

$$\frac{d\psi_1}{dt} = (\vec{G}_3 - \vec{G}_6) \tag{4.8}$$

where $\vec{G}_3$ is f_s times the precipitation rate (LT^{-1}).

4.3.4. Infiltration

Infiltration ($\vec{G}_0$) is handled according to the approach of Freeze (Freeze 1978) by

$$\vec{G}_0 = \Gamma grad\,\psi \tag{4.9}$$

where

$$\Gamma = K(\psi_3) \qquad grad\,\psi = \frac{(\psi_2 + z) - (\psi_3 + z_u)}{d} \tag{4.9a}$$

$K(\psi_3)$ is the vertical hydraulic conductivity of the top soil layer [L/T], z is the land surface elevation, z_u the elevation of the top soil layer and d is a specified vertical distance across which the head gradient is calculated. This coupling strategy is based on continuity in hydraulic head across the surface skin thickness ($2d$). $K(\psi_3)$ is calculated using van Genucten equation (discussed later in Eq. 4.11a).

4.3.5. Unsaturated-Saturated Flux

The ODE defining the change in unsaturated zone soil moisture depth is given by

$$\frac{d\psi_3}{dt} = \vec{G}_0 - \vec{G}_1 \tag{4.10}$$

Flux between saturated-unsaturated zones is calculated using Richard's equation (1931) by assuming a vertical exchange across a moving boundary (water table interface). The approach is similar to (Duffy 2004). The vertical flux at the water table can be approximated by (derivation details in Appendix III, section 4.10):

$$\vec{G}_1 = \frac{K_u(\psi_3)K_s z_b(\alpha(z - z_b - \psi_4) - 2(-1 + S^{\frac{n}{1-n}})^{\frac{1}{n}})}{\alpha(K_u\psi_4 + K_s(z - z_b - \psi_4))} \tag{4.11}$$

where $K_u(\psi_3)$ and S of the unsaturated zone is calculated according to van Genuchten (1980) equation as

$$K_u(\psi_3) = S^{0.5}(1 - (1 - S^{\frac{n}{n-1}})^{\frac{n-1}{n}})^2 \quad \text{and} \quad S = \frac{\psi_3}{z - z_b - \psi_4} \tag{4.11a}$$

α and n in the above equations are van Genuchten' soil retention parameters. Similar derivations for vertical flux using other $K_u - S$ relationships from Brooks-Corey (1964), Srivastav and Yeh (1991) are also incorporated in the model.

4.3.6. Groundwater Flow

Lateral ground water flow $\vec{F}_2$ is governed by Darcy-type flow and the conductance and gradient terms between neighboring control volumes (shown in Figure

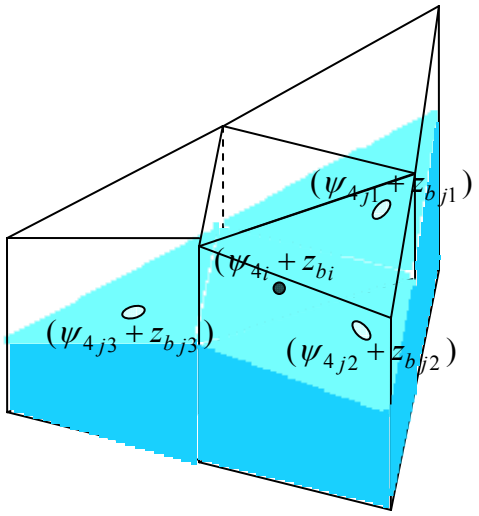

Figure 4.3 Groundwater flux across all the three prismatic kernel edges depends on the head gradient across it

4.3) are evaluated as

$$\Gamma = K_{eff} \qquad grad\psi_{ij} = \frac{(\psi_{4i} + z_{bi}) - (\psi_{4j} + z_{bj})}{d_{ij}} \tag{4.12a}$$

The ODE for head in saturated zone is written as

$$\frac{d\psi_4}{dt} = \vec{G}_1 + \frac{1}{A}\left(\sum_{j=1}^{3} UW[\psi_{4i}, \psi_{4j}] e_j \Gamma_j grad\psi_{ij}\right). \tag{4.12}$$

4.3.7. Surface Overland Flow

The transient flow of water on the land surface ($\vec{F}_0$) is estimated by either a kinematic wave or diffusion wave approximation to the depth-averaged shallow water equations. Assuming a negligible influence of inertial forces and shallow depth of water ψ_2(L), the conductivity, Γ and gradient term, $grad\psi$ in Eq. (4.3) for the diffusion wave approximation of St. Venant's equation is calculated using Gottardi and Venutelli (1993) by

$$\Gamma = \frac{\psi_{2i}^{2/3}}{n_s}(\nabla_s(\psi_{2i} + z_i))^{-\frac{1}{2}} \text{ and } grad\psi_{ij} = \frac{(\psi_{2i} + z_i) - (\psi_{2j} + z_j)}{d_{ij}} \tag{4.13}$$

where $\nabla_s\psi$ is the gradient of overland flow head in the direction of maximum slope. $\nabla_s\psi$ for a triangular element is approximated by calculating the slope of the triangular stencil (Pan and Cheng 1993) shown in Figure 4.4. We reiterate at this point that overland flow flux is calculated between all neighboring elements of a triangle according to Eq. (4.4). The maximum slope calculation is performed only to calculate the diffusive conductivity term in (13). Details of the slope calculation can be found in Appendix II (section 4.10). We note that for triangular elements that are adjacent to channels, the triangular slope stencil is bounded by a channel element and the calculation of slope uses total heads from two neighboring triangular elements and a channel as shown in Figure 4.4. Substituting the simplified conductivity and gradient relationships of Eq. (4.13) in Eq. (4.5) adequately resolves backwater effects and is applicable to flow

on flat surfaces (di Giammarco 1996). The kinematic wave approximation requires a different

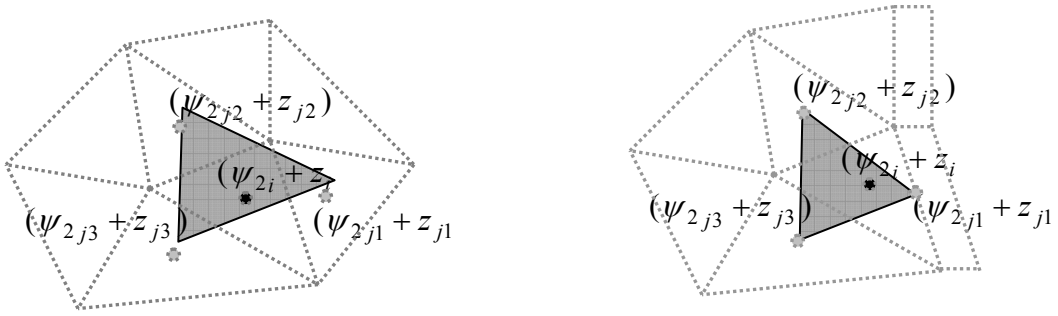

Figure 4.4 $\nabla_s\psi$ for the unit element *i* in Eq. (4.13) is calculated by approximating a triangular stencil over neighboring elements. The graphic on the right addresses the case when a prismatic element neighbors a river. The expression for the gradient is in Appendix II (section 4.10).

term given by $\Gamma = \frac{\psi_2^{2/3}}{n_s^{1/2}}\nabla_s z$. The kinematic approximation while supported in PIHM is not considered in the simulations presented in this study. The semi-discrete ODE for overland flow depth reduces to

$$\frac{d\psi_2}{dt} = (\vec{G}_3 - \vec{G}_7 + \vec{G}_5 + \vec{G}_6) - \vec{G}_0 + \frac{1}{A_i}\left(\sum_{j=1}^{3}\vec{F}_{0j}UW[\psi_{1i},\psi_{1j}]e_j + \left\|\vec{F}_1((\psi_{1i}+z_i)-(\psi_{5j}+z_{rj}))L_j\right\|\right) \quad (4.14)$$

where $\vec{G}_3$ is (1-*vFrac*) times the precipitation rate (LT^{-1}). We note that $\|\ \|$ are conditional terms which exist only for the grids that are neighbor of a river element. The flux of overland flow across river banks, $\vec{F}_1$, is defined in the next section. *UW*[] is an upwind function which identifies the upstream head or flow-depth (out of its two arguments) for overland flow (and also for channel and groundwater flow that are discussed later in the text). For an overlandflow case, gradient of total overland flow head is considered positive from upstream to downstream.

4.3.8. Surface Overland Flow to River

Surface flow across the channel banks ($\vec{F}_1$) is calculated using Robertson (1985) as

$$\vec{F}_1 = C_d \frac{2}{3}\sqrt{2g}((\psi + z)_u - \max[(\psi + z)_d, z_{rb}])^{1/2} \qquad (4.15)$$

where $(\psi + z)_u$ and $(\psi + z)_d$ are the upwind and downwind head respectively as characterized by whichever is the higher and lower head that exists across the channel bank. The downwind head is a boolean choice between total streamflow head and river bank elevation depending on whether the bank is submerged or not as depicted in Figure 4.5.

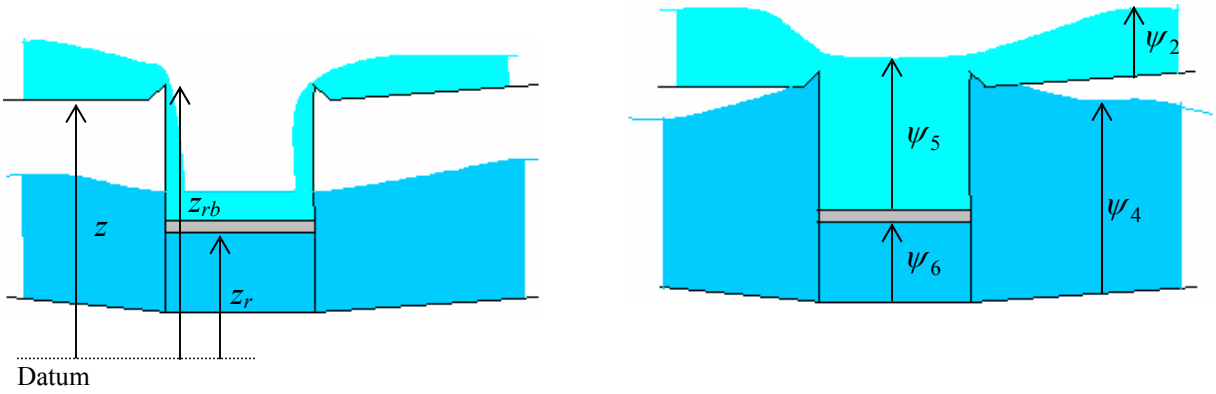

Figure 4.5 Two cases of surface flow across the "weir/dam" type channel bank. Case on the left pertains to when river stage is lower than the river bank height while case on the right has river stage larger than the bank height. We note that for the both cases shown above, $(\psi + z)_u$ in Eq. (4.15) will be (z+ψ_2)

4.3.9. Channel Flow

Flow through a network of rivers and channels are characterized by the one-dimensional diffusion/kinematic wave approximation to the St. Venant equations. The conductance and gradient terms are derived in a similar manner as in Eq. (4.10) as

$$\Gamma = \frac{\psi_5^{2/3}}{n_s}\left(\nabla(\psi_5 + z_r)\right)^{-\frac{1}{2}} \qquad grad\psi_{ij} = \frac{(\psi_{5i} + z_{ri}) - (\psi_{5j} + z_{rj})}{d_{ij}} \qquad (4.16)$$

The semi-discrete ODE defining the river flow is represented as

$$\frac{d\psi_5}{dt} = \frac{1}{A_i}\left(\sum_{j=1}^{2}\Gamma_j grad\psi_{ij} UW[\psi_{5i}, \psi_{5j}]e_j + \sum_{j=1}^{2}\vec{F}_{1j}(UW[\psi_{2j} + z_j, \psi_{5i} + z_{ri}]L_i)\right)$$

$$+\frac{1}{A_i}\sum_{j=1}^{2}\vec{F}_{3j}(UW[\max[\psi_{4j}+z_{bj}-z_{ri},0],\psi_{5i}]L_j)-\vec{G}_2+\vec{G}_3-\vec{G}_7 \qquad (4.17)$$

where $\vec{G}_3$ is precipitation on the river surface.

4.3.10. Channel and Aquifer Interaction

The channel interacts with aquifer through its bed and edges as shown in Figure 4.2. Lateral flux exchange through the channel edges can be calculated by

$$\vec{F}_3 = \Gamma grad\,\psi_{ij} \qquad (4.18)$$

where conductance and gradient terms are

$$\Gamma = K_{eff} \qquad grad\,\psi_{ij} = \frac{(\psi_{5i}+z_{ri})-(\psi_{4j}+z_{bj})}{d_{ij}} \qquad (4.18a)$$

Flux exchange through the river bed follows the same equations as (4.18a) until the river aquifer becomes hydraulically disconnected after which the gradient is dependent on the head in river only (Rushton and Tomlinson 1979).

4.3.11. Sub-Channel Groundwater Flow

Ground water flow beneath the river interacts with the river as well as the neighboring aquifer elements. Gradient and conductance terms along and lateral to the channel are calculated as

$$\Gamma = K_{eff} \qquad grad\,\psi_{ij} = \frac{(\psi_{6i}+z_{bi})-(\psi_{6j}+z_{bj})}{d_{ij}} \qquad (4.19a)$$

$$\vec{F}_4 = K_{eff}\frac{(\psi_{6i}+z_{bi})-(\psi_{4j}+z_{bj})}{d_{ij}} \qquad (4.19b)$$

The ODE defining the flow is written as

$$\frac{d\psi_6}{dt} = \frac{1}{A_i}\sum_{j=1}^{2}\Gamma_j grad\,\psi_{ij} UW[\psi_{6i},\psi_{6j}]e_j$$

$$+\frac{1}{A_i}\sum_{j=1}^{2}\vec{F}_{4j}(UW[\min[\psi_{4j}, z_{ri}-z_{bj}], \psi_{6i}]L_j+\vec{G}_2 \qquad (4.19)$$

4.3.12. Macropore Infiltration

Preferential flow through macropores in forested catchments such as root holes, cracks or pipes in soils, or through dissolution features, joints, and fractures in bedrock lead to large and fast infiltration and recharge to groundwater (Anderson 1997). These macroporous features may result in bypassing of most of the infiltration from the surface soil layer directly to deeper layers. Even though the macroporous volume is small relative to the soil matrix (~ 1 % of the pore volume), the volumetric transport capacity can be significant to the overall flow. The critical pore size at which infiltration can be classified as macropore flow has been discussed in Beven and Germann (1982).

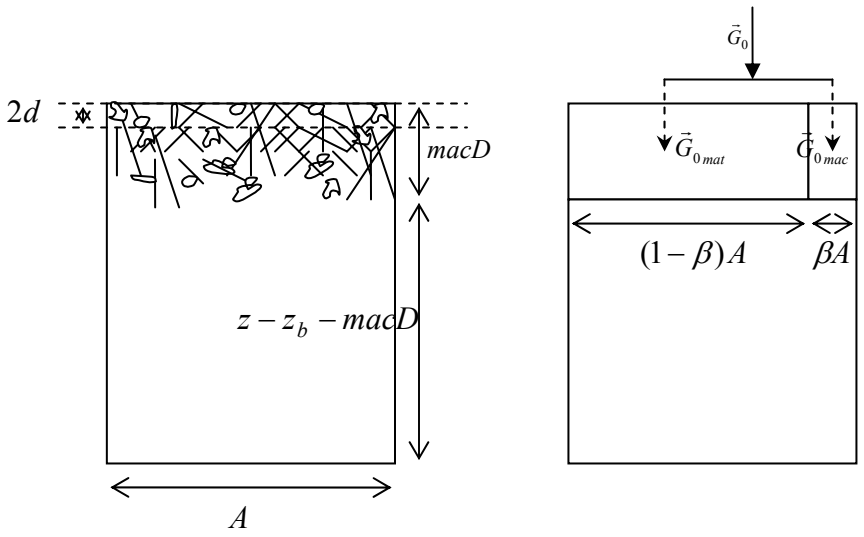

Figure 4.6 Graphic on the left shows how PIHM defines the depth of macropores (*macD*). The surface "skin-depth" *2d* is defined as the depth over which the infiltration is calculated. The conceptual model of infiltration/exfiltration based flow is shown in the right graphic where the system is divided into a dual matrix with micropore and macropore media

Several studies have focused on approximating the macropore flow contributions to subsurface flow (Hutson and Wagenet 1975). Vanderkwaak (1999) used a dual continua approach by calculating heads and interacting fluxes in macropores and soil matrix separately and assuming Richard's equation to be valid in each of them. Gerke and van

Genuchten (1993) and Mohanty et al. (1997) studied the effect of macropores on soil hydraulic properties using multi-domain models. Here we follow a simpler dual-domain approach (Hoogmoed and Bouma 1980). The approach represents an equivalent matrix-macropore system that is assumed to follow Richard's equation with total infiltration/exfiltration rate to be equal to sum of matrix infiltration ($\vec{G}_{0mat}$) and macropore infiltration ($\vec{G}_{0mac}$) as shown in Figure 4.6. The net conductivity of the equivalent system is determined by the head difference that exists across the infiltration layer (Chen and Wagenet 1992) as shown in Table 4.2. $\vec{G}_0$ and $grad\psi$ in Table 4.2 are

Table 4.2 Effective macroporous-soil infiltration rate modeled as a dual matrix-macropore system for different water application rate conditions. $\vec{G}_{0mat}$ and $\vec{G}_{0mac}$ are matrix and macropore infiltration rates. Explanation of symbols is in Appendix I (section 4.10)

calculated according to Eq. (4.9) and

Condition	$\vec{G}_{0mat}$	$\vec{G}_{0mac}$
$\psi_3 = z - z_b - \psi_4$	$K_{matV}[S=1](1-\beta)grad\psi$	$K_{macV}[S=1]\beta grad\psi$
$\vec{G}_0 < K_{matV}[S]$	$\vec{G}_0$	---
$\vec{G}_0 > K_{matV}[S]$ and $\vec{G}_0 < K_{\max}$	$K_{matV}[S](1-\beta)grad\psi$	$K_{macV}[S]\beta grad\psi$
$\vec{G}_0 > K_{matV}[S]$ and $I > K_{\max}$	$K_{matV}[S](1-\beta)grad\psi$	$K_{macV}[S=1]\beta grad\psi$

$$K_{\max} = K_{matV}[S](1-\beta) + K_{macV}\beta \tag{4.20}$$

We note that the conditional statement in the second row (in Table 4.2) means that if the water application rate on the soil surface is less than the hydraulic conductivity of the matrix, the water flow rate through the equivalent system will be limited by the application rate and the equivalent conductivity will be equal to the matrix conductivity at a given saturation. The third row defines the conductivity when the infiltration rate is greater than the conductivity of the soil matrix but less than $K_{\max}$. The last row is the equivalent conductivity when the application rate is greater than $K_{\max}$. In this case water

will flow through both the matrix and macropores with majority of the flow contributed through macropores.

4.3.13. Macroporous Stormflow

In addition to the increase in soil infiltration capacity, a second effect of a macroporous soil is the possible lateral conduction of subsurface stormflow (Mosley 1982). A macropore system with sufficient connectivity over a particular soil depth and distance leads to quick transmission of soil water as subsurface stormflow or interflow. The depth of this interflow layer is assumed to be the depth of the macroporous soil, which will depend on the vegetation type and root distribution, organic content and geologic structure. The net conductivity for lateral flow is dependent on the macroporous soil thickness and soil saturation given by:

$$K_{eq} = K_{matH}[S](1-\beta) + K_{macH}[S]\beta \tag{4.21}$$

The percentage of macropore that becomes active is assumed here to be linearly dependent on the average saturation of macroporous soil layer i.e.

$$K_{macH}[S] = K_{macH}[S=1].S \tag{4.21a}$$

Given the relatively coarse spatial discretization that is used in the model application, lateral flow through karst fractures can be modeled as subsurface stormflow.

4.3.14. Specified Flux or Head Conditions

Specified flux, hydraulic head or mixed boundary conditions are implemented for watershed boundaries, river outlets, injections/withdrawals/controls and hydraulic structures like weirs, wells, dams etc. Dirichlet, Neumann or Cauchy boundary conditions (Morse et al. 1982) can be applied to any of the state variables on any of the element edges, both prismatic watershed elements and linear river elements. Typically specified conditions incorporated in PIHM are a) flow/no-flow condition (at watershed boundaries), b) critical depth boundary condition (at weirs, falls or flow into deep lakes) given by

$$\vec{F}_5 = \sqrt{g(\psi_5 - z_w)} \tag{4.22a}$$

where z_w is the height of weir and c) zero-gradient boundary condition (at the channel outlet in alluvial plans) given by

$$\vec{F}_5 = \frac{1}{n}\left(\frac{A}{P}\right)^{2/3} S_o^{1/2} \tag{4.22b}$$

where A is the cross-sectional area of channel, P is wetted perimeter and S_o is the slope of the bed.

4.4. Numerical Coupling: Solution Strategy and Kernel Flexibility

The local coupling of ODEs corresponding to each physical process forms the model *kernel* within the prismatic 3D element. Assembling the kernel over the model domain forms the global ODE system, assuring a fully coupled or direct numerical coupling procedure. All state variables are solved simultaneously and advance together at each time step. The time step is adaptively determined by the fastest time scale of the interacting processes. The strategy requires a stiff solver. Appendix IV (section 4.10) details the mathematical explanation of stiffness arising in a representative coupled system and explains the limitation of the explicit solution methodology to solve such a system.

4.4.1. Numerical Solver

The Newton–Krylov implicit solver is a typical choice for large non-linear stiff ODE system (Jones et al. 2001, 2001). Here we use the CVODE solver (Cohen and Hindmarsh 1994) from the SUNDIALS package to solve the system of stiff ODEs. CVODE uses a combination of the Backward Difference Formula (BDF) with linear Krylov iteration, and a preconditioned GMRES algorithm (Byrne 1992). Adaptive time-stepping and an order-adjustment scheme alleviate the computational burden posed by the implicit solver. The internal time steps taken by the solver becomes smaller in response to rapid changes in state triggered by precipitation events. Large precipitation events lead to generation of overland flow, resulting in increased interaction of surface-subsurface processes, thus

further increasing the stiffness of ODE system. The solvers' treatment of stiff terms provides solutions which are accurate at slow scales and stable at fast scales (due to channel flow, overland flow and stream-aquifer interactions).

4.4.2. Kernel Flexibility

An important feature of the PIHM formulation is that its data structure remains isolated and independent from CVODE's data structure. This approach allows the user to easily alter the system of equations in the kernel without having to manually change the numerical discretization. Multiple formulations can be activated simply using boolean switches on the right hand side of ODE. This provides the user a unique flexibility in the choice of process equations used in a particular kernel, depending on the model purpose or other computational constraints. As an example, for modeling large western watersheds with mountainous upland topography with dry valleys, the snow-melt process can be removed over part of the domain. The simplicity of using a "switch" without having to reformulate the numerical discretization is also useful for testing trial constitutive relationships and new theoretical formulations.

4.5. Model Application: Site Description and Data Needs

Application of the PIHM model has been carried out for the Little Juniata River Watershed, located in south central Pennsylvania. The watershed size is 845.6 sq. km and is within the US National Weather Service (NWS) mid-Atlantic river forecast center (MARFC) area of forecast responsibility. The watershed is characterized by significant complexity of the bedrock geology and is a part of Susquehanna River Basin Hydrologic Observing System (www.srbhos.psu.edu).

4.5.1. Topographic-Geologic-Climatic Framework of Little Juniata Watershed

The topography of this region is characterized by mountains and north-east to south-west oriented valleys. There are four main streams in the watershed: Bald Eagle Creek, Spruce

Creek, Sinking Valley and the Little Juniata River (see Figure 4.1). The headwaters form the western boundary of the Susquehanna River Basin in this region. The Little Juniata River is the longest stream with length of 82 km. Physiographically, the watershed is within a transition zone between the Appalachian Plateau and the Ridge and Valley provinces.

Topography ranges from 204 to 800m above sea level, with the slope ranging from 0 to 55 degrees. There are significant orographic effects in the region, with precipitation determined by both orientation and altitude of the terrain (Hosler 1963). Prefrontal precipitation has a critical impact on snowpack conditioning and watershed rainfall-runoff response during and after the passage of the front. Wintertime cold fronts

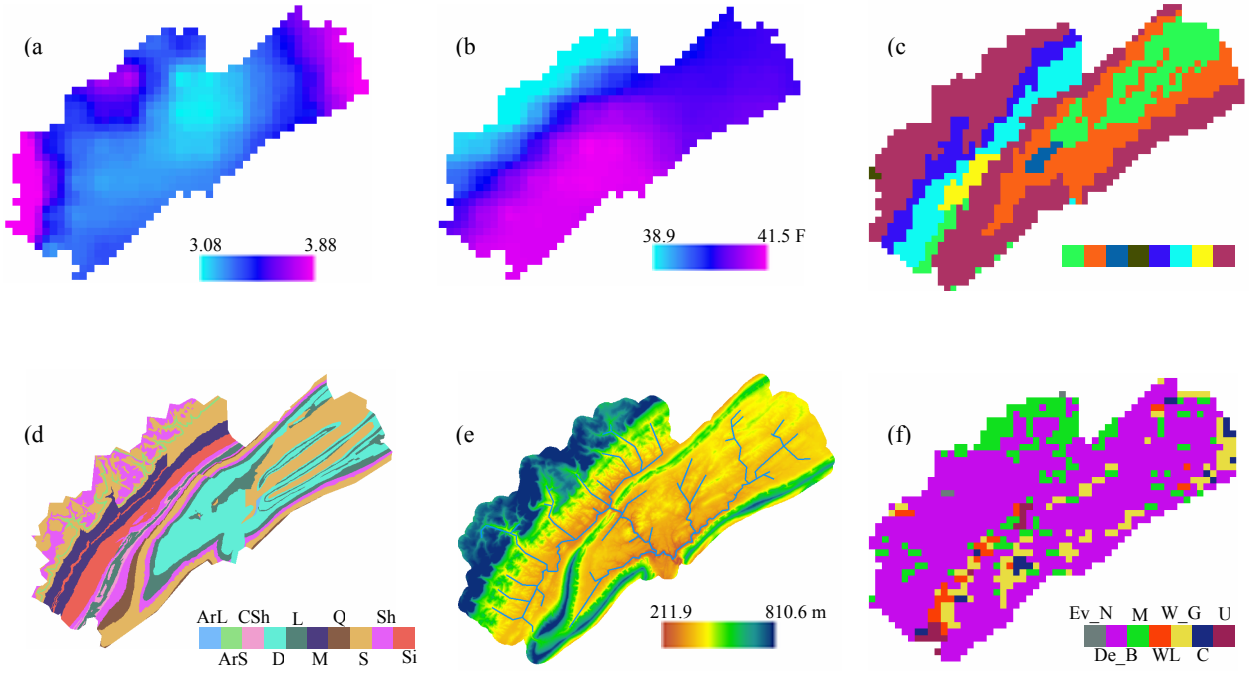

Figure 4.7 Distributed data map of a) Precipitation (Nov, 1983) b) Temperature (Nov, 1983) c) Soils d) Geology e) Elevation and f) Land Cover for Little Juniata Watershed. Data sources are listed in Table 4.3

consistently cause severe rainfall in the windward side of the orographic crest (Barros and Kuligowski 1998).

The geology of the Little Juniata watershed consists of carbonate and siliclastic mix of around ten bedrock strata including: Argillaceous limestone (ArL), Argillaceous sandstone (ArS), Calcareous shale (CSh), Dolomite (D), Limestone (L), Mudstone (M),

Quartzite (Q), Sandstone (S), Shale (Sh) and Siltstone (Si). The valleys of Spruce Creek and Sinking Valley are predominantly carbonates of limestone and/or dolomite, while the higher elevations are predominantly weather-resistant siliclastic sandstones and shales. Karst valleys dominated by sinkholes and forested headwaters contribute to the importance of macropore dominated flow regimes which may also be reflected in the streamflow hydrograph response during large storms.

4.5.2. Distributed Data Sources

The heterogeneity in the distribution of land cover, surface and bedrock topography, hydrogeology, and atmospheric forcing, all impact the duration, timing, and dynamics of interactions among the physical processes in the watershed. The necessary data sources for PIHM simulations are listed in Table 4.3. Figure 4.7 shows the spatial distribution of geology, soil, land cover, precipitation and elevation. The seven land cover types in this watershed are Evergreen-Needleleaf forest (Ev_NL), Deciduous Broadleaf Forest (De_BL), Mixed cover (M), Woodland (WL), Wooded Grass Land (W_GL), Crop (C) and Urban (U) with aerial coverage percentage being equal to 0.1 %, 73.8 %, 10.7 %, 3.4 %, 9.0 %, 1.9 % and 0.7 % respectively. We will show that hydrology of this bedrock aquifer system is very sensitive to the diversity in land cover and geology, with very important effects on the patterns and timing of recharge and baseflow to streams. Within the vadose zone, unsaturated hydraulic properties for porosity are derived from sand-silt-clay fraction and bulk density data obtained from the STATSGO soil database (Miller and White 1998). The Rosetta software (Schaap and Leij 1998) is used to predict hydraulic retention parameters and uncertainty range used in the Van Genuchten Eq. (4.11a). All types of physiographic, geologic and climate forcing distributed data and other topological relations are appropriately mapped to the model unstructured grid and discretized linear river elements in an automated way using PIHMgis (Bhatt et al. 2008).

Table 4.3 A-priori distributed data requirements for a PIHM model simulation and the sources from which distributed parameters were derived

Feature/ Time Series	Property	Source
Soil	Porosity; Sand, Silt, Clay Fractions; Bulk Density	STATSGO http://www.ncgc.nrcs.usda.gov/products/datasets/statsgo/
Geology	Bed Rock Depth; Horizontal and Vertical Hydraulic Conductivity	http://www.dcnr.state.pa.us/topogeo/, http://www.lias.psu.edu/emsl/guides/X.html
Land Cover	LAI	http://glcf.umiacs.umd.edu/data/landcover/data.shtml, http://ldas.gsfc.nasa.gov/LDAS8th/MAPPED.VEG/LDASmapveg.shtml;
	Manning's Roughness	Hernandez et. al., 2000
River	Topology: From Node – To Node, Neighboring Elements;	Derived using PIHMgis (Bhatt et. al., 2008)
	Manning's Roughness;	Dingman (2002)
	Coefficient of Discharge	ModHms Manual (Panday and Huyakorn, 2004)
	Shape and Dimensions;	Derived from regression using depth, width and discharge data from http://nwis.waterdata.usgs.gov/usa/nwis/measurements
Forcing	Precipitation, Temperature	Gauge data obtained from MARFC. 6 hourly precipitation point data is spatially gridded such that it conforms to the monthly precipitation distribution map obtained from parameter-elevation regressions on independent slopes model (PRISM) (Daly et. al., 1994, 1997)
DEM		http://seamless.usgs.gov/
Streamflow		http://nwis.waterdata.usgs.gov/nwis/sw
Groundwater		http://nwis.waterdata.usgs.gov/nwis/gw

4.6. Stream Flow and Groundwater Head Prediction Results

The model implementation is performed using a-priori parameters exclusively for soil, vegetation and other hydrogeologic properties. A limited (manual) calibration was

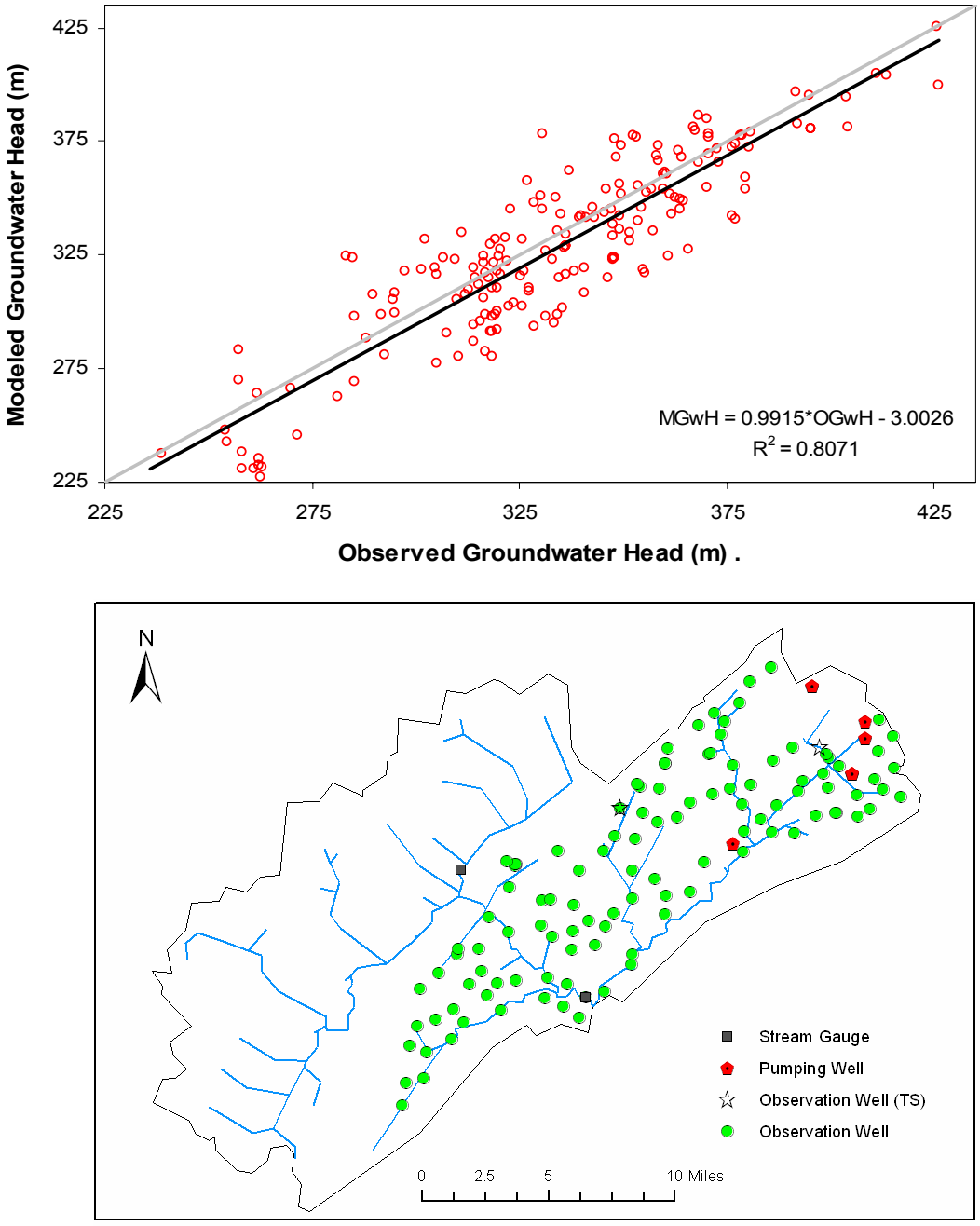

Figure 4.8 Modeled groundwater head (MGwH) vs. Observed groundwater head (OGwH) for the observation wells (shown in the lower graphic) for the 1983 -84 period of the model run. Data source for observed head: http://nwis.waterdata.usgs.gov/nwis/gw

carried out to improve the fit of model to observations. The calibration was first performed on a steady-state solution using normal (long term average) climate forcing and then the subsurface conductivity calibrated parameters obtained from it were used during the transient calibration. The steady state calibration provides a long term water balance in terms of the "normal" or long term mean conditions for precipitation and evapo-transpiration from the land surface and vegetation. The steady-state solution also is used to reduce "spin-up" time for groundwater flow, and applying the normal groundwater spatial map as the initial condition in the transient solution. The transient simulation is conducted for a period of 2 years from Nov, 1, 1983 to Oct, 31, 1985. The simulation period was selected based on the availability of the maximum number of well data (both spatial and temporal) for calibration. The average precipitation during the first year of the simulation period was 2.8 mm/d which is almost identical to the long term normal precipitation of the basin.

Model performance was initially assessed by comparing predicted ground water

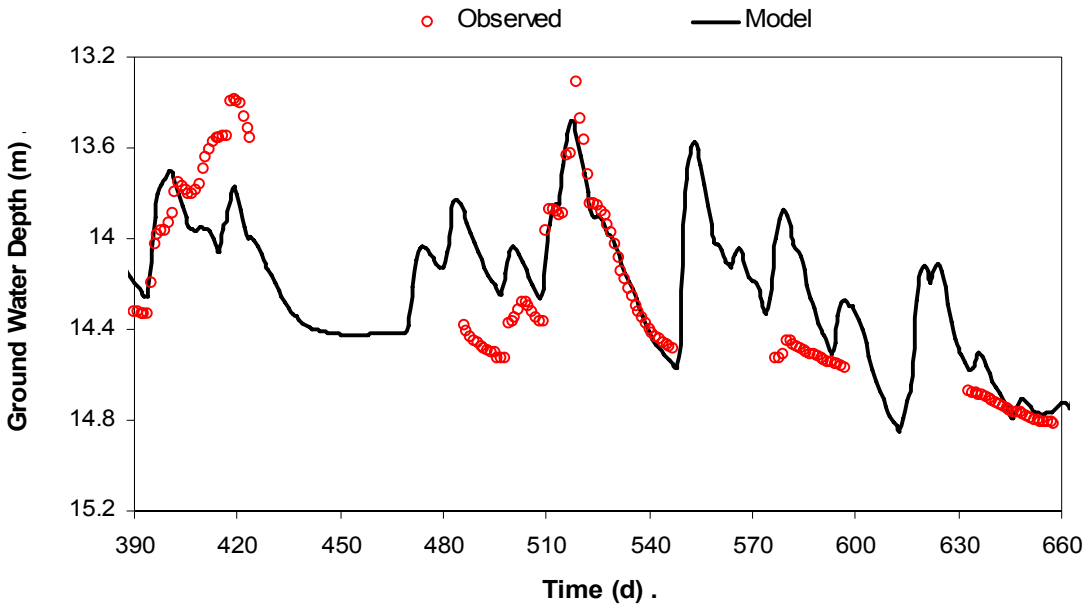

Figure 4.9 Modeled and Observed ground water depth time series. Data source for observed head: http://nwis.waterdata.usgs.gov/nwis/gw

levels with observed values at 132 different locations (see Figure 4.8). This allowed us to establish the overall scale and pattern of groundwater storage (depth to water table) in the model. Groundwater time series were only available at one location, although it was still

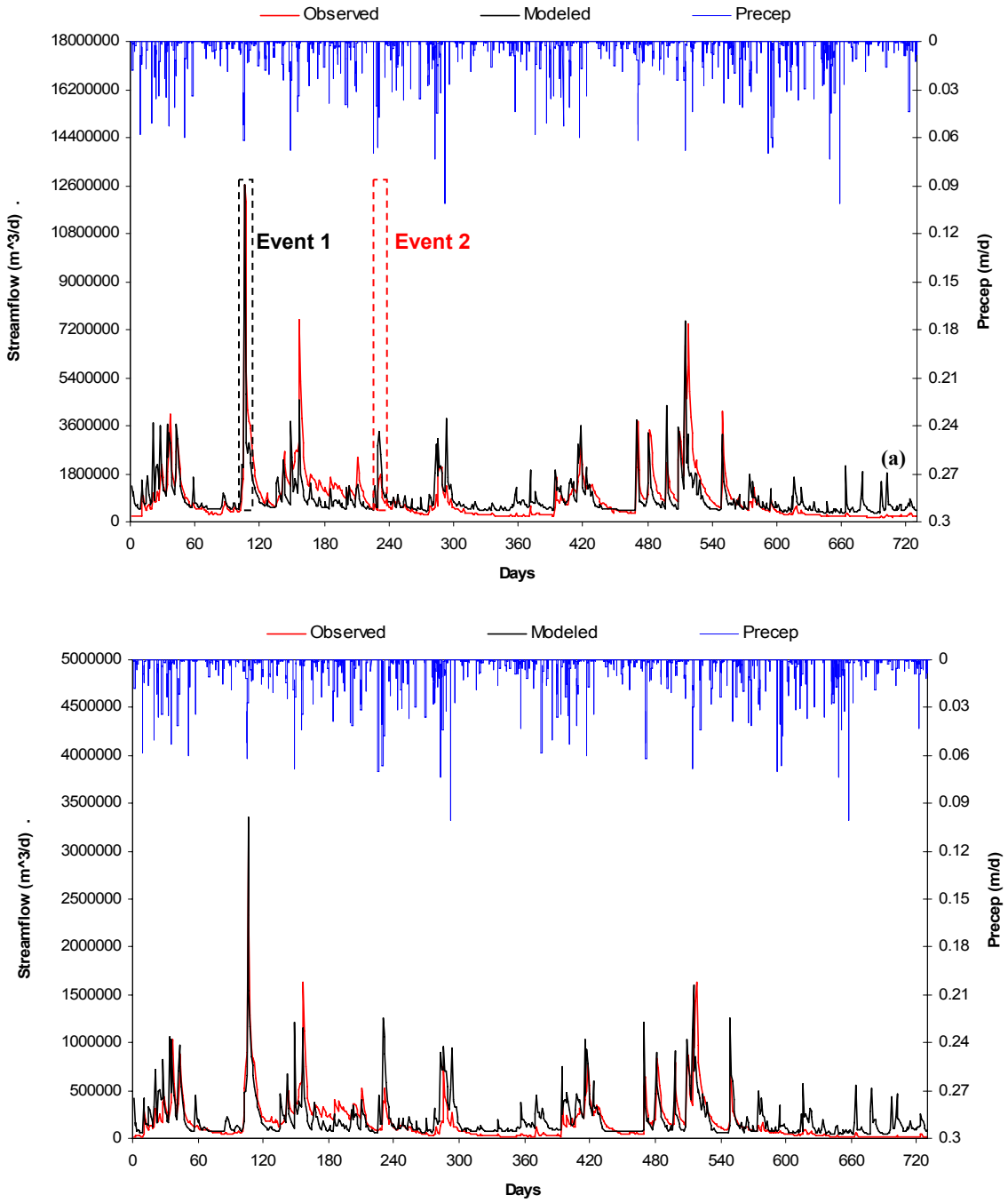

Figure 4.10 Observed and Modeled Streamflow at a) Little Juniata River Observation Station b) Bald Eagle Creek Observation station. Data source for observed head: http://nwis.waterdata.usgs.gov/nwis/sw

useful for evaluating the timing of the seasonal cycle of groundwater level changes, and for event response on groundwater levels. Figure 4.8 gives a comparison of the instantaneous observed and predicted ground water levels, and the location of observation

wells. We note that these instantaneous observations were measured on different dates during the simulation period, and the regression pairs (observed and predicted) represent the same date. A total of 190 observations were available for the simulation period. During the transient calibration, surface and subsurface hydrogeologic properties were modified in order to capture the time scale of the recession limb of the streamflow and groundwater hydrographs. For simplicity and tractability, uniform calibration of parameters, meaning that a parameter type was nudged by a similar percentage all over the watershed, was carried out. Figure 4.9 shows the modeled and observed ground water depth time series. As stated earlier, limited calibration was performed to achieve this match. Streamflow time series were available at the watershed outlet and at one internal gauging station (see Figure 4.8b). Figure 4.10 shows daily observed and simulated stream outflow for the Little Juniata River and Bald Eagle Creek. The simulated streamflow (Figure 4.10) was again obtained by manual adjustment of individual soil and hydrogeologic parameters over the model domain while assessing the sensitivity of local streamflow to each parameter. The model captures the event scale and seasonal streamflow response reasonably well.

The effectiveness for using a-priori data and a simple manual calibration for distributed models has also been discussed by (Ivanov et al. 2004). The coefficient of determination, which explains the amount of dispersion captured by the modeled time series of the observed time series (Krause et al. 2005), for Bald Creek and Little Juniata is 0.7 and 0.74 respectively. The statistics suggest observed surface-discharge volumes and timings are reasonably captured with minimal calibration.

4.7. Simulating Multi-Scale, Multi-Process Behavior

The goal of this research has been to explore whether fully coupled processes and a-priori data form a practical basis for application of integrated models at the mesoscale, and to further see if this model-data coupling strategy leads to any new or interesting results that might not be obvious from weakly coupled or uncoupled approaches. Recall that our approach is based on a direct or natural coupling of the equations within a finite volume or “kernel”. We show here several examples where unexpected dynamics emerge and

that the predicted phenomenon is hydraulically plausible but will require new experiments to verify. We avoid interpretation of "emergent" or self-organized behavior at this stage since most of what we observe seems to be more simply explained (i.e. principle of "lex parsimoniae"). The simulation was run on an unstructured grid generated with a minimum spatial scale of 0.048 km^2 for the watershed and 150 m for river while the minimum temporal discretization was set at 10^{-5} min. We remind the readers that depending on the dynamics of the interacting processes, the temporal discretization increases/decreases adaptively during the simulation. The spatio-temporal adaptive nature of the solution captures fine-to-large scale interactions between processes, topography and landuse/land-cover characteristics. Our focus here is on coupling behavior at event, daily, monthly and seasonal time scales. All of the presented results are for a 2 year simulation period from Nov 1983 to Oct 1985.

4.7.1. Interception, Evaporation, and Transpiration Dynamics

Interception, evaporation and transpiration are the primary controls on atmosphere-land surface exchange. These phenomena have been shown to be particularly critical to recycling of precipitation (Eltahir and Bras 1994), and represent some of the most difficult and uncertain fluxes to evaluate at the watershed scale. In addition, the fully coupled model also allows us to explore how the details of land surface fluxes are related to the subsurface and stream response. In particular we are interested in land surface flux partitioning that is related to water table recharge. Using a priori data from the NLCD and spatially interpolated forcing data from NWS gauge stations and PRISM (Daly et al. 1997), PIHM simulates each flux and the results are discussed in the next 3 subsections.

4.7.1.1 Interception by Vegetation

As expected, the pattern of forcing (precipitation, temperature, wind speed, and net radiation) and the leaf area index (LAI) for each land cover type were found to be the first-order control on the spatio-temporal distribution of interception storage. Figure

4.11a shows monthly average variations of interception for individual land cover types and for the watershed as a whole. Average interception storage for each land cover type is

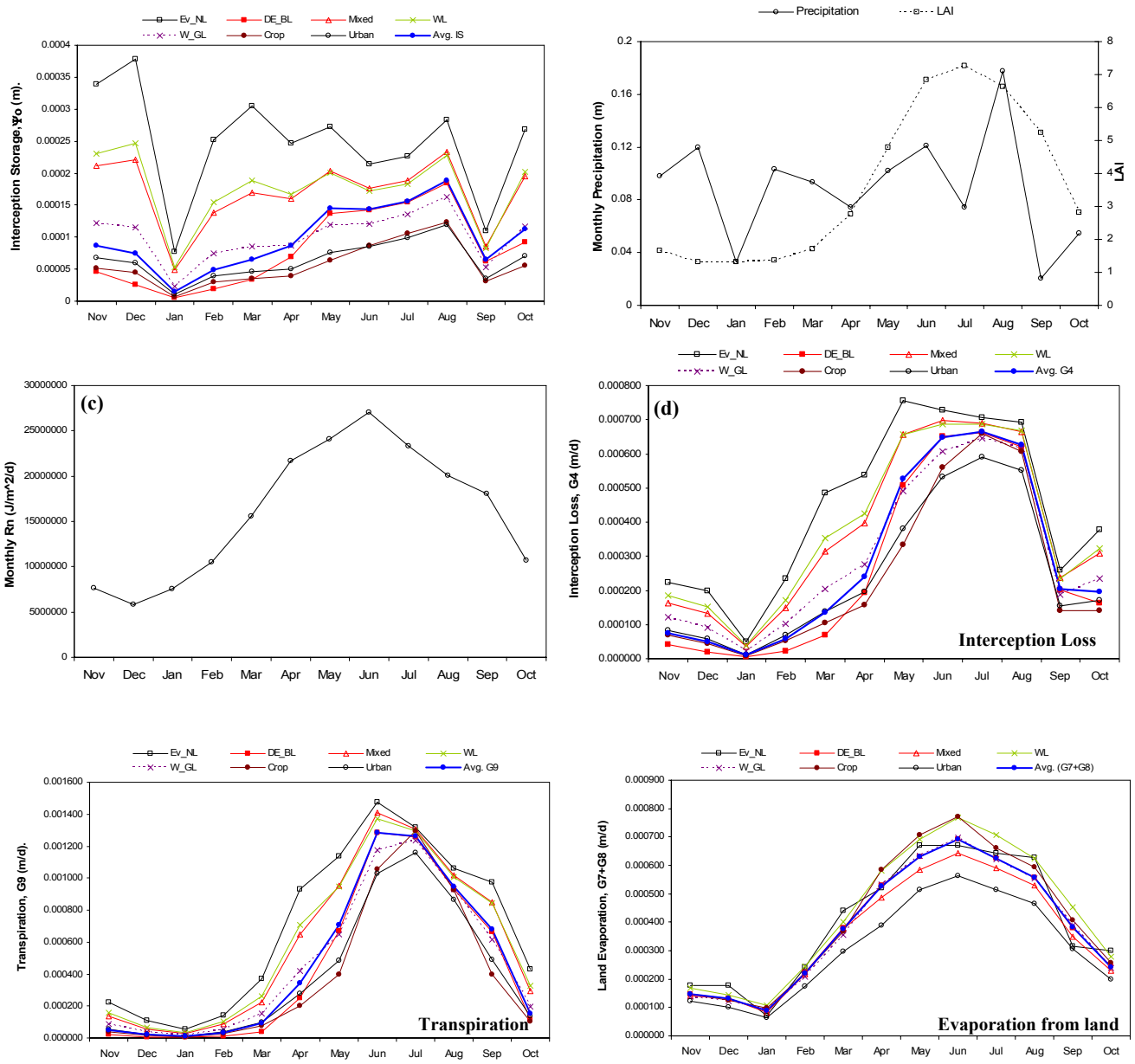

Figure 4.11 a) Average monthly interception storage for different land cover types. Expectedly, variation in interception storage is correlated with precipitation. b) Variation of monthly precipitation and LAI. c) Monthly average of incoming solar radiation (Rn) d) Monthly aveage of evaporation from interception storage ($\vec{G}_4$) shows signatures of its dependence on interception storage (maximum in August) and Incoming solar radiation (maximum in June e) Temporal variation in monthly transpiration ($\vec{G}_9$) has a strong dependence on LAI and radiation. f) Monthly evaporation from overland flow and the upper soil layer ($\vec{G}_7 + \vec{G}_8$) is found to follow annual cycle of temperature and radiation

positively correlated with their respective Leaf Area Indices (LAIs), shown in Figure 4.11b. Evergreen Needleleaf (Ev_NL) is observed to have the maximum annual average interception while agricultural crops have the minimum annual average interception of all vegetation classes. Though higher interception storage of Ev_NL is the direct consequence of its larger LAI, we note that this appears to be over-predicted by the LDAS data set (http://ldas.gsfc.nasa.gov/LDAS8th/EROSveg2/LDASvegetation2.shtml). Overall, the integrated model shows a strong sensitivity to the vegetation type with the cumulative annual interception storage varying from 2 mm for agricultural crops to 90 mm for Ev_NL.

4.7.1.2 Temporal Variation of Evaporation and Transpiration

Evaporation can occur from interception, overland flow, and the top soil layer. Transpiration varies with each land cover type and differs in terms of eco-hydrologic controls, time scales, time of occurrence, quantity and atmospheric feedbacks. Figure 4.11d illustrates how monthly variation of interception loss in PIHM is largely controlled by forcing (precipitation and the seasonal energy available for evaporation, shown in Figure 4.11b and 4.11c). In summer, average air temperature and solar radiation leads to higher interception loss, with maximum evaporation being in June. September and January demonstrate a warm and cold month with very low precipitation and low interception loss. Monthly variation of transpiration also follows a similar trend with highest and lowest values during summer and winter (October to March) respectively (see Figure 4.11e). A closer look reveals an inverse relationship between the fraction of total evapotranspiration rate due to transpiration and interception loss as shown in Figure 4.12a. With increasing wetted area of the plant canopy, water available for canopy evaporation increases. At the same time when interception storage increases, the leaf area that contributes to transpiration tends to decrease (Savenije 2004). The inverse relationship is not valid for soil moisture, radiation and air-temperature induced limit conditions when stomatal resistance assumes extreme values. Overall, the integrated model shows a strong sensitivity to the vegetation type with the annual average ratio of P/ET_{actual} in the range of 1.75 to 2.6 from Ev_NL to agricultural crops. Evaporation from

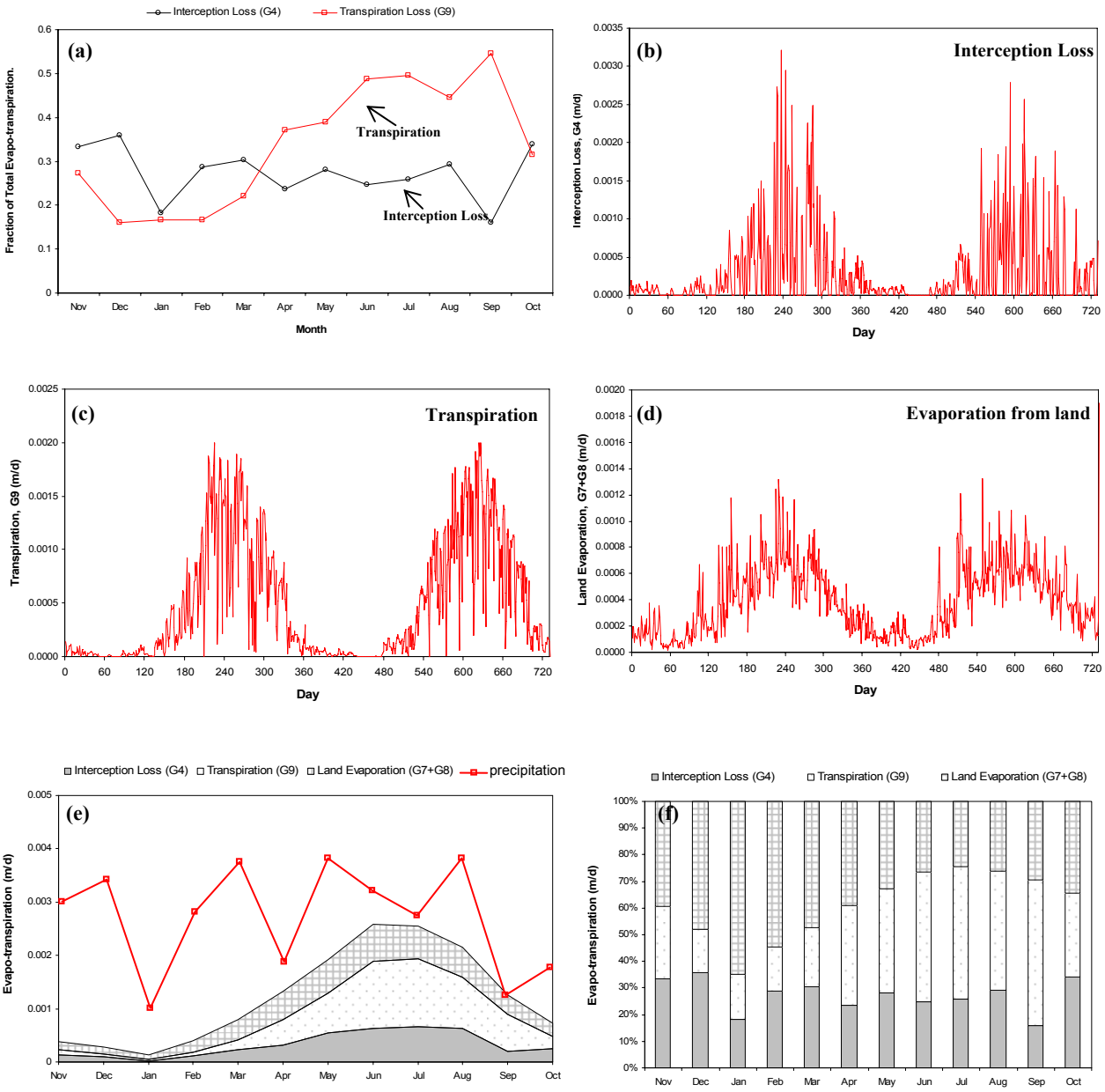

Figure 4.12 a) Variation of fractional loss components (transpiration and interception loss) with respect to total evapotranspiration. We note that when fraction of transpiration to total evapo-transpiration increases, the corresponding fraction of interception loss decreases and vice-versa. b) Annual variation of daily interception loss rate, $\vec{G}_4$ (Annual average $\vec{G}_4$ = 0.000288 m/d) c) Annual variation of daily transpiration loss rate, $\vec{G}_9$ (Annual average $\vec{G}_9$ = 0.000466 m/d) d) Annual variation of daily evaporation rate from ground, $\vec{G}_7 + \vec{G}_8$ (Annual average $\vec{G}_7 + \vec{G}_8$ = 0.000387 m/d). e) Average monthly precipitation and evapotranspirative loss f) Relative percentage contribution of each evapo-transpirative flux component

overland flow and shallow soil depth is often limited by the availability of moisture for evaporation. Since the monthly variation in precipitation pattern is not extreme and is

reasonably distributed over the year, the seasonal variation in ground evaporation is largely due to incoming solar forcing as shown in Figure 4.11f.

The different time scales for the evaporative flux components (interception loss, overland flow, land surface, and transpiration losses) are clearly revealed in the 2-year daily simulation. In Figure 4.12b we observe that evaporation from interception in the model has both a short time scale (in response to storm events) and a seasonal time scale that modulates the interception based on seasonal temperature. We note that the model produces evaporative fluxes year round. The relative average monthly contribution of each evaporation component is shown in Figure 4.12f. Transpiration dominates the total evaporative flux in summer with its contribution being as high as 54 % and then decreasing to as low as 16 % of the total in winter, with an annual mean of around 34 %. An important predicted flux in PIHM is recharge to the water table. Figure 4.12e shows that most of the water available for recharge to the watershed happens during winter. The effect of this on the water availability for the remainder of the year is somewhat complex. The winter and spring recharge moves as lateral groundwater flow, supplying rates and time scale of baseflow for the rest of the season. It also contributes to evapotranspiration where shallow water table conditions provide the principal source of soil moisture and vertical upward flow. We examine the spatial implications of a shallow water table on evapotranspiration rate next.

4.7.1.3 Evapotranspiration Dependence on Topography and Groundwater

Spatial variations of each annual evaporative flux components predicted in PIHM are shown in Figure 4.13. Figure 4.13a-b shows that transpiration and interception loss closely resembles the vegetation distribution pattern (Figure 4.7f). Regions with Mixed Land Cover (M) have the highest interception and transpiration loss while regions with urban landcover (U) have the smallest losses (also observed in Figure 4.11). The majority of the watershed is covered by deciduous broad leaf vegetation (De_BL), which has intermediate evaporative flux values. Evaporation from ground and overland flow ($\vec{G}_7 + \vec{G}_8$) has a spatial pattern (Figure 4.13c) that bears a resemblance to topography (Figure 4.7e). At higher elevations, the evaporative losses from land appear to be lowest

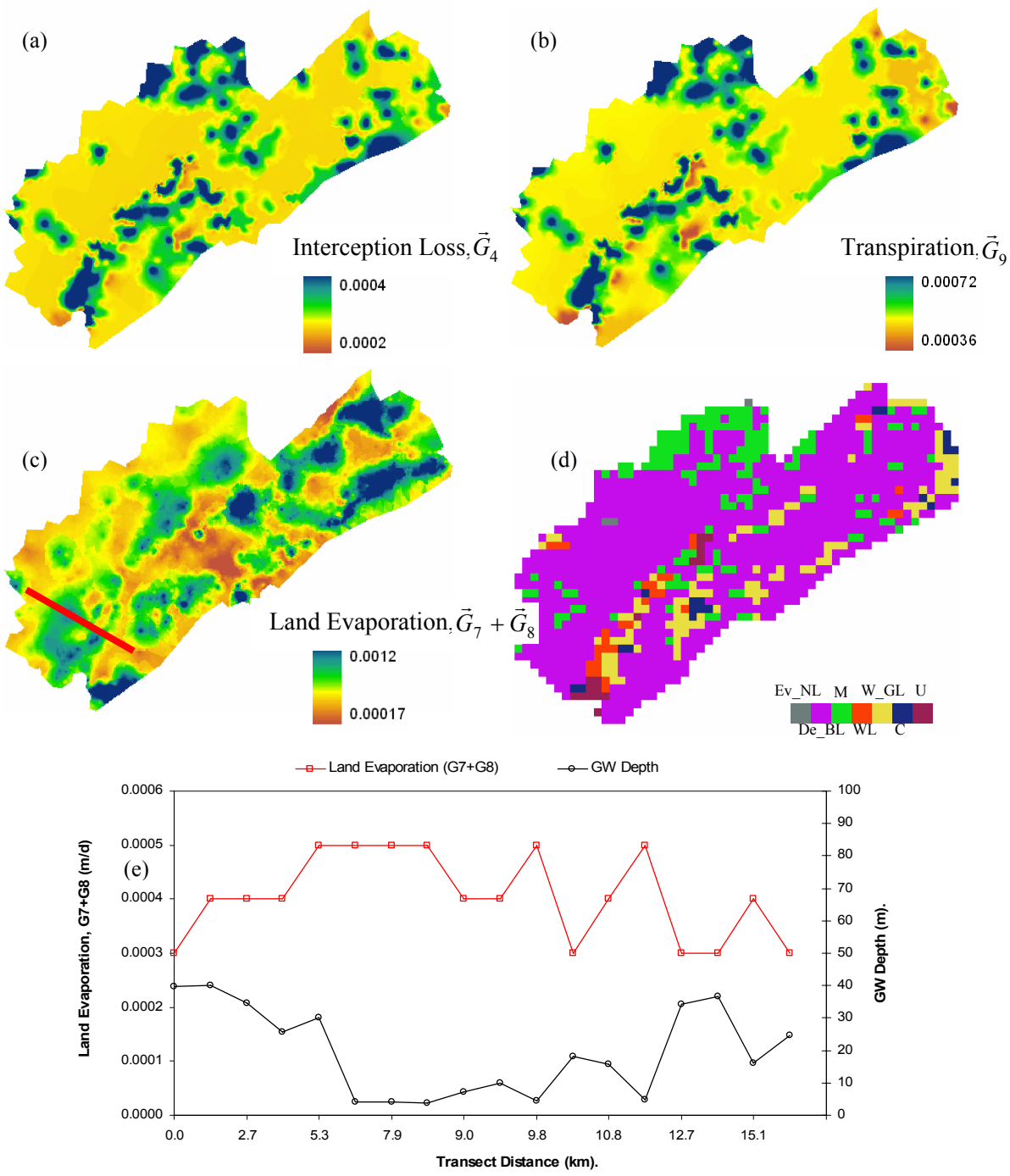

Figure 4.13 Spatial pattern of annual average evaporation from a) canopy and b) transpiration closely reflect the vegetation pattern. (shown in (d)). Spatial pattern of ground evaporation (shown in (c)) strongly depends on the depth of ground water and recharge pattern. Figure (e) shows that the variation of evaporation from ground ($\vec{G}_7 + \vec{G}_8$) along a transect across the valley (shown as a rectangular strip in (c)) follows an inverse relationship to ground water depth (and elevation). $\vec{G}_7 + \vec{G}_8$ are larger where there are shallow groundwater conditions (at lower elevations) and vice-versa

while the highest values are found at lower elevation. By plotting the evaporative flux components along an elevation transect (shown as red band in Figure 4.13c) in Figure 4.13e, we observe that ($\vec{G}_7 + \vec{G}_8$) have an inverse relationship to average ground water depth. Shallow water table conditions in the valleys (regions along the transect with lower elevations) result in higher evaporative losses since the capillary fringe supplies water to the unsaturated soil above the water table. The relationship is accentuated in regions of large elevation gradient. Thus topography and depth to groundwater add to the complex spatial pattern of evaporative losses which are primarily influenced by the spatial distribution of precipitation, heterogeneity of land cover/soil types and geology.

4.7.2. Streamflow Dynamics

Using the fully coupled formulation in PIHM, it is possible to explore a full range of river interactions with groundwater flow and overland flow. Our first finding is that the flow in a stream, the hydraulic dimensions, and the interaction of channel flow with the aquifer, apparently change at all scales within the watershed. PIHM simulations predict 7 separate fluxes for each stream reach in the model such as stream- aquifer interactions from right, left, upstream, downstream and beneath the channel and stream-overload flow interaction from right and left. To demonstrate the point at the watershed scale, the predicted mean annual streamflow distribution map for the river network in Little Juniata watershed is shown in Figure 4.14(a). Expectedly, flow in the main stem (3rd order) of Little Juniata River is the largest. The average flows in 1st, 2nd and 3rd order streams are 1.35E4, 7.83E4 and 3.975E5 m^3/d respectively. In terms of the average annual flow there is a simple increase in discharge from headwater to outlet. We can also examine the annual flow-extreme maps for the network, by plotting the predicted maximum and minimum streamflow for each reach as shown in Figure 4.14b and Figure 4.14c respectively. There is huge seasonal variation in water availability in the stream with flow during the driest periods to be only around 3 % of the flow amount during the wettest periods. Overall, the predicted max, min, and mean all show a relatively smooth but decidedly different increase in flow from headwater to outlet. So one might ask the question, what are the combinations of baseflow and surface flow that produce this

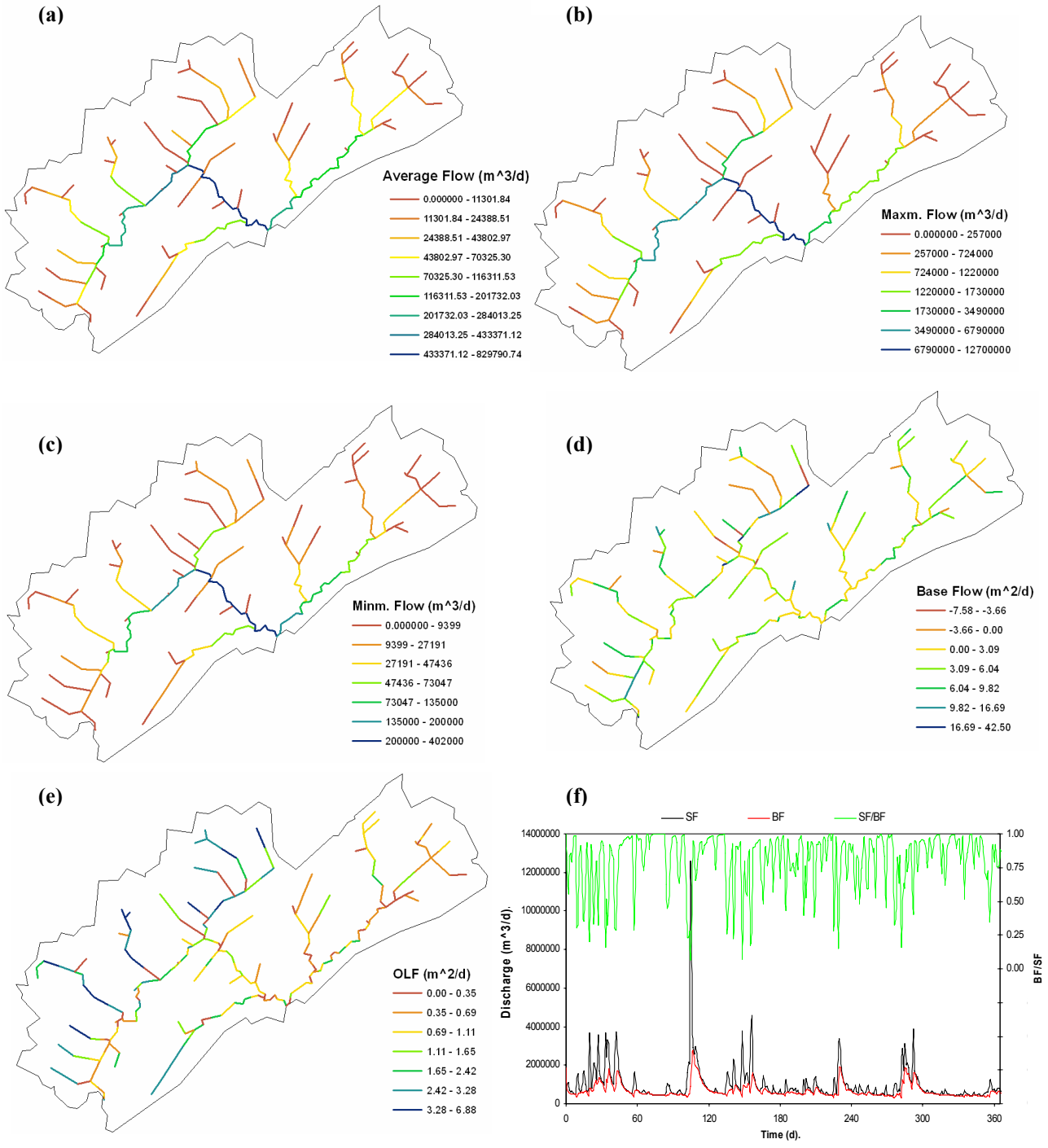

Figure 4.14 (a) Spatial distribution of annual average flow in the stream network of Little Juniata Watershed. b) Maximum and c) minimum flow in each section of river. d) Baseflow (BF) and e) overland flow (OLF) contribution to river per unit length of stream varies heterogeneously depending on local topography and hydrogeologic properties. f) Base flow contribution (BF) to total streamflow (SF) varies temporally throughout the year

simple space-time pattern? Figure 4.14d and 4.14e show the rates of base flow and overland flow per unit length for each stream reach (right+left bank) for the watershed. We note that the distribution is very heterogeneous with no simple relationship to stream order. Local examination shows that the balance of surface-subsurface contribution to the reach depends on the adjacent topography (slope, curvature, contributing area, etc.), vegetation type, and hydraulic conductivities of stream bed and the aquifer. A negative base flow is predicted in some reaches (Figure 4.14d) indicating an annual loss of water to the aquifer within that reach. During drier periods, most of the stream flow (>95%) is contributed by baseflow. Figure 4.14f shows the time series of the fraction of baseflow to streamflow for a yearly simulation. On an annual basis, 68% of the streamflow is contributed from baseflow.

4.7.3. Groundwater Recharge

Recharge, or the vertical flux of water to/from the water table is perhaps the least understood flux in a watershed. This fundamental flux is the essential component for sustaining groundwater aquifers and baseflow to streams, however it is for the most part unmeasured. The predicted recharge to the groundwater ($\vec{G}_1$) is expressed in PIHM as a complex function of both the soil moisture/pressure and the height of the water table (see Eq. 4.11). Figure 4.15a shows the predicted spatially averaged annual recharge time series for the Little Juniata. Positive recharge denotes vertical flux from the unsaturated to the saturated zone and negative recharge represents a loss from the water table. Negative recharge denotes a combination of a) a high capillary potential in unsaturated zone due to evaporation/transpiration loss (upward flow), and b) exfiltration from shallow groundwater at the land surface. We observe that during summer (from July to October), a net negative recharge situation generally exists in the Little Juniata watershed. This implies a net flow of moisture from saturated to unsaturated zone caused by the negative potential created by evaporative and transpirative loss from shallow water table zones, seepage zones or wetlands. We also note that recharge events are rapidly varying in summer (changing signs from positive to negative within short time intervals) as opposed

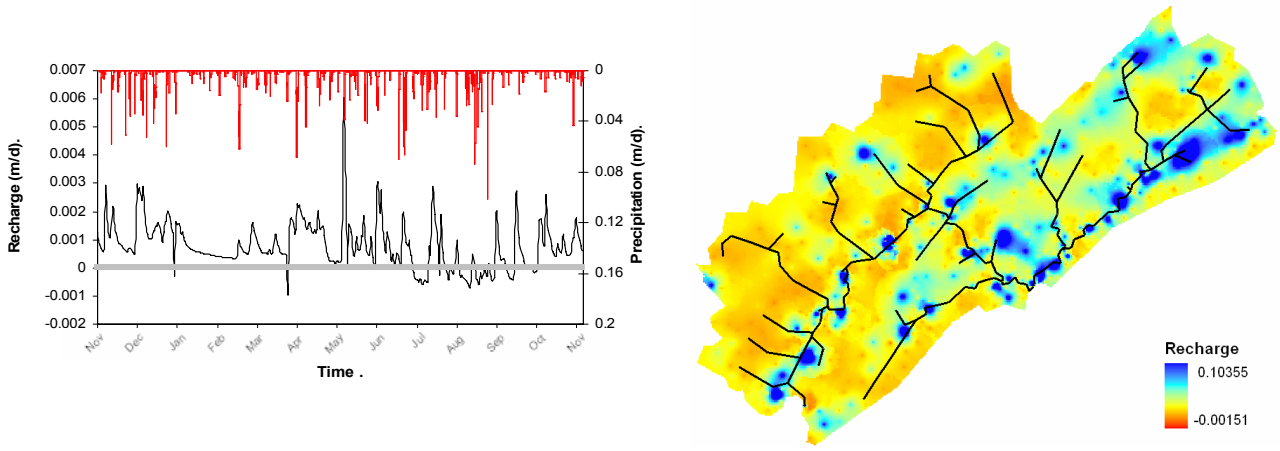

Figure 4.15 The first graphic shows the temporal variation of spatially averaged recharge to groundwater for the entire watershed. The second figure is the spatial distribution of average annual recharge. We note that recharge is more often negative from July to Oct (with the exception of during and after storm events). This is the result of the significant negative potential created in unsaturated zone during the summer drought. On the other hand, localized high recharge rates (blue color, dark grey in black and white) are observed where convergent topography focuses surface runoff and infiltration in high permeability or macroporous soils and bedrock. These are likely sites for wetland conditions.

to winter (positive only). The slow variation in winter is because of the lower conductivity of frozen top soil layer which reduces the infiltration rate. The spatial distribution of recharge is found to be closely related to land cover type, hydraulic conductivity of the soil surface and geology, and topography. Figure 4.15b illustrates a large positive groundwater annual recharge component near the streams and adjacent valleys. At the higher elevations, net annual recharge is much smaller. Although we have limited data to verify the simulated results, the valley soils seem to have a strong macropore effect on recharge which is enhanced by overland flow from adjacent steeper terrain. It may also be that the valley limestone-derived soils tend to maintain water in the soil matrix more efficiently than upland soils (of finer grain size). Recall that macropore flow in PIHM is initiated when the soil matrix is near saturation or when overland flow is occurring.

4.7.4. Streamflow-Groundwater Dynamics and Local Topographic Control

An important aspect of fully coupled processes in PIHM is the ability to examine details of exchanging water along the river or riparian corridor. For the Little Juniata we

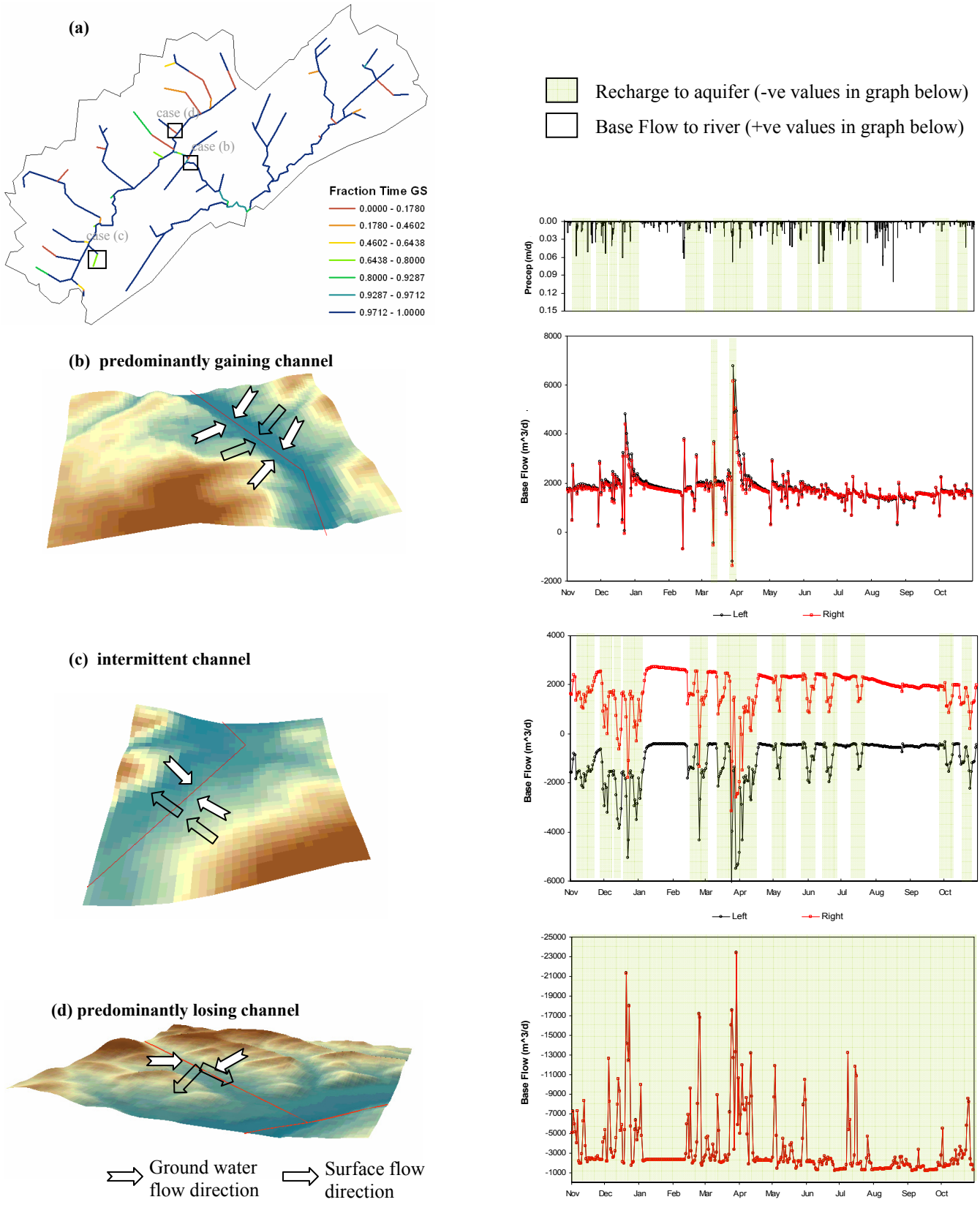

Figure 16 (a) Shows the percent of time each stream section is gaining (GS) during the period of simulation. Distribution of gaining and loosing sections of stream along with typical streamflow-aquifer dynamics for three cases viz. b) predominantly gaining, c) intermittently gaining and loosing and d) always loosing

find that the simulated exchange of water between the channel and the local groundwater is quite complex and that a simple classification of gaining and losing channel reaches does not quite describe the dynamics over all time scales. We find that the classical flow exchange of groundwater and surface water is better described in terms of the relative frequency of gaining or losing channels. The 3 conditions are: a) a *predominantly losing* reach (loses flow >90% of the time), b) a *predominantly gaining* reach (gains water >90% of the time), and c) an *intermittent gaining/losing* reach. Figure 4.16a shows the distribution of the fraction of time over the 2 year simulation that each stream section gains water as base flow. We note that one minus the fraction of time the stream is gaining water represents the frequency of losing or non-gaining. In the Little Juniata watershed there is a large streamflow contribution from the baseflow, because of macropores and localized highly permeable (karst) geology, resulting in most of the stream sections being predominantly gaining for most of the year. On the average a typical stream section in the watershed is gaining 88% of the time during the 2 year simulation period. 1st order, 2nd order and 3rd order streams are observed to be gaining for increasingly larger times varying from 78% to 93% to 98% respectively. However, there are many reaches where predominantly losing flow is predicted by the model.

Figure 4.16b-d shows the baseflow hydrograph for the simulation period for three cases discussed above. Note that baseflow hydrographs are predicted independently for each side of a channel reach. This is important particularly in cases where there is a marked difference in groundwater head of the aquifer on the either side of the channel. This results in negative baseflow contribution to one side of the aquifer and positive base flow contribution to the opposite. Such a channel is referred to here as a "flow-through" channel. Occurrence of "flow-through" channels generally occurs where there is a sharp topographic change on opposite sides of the stream, or there exists a shallow impermeable rock layer on one side of the channel, or a high permeability zone on one side of the channel. Figure 4.16c shows an intermittently gaining reach which also happens to be "flow through channel" section. During wet seasons, the stream receives base flow from one side but then recharges the aquifer on the other side at higher rate due to local hydraulic gradients. During relatively dry periods "flow through" behavior of the reach continues, but the river experiences a net gain of water. During and shortly after

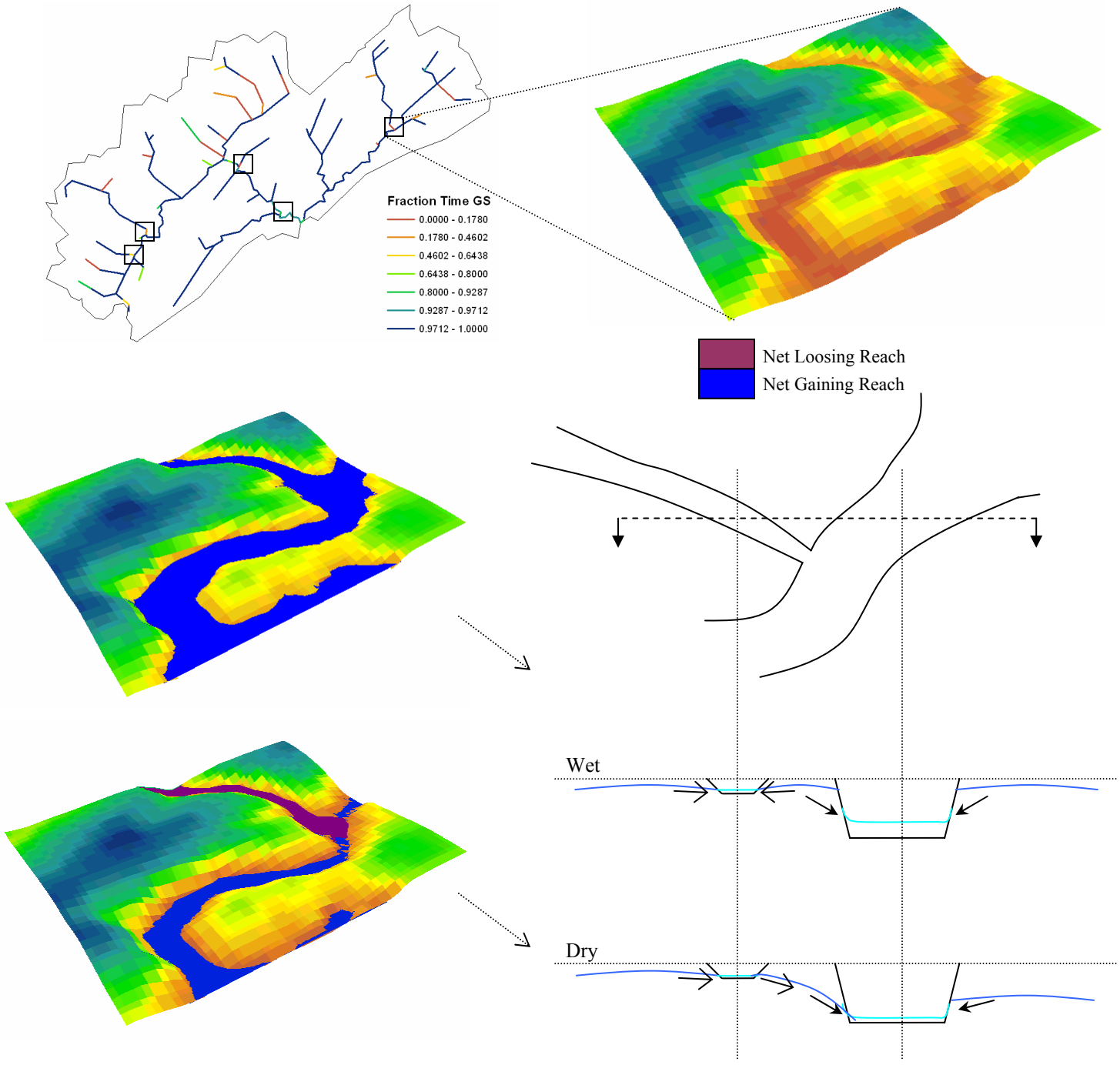

Figure 4.17 Complexity of flow at stream junctions. Mouth of the tributaries that drain to a large and deep river are prone to be losing reaches, particularly in dry conditions because of large depression created by the main river. Similar behavior is observed at multiple locations (marked by bounded rectangles in top-left figure) across the watershed.

large storm events, Figure 4.16c shows that the river loses water through bank infiltration, thus reducing the flood level and recharging the aquifer. The volume of this *bank recharge* depends on duration, height, and shape of the flood hydrograph, as well as on the transmissivity and storage capacity of the aquifer and the permeability of the stream sediments. This successive discharge and recharge of the aquifer has a buffering effect on the runoff regimes of rivers (Brunke and Gonser 1997) and is likely a critical but unresolved element in stream-aquifer contamination. Overall, the intermittent gaining/losing behavior is common in many flow-through reaches in this watershed. Figure 4.16d illustrates a predominantly losing stream. We note that such streams are more likely to exist on relatively steep hillslopes where groundwater level is always below the stream bed. These streams are often ephemeral with significant flow only during storm events. Figure 4.16d shows the baseflow hydrograph in response to precipitation events, and that the stream reach loses flow 98% of the time.

Figure 4.17 illustrates the effects of stream morphology and stream order on the surface-groundwater exchange. The example shows how predominantly gaining tributaries can switch regime at the confluence with higher order channels. A conceptual model for this change in regime seems to depend on the seasonal conditions as illustrated in Figure 4.17. During the wet or high runoff season, both the tributary and the higher order channel are gaining flow. However in the dry season, lower ground water table conditions lead to the tributary outlet switching to a losing channel. Thus it can be concluded that the distribution of predominantly gaining or losing and intermittent streams are highly influenced by the seasonal groundwater conditions and the local physiography (Woessner 2000). This condition is also likely to be related to the timing, intensity and pattern of precipitation within each tributary in addition to the effects of landscape morphology.

4.7.5. Seasonal Event-Based Coupled Dynamics

Next we examine the impact of forcing and land interactions on the magnitude of runoff in different seasons. Figure 4.18a-b illustrates two storm events (also identified in Figure 4.10) averaged for the entire watershed area, each of 10 days duration and with

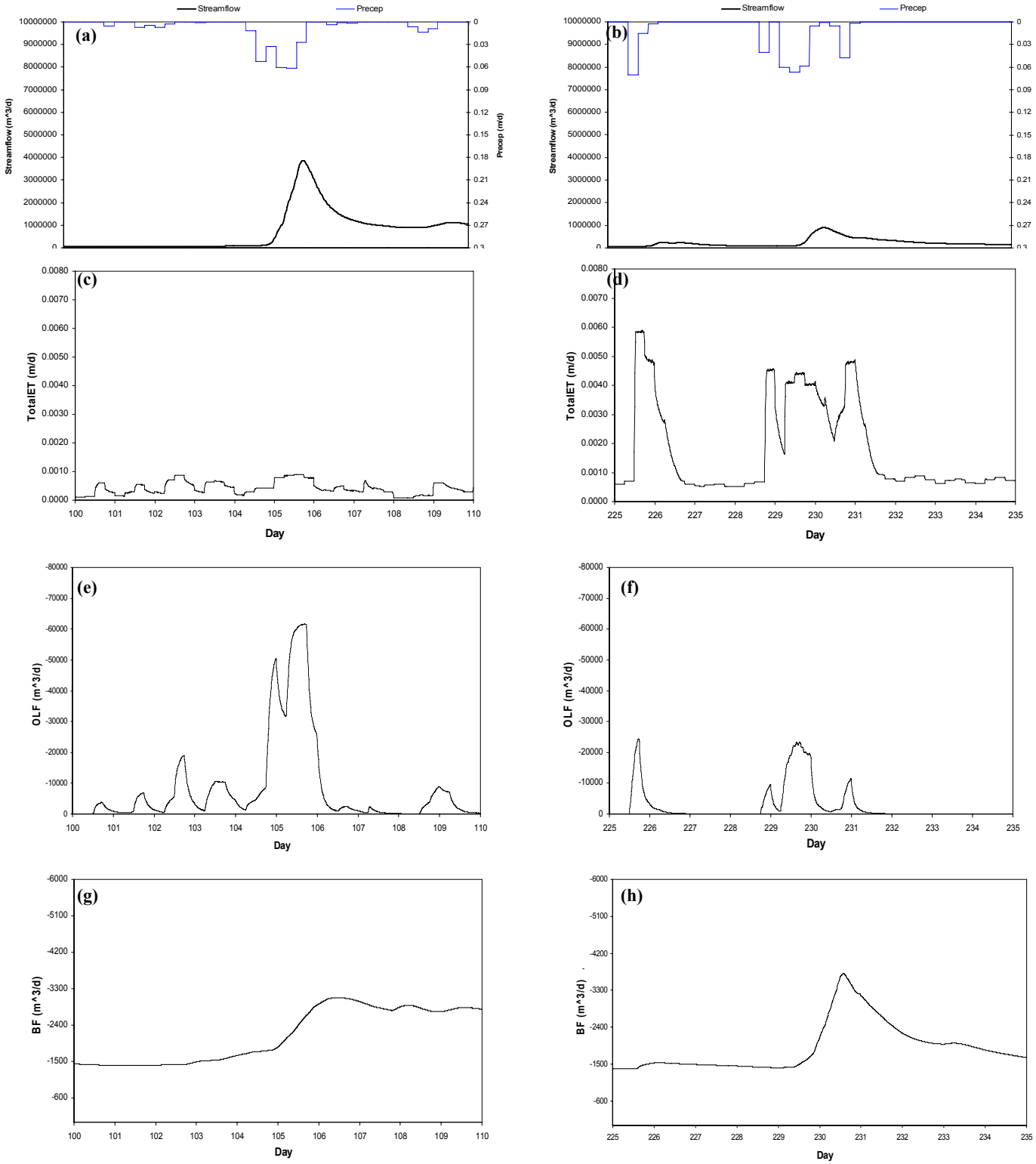

Figure 4.18 Nonlinear state effects on seasonal forcing. Two events of 10 day duration each, one from winter (Event 1) and the other from summer (Event 2), produce markedly different hydrographs as shown in (a) for Event 1 and (b) Event 2. (c-d) show that the total evapotranspiration loss during Event 2 is much larger than for 1. Thus the net available water for overland flow (e-f) and base flow (g-h) to the river is less for Event 2.

very similar intensity. The runoff hydrographs are for the watershed outlet. Event 1 takes place in winter (February) while Event 2 takes place in summer (June). The total amount of precipitation in summer event is in fact larger (9.4 cm) than the winter 1 (7.7 cm), although the streamflow generated for summer storm is much less. This difference in watershed response can be explained by the partitioning of precipitation (see Figure 4.18c-h) as it interacts with vegetation (interception loss) and ground (evapotranspiration). Dense summer vegetation with large LAI, produces much greater interception storage (~ 0.199 mm) in the summer. We also note that the higher summer temperature results in larger interception loss thus reducing the throughfall contribution to overland flow and groundwater recharge. Infiltration loss during the summer event is also larger due to the larger seasonal soil moisture deficit and generally lower water table. All this results in a net smaller contribution of baseflow (see Figure 4.18g-h) and overland flow (see Figure 4.18e-f) to the streamflow in summer, inspite of larger intensity storms. Overall, evapotranspiration, interception storage and initial watershed state play a crucial role in determining overland and subsurface flow response.

4.8. Conclusions

This paper presents the coupling strategy and a mesoscale application of the PIHM model. A range of issues that arise from the coupling of data, process and numerical solution are discussed. We note that the strategy for unstructured mesh decomposition, the local definition of kernel (system of equations), and use of an advanced implicit solver are critical elements of accurate and efficient modeling. We use an adaptive discretization methodology to resolve the necessary spatial scales in PIHM. By applying the model to simulate a mesoscale river basin, the Little Juniata watershed, we show how stream-aquifer interactions are a function of local topography, land cover, geology and soil type. Although there are many variables at work, the a-priori parameters and their limited nudging used in PIHM, and the natural coupling of the equations lead to very plausible explanations and several useful predictions of the hydrologic, climatic and ecological conditions that exist in the Little Juniata throughout the water year. The time scales of process interactions are found to vary spatially and temporally.

Evapotranspiration, and particularly interception loss is shown to play a crucial role in determining overland and subsurface flow response. Limited observed data for groundwater, and streamflow still allowed us to make an initial validation of the watershed dynamics and to make qualitative predictions for internal fluxes between all states in the watershed. New predictions in terms of distributed spatio-temporal stream-aquifer interaction (gaining/loosing streams) maps, groundwater recharge maps, distributed stream flow maps and process separation at multiple scales is obtained. We attempt to make a case for the importance of an integrated modeling framework, which in the future will also require a new kind of observing system that can resolve and test the coupled dynamic predictions beyond the a-priori data used here. The integrated theory provides a new way to "explore" hydrologic states and can be used to develop scenarios of change for parameters, forcing data sets, and new descriptions of the physical processes. The success of this fully-coupled model in predicting the stream flow hydrographs at the outlet and internal points in a basin of this size (~900 sq. km) while also capturing process interactions within in the watershed at adaptively fine time scales lends credence to the potential of using fully coupled distributed hydrologic models for operational forecasting, water management, as well as a research and analysis tool to answer and unravel science questions.

4.9. References

Abbott MB, Bathurst JC, Cunge JA, O'Connell PE, Rasmussen J. An Introduction to the European Hydrological System – Systeme Hydrologique Europeen, "SHE", 2 : History and Philosophy of a Physically-based, Distributed Modelling System. Journal of Hydrology, 87, 61-77; 1986.

Anderson S, Dietrich W, Montgomery D, Torres R, Conrad M, Loague K. Subsurface flow paths in a steep, unchanneled catchment. Water Resources Research 33(12); 1997.

Barros AP, Kuligowski RJ. Orographic Effects During a Severe Wintertime Rainstorm in the Appalachian Mountains. Monthly Weather Review, 126, 2648-2672; 1998

Beven K, Germann PF. Macropores and water flow in soils. Water Resources Res. 18 (5). 131 1-1325; 1982

Beven KJ. Distributed models, in M.G. Anderson and T.P. Burt (Eds) Hydrological forecasting, Wiley, Chichester; 1985

Bhatt G, Kumar M, and Duffy CJ. Bridging the gap between geohydrologic data and distributed hydrologic modeling. In Proceedings of International Congress on Environmental Modeling and Software; 2008

Blayo E, Debreu L. Adaptive mesh refinement for finite-difference ocean models: first experiments. J. Phys. Ocean., 29 (6), 1239-1250; 1999

Blondin C. Parameterization of land-surface processes in numerical weather prediction, in Land Surface Evaporation; Measurements and Paramrleizuliun, edited by T.J. Schmugge and J.C. Andre, pp. 31-54, Springer-Vedag, New York; 1991

Bosch JM, Hewlett JD. A review of catchment experiments to determine the effect of vegetation changes on water yield and evapotranspiration. J. Hydrol., 55, 3-23; 1982

Bougeault P. Parameterization schemes of Land-Surface processes for mesoscale Atmospheric models. In Land Surface Evaporation, edited by T. J. Schmugge and J. Andre´ (New York: Springer-Verlag), pp. 55–92; 1991

Brooks RH, Corey AT. Hydraulic properties of porous media, Hydraulic Paper #3. Colorado State University, Ft. Collins, CO; 1964

Brown DL. An analysis of transient flow in upland watersheds: interactions between structure and process Ph.D. dissertation, University of California, Berkeley, California; 1995

Brunke M, Gonser T. The ecological significance of exchange processes between rivers and ground-water. FreshwaterBiol 37:1–33; 1997

Byrne GD. Pragmatic experiments with Krylov methods in the stiff ODE setting. In Computational Ordinary Differential Equations, J. Cash and I. Gladwell, Eds. Oxford University Press, Oxford, U.K., 323-356; 1992

Chen ZT, Guevara JA. Systematic selection of very important points (VIP) from digital terrain models for constructing triangular irregular networks. Proceedings, AUTO-CART0 8, Baltimore 1987, pp. 50-56; 1987

Chen C, Wagenet RJ. Simulation of water and chemicals in macropore soils. Journal of Hydrology 130, 105-149; 1992

Cohen SD Hindmarsh AC. CVODE user guide. Technical report UCRL-MA-118618, Lawrence Livermore National Laboratory; 1994

Courant R, Friedrichs K, Lewy H. Uber die partiellin differenzengle-ichungen der mathematischen physik. Math Ann;110:32-74; 1928

Daly C, Neilson RP, Phillips DL. A statistical-topographic model for mapping climatological precipitation over mountainous terrain, J. Appl. Meteorol, 33, 140-158; 1994

Daly C, Taylor GH, and Gibson WP. The PRISM approach to mapping precipitation and temperature, paper presented at 10th Conference on Applied Climatology, Am. Meteorol. Soc., Reno, Nev., Oct. 20-24, 1997

Deardorff JW. Efficient prediction of ground surface temperature and moisture, with inclusion of layer of vegetation. Journal of Geophysical Research, 83, 1889–1903; 1978

Dickinson RE. Modelling evapotranspiration for three-dimensional global climate models. In Climate Processes and Climate Sensitivity, Geophysical Monograph Service, 29, edited by J. E. Hansen and T. Takahashi, AGU (Washington, DC: AGU), pp. 58–72; 1984

Di Giamarco, Todini PE, and Lamberti P. A conservative finite elements approach to overland flow: the control volume finite element formulation. J. Hydrol., 175 pp.267-291; 1996

Dingman SL. Physical Hydrology, Macmillan, pp. 370-373; 2002

Duffy CJ. Semi-Discrete Dynamical Model for Mountain-Front Recharge amd Water Balance Estiamation. In: Groundwater Recharge in a Deseart Environment: The Southwestern US, Editos: J. Hogan, F. Phillips, B. Scanlon, Water Science and Application Monograph, American Geophysicsl Union. Pp.236-255; 2004

Eltahir EAB, Bras RL. Precipitation recycling in the Amazon basin. Quarterly Journal of the Royal Meteorological Society 120: 861–880; 1994

Fairbanks J, Panday S, Huyakorn PS. Comparisons of linked and fully coupled approaches to simulating conjunctive surface/ subsurface flow and their interactions. In: Seo, Poeter, Zheng, Poeter, editors. MODFLOW 2001 and Other Modeling Odysseys—Conference Proceedings, Golden, CO;p. 356–61; 2001

Feng K, Molz FJ. A 2-D, diffusion-based, wetland flow model. Hydrol., 196: 230-250; 1997

Freeze RA. Mathematical Models of Hillslope hydrology, in M.J. Kirkby (ed), Hillslope Hydrology, Wiley, New York, pp. 177-225; 1978

Gerke HH, van Genuchten MT. A dual-porosity model for simulating the preferental movement of water and solutes in structured porous media. Water Resour. Res. 29,305–319; 1993

Gottardi G, Venutelli M. A control-volume finite-element model for two-dimensional overland flow. Adv Water Resour ;16:277–84; 1993

Govindaraju RS, Kavvas ML. Dynamics of moving boundary overland flows over infiltrating surfaces at hillslopes. Water Resour Res;27(8):1885–98; 1991

Graham DN and Refsgaard A. MIKE SHE: a distributed, physically based modeling system for surface water/groundwater interactions. In: Seo, Poeter, Zheng, Poeter, editors. MODFLOW 2001 and Other Modeling Odysseys—Conference Proceedings, Golden, CO; p. 321–7; 2001

Herdendorf CE. Morphometric Factors in the Formation of Great Lakes Coastal Wetlands. Aquatic Ecosystem Health and Management 7(2):179−197; 2004

Hernandez M, Miller SN, Goodrich DC, Goff BF, Kepner WG, Edmonds CM, Jones KB. Modeling Runoff Response to Land Cover and Rainfall Spatial Variability in Semi-arid Watersheds. Journal of Environmental Monitoring and Assessment, 64: 285-298. Kluwer Academic Publishers; 2000

Hoogmoed WD, Bouma J. A simulation model for predicting infiltration into cracked clay soil. Soil Sci.Soc. Am. J. 44:458-461; 1980

Hornbeck JW, Pierce RS, Federer CA. Streamflow changes after forest clearing in New England. Water Resour. Res., 6, 1124-1132; 1970

Hosler CL, Davis LG, Booker DR. Modification of convective systems by terrain with local relief of several hundred meters. Z. Angew. Math. Phys., 14, 410–418; 1963

Hutson JL, Wagenet RJ. A multiregion model describing water flow and solute transport in heterogeneous soils. Soil Sci.Soc. Am. J. 59, 743–751; 1975

Huyakorn PS, Springer EP, Guvanasen V, Wadsworth TD, A three dimensional finite element model for simulating water flow in variably saturated porous media. Water Resour Res;22(12):1790–808; 1986

Ivanov VY, Vivoni ER, Bras RL, Entekhabi D. Catchment hydrologic response with a fully distributed triangulated irregular network model, Water Resourc Res., Vol. 40; 2004

Jarvis PG, The interpretations in the variations in leaf water potential and stomatal conductance found in canopies in the field. Philos Trans R Soc London, Ser B 273: 593–610; 1976

Jenny H. Factors of Soil Formation; A system of quantitative pedology: New York, Dover Publications, Inc., 281 p.; 1994

Jones JE, Woodward CS. Preconditioning Newton–Krylov methods for variable saturated flow. In: Bentley LR, Sykes JF, Brebbia CA, Gray WG, Pinder GF, editors. Computational methods in water resources, Vol. 1. Rotterdam: Balkema; 2000. p. 101–6; 2000

Jones JE, Woodward CS. Newton–Krylov-multigrid solvers for large-scale, highly heterogeneous, variably saturated flow problems. Adv Water Resour 2001;24:763–74; 2001

Langevin C, Swain E, Wolfert M. Simulation of Integrated Surface-Water/Ground-Water Flow and Salinity for a Coastal Wetland and Adjacent Estuary. Journal of Hydrology 314 (1-4), 212-234; 2005

Kollet SJ, Maxwell RM. Integrated surface-groundwater flow modeling: A free-surface overland flow boundary condition in a parallel groundwater flow model, Advances in Water Resources, (29)7, 945-958; 2006.

Krause P, Boyle DP, Base F. Comparison of different efficiency criteria for hydrological model assessment, Advances in Geosciences, Vol. 5, pp 89-97, 16-12-2005; 2005

Kumar M, Bhatt G, Duffy CJ. An efficient domain decomposition framework for accurate representation of geodata in distributed hydrologic models, International Journal of GIS; 2008

Kumar M, Bhatt G, Duffy CJ. Shared data model to support sensor network data in hydrologic models. In Proceedings of International Congress on Environmental Modeling and Software; 2008

Miller DA, White RA. A conterminous United States multi-layer soil characteristics data set for regional climate and hydrology modeling, Earth Interactions 2, (available at http://EarthInteractions.org); 1998

Mohanty BP, Bowman SR, Hendrickx JMH, van Genuchten MT. New piecewise-continuous hydraulic functions for modeling preferential flow in an intermittent-flood-irrigated field. Water Resour. Res. 33, 2049–2073; 1997

Morse PM, Feshbach H. Methods of Theoretical Physics, Part I. New York: McGraw-Hill, p. 657; 1953

Mosley MP, Subsurface How velocities through selected forest soils, South Island, New Zealand, J. Hydrol. 55, 65-92; 1982

Nanson GC. Point bar and floodplain formation of the meandering Beatton River, northeastern British Columbia, Canada Sedimentology 27 (1), 3–29; 1980

Pan D, Cheng JC. Upwind Finite-Volume Navier Stokes Computations on Unstructured Triangular Meshes, AIAA Journal, Vol 3, 9; 1993

Panday S, Huyakorn PS. A fully coupled physically-based spatially-distributed model for evaluating surface/subsurface flow. Adv Water Resour 27:361–382; 2004

Paniconi C, Wood EF. A detailed model for simulation of catchment scale subsurface flow processes, Water Resour. Res., 29(6), 1601-1620; 1993

Perkins SP, Koussis AD. Stream–aquifer interaction model with diffusive wave routing. Journal of Hydraulic Engineering, American Society of Civil Engineers 122 (4), 210–218; 1996

Perillo GME, Minkoff DR, Piccolo MC. Novel mechanism of stream formation in coastal wetlands by crab–fish–groundwater interaction, Earth and Environmental Science, Vol. 25, 4; 2005

Qu Y, Duffy CJ. A semi-discrete finite volume formulation for multi-process watershed simulatioin, Water Resourc. Res; 2007

Richards LA. Capillary conduction of liquids in porous mediums. Physics 1:318–333; 1931

Refsgaard J, Storm B. MIKE SHE, pp 809-846 in Computer Models for Watershed Hydrology, Water Resource Public., Fort Collins, Colorado; 1996

Rushton KR, Tomlinson LM. Possible mechanisms for leakage between aquifers and rivers. J Hydrol 40:49–65; 1979

Roberson JA, Crowe CT. Engineering fluid mechanics. third ed. Boston: Houghton Mifflin Company; 1985; 1985

Rutter AJ, Morton AJ. A predictive model of rainfall interception in forests, 111. Sensitivity of the model to stand parameters and meteorological variables. J. Appl. Ecol. 14:567-588; 1977

Savenije HHG. The importance of interception and why we should delete the term evapotranspiration from our vocabulary. Hydrological Processes, 18(8):1507-1511; 2004

Schaap MG, Leij FJ. Database Related Accuracy and Uncertainty of Pedotransfer Functions, Soil Science 163:765-779; 1998

Schmidt M, Kerschgens M, Hübener H, Sogalla M. Simulating evapotranspiration in a semi-arid environment, Theoretical and Applied Climatology, (Vol. 80) (No. 2/4) 153-167; 2005

Shuttleworth WJ Evaporation. Chapter 4. In Handbook of Hydrology, Maidment DR. McGraw-Hill: New York, USA; 1993

Srivastava R, Yeh T. Analytical solutions for one-dimensional, transient infiltration toward the water table in homogeneous and layered soils. Water Resources Research 27(5); 1991

Strelkoff T. Numerical solution of Saint Venant equations. ASCE Proceedings, Journal of Hydraulic Dicision 96: 223-252; 1970

Tóth J. A conceptual model of the groundwater regime and the hydrogeologic environment. J Hydrol 10:164–176; 1970

USACE. Snow Hydrology, Summary report of the Snow Investigations, U.S. Army Corps of Engineers, North Pacific Division, Portland, Oregon; 1956

USACE UNET. One-dimensional unsteady flow through a full network of open channels, User's Manual. US Army Corps of Engineers, Hydrologic Engineering Center, Davis, CA; 1997

Valorani M, Goussis DA. Explicit Time-Scale Splitting Algorithm for Stiff Problems: Auto-ignition of Gaseous Mixtures behind a Steady Shock. Journal of Computational Physics, 169, 44-79; 2001

VanderKwaak JE. Numerical simulation of flow and chemical transport in integrated surface–subsurface hydrologic systems, Doctorate Thesis, Department of Earth Sciences, University of Waterloo, Ontario, Canada; 1999

van Genuchten, MT. A closed-form equation for predicting the hydraulic conductivity of unsaturated soils. Soil. Sci. Soc of Am. J. 44, 892–898; 1980

Vivoni ER, Ivanov VY, Bras RL, Entekhabi D. Generation of triangulated irregular networks based on hydrological similarity, Journal of hydrologic engineering, 9, 4. 288-302; 2004

Whipkey RZ, Kirkby MJ. Flow within the soil. In Hillslope Hydrology, Kirkby MJ (ed.). Wiley: Chichester; 121–144; 1978

Winter TC. Relation of streams, lakes and wetlands to groundwater flow systems, Hydrogeology Journal 7, 28-45; 1999

Woessner WW. Stream and fluvial plain ground water interactions: rescaling hydrogeologic thought. Ground Water 38(3): 423–429; 2000

Yeh GT, Huang GB. A Numerical Model to Simulate Water Flow in Watershed Systems of 1-D Stream-River Network, 2-D Overland Regime, and 3-D Subsurface Media (WASH123D: Version 1.5), Technical Report. Dept. of Civil and Environmental Engineering, University of Central Florida, Orlando, Florida; 2003

4.10. Appendix

Appendix I

β	Percentage area fraction of macropore
C_d	Coefficient of discharge (Dimensionless)
C_{pa}	Specific heat capacity of air at constant pressure ($L^2T^{-2}\theta^{-1}$)
Δ	Slope of saturation vapor pressure curve ($MLT^{-2}\theta^{-1}$)
e_j	Width of a triangular edge
$(e_{sz}-e_z)$	Vapor pressure deficit ($ML^{-1}T^{-2}$)
f_s	Snow Fraction
vFrac	Fractional areal vegetation cover
$\vec{F}_0$	Lateral surface flux exchange (LT^{-1})
$\left\|\vec{F}_1\right\|$	Lateral surface flux exchange between overland flow and channel (LT^{-1})
$\vec{F}_2$	Lateral groundwater flux exchange (LT^{-1})
$\left\|\vec{F}_3\right\|$	Lateral flux exchange between channel and ground water (LT^{-1})
$\left\|\vec{F}_4\right\|$	Later groundwater flux exchange between sub-channel and triangular watershed element (LT^{-1})
$\vec{F}_5$	Flux exchange between river segments (LT^{-1})
γ	Psychometric constant ($ML^{-1}T^{-2}\theta^{-1}$)
g	Acceleration due to gravity (LT^{-2})
$\vec{G}_0$	Infiltration/Exfiltration rate (LT^{-1})
$\vec{G}_1$	Recharge flux between unsaturate zone and ground water (LT^{-1})
$\vec{G}_2$	Vertical flux exchange between channel bed and ground water (LT^{-1})
$\vec{G}_3$	Net precipitation flux to the canopy/ground/river (LT^{-1})
$\vec{G}_4$	Evaporation from canopy (LT^{-1})
$\vec{G}_5$	Throughfall drainage (LT^{-1})
$\vec{G}_6$	Snow melt (LT^{-1})
$\vec{G}_7$	Evaporation from overland flow (LT^{-1})
$\vec{G}_8$	Evaporation from upper soil layer (LT^{-1})
$\vec{G}_9$	Transpiration (LT^{-1})
K_{eff}	Effective conductivity (arithmetic/harmonic mean of the neighboring conductivities
K_{eq}	Equivalent hydraulic conductivity of dual matrix-macropore system
$K_{macV}[S]$	Vertical macropore hydraulic conductivity

$K_{macH}[S]$	Horizontal macropore hydraulic conductivity
$K_{\max}$	Maximum hydraulic conductivity of dual matrix-macropore system
$K_{matV}[S]$	Vertical matrix hydraulic conductivity at saturation S
$K_{matH}[S]$	Horizontal matrix hydraulic conductivity at saturation S
K_u	Vertical conductivity of the unsaturated zone
L_j	Length of a channel segment
n_s	Manning's coefficient ($L^{-1/3}T$)
Q^*	Net radiation (MT^{-3})
r_a	Atmospheric diffusion resistance (TL^{-1})
S	Saturation of the unsaturated zone
S_l	Sink flux from ground water (LT^{-1})
Sf	Surface Overland Flow (LT^{-1})
Sf_r	Surface Flow from Land to River(LT^{-1})
T_a	Air Temperature (T)
T_b	Base Temperature (T)
$vFrac$	Vegetation Fraction (Dimensionless)
z_r	River bed elevation (L)
z_{rb}	River bank elevation (L)
z_b	Aquifer bed elevation (L)
z_i	Surface elevation at i^{th} control volume

Appendix II

$$grad\psi\big|_x = \frac{y_2(z_1 - z_0) + y_1(z_0 - z_2) + y_0(z_2 - z_1)}{x_2(y_0 - y_1) + x_0(y_1 - y_2) + x_1(y_2 - y_0)} \tag{4.23a}$$

$$grad\psi\big|_y = \frac{x_2(z_1 - z_0) + x_1(z_0 - z_2) + x_0(z_2 - z_1)}{y_2(x_0 - x_1) + y_0(x_1 - x_2) + y_1(x_2 - x_0)} \tag{4.23b}$$

$$grad\psi = \sqrt{(grad\psi\big|_y)^2 + (grad\psi\big|_x)^2} \tag{4.24}$$

where x_i, y_i and z_i are coordinates of neighboring cell centers and $z_i = z + \psi$

Appendix III

Using Richard's equation and mass balance at the unsaturated-saturated zone interface as shown in Figure 4.19 we get

$$\vec{G}_1 = K_u \frac{\psi_u - \psi_{us}}{0.5(z - z_b - \psi_4)} = K_s \frac{\psi_{us} - (z_b + \psi_4)}{0.5\psi_4} \quad \Rightarrow \quad \psi_{us} = \frac{2K_u K_s(\psi_u - (\psi_4 + z_b))}{K_s(z - z_b - \psi_4) + K_u \psi_4} \tag{4.25}$$

Replacing ψ_{us} in the expression for $\vec{G}_1$ and using van-Genuchten's $\psi - S$ relationship (Eq. 11a) in the unsaturated zone we get equation 11

$$G_1 = \frac{K_u K_s z_b(\alpha(z - z_b - \psi_4) - 2(-1 + S^{\frac{n}{1-n}})^{\frac{1}{n}})}{\alpha(K_u \psi_4 + K_s(z - z_b - \psi_4))} \tag{4.26}$$

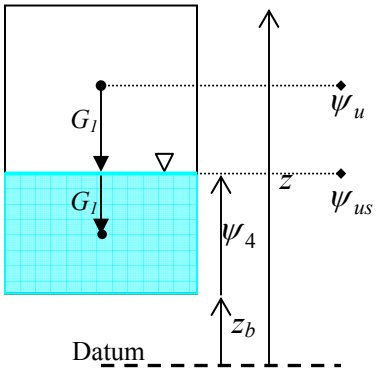

Figure 4.19 Vertical cross-section of a subsurface control volume

Appendix IV

A representative non-linear "stiff" ODE system with a combination of faster and smaller time scales is

$$\frac{dy}{dt} = g(y), \qquad y(0) = y_0 \tag{4.27a}$$

where y and g are N dimensional state and functional vectors respectively. The right hand side of the above equation can be linearized to obtain

$$\frac{dy}{dt} = g(y) = \frac{dg_i}{dy_j} y_i = JY = (A\lambda B)Y$$

An example of one such stiff ODE system defined on a PIHM kernel is an interaction between overland and ground water flow processes. Assuming a shallow groundwater condition with direct interaction between surface and ground water, Eq. (4.27b) shows a simplified representation of process interactions on a model kernel i that neighbors j (in

accordance with Eq. 4.5) using a 2-dimesional stiff ODE system with state vector $y \equiv (\psi_2, \psi_4)$.

$$\begin{pmatrix} \dfrac{d\psi_2}{dt} = S_0 - (S_4 + S_5) - \dfrac{1}{n}\psi_{2_i}{}^{5/3}\dfrac{\psi_{2_i} - \psi_{2_j} + (z_i - z_j)}{d}\dfrac{L}{A} - K_v\dfrac{\psi_{2_i} - \psi_{3_i} + (z_i - z_{u_i})}{(z_i - 0.5z_{u_i})} \\ \dfrac{d\psi_4}{dt} = K_v\dfrac{\psi_{2_i} - \psi_{3_i} + (z_i - z_{u_i})}{(z_i - 0.5 * z_{u_i})} - K_h\dfrac{\psi_{4_i} - \psi_{4_j} + (z_{b_i} - z_{b_j})}{d}\psi_{4_{ij}}\dfrac{L}{A} \end{pmatrix} \tag{4.27b}$$

The eigenvalue of the jacobian for ODE system in (4.27b) will be

$$\begin{pmatrix} \lambda_1 \\ \cdots\cdots \\ \lambda_2 \end{pmatrix} = \begin{pmatrix} (-\dfrac{1}{n}\psi_{2_i}{}^{5/3}\dfrac{(1+\dfrac{5}{3}\dfrac{\psi_{2_i} - \psi_{2_j} + (z_i - z_j)}{\psi_{2_i}}}{dA}L - \dfrac{K_v}{(z_i - 0.5z_{u_i})} \\ \cdots\cdots\cdots\cdots\cdots\cdots\cdots\cdots\cdots\cdots\cdots\cdots \\ -\dfrac{K_h(\psi_{4_{ij}} + (\psi_{4_i} - \psi_{4_j} + (z_i - z_j))/2)}{dA}L \end{pmatrix}$$

We note that with typical values of the states and roughness and conductivity parameters in (4.27b), the ratio $\lambda_1 / \lambda_2 \approx \dfrac{\psi_2{}^{5/3}}{n\psi_4 K_h}$ means $\lambda_1 > \lambda_2$. In the same vein, assuming that M eigenvalues of the total N for the global ODE system (shown in Eq. 27a) are very large, the exact solution obtained from a first order explicit method (Valorani et al. 2001) can be written as

$$y_{ex}(t) = (\sum_{i=1}^{M} a_i e^{\frac{\ln|1-\lambda_i \Delta t|}{\Delta t}t} e^{\frac{i\pi t}{\Delta t}} b_i + \sum_{i=M+1}^{N} a_i e^{\frac{\ln|1-\lambda_i \Delta t|}{\Delta t}t} e^{\frac{i\pi t}{\Delta t}} b_i) y_0 \tag{4.27c}$$

where $y_{ex}(t)$ is the explicit solution. For the explicit solution to be stable, the following conditions need to be satisfied.

$\forall i \quad \ln|(1 - \lambda_i \Delta t)| <= 0$ ➔ $|1 - \lambda_i \Delta t| <= 1$ ➔ $\Delta t \leq 1/|\lambda_i|$

Since $|\lambda_1| > |\lambda_2| > |\lambda_3| > \ldots\ldots\ldots |\lambda_M| >> |\lambda_{M+1}| > \ldots\ldots\ldots\ldots\ldots\ldots |\lambda_N|$, the stability of the explicit system will require $\Delta t \leq 1/|\lambda_1|$. For a stiff system with very large λ_1, Δt will be very small. We note that these stability requirements are in addition to the CFL stability condition (Courant et al. 1928) which depends on grid size, Courant number, velocity and depth of flow in other similar flow systems. On the contrary, the implicit solution (Valorani et al. 2001) given by

$$y_{im}(t) = (\sum_{i=1}^{M} a_i e^{\frac{-\ln(1+\lambda_i \Delta t)}{\Delta t}t} b_i + \sum_{i=M+1}^{N} a_i e^{\frac{-\ln(1+\lambda_i \Delta t)}{\Delta t}t} b_i) y_0 \tag{4.27d}$$

is always stable for all $\lambda_i \Delta t > 0$.

CHAPTER 5:

A Second Order Accurate, Finite Volume Based, Integrated Hydrologic Modeling (FIHM) Framework for Simulation of Surface and Subsurface Flow

5.1. Introduction

Understanding and predicting of flow on the surface and in the subsurface necessitates recognizing "that surface water and ground water are simply two manifestations of a single integrated resource" (Winter et al., 1998). This recognition has stimulated the development of numerical models capable of simulating the interactions between surface and subsurface flow. The accuracy of the simulation relies heavily on a) the choice of governing equations used to simulate a flow behavior (e.g. 3D Richards' equation for subsurface flow), b) the numerical methodology chosen to solve the governing equations (e.g. finite difference or volume) and the order of its accuracy, c) the accuracy of representation of hydrogeologic data on the model grids (details in Kumar et al., 2009a), and finally d) the discretization methodology (unstructured or structured mesh) and its resolution. Coupled surface-subsurface models include InHM (Vanderkwaak, 1999), MIKE SHE (Graham and Refsgaard, 2001), WASH123D (Yeh and Huang, 2003), MODHMS (Panday and Huyakorn, 2004), PARFLOW-Surface Flow (Kollet and Maxwell, 2006) and PIHM (Qu and Duffy, 2007; Kumar et al., 2009b) Among these, MIKE SHE, MODHMS and PARFLOW-Surface Flow use finite difference methods while InHM and WASH123D are based on finite element methods. Finite difference based models have some significant advantages in terms of ease of meshing the domain, simple topological structure and ease of parallelization, but the rigidity of the structured grids in conforming to curvilinear geometries and representation of heterogeneities (Kumar et al., 2009a) make it prohibitive to perform accurate large scale simulations. Barrash and Dougherty (1997) and the USEPA (1994) also reported loss of accuracy in predicting hydraulic heads near regions of steep head gradients and boundaries using finite difference models. The inaccuracy can be reduced by performing relatively fine localized discretization in areas of steep head gradient (Leake and Claar, 1999; Mehl and Hill, 2004), however this results in long execution times. Also, the conservation property in the finite difference based models is only satisfied for infinitesimal grid size. An alternate solution strategy is the traditional Galerkin finite element methods which are used to solve diffusion wave equations in WASH123D. These methods ensure continuity in gradient at the discretization boundary but there is no local conservation of mass

within each discretized unit element (Di Giammarco et al., 1996). Control volume finite element (CVFE) methods alleviate this problem (InHM is based on CVFE) and are able to conserve mass.

Here we develop a second order accurate, fully coupled, finite volume based integrated hydrologic modeling (FIHM) framework for unstructured grids. The primary advantages of this methodology are the conservation of the solution property within each discretized element, use of spatially-adaptive and boundary-fitting unstructured mesh which can be generated using boundary constraints pertaining to topography, hydrogeology or climate (Kumar et al., 2009a), and numerical robustness achieved due to validity of local extremum diminishing (LED) property on each grid cell. The constrained unstructured mesh leads to enhanced efficiency in capture of topographic spatial variations with least number of elements, and also for the accurate capture of the complex geometries of topographic, geologic and morphologic features. A higher order scheme for overland flow (Lin et al. 2003; Fiedler and Ramirez, 2000) and subsurface flow (Manzini and Ferraris, 2004) yields improved simulation of states and derived hydraulic conductivity fields both in areas of smooth and steep gradients. The model simulates overland flow by solving the diffusion wave approximation of St. Venant's equation. Vadose zone pressure distribution is simulated by solving the nonlinear, three dimensional Richards equation. The model treats the complete subsurface regime with unsaturated and saturated flow as a unified whole. The second order accuracy of the scheme is achieved through the use of higher order approximations of the flux at the cell faces (Turkel, 1985). We note that first-order finite volume models such as PIHM (Kumar et al., 2009b; Qu and Duffy, 2007) which are based on a piecewise constant head representation within an element lead to smearing of discontinuities and are particularly inaccurate for simulation in orthotropic and anisotropic media (Pasdunkorale and Turner, 2003). The second order formulation in FIHM is supported by a continuously differentiable multidimensional slope limiter (developed by Jawahar and Kamath, 2000) to avoid spurious oscillations. The evaluation of local gradient at each edge of the control volume necessitates head magnitude at the cell-centers and vertices. The model uses a pseudo-Laplacian based reconstruction mechanism (Holmes and Connell, 1989) to obtain vertex head values from the cell averages (which are the primary unknowns). The

reconstruction procedure is of fundamental importance to achieve optimally accurate normal flux at the edge (Bertolazzi and Manzini, 2004; Ollivier-Gooch and Altena, 2002). The model also handles modification of the flow field due to arbitrarily oriented anisotropy of hydrogeologic and physiographic properties. This is particularly important in regions with directional hydraulic conductivity or surface roughness. The majority of existing computational methods for anisotropic conductivity employ structured, body-fitted meshes where, in order to avoid dealing with cross derivatives, they align their coordinate system with the principal directions of the conductivity tensor. Such a methodology is not easy to use in problems with multiple anisotropic materials. Even the finite volume based models are generally not designed to handle both inhomogeneity and general anisotropy. The model detailed in this paper handles the media inhomogeneities in combination with full-tensor anisotropy by evaluating both the normal and tangential components of edge gradients.

The objectives of this paper are to detail the second order accurate finite volume modeling framework for coupled surface and subsurface simulation and demonstrate its capability to simulate and improve understanding of process interactions. Specifically we strive to understand why coupling of processes is needed and how the interaction between processes influences hydrologic states in the neighboring continua. Also, the influence of topographic and physiographic properties on process simulation will be explored. Complete details of testing and validation of the model are available in Kumar et al. (2009d). The eight problems presented in this paper are chosen to highlight the model's capabilities and verify and explore individual processes and the interaction between them.

5.2. Governing Equations

The equations governing two dimensional head distribution on the surface and a three dimensional pressure distribution in the subsurface are presented below. Processes describing water movement on the surface and in the subsurface zone are first discussed, followed by coupling behavior between them

5.2.1. Overland Flow

Overland flow is generally defined by the shallow water St. Venant's equation. The equation is derived by depth averaged integration of the three-dimensional Navier–Stokes equations. Application of a boundary condition on the free surface and continuity of flux on the ground surface during integration introduces a term that couples it to the vadose zone (Weiyan, 1992). Here we use a diffusion-wave flow based approximation of St. Venant's equation with vadose zone-surface flow coupling terms as detailed in Gottardi and Venutelli (1993) by

$$\{\frac{\partial}{\partial x}[\psi_o K_x(\psi_o)\frac{\partial h_o}{\partial x}]+\frac{\partial}{\partial y}[\psi_o K_y(\psi_o)\frac{\partial h_o}{\partial y}]-Q_{og}\}+Q_{ss}=\frac{\partial \psi_o}{\partial t} \quad (5.1a)$$

or equivalently, $$\{\nabla.(\psi_o K(\psi_o)\nabla h_o)-Q_{og}\}+Q_{ss}=\frac{\partial \psi_o}{\partial t} \quad (5.1b)$$

where $K(\psi_o)$ is the diffusive conductance vector, ψ_o is the overland flow depth, h_o (= $z_s+\psi_o$) is the total overland flow head, z_s is the elevation of the ground surface, Q_{ss} is volumetric flux per unit area due to the sources or sinks, which can includes precipitation and evapotranspiration, and Q_{og} is the vertical flux exchange per unit area between surface and subsurface flow. The diffusive conductance term is given by

$$K(\psi_o)\big|_{x,y}=\frac{\psi_o^{2/3}}{n\big|_{x,y}}\frac{1}{(\frac{dh_o}{ds})^{1/2}} \quad (5.2)$$

where n is Manning's roughness coefficient and s is the direction of maximum slope. We note that the overland flow equation is a nonlinear parabolic equation due to the nature of the diffusive conductance. The assumptions inherent in the diffusion-wave approximation of St. Venant's equation include depth-averaged flow velocities, a hydrostatic vertical head distribution, mild bed slopes, neglecting inertial terms, and a dominant bottom shear stress. The equation is able to adequately resolve backwater effects.

5.2.2. Variably Saturated Subsurface Flow

Three-dimensional vadose zone flow in a heterogeneous porous medium is governed by Richard's equation for variably saturated flow (Huyakorn and Pinder, 1983) given by

$$\frac{\partial}{\partial x}[K_x(\psi)\frac{\partial h_g}{\partial x}]+\frac{\partial}{\partial y}[K_y(\psi)\frac{\partial h_g}{\partial y}]+\frac{\partial}{\partial z}[K_z(\psi)\frac{\partial h_g}{\partial z}]+Q_{ss}=[S.S_s+C(\psi)]\frac{\partial \psi}{\partial t} \qquad (5.3a)$$

or equivalently, $$\nabla.(K(\psi)\nabla h_g)+Q_{ss}=[S.S_s+C(\psi)]\frac{\partial \psi}{\partial t} \qquad (5.3b)$$

where, $K(\psi)$ is the hydraulic conductivity vector, ψ is the potentiometric head, h_g is the total head, S is the soil saturation, S_s is the specific storage, $C(\psi)$ is the specific moisture capacity and Q_{ss} is volumetric flux per unit volume due to the sources or sinks which can include pumping at wells. The $[S.S_s+C(\psi)]$ term in the variably saturated equation describes the storage properties of the medium. We note that as the soil pressure head, ψ , becomes positive and the pores saturate with water, the specific moisture capacity, $C(\psi)$, converges to zero and the soil saturation, S, converges to one. The soil characteristic functions $K(\psi)$ and $C(\psi)$ can be represented by several different empirical and theoretical methods (e.g. Brooks and Corey, 1966; Mualem, 1976; Haverkamp et al., 1977; van Genuchten, 1980).

5.2.3. Coupling Between Overland and Subsurface Flow

The coupling of the surface and vadose zone flow is incorporated by ensuring continuity of normal vertical flux and pressure head at the surface-subsurface interface. The methodology is equivalent to "conductance concept" (Vanderkwaak, 1999) if the thickness of the interficial domain goes to zero. Flux continuity across the surface, subsurface domain is ensured by equating Q_{og} (in Eq. [5.1]) to vertical flux term $K_z\frac{\partial h_g}{\partial z}$ (in Eq. [5.3]) as discussed in Discacciati and Quarteroni (2002). The equivalent vertical conductivity, K_z is evaluated as

$$K_z = \begin{cases} K_z(\psi) & \dfrac{\partial h_g}{\partial z} < 0 \\ K_z(\psi = 0) & \dfrac{\partial h_g}{\partial z} \geq 0 \end{cases} \tag{5.4}$$

We note that $\frac{\partial h_g}{\partial z} < 0$ corresponds to a negative downward gradient condition which essentially translates to flux in upward direction (exfiltration). Also, continuity in head is ensured by setting

$$h_o\big|_{z=surface} = h_g\big|_{z=surface} \tag{5.5}$$

The physical equations defined on the problem domain are now defined on each discretized element (control volume) using a finite volume strategy.

5.3. Finite Volume Framework

5.3.1. Domain Decomposition

FIHM uses a semi-discrete finite volume formulation to spatially discretize hydrologic process equations in the problem domain. The first step in doing so is the tessellation of the domain into collection of non-overlapping elements (control volumes) using an efficient domain decomposition algorithm. We use constrained Delaunay triangulation to decompose the problem domain. In 3-D, the triangulations are projected in depth to form prismatic elements. The Delaunay property of the grid leads to a large decrease in the number of nodes/elements with respect to structured meshes (Shewchuk 1996). Constraining of the Delaunay triangulations gives additional advantages through better representation of line-features such as boundaries between zones having different soil types, or land-use/ land-cover, rivers and sub-watershed divides (Kumar et al., 2009a). The unique advantage of using thematic classes as constraints for unstructured grids is that all class boundaries (vegetation and/or soil polygons) are honored by the decomposition, thus resulting in a model grid where every cell contains a single class. This reduces the data uncertainty arising from subgrid variability of mixed classes or themes within a model grid cell (Kumar et al. 2009a). The decomposition strategy

generates high-quality unstructured grids with user-specified geometrical constraints such as element size and "roundness". The algorithmic details of generation of constrained Delaunay triangulations using GIS feature objects has been discussed in Kumar et al. 2009a. More importantly, the decomposition strategy has been integrated with a "shared data model" which leads to coupling of the GIS with the hydrologic model (Kumar et al., 2009b). The integrated software framework facilitates rapid prototyping of meshes and data definitions resulting in efficient parameter steering, grid design, real time visualization and decision support. In summary, the "support-based" domain decomposition and unstructured grid framework provides a close linkage between geo-scientific data and FIHM (http://sourceforge.net/projects/pihmgis/).

5.3.2. Semi-Discrete Finite Volume Formulation

The governing partial differential equations (PDEs) describing surface and subsurface flow (Eqs. [5.1] and [5.3]) are defined for each control volume using a semi-discrete finite volume formulation. The formulation entails discretization of a partial differential equation (PDE) of a conservative scalar variable, ψ in space. We consider a generalized PDE (for surface or subsurface flow) as

$$\frac{\partial \psi}{\partial t} = \nabla.(\psi U) + \nabla.(\Gamma \nabla \psi) + Q_{ss} \qquad (5.6)$$

or the rate of change in ψ = (Advective Flux) + (Diffusive Flux) + (Source/Sink), where U is the flux velocity vector, Γ is the conductivity tensor, and Q_{ss} is rate of increase/decrease in ψ due to sources/sinks. The PDE in Eq. [5.6] is reduced to an ordinary differential equation (ODE) by integration over an arbitrary three dimensional control volume, V_i, in the model domain

$$\int_{V_i} \frac{\partial \psi}{\partial t} dV = \int_{V_i} \nabla.(\psi U) dV + \int_{V_i} \nabla.(\Gamma \nabla \psi) dV + \int_{V_i} Q_{ss} dV \qquad (5.7)$$

By applying Gauss's theorem on the advective and diffusive terms on the right hand side of the Eq. [5.7], we obtain

$$\frac{\partial}{\partial t}\int_{V_i}\psi dV = \int_{A_{ij}}\vec{n}.(\psi U)dA + \int_{A_{ij}}\vec{n}.(\Gamma\nabla\psi)dA + \int_{V_i}Q_{ss}dV \qquad (5.8)$$

where $\vec{n}$ is the normal vector to the surface j of the control volume i.By integrating the individual flux terms in Eq. [5.8] over a prismatic volume, we obtain a generic semi-discrete form of ODE that defines all the hydrologic processes incorporated in the finite volume as

$$A_i\frac{d\overline{\psi}}{dt} = \sum_j \vec{n}.\vec{C}A_{ij} + \sum_j \vec{n}.\vec{D}A_{ij} + \overline{Q}_{ss}V_i \qquad (5.9)$$

where $\overline{\psi}$ (L) is the average volumetric conservative scalar per unit planimetric prismatic volume area A_i, $\vec{C}$ and $\vec{D}$ are the advective and diffusive flux respectively, $\vec{n}$ is normal vector to the face of control volume and $\overline{Q}_{ss}$ is the average source/sink rate per unit control volume. We use this approach to convert the governing PDEs for surface (Eq. [5.1]) and subsurface (Eq. [5.3]) flows to their semi-discrete form of ODEs. As discussed in the previous section, both governing equations are parabolic diffusion based PDEs, so the convective flux $\vec{C}$ in Eq. [5.9] will be equal to zero. We can express the semi-discrete forms of [5.1] and [5.3] as

$$A_i\frac{d\psi_o}{dt} = \sum_{j=1}^{3}\vec{n}_j.\vec{F}_j + \sum_{k=1}^{2}\vec{n}_k.\vec{G}_k + Q_{ss}V_i \qquad (5.10)$$

$$\{A_i[S.S_s + C(\psi)]\frac{d\psi}{dt} = \sum_{j=1}^{3}\vec{n}_j.\vec{F}_j + \sum_{k=1}^{2}\vec{n}_k.\vec{G}_k + Q_{ss}V_i\}\Big|_m \qquad (5.11)$$

where $\vec{F}_j$ and $\vec{G}_k$ are lateral and vertical flux vectors. j and k denote the faces of the i^{th} control volume element and m is the vertical discretization index. We note here that since the control volumes are prismatic in shape, there are a total of five faces (edges), three vertical faces on the side of the prism and two horizontal faces on the top and bottom of the prism.

5.3.3. Vertical Flux Calculation

The vertical subsurface flux term $\vec{G}_k$ at the interface between m^{th} and $(m+1)^{th}$ layer (see Figure 5.1) is calculated by imposing continuity of flux and head at the interface

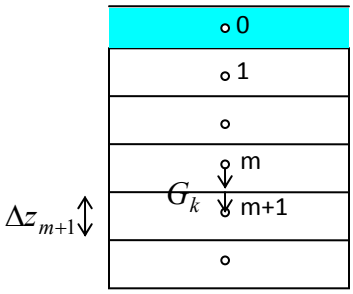

Figure 5.1 Vertical discretization of each prismatic element. Δz_{m+1} is thickness of $(m+1)^{th}$ discretization layer. Layer 0 (shaded) corresponds to overland flow. G_k is the vertical flux at the interface of the m^{th} and $(m+1)^{th}$ layers

and is given by

$$\vec{G}_k = K(\psi)\big|_{m,m+1} A_i \nabla h \tag{5.12a}$$

We note that continuity in flux requires

$$\vec{G}_k\Big|_{m,m+1} = \vec{G}_k\Big|_{m,m+1/2} = \vec{G}_k\Big|_{m+1/2,m+1} \tag{5.12b}$$

Or $$K(\psi)\big|_m A_i\left(\frac{(h)_m - (h)_{m+1/2}}{0.5\Delta z_m}\right) = K(\psi)\big|_{m+1} A_i\left(\frac{(h)_{m+1/2} - (h)_{m+1}}{0.5\Delta z_{m+1}}\right)$$

This results in calculation of the vertical flux as

$$\vec{G}_k\Big|_{m,m+1} = \frac{2K(\psi)\big|_{m+1} K(\psi)\big|_m}{K(\psi)\big|_{m+1}\Delta z_m + K(\psi)\big|_m \Delta z_{m+1}} A_i((h)_m - (h)_{m+1}) \tag{5.13}$$

Both the flux and the vertical anisotropy along z-axis have been assumed to be normal to the control volume face in this analysis. The flow between surface and subsurface domains follows similar conceptualization. The flux at the topmost face of the subsurface prismatic volume ($\vec{G}_k$ in Eq. [5.11]) is equal to the bottom flux from the overland-flow control volume ($\vec{G}_k$ in Eq. [5.10], which is the same as Q_{og} in Eq. [5.1]). The coupling flux $\vec{G}_k$ in this case can be calculated as

$$\vec{G}_k\Big|_{0,1} = \vec{G}_k\Big|_{0,1/2} = \vec{G}_k\Big|_{1/2,1} \qquad \text{(continuity in flux)} \tag{5.14a}$$

By ensuring continuity in head at the land surface ($h_0 = h_{1/2}$) and evaluating the effective vertical conductivity as in Eq. [5.4], reduces the above equation to

$$\vec{G}_k\Big|_{0,1} = K_z A_i \left(\frac{(h)_0 - (h)_1}{0.5\Delta z_1}\right) \tag{5.14b}$$

Note that $(h)_0$ and $(h)_1$ in the above equation are h_o and h_g in Eqs. [5.1] and [5.3] respectively.

5.3.4. Lateral Flux Calculation

The normalized lateral flux term ($\vec{n}_j.\vec{F}_j$) for surface flow in Eq. [5.10] is derived as

$$\vec{n}_j.\vec{F}_j = \int_{A_{ij}} \vec{n}.(K(\psi_o)\nabla h_o)dA = \int_{\xi_{ij}} \vec{n}.(\psi_o K(\psi_o)\nabla h_o)d\xi = UW[\psi_o K(\psi_o)\nabla h_o]\Big|_{\xi_{ij}}.\xi_{ij} \tag{5.15a}$$

and for the subsurface flux in Eq. [5.11] is derived as

$$\vec{n}_j.\vec{F}_j = \int_{A_{ij}} \vec{n}.(K(\psi)\nabla h_g)dA = \int_{\xi_{ij}} \vec{n}.(\Delta z K(\psi)\nabla h_g)d\xi = UW[\Delta z K(\psi)\nabla h_g]\Big|_{\xi_{ij}}.\xi_{ij} \tag{5.15b}$$

where ξ_{ij} is the j^{th} edge (or face) of element i, ψ_o is the overland flow depth, $UW[]$ is an upwind function and Δz is the vertical discretization thickness of a given subsurface control volume. We note that the line integrals in Eq. [5.15] are computed by applying second-order mid-point quadrature rule to upstream numerical fluxes (Blazek, 2001). The calculation of lateral flow terms for both surface and subsurface flow (in Eq. [5.15]) crucially depends on the evaluation of gradient and head terms on the edge faces of each control volume. In the following discussion, h corresponds to total head of either subsurface head or overland flow head.

5.3.4.1. Edge Gradient Calculation

The first step in the formulation of the discrete gradient for internal or boundary edges consist of defining the one-sided gradient. The gradient calculation for the variational

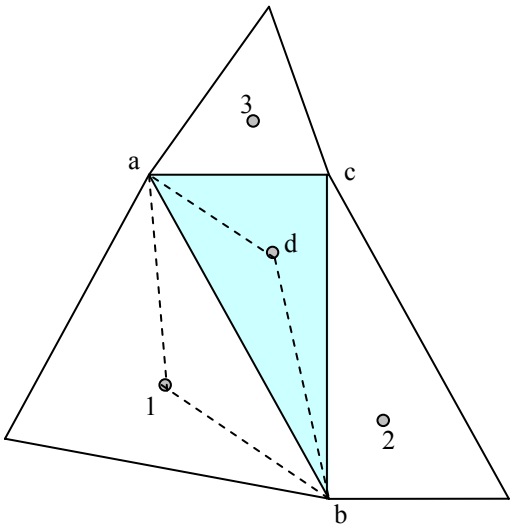

Figure 5.2 Plan view of a typical tessellation where Δabc is surrounded by three neighboring elements (having centers 1, 2 and 3). Flux calculation on any edge ab of Δabc uses heads at vertices a and b of the triangle and at cell centers 1 and d.

triangle $\Delta a1b$ (shown in Figure 5.2) for the edge ab is calculated using the Green-Gauss theorem as

$$\nabla h = \frac{1}{A}\oint_{\xi} \vec{n}.hd\xi \tag{5.16}$$

where ξ is the edge vector and A is the area of the $\Delta a1b$. Along the x and y directions, the gradient reduces to

$$(\nabla h)_{a1b}\big|_x = -\frac{y_a(h_b - h_1) + y_1(h_a - h_b) + y_b(h_1 - h_a)}{x_a(y_b - y_1) + x_1(y_a - y_b) + x_b(y_1 - y_a)} \tag{5.17a}$$

$$(\nabla h)_{a1b}\big|_y = -\frac{x_a(h_b - h_1) + x_1(h_a - h_b) + x_b(h_1 - h_a)}{y_a(x_b - x_1) + y_1(x_a - x_b) + y_b(x_1 - x_a)} \tag{5.17b}$$

The absolute gradient for the left variational triangle of edge ab is given by

$$\nabla h\big|_L = (\nabla h)_{a1b} = \sqrt{((\nabla h)_{a1b}\big|_x)^2 + ((\nabla h)_{a1b}\big|_y)^2} \tag{5.18}$$

We note that the gradient calculation in Eq. [5.17] and [5.18] depends both on the cell center heads (such as h_1) and the vertex heads (such as h_a and h_b). We use a multi-dimensional linear (second-order) reconstruction scheme within the framework of cell-centered finite-volume discretization to determine vertex values from cell averages.

5.3.4.1.1. Vertex Reconstruction. A second order accurate modified pseudo-Laplacian procedure (Jawahar and Kamath, 2000) is used to obtain vertex values from the corresponding cell-centered values (Holmes and Connell, 1989). The method outperforms the traditionally used inverse-distance weighted interpolation which is observed to have less than second order accuracy (Frink, 1994). For any vertex of the mesh, we first define the reconstruction

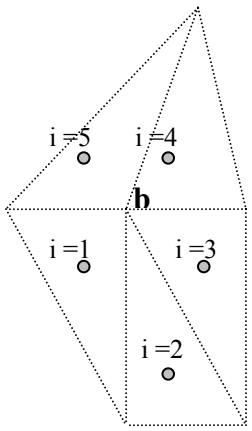

Figure 5.3 Head reconstruction at an arbitrary vertex b in a tessellation using a pseudo-Laplacian procedure (Jawahar and Kamath, 2000) uses head values at the centers of all the cells which share a node at b

stencil as the union of the cells that share the vertex; then, we calculate a cell weight for every element of the stencil. Figure 5.3 shows a representative stencil for the vertex *b*. The value of head at vertex *b* is calculated as

$$h_b = \sum_{i=1}^{M} \frac{\omega_i}{\sum_{i=1}^{M} \omega_i} h_i \tag{5.19}$$

where M is the number of cells sharing the vertex and ω_i s are the cell weights that are made to satisfy the zero pseudo-Laplacian condition (Kim et al., 2003). The weighted interpolation formula is linearly consistent. The individual weights are calculated by using Lagrange multipliers λ_x and λ_y as

$$\omega_i = 1 + \lambda_x (x_i - x_b) + \lambda_y (y_i - y_b) \tag{5.20}$$

where

$$\lambda_x = \frac{I_{xy}R_y - I_{yy}R_x}{I_{xx}I_{yy} - I_{xy}^2} \qquad \lambda_y = \frac{I_{xy}R_x - I_{xx}R_y}{I_{xx}I_{yy} - I_{xy}^2} \tag{5.21a}$$

$$I_{xx} = \sum_{i=1}^{M}(x_i - x_b)^2 \;,\; I_{yy} = \sum_{i=1}^{M}(y_i - y_b)^2 \;,\; I_{xy} = \sum_{i=1}^{M}(x_i - x_b)(y_i - y_b)\,, \tag{5.21b}$$

$$R_x = \sum_{i=1}^{M}(x_i - x_b) \qquad R_y = \sum_{i=1}^{M}(y_i - y_b) \tag{5.21c}$$

This procedure gives most of the benefits of a true Laplacian and is also computationally inexpensive. It is important to realize that this reconstruction step is required by all vertices of the mesh, whether the vertex is internal or on the boundary of the computational domain. Extraneous cell weights (negative or positive values that are greater than 2) which are sometimes obtained at the boundaries (Frink and Pirzadeh, 1998) are clipped based on Jawahar and Kamath (2000). The modification of weights, which is only carried out for the boundary vertices, is not expected to have a significant impact on accuracy since subsequent imposition of boundary conditions at these locations would weaken the effect.

5.3.4.2. Calculation of Head at an Edge using Linear Reconstruction

The overland flow depth value at an edge in Eq. [5.15a] can be approximated by either using an upwind cell-centered value (characteristic of first order methods) or obtaining an interpolated value at the mid-point of the edge. First order upwind methods introduce large and often unacceptable numerical diffusion. Here we use a second order estimate of the solution at the edge by approximating the edge depth using a multidimensional linear reconstruction process. The underlying assumption is a piecewise linear distribution of flow depth within a cell. We note that in order to satisfy c-property (Bermudez and Vasquez, 1994), instead of linear distribution of flow depth, we perform interpolation of the total head at the edge and then subtract the elevation at the edge to obtain flow depth at the edge. The higher order edge estimate, h_ξ, is calculated by

$$h_\xi = h_c + \vec{r}.\nabla h_l \tag{5.22}$$

where h_c is the head at the cell center, $\vec{r}$ is the position vector of the mid-point of the edge face with respect to the cell center and ∇h_l is the limited cell gradient. This

reconstruction technique is based on a wide computational stencil and does not strongly depend on vertex values to preserve stability for highly distorted grids.

5.3.4.2.1. Limited Gradient Calculation. The linear reconstruction can cause spurious numerical oscillations when approximating strong gradient solutions. The problem is alleviated by a limiter based gradient calculation that locally monotonizes the reconstructed solution by limiting the slope of the reconstructed variables. The limiter helps in achieving smooth transition for both discontinuous jumps and continuous gradients. Here we use a multidimensional limiter of Jawahar and Kamath (2000) which is shown to be effective for strong discontinuities, even on a grid which is composed of highly distorted triangles. This is in contrast to the often used nondifferentiable extremum seeking limiters such as the ones based on the MUSCL approach (Hubbard, 1999), which are strongly dependent on grid connectivity. The limiting procedure consists of calculation of limited gradient (∇h_l) by taking the weighted average of the unlimited gradients (∇h_u) in the neighboring elements as

$$\nabla h_l = \omega_1 (\nabla h_u)_1 + \omega_2 (\nabla h_u)_2 + \omega_3 (\nabla h_u)_3 \tag{5.23}$$

where the weights are

$$\omega_1 = \frac{g_2 g_3 + \varepsilon^2}{g_1^2 + g_2^2 + g_3^2 + 3\varepsilon^2} \quad \omega_2 = \frac{g_3 g_1 + \varepsilon^2}{g_1^2 + g_2^2 + g_3^2 + 3\varepsilon^2} \quad \omega_3 = \frac{g_1 g_2 + \varepsilon^2}{g_1^2 + g_2^2 + g_3^2 + 3\varepsilon^2} \tag{5.24}$$

and g_1, g_2 and g_3 are the square of the L_2 norm of the unlimited elemental gradients given by $g_1 = \left\|(\nabla h_u)_1\right\|^2$, $g_2 = \left\|(\nabla h_u)_2\right\|^2$ and $g_3 = \left\|(\nabla h_u)_3\right\|^2$. ε is a small number introduced to prevent indeterminacy. The limiting weights in Eq. [5.23] are reduced to $\frac{1}{3}$ when all the three elemental gradients are equal.

5.3.4.2.2. Unlimited Gradient Calculation. The unlimited gradient of an element, ∇h_u, is the area weighted average of gradients calculated on its edges, ∇h_e. This implies that

$$\nabla h_u = \sum_{i=1}^{3} (A_e)_i (\nabla h_e)_i \tag{5.25}$$

where $(A_e)_i$ is the cumulative area of the variational triangle on the either side of edge i. Using Figure 5.2, the edge gradient on an arbitrary face *ab* can be calculated as

$$(\nabla h_e)_{ab} = \frac{A_{ab1}\nabla h_{ab1} + A_{abd}\nabla h_{abd}}{A_{ab1} + A_{abd}} \tag{5.26}$$

We note that in the above equation $(A_e)_{ab} = A_{ab1} + A_{abd}$. For faces located on the boundaries, the solution at ghost elements is used to provide the same stencil to compute the face gradients.

5.3.4.3. Normalized Lateral Flux in Heterogeneous Anisotropic Domain

Evaluation of normalized flux at an edge must take into account the contribution of arbitrarily oriented anisotropy at the control volume interface. The normalized flux $\vec{n}_j.\vec{F}_j$ in a two dimensional anisotropic domain with principal axes oriented as shown in Figure 5.4 can be resolved into x and y components as

$$\vec{n}.\vec{F} = \vec{n}.(F_x\hat{i} + F_y\hat{j}) = \vec{n}.(K_x\nabla h_x\hat{i} + K_y\nabla h_y\hat{j})A_\xi \tag{5.27}$$

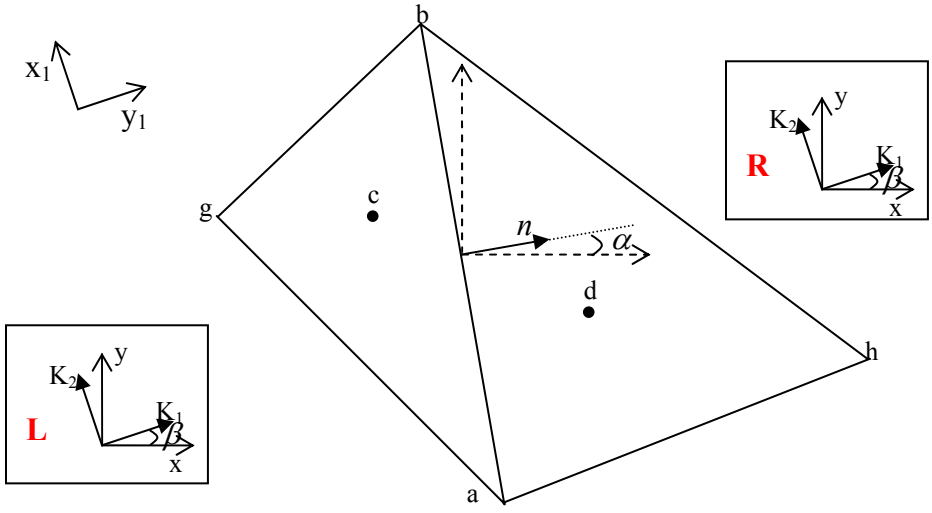

Figure 5.4 Arbitrarily oriented anisotropy in adjacent cells sharing interface ab. Note that principal conductivities (**K_1**, **K_2**) and their orientation (angle β) with respect to the global Cartesian coordinate system (x,y) for both left (L) and right (R) cells can be different. (x_1,y_1) is a local coordinate system that is oriented along the directions of the principal axes of anisotropy. The vector normal to interface ab is at an angle α to the global x-axis.

where ∇h_x and ∇h_y are calculated as in Eq. [5.17], and K_x and K_y are hydraulic conductivity components in the x and y directions respectively. A_ξ is the edge interaction-flux area which is equal to $\psi_o \xi$ for surface flow and $\Delta z \xi$ for vadose zone. Assuming that principal conductivities K_1 and K_2 are oriented at an angle β to the global x-y axes, Eq. [5.27] becomes

$$\vec{n}.\vec{F} = A_\xi(((K_1 Cos^2\beta + K_2 Sin^2\beta)\nabla h_x + (K_1 - K_2)Cos\beta * Sin\beta \nabla h_y)\hat{i}$$
$$+ ((K_1 - K_2)Cos\beta * Sin\beta \nabla h_x + (K_1 Sin^2\beta + K_2 Cos^2\beta)\nabla h_y)\hat{j}).\vec{n} \quad (5.28)$$

We note the conductivities in the above equation can be either a diffusive conductivity shown in Eq. [5.2] for the surface flow or a hydraulic conductivity of the subsurface domain. Taking into account the orientation of normalized flux which is at an angle α to the global x-axis (see Figure 5.4), Eq. [5.28] can be rewritten as

$$\vec{n}.\vec{F} = A_\xi((K_1 Cos^2\beta + K_2 Sin^2\beta)\nabla h_x + (K_1 - K_2)Cos\beta * Sin\beta \nabla h_y)Cos\alpha$$
$$+ ((K_1 - K_2)Cos\beta * Sin\beta \nabla h_x + (K_1 Sin^2\beta + K_2 Cos^2\beta)\nabla h_y))Sin\alpha \quad (5.29)$$

By replacing $\nabla h_x = \nabla h Cos\theta$ and $\nabla h_y = \nabla h Sin\theta$ in Eq. [5.29], the equation transforms to

$$\vec{n}.\vec{F} = A_\xi(K_1 Cos(\theta - \beta)Cos(\alpha - \beta) + K_2 Sin(\theta - \beta)Sin(\alpha - \beta))\nabla h \quad (5.30)$$

where θ is angle of orientation of ∇h to the x-axis. An alternative derivation of Eq. [5.30] using a coordinate system that is oriented along the direction of principal conductivities is in Appendix 1.

5.4. Numerical Results

To illustrate the effectiveness of the developed modeling framework, eight test case problems are presented in this paper. Complete testing and validation of the model, using additional test cases, is detailed in Kumar (2009d).

5.4.1. 1D Infiltration Through Layered Soil

An unsaturated vertical flow experiment in a two-layered soil was used to verify flow behavior in the unsaturated zone. We compare the simulation result with analytical solutions obtained by Srivastava and Yeh (1991). Exponential functional forms were used to denote the saturation pressure-head relations and conductivity curves in both the layers as shown in Eq. [5.31].

$$K(\psi) = K_s e^{\alpha\psi} \quad \text{and} \quad S = e^{\alpha\psi} \tag{5.31}$$

where K_s is saturated hydraulic conductivity and α is a soil pore size distribution parameter. The α of the two layers is set to be equal to 0.1/cm, and K_s for the lower and upper layers are equal to 1 and 10 cm/hr respectively. The thickness of each layer is 100 cm. θ_r and θ_s (residual and saturated moisture contents respectively) are taken as 0.06 and 0.4 respectively. The domain is discretized into 200 prismatic layers of 1 cm thickness each. Initial pressure distribution in the two layers corresponds to the steady state infiltration profile when a constant flux is applied at the soil surface and a prescribed pressure is maintained at the lower boundary. Solutions are obtained for wetting and drying cases to test the robustness of the model. During wetting scenario, the

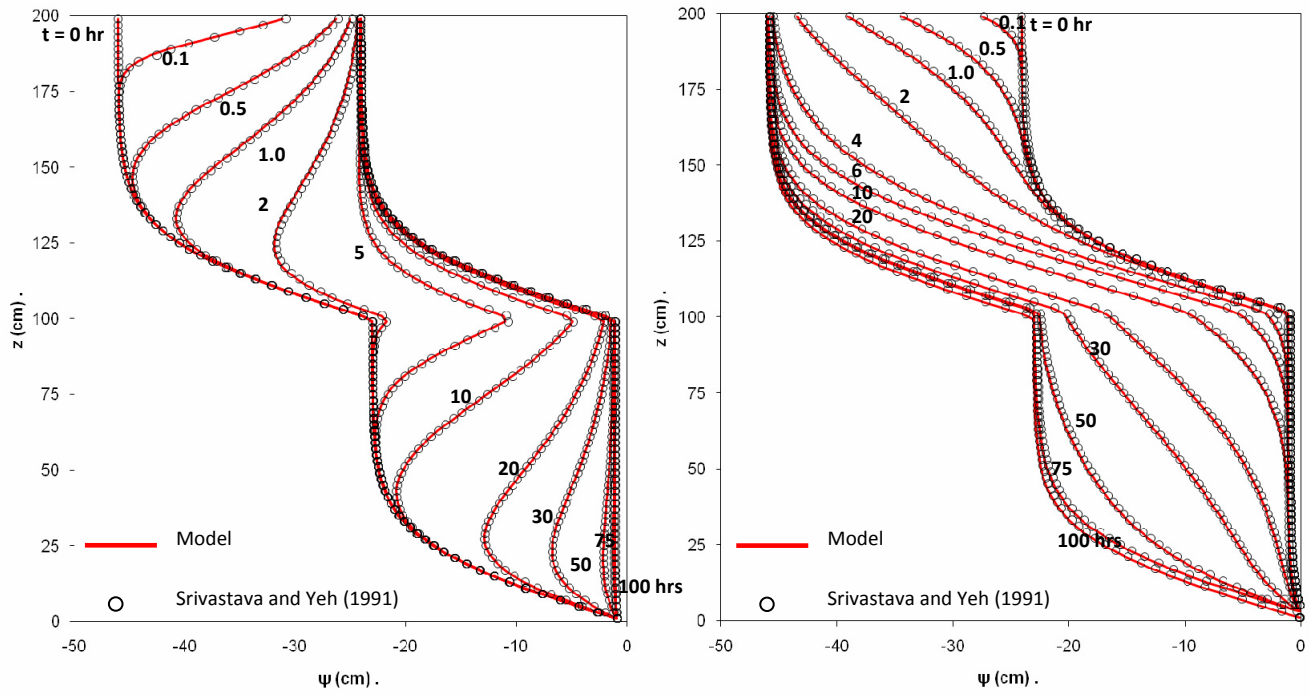

Figure 5.5 Wetting (left) and drying case (right) cases for an infiltration experiment in a layered soil based on Srivastava and Yeh (1991).

infiltration rate (constant flux at the top of soil column), initially equal to 0.1 cm/hr, is suddenly increased to 0.9 cm/hr at the start of simulation, while for the drainage scenario, it is decreased from an initial value of 0.9 cm/hr to 0.1 cm/hr. Figure 5.5 shows calculated pressure head distributions at selected times during the infiltration event as computed with the analytical equation derived in Srivastava and Yeh (1991) and the numerical model presented in this paper. We note that in both the cases, infiltration starts in the upper, high conductivity layer. Once the wetting front reaches the top of the less conductive layer, the pressure head at the interface increases rapidly to translate the flux and maintain mass balance. An excellent match between numerical and analytical models is observed.

5.4.2. 2D Variably Saturated Flow

The variably saturated formulation in the numerical model is verified by simulating the water table elevation in a transient, two-dimensional, constant recharge setting. The experiment has been presented by Vauclin et al. (1979) and was also used by Clement et al. (1994) to verify their two-dimensional variably saturated model. The model domain consists of a rectangular soil slab 6 m long, 2 m high and 0.05 m thick. The initial water table is set at 0.65 m. At the soil surface, a constant flux of 0.14791 m/hr is applied over a width of 1.00 m in the center, while rest of the top surface is covered to prevent any evaporative loss. Taking advantage of the symmetry of the domain, for computational efficiency only the right side of the domain is modeled. This translates to a left boundary having a no-flow property and the constant flux application of 0.14791 m/hr in the left 0.50 m of model domain. The water level at the right side boundary is maintained at 0.65 m during the simulation. The soil hydraulic condition in the entire domain was defined according to van Genuchten (1980) model as fitted by Clement et al. (1994). The saturated hydraulic conductivity is 0.35 m/hr and the saturated and residual moisture contents are equal to 0.3 and 0.01 respectively. Van Genuchten model parameters α and n are equal to 3.3 m and 4.1 respectively. The domain is discretized into 1200 prismatic elements with a uniform vertical resolution of 0.05 m. The simulated water table elevations at selected times after the start of recharge are shown in Figure 5.6. An

excellent agreement between the model results and the experimental observations is noted.

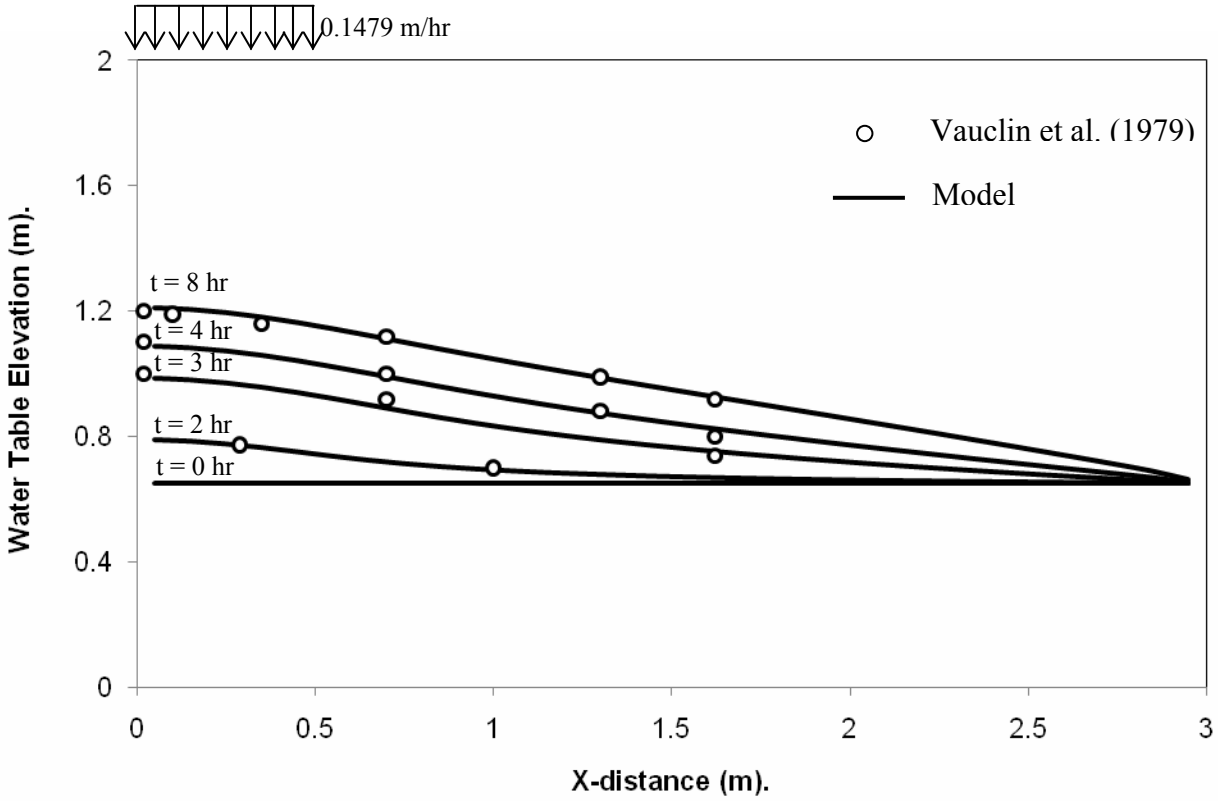

Figure 5.6 Simulation of water table increase due to recharge in a homogenous, 2D variably-saturated soil column

5.4.3. Pumping in 3D Homogeneous Orthotropic Domain

Verification of the 3D variably saturated component in the numerical model was performed by comparing pumping test results in an artificial, asymmetric and orthotropic domain to results obtained by 3DFEMWATER (Yeh and Cheng, 1994). The domain is cuboidal in shape with dimensions of 72 m (in z) by 800 m (in y) by 1000 m (in x) as shown in Figure 5.7. The pumping well is located at (x, y) = (540, 400 m). Initially the whole domain is in hydrostatic equilibrium with total head being 60 m everywhere. The top, bottom, front and rear extremes of the domain are no-flow boundaries while the head on the left and right boundaries is held constant at 60 m. For the time of simulation, the

head at the well is lowered and maintained at a height of 30 m. As a result, the water table profile changes continuously till the system reaches steady-state. The soil is

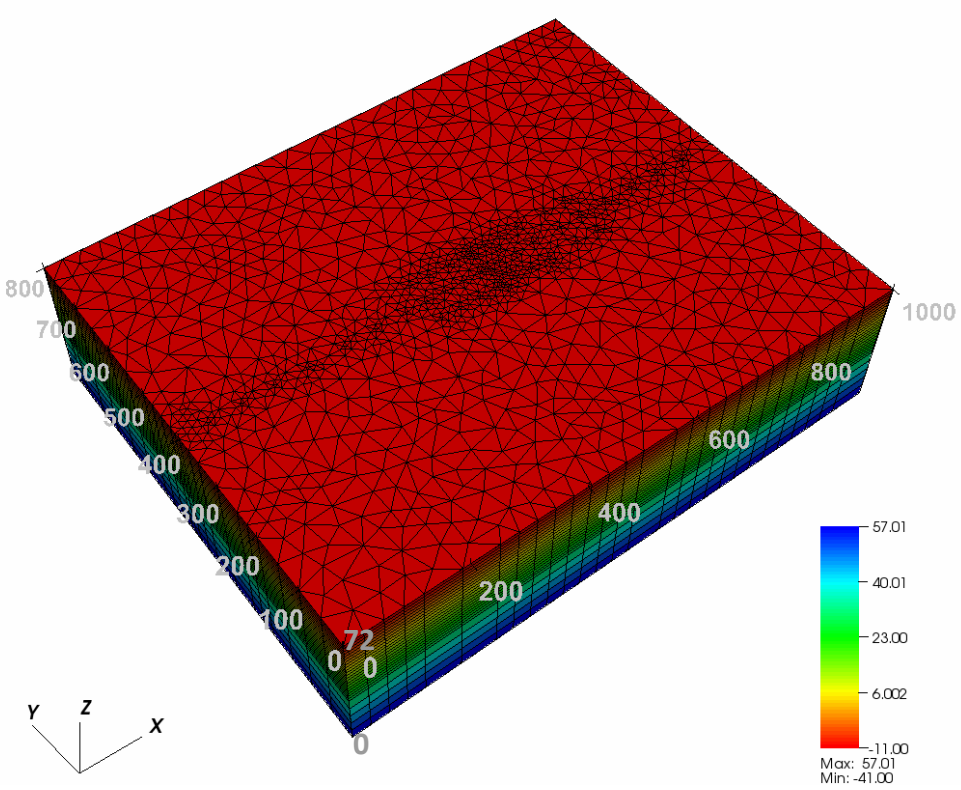

Figure 5.7 Initial head distribution for a 3D well pumping experiment in an orthotropic media. The well is located at (x, y) = (540, 400 m). The domain is discretized into 67522 prismatic elements. Finer discretization along x-z plane passing through the well was utilized to compare the results with existing solutions.

anisotropic with saturated hydraulic conductivity components in x, y and z directions being equal to 5 m/d, 0.5 m/d and 2 m/d respectively. The porosity, θ_s, and residual moisture capacity, θ_r, of the medium are equal to 0.25 and 0.0125 respectively. The moisture content, unsaturated conductivity and head are related through a variant of the van Genuchten equation as shown below

$$\theta = \theta_r + \frac{\theta_s - \theta_r}{1 + (\alpha|\psi_a - \psi|)^{\beta}} \qquad K_r = \left(\frac{\theta - \theta_r}{\theta_s - \theta_r}\right) \tag{5.32}$$

where ψ_a is air entry pressure and β and $\alpha_.$ are potentiometric parameters. The values of ψ_a, β, and $\alpha_.$ are 0, 0.5 and 2.0 respectively. The specific storage was assumed to be zero. The model domain was discretized into 2597 elements horizontally and 26 layers vertically. Top 21 layers were of thickness 2 m while the remaining five were of thickness 6 m each. This dichotomy in discretization coincided with the height of well head (30 m from the bottom). The steady state solution was also obtained for a horizontally isotropic case too by considering conductivity along the y-axis to be equal

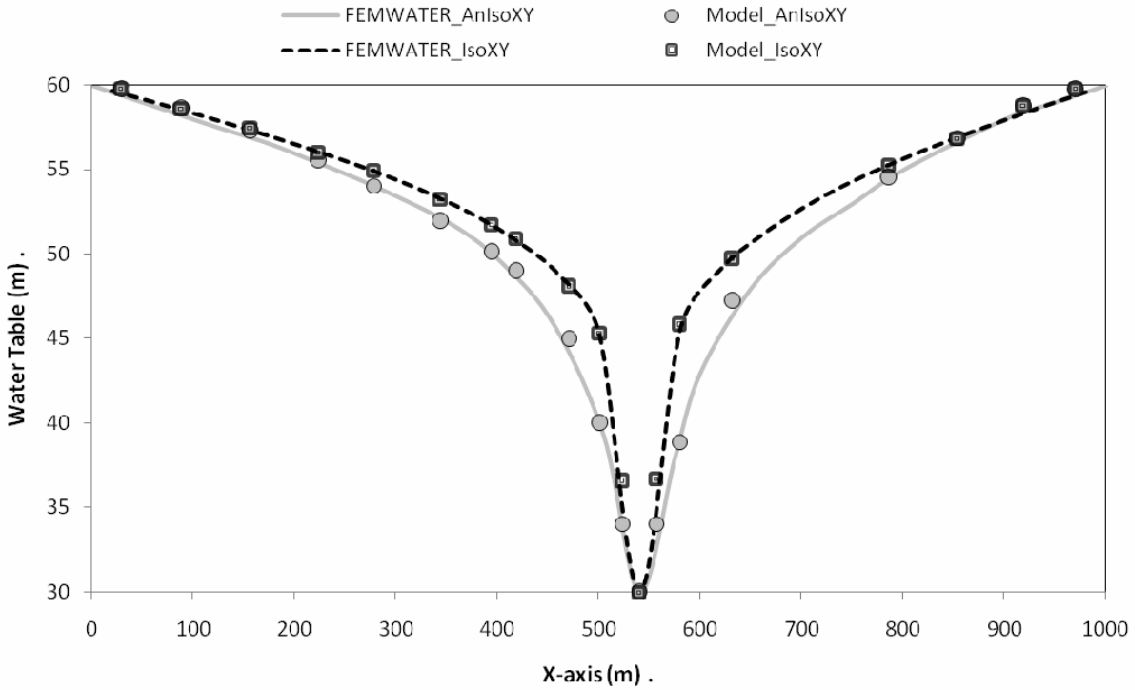

Figure 5.8 Water table drawdown at steady state in an orthotropic media.

that along the x-axis, 5m/d. Modeled water table elevations were compared with the results obtained from 3DFEMWATER (Yeh and Cheng, 1994) along a cross-section in the x-z plane passing through the center of the well. An excellent match between the two results is observed and is shown in Figure 5.8. In the second case, the larger hydraulic conductivity in the y-direction impacts the cone of depression that develops in the x-direction as well, with less drawdown occurring at a given location. This experiment verifies the conceptualization of 3D variably saturated flow in presence of constant head (at the well and at the left and right extremes) and no-flux (at the top and bottom extremes) boundary condition in an orthotropic media. We further explore the effect of

anisotropy on variably saturated flow a) when principal directions of anisotropy are not aligned with model domain orientation and, b) in a heterogeneous, anisotropic domain in the next two sections.

5.4.4. Flow Modification Due to Phase Shifted Anisotropy

In an anisotropic domain with principal axes direction not being coincident with the direction of maximal gradient, the resultant flux vector gets oriented in a new direction. Additionally, if the model grid coordinates are not oriented in the principal axes direction, numerical simulation for the flux necessitates proper resolution of each flux component due to anisotropy. Flow modification due to the phase shift is explored further using a setup very similar to the one explained in the previous section. The properties of the model domain in this experiment are the same as those in the previous section unless specified otherwise. For computational efficiency, the aquifer's thickness was reduced to 2 m (in z) and vertical discretization was limited to one layer. The initial head in the model domain is set to 0 m. A reduced head of -30 m is maintained at the well location during the simulation. Two numerical experiments were conducted to observe the relative change in flow behavior. In the first experiment, the principal directions of saturated anisotropic conductivity (equal to 20 m/d and 0.5 m/d in horizontal and 2 m/d in vertical) are oriented along the grid coordinates. The second experiment has principal directions of horizontal conductivity oriented at a 30 degree angle to the model coordinates. The results of both simulations are shown in Figure 5.9. Due to the acute anisotropy, the potentiometric drawdown contours are elliptical and their major axis is oriented along the principal direction of anisotropy. Several other models (such as MODFLOW and ModHMS) are also able to simulate anisotropic flow in a homogeneous domain by avoiding cross-derivative terms through alignment of the model coordinate system along the direction of anisotropy. FIHM is unique in terms of its flexibility to simulate flow behavior in heterogeneous, anisotropic domain with multiple anisotropic zones. This is achieved by a) constrained domain decomposition of the heterogeneous domain such that each elemental volume is assigned a unique property only. The constrained unstructured meshes also preserve the boundaries accurately. b) a generic formulation of anisotropic

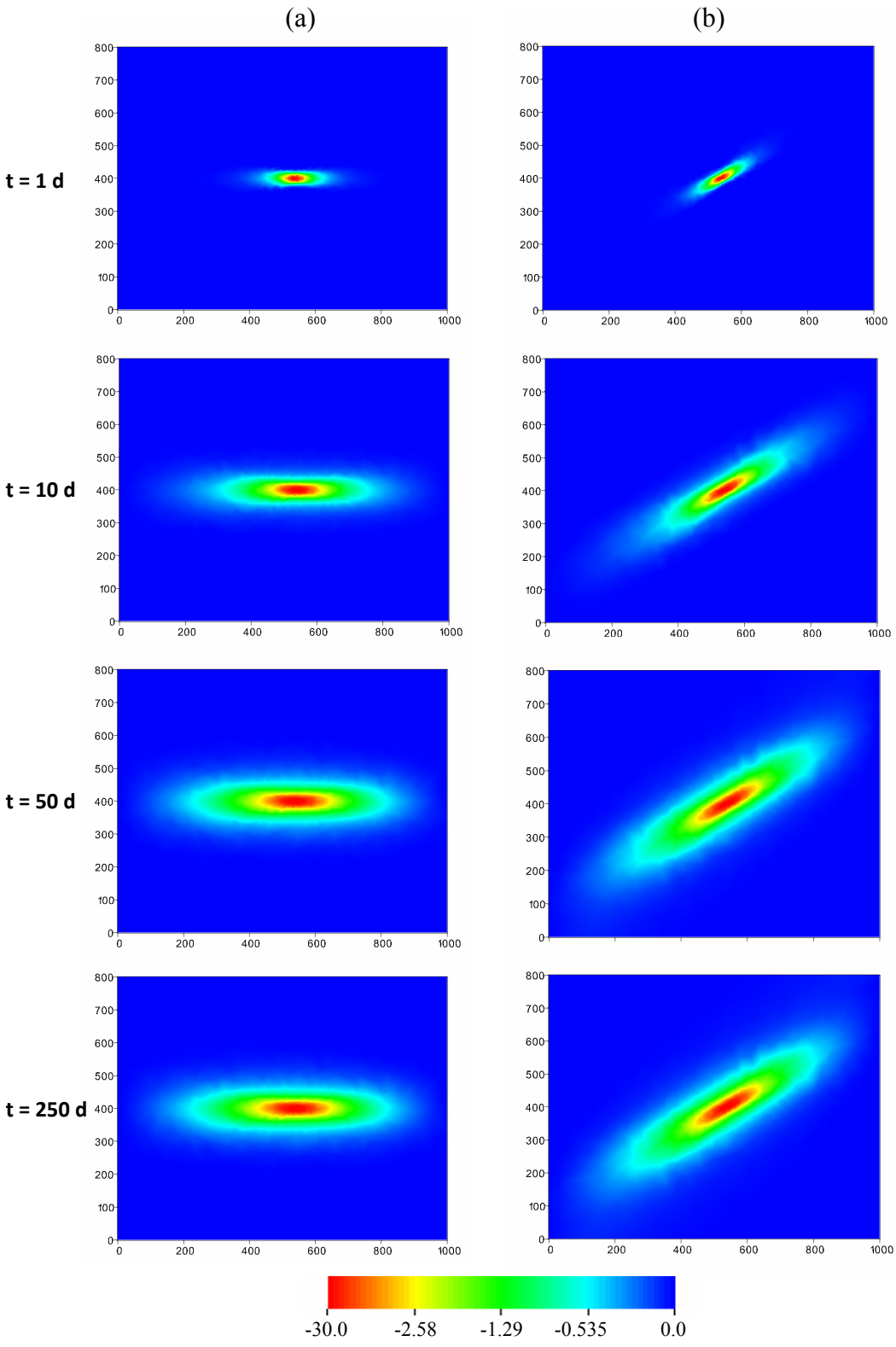

Figure 5.9 Transient well drawdown in an anisotropic domain with principal axis of conductivity a) oriented along the direction (x-y) of gradient due to specified head on left and right boundaries (equal to 60 m and 30 m, respectively), and b) oriented at 30 degrees angle to gradient direction. Note the rotation of the cone of depression along the principal direction of conductivity in case (b).

flux on arbitrarily oriented control volume faces. A representative simulation in heterogeneous, anisotropic domain is presented next.

5.4.5. Flow in Heterogeneous Anisotropic Domain

In this experiment we explore the flow behavior due to heterogeneity in conductivity and in anisotropy. The domain considered is a 1000 m (along x) by 800 m (along y) by 2 m (along z) cubical block. The conductivity, moisture content and saturation relations are the same as used in the previous experiment. The initial head in the model domain is set to 0 m. The top and bottom extremes of the domain are no-flow boundaries while the head on the left and right boundaries are held constant at 0 m and -30 m respectively. A rectangular subdomain of dimensions 200 m (along x) by 160 m (along y) by 2 m (along z) exists at the center of the experimental region. The domain is decomposed into 3948 prismatic elements. We note that subdomain boundary was used as a constraint in generation of Delaunay triangulations. Figure 5.10 shows the decomposed domain and the conductivity properties relevant to each region. Four setups were considered: a) soil properties in the rectangular subdomain are the same as in rest of the domain

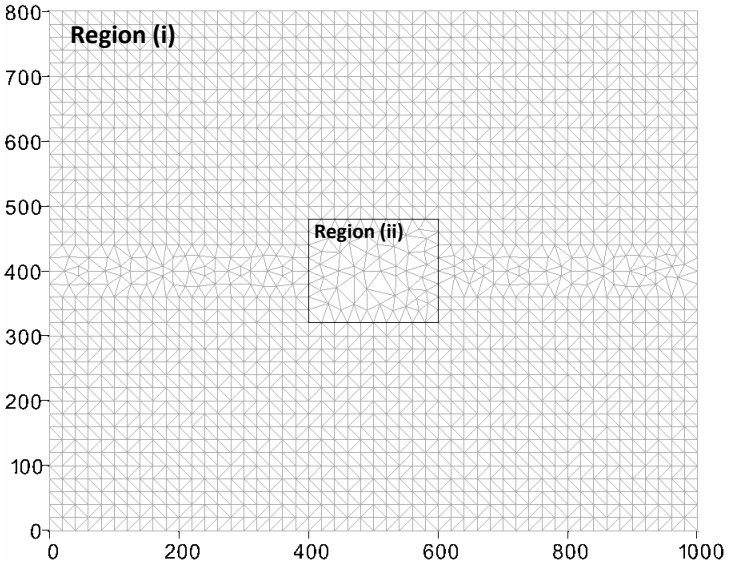

Case	Region (i)	Region (ii)
a	0.5 m/d, 20 m/d	0.5 m/d, 5 m/d
b	0.5 m/d, 20 m/d	0.5 m/d, 20 m/d, 45 ^{0}
c	0.5 m/d, - 45 ^{0}, 20 m/d	0.5 m/d, 20 m/d, 45 ^{0}
d		

Figure 5.10 Setup to study anisotropic heterogeneous flow. Four subsurface flow experiments were explored by setting the hydraulic conductivity and its orientation in region (i) and region (ii) to be different. The domain is discretized into 3948 prismatic elements. We note that boundary for region (ii) has been used as a constraint in generation of triangles.

(homogeneous, anisotropic); b) soil conductivity in the subdomain is different (lower) than in rest of the region, though the principal direction of conductivity is oriented along the model coordinates everywhere (heterogeneous, anisotropic); c) soil conductivity is

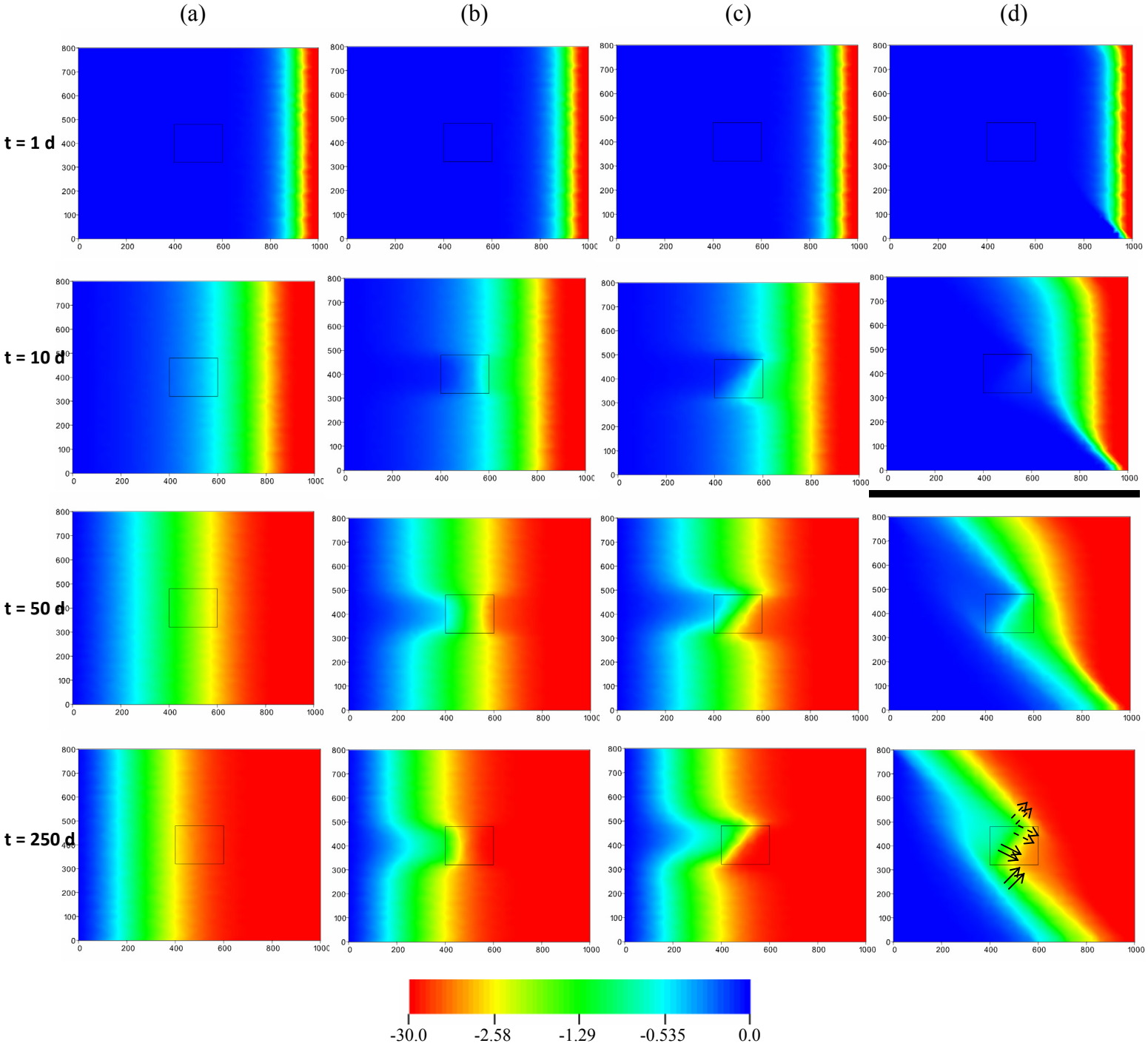

Figure 5.11 Transient subsurface flow in an anisotropic heterogeneous domain. The details regarding conductivity configuration for four cases considered are shown in Figure 5.10.

same everywhere in the region, however the principal direction of anisotropy in the subdomain is oriented at 45 degrees angle to the model coordinates (heterogeneous, phase shifted anisotropy) and d) similar to the case (c) though the principal direction of conductivity in rest of the domain is oriented at 135 degrees to positive x direction.

Results of simulation for each case are shown in Figure 5.11. Figure 5.11(a) shows a uniform variation in head from left to right boundaries. Due to the introduction of heterogeneity by a low conducting rectangular subdomain, the contour intervals within the subdomain are contracted (Figure 5.11(b)). This is expected as the larger head gradient in the subdomain ensures mass balance even though its conductivity is lower than rest of the domain. Figure 5.11(c) shows the modification of head due to the change in principal axes orientation of anisotropy in the subdomain. The head contours inside the subdomain are oriented in direction of preferred conductivity, at an angle of 45 degrees clockwise to the x-axis. Figure 5.11(d) shows a more complex case with the anisotropy in the rest of the domain being rotated in a counter-clockwise direction such that the principal axes of anisotropy in the two regions are orthogonal to each other. This leads to formation of convergence (at the lower interface of subdomain) and divergence (at the upper interface of subdomain) zones in the flow domain. This is particularly significant and shows how preferred conductivity directions might affect the contaminant mixing/spreading in a region.

5.4.6. Transient 3D Variably Saturated Flow

The numerical model was validated using data from an unconfined sand aquifer pumping test performed by Nwankwor et al. (1984). The 9 m thick aquifer is assumed to be in hydrostatic equilibrium at the start of pumping test, with total head everywhere being equal to 6.7 m. The pumping well has an inner diameter of 0.15 m with a 4 m screen located at the bottom of the aquifer. The discharge rate of 60 l/ min was maintained during the entire test which lasted 1440 mins. Head values were measured using piezometers, tensiometers and gamma access tubes installed at different radial distances from the pumping well (Nwankwor et al., 1984, 1992). The saturated conductivity of the sand aquifer was equal to 6.6×10^{-5} m/s in the horizontal direction and 4.2×10^{-5} m/s

vertically. The specific storage, S_s, of the aquifer is 3.2 x 10^{-4} /m while the porosity and residual moisture content of the sand were equal to 0.37 and 0.07 respectively. The moisture content and potentiometric head are related through the van Genuchten model (1980) as shown below

$$\theta = \theta_r + \frac{\theta_s - \theta_r}{(1 + (\alpha|\psi|)^n)^{1-1/n}} \tag{5.33}$$

where α = 1.9/m and n = 6.095 respectively. Unsaturated conductivity, $K(\theta)$, and moisture content, θ, were related through

$$K(\theta) = 0.007195\theta^{4.72} \tag{5.34}$$

Akindunni and Gillham (1992) observed that the drawdowns were insignificantly small beyond 70 m from the pumping well and so we conservatively set the external boundary

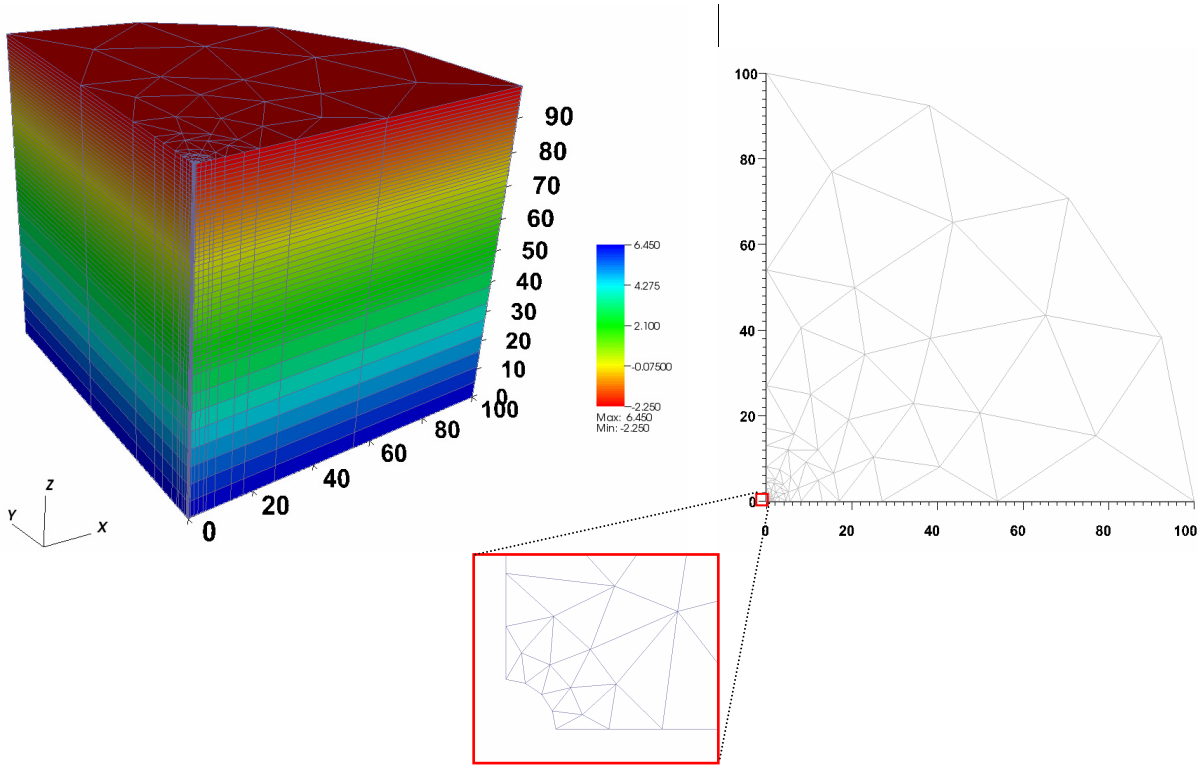

Figure 5.12 Setup for validation of 3D variably saturated flow using Nwankwor et al. (1996) experiment. Due to symmetry, only one-quarter of the domain has been simulated. The initial conditions with the water table elevation in the aquifer at 6.7 m from the bottom are shown. The domain was discretized into 6762 elements. Well has been simulated as constant flux boundary condition applied on the inner curvilinear boundary (shown in zoomed panel).

of the domain to be at a radial distance of 100 m from the well. All of this translates to a cylindrical model domain of dimension 9 m thick and an outer radius of 100 m. Taking advantage of the symmetry of the problem, for computational efficiency we simulated only a quarter of the domain as shown in Figure 5.12. The domain is discretized into a total of 6762 prismatic elements which includes 49 layers vertically. Variable discretization thickness was used with top 23 layers (in unsaturated zone) being 0.1 m thick, next 18 layers (until the start of well screen) being 0.15 m thick and remaining 8 layers were 0.5 m thick. The outer boundary was assigned no-flux boundary condition while the boundary condition at the well (see inset in Figure 5.12) was constant flux. The value of the flux through each element's edge was equal to the total flux divided by the percentage wall area. Figure 5.13a shows the simulated and observed drawdown curves at horizontal distances of 5 and 15 m from the pumping well and at the depth of 7 m from the surface. A good agreement between the field data and the model results is observed. We explored further to examine the significance of drainage processes above the water table on the drawdown response in unconfined aquifers. We find that the recharge gradient at the water table reaches its maximum value (Figure 5.13b) during the delayed response periods (Figure 5.13a). Figure 5.13b also shows that the increase in recharge (gradient) can be correlated with the "excess storage" when more water is stored above the water table relative to hydrostatic conditions due to the extension of capillary zone (Akindunni and Gillham, 1992)); during this period, capillary fringe thickness (at 5 m distance) is observed to be as much as 5.6 % greater than prior to pumping. After the initial period of rapid drawdown (Figure 5.13a) and concurrent development of large vertical gradient (Figure 5.13b), drainage from the vadose zone reaches its maximum, yielding water to the well causing the drawdown curves to level off during the middle of the test. We also observe that the magnitude of the vertical gradient decreases with increasing distance from the well, suggesting that at large distances, flow is predominantly radial.

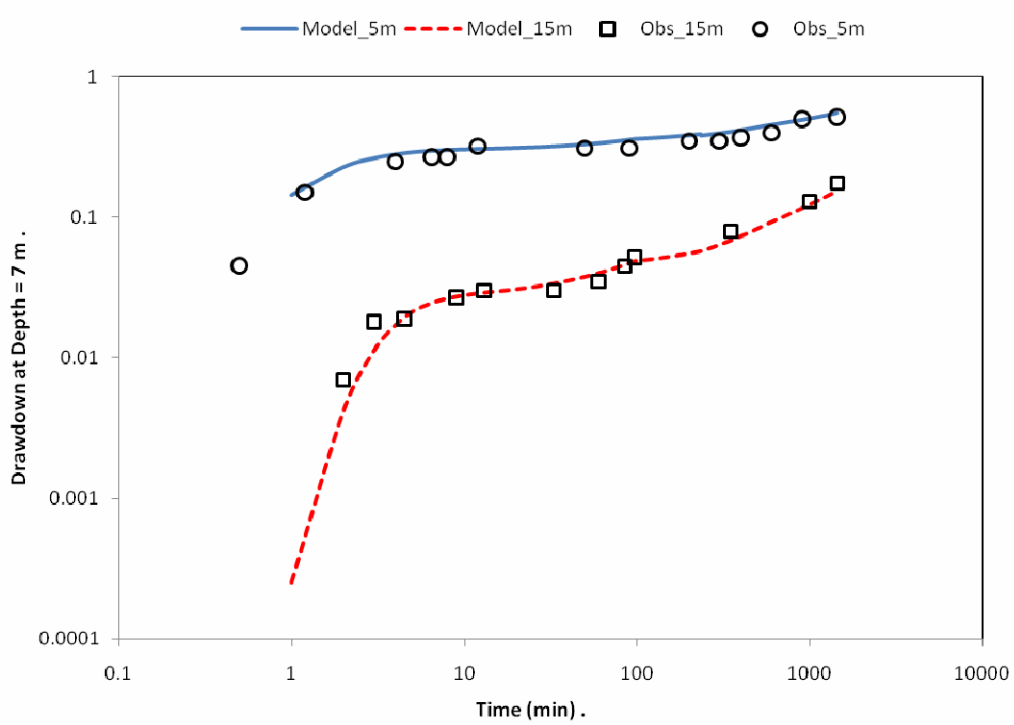

Figure 5.13a Drawdown (m) measured at depth 7 m from the land surface and at a radial distance of 5 and 15 m from the well casing. Observed data (Obs) were obtained from Nwankwor et al. (1996).

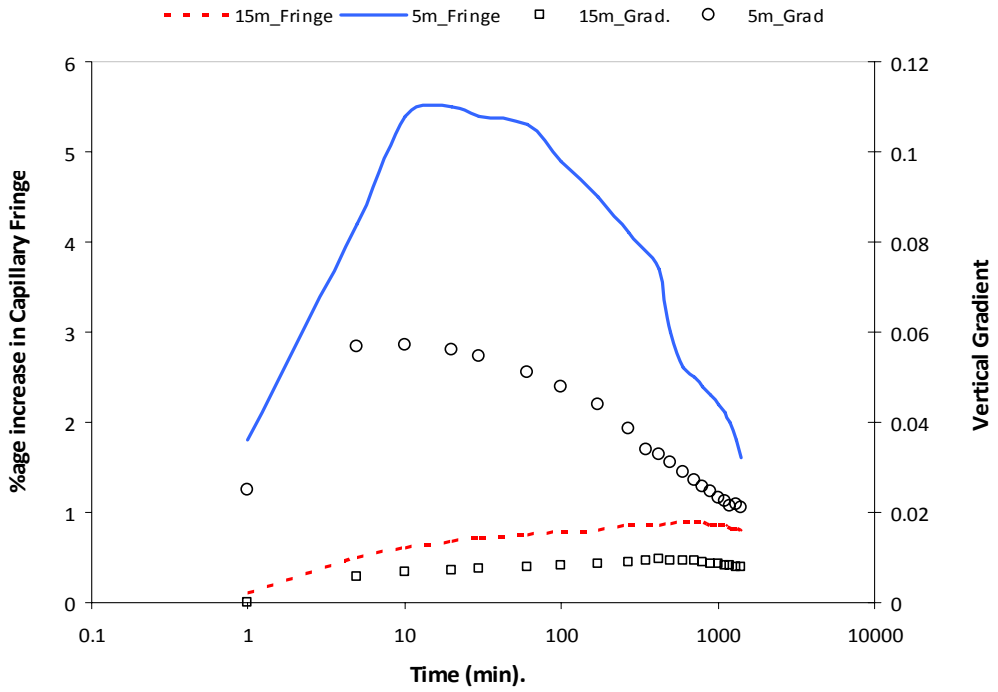

Figure 5.13b Extension of capillary fringe above the water table and the vertical gradient at the water table at distances 5 amd 15 m from the well axis. Delayed yield of water from the capillary fringe is observed at times with maximum vertical gradient at the water table.

5.4.7. 2D Overland Flow

The overland flow component in the model is verified using the rainfall-runoff example on a titled V-catchment as simulated by Di Giammarco et al. (1996) and VanderKwaak (1999). The problem setup is shown in Figure 5.14. Rainfall is simulated over the V-catchment for a 90 minute duration. The Manning's roughness coefficient on the slopes

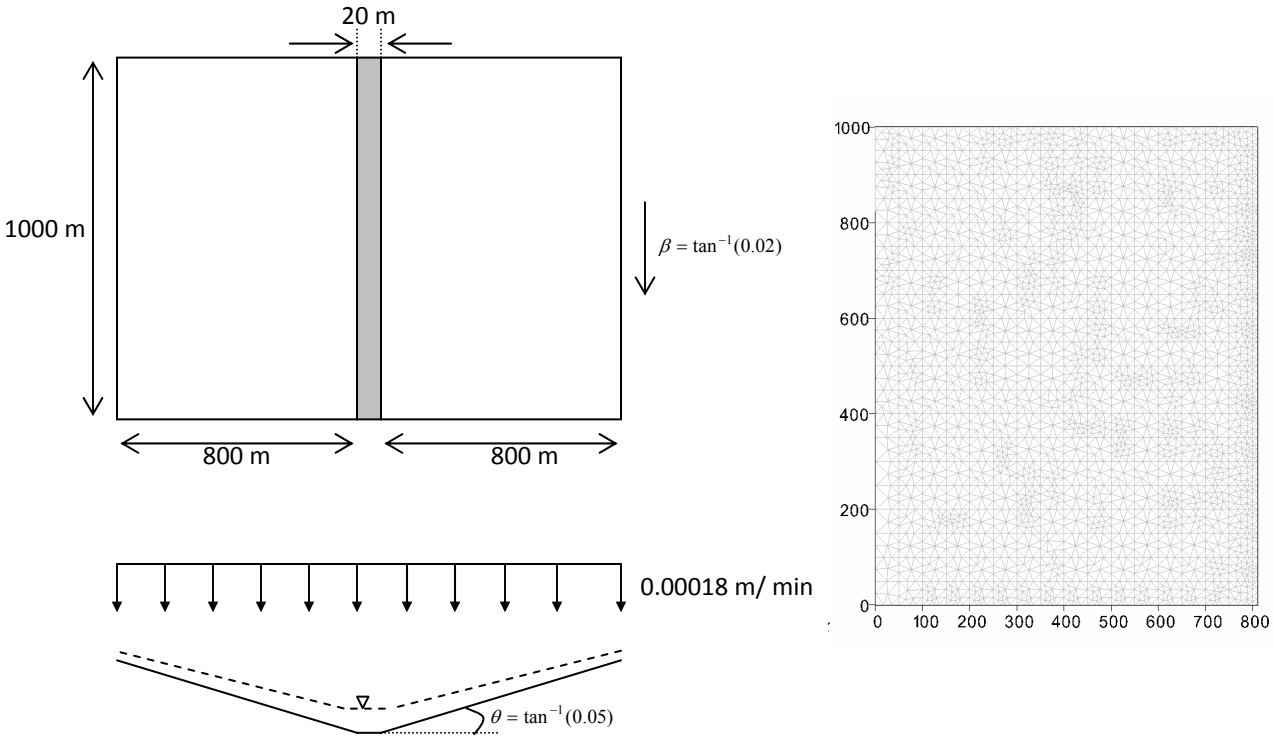

Figure 5.14 Setup for V-catchment experiment to verify overland flow. Taking advantage of the symmetry of the problem, discretization of the domain is performed only on the left half of the full catchment. 5777 cells were used in discretization.

and the channel are 0.015 and 0.15 respectively. Taking advantage of the symmetry of the problem, only one half of the domain is simulated. The domain is discretized into 5777 cells. Boundary conditions are no-flow except at the channel outlet where it is assumed to satisfy critical depth condition. We compare the simulated outflow hydrograph with the results obtained by ModHMS (Panday and Huyakorn, 2004), InHM (Vanderkwaak, 1999) and Di Giammarco et al. (1996). An excellent agreement with results from other models is observed in Figure 5.15. We also show the overland flow depth contours in the V-catchment at different times in Figure 5.16. The asymmetrical slope of the domain in x and y direction essentially controls the shape of contours.

Expectedly the change in water depths is faster along x-direction (larger surface slope) as evident by closer contours. At 90 min in the simulation, largest flow accumulation is seen in the channel region of the catchment. After the rainfall has stopped, the flow depth recedes from the catchment slopes.

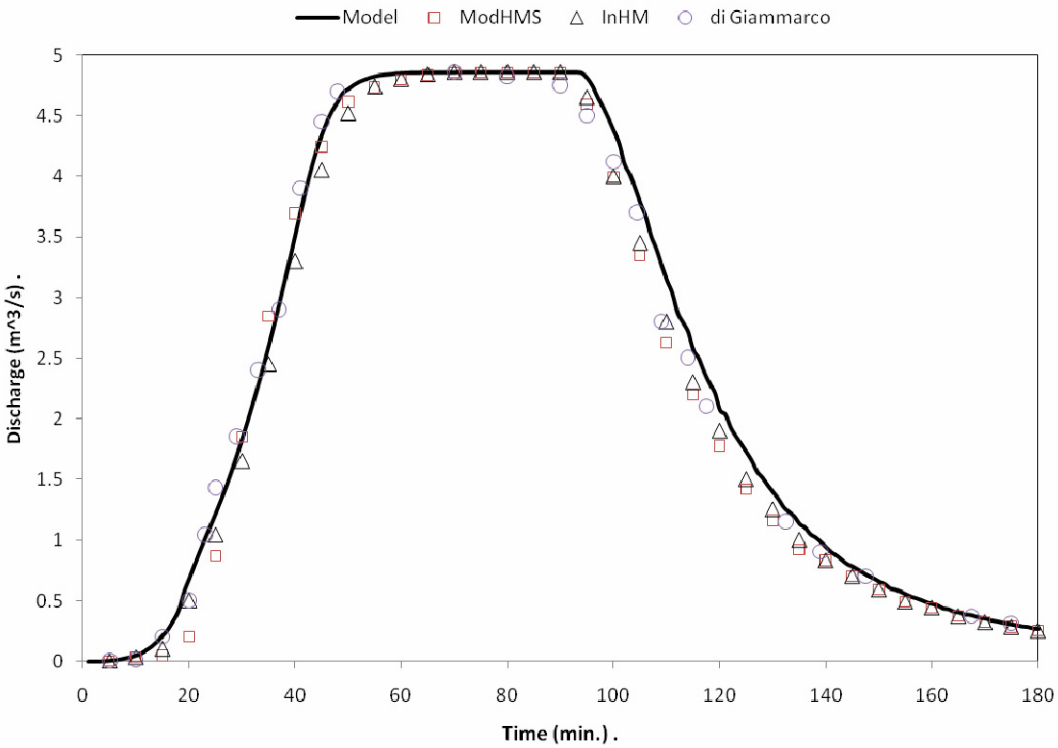

Figure 5.15 Outflow hydrograph obtained from the V-catchment experiment (di Giammarco et al., 1996).

5.4.8. Coupled Surface-Subsurface Flow

Validation of coupled surface-subsurface flow was performed by simulating a laboratory experiment performed by Abdul and Gilham (1984). The experimental setup consisted of a Plexiglass tank of dimensions 140 cm (along x), 120 cm (along z) and 8 cm (along y). The tank was packed with sand of porosity = 0.34 and van Genuchten parameters α and n for wetting and drying equal to 0.024/cm and 5, and 0.015/cm and 8 respectively. The saturated conductivity of sand was equal to 3.5 x 10^{-5} m/s while the average specific yield was determined to be 0.007 (Abdul and Gilham, 1984). Sand was packed in the tank such that it formed a sloping upper surface (slope = 12^{o}) with its toe at a height of 74 cm from the bottom. The initial water table was at 74 cm. Water was applied uniformly over the surface at a rate of 0.011945 cm/s for twenty minutes. A screened tube at the toe of the

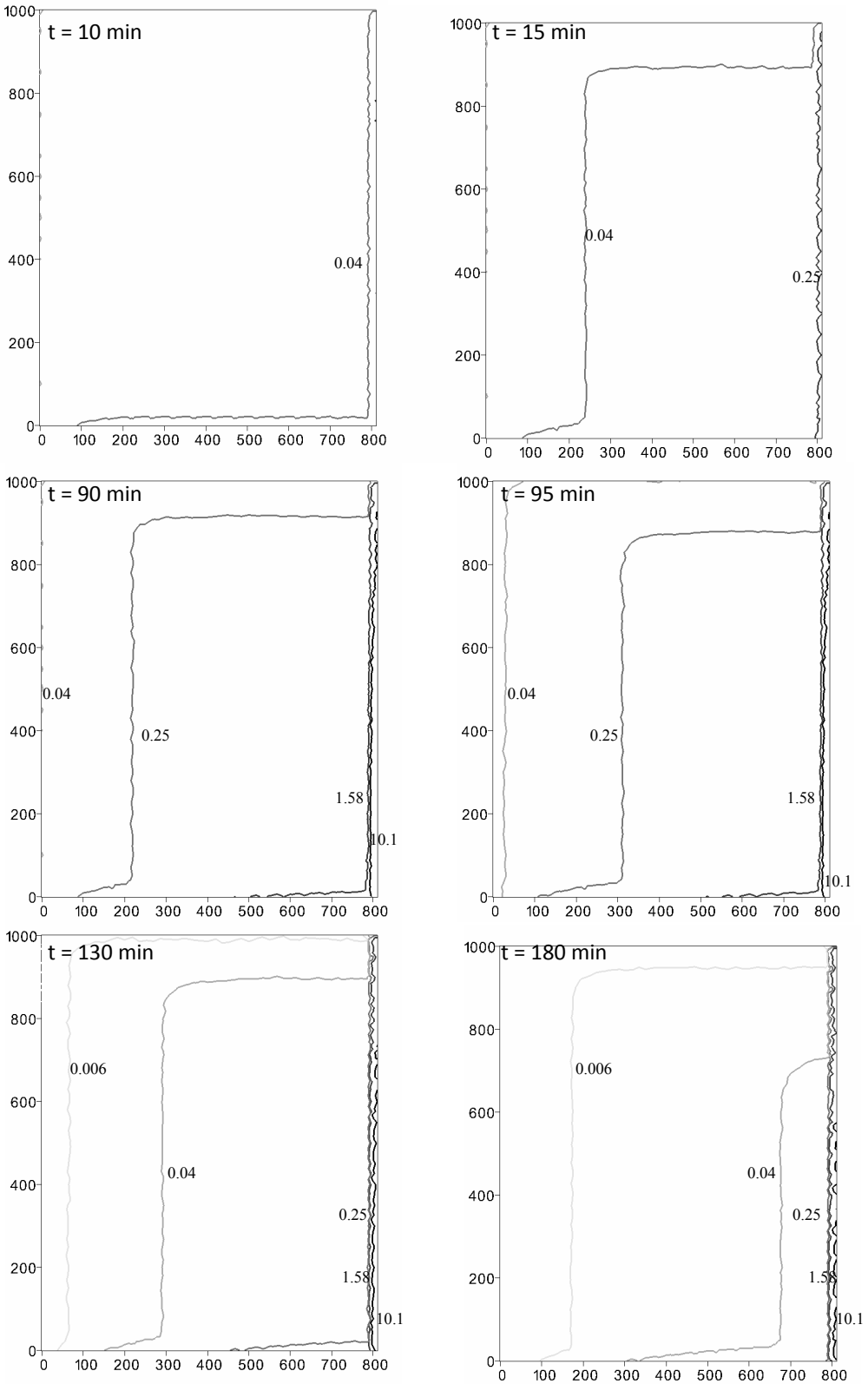

Figure 5.16 Transient overland flow depth contours (in cm) during the diffusion wave simulation on the V-catchment. Large overland flow depth is consistently observed in the channel section of catchment into which all the water ultimately drains.

slope collected generated outflow. We discretized the domain into 25 layers, with the bottom six layers being of thickness 10 cm each, followed by a transition layer of thickness 5 cm and then 19 prismatic layers of uniform thickness until the top. Laterally the domain was discretized into 140 elements (shown in Figure 5.17). Boundary conditions on all sides are no-flux except at the surface outlet where it is considered to follow a critical head condition. Figure 5.18 shows the outflow hydrograph simulated by InHM (VanderKwaak, 1999) and FIHM for the given experimental settings (Base case), and from the observations (Abdul and Gilham, 1984). The hydrograph shape and the

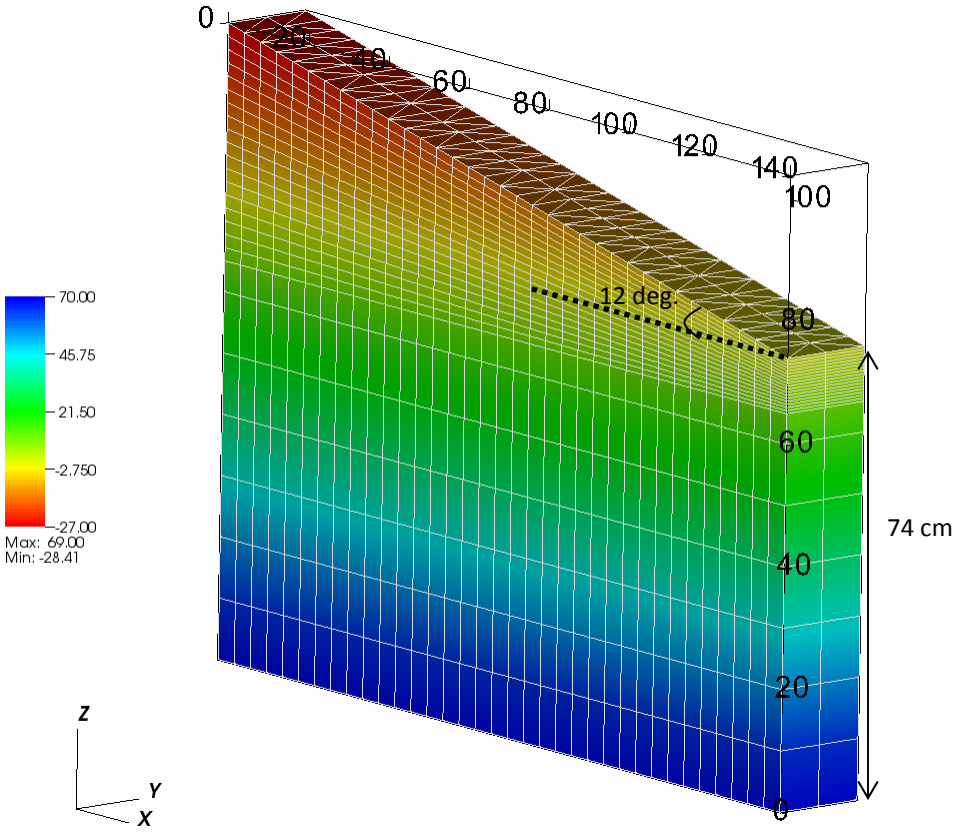

Figure 5.17 Setup to study surface-subsurface flow generation using plexiglass soil column as presented in Abdul and Gilham (1984). The soil column is initially in hydrostatic equilibrium with the water table at an elevation of 74 cm from the bottom.

peak magnitudes simulated by FIHM are consistent and closely match the observations, with a transient steady state condition obtained after approximately 270s. We note that the FIHM simulation better captures the ascending and the receding limb of the hydrograph

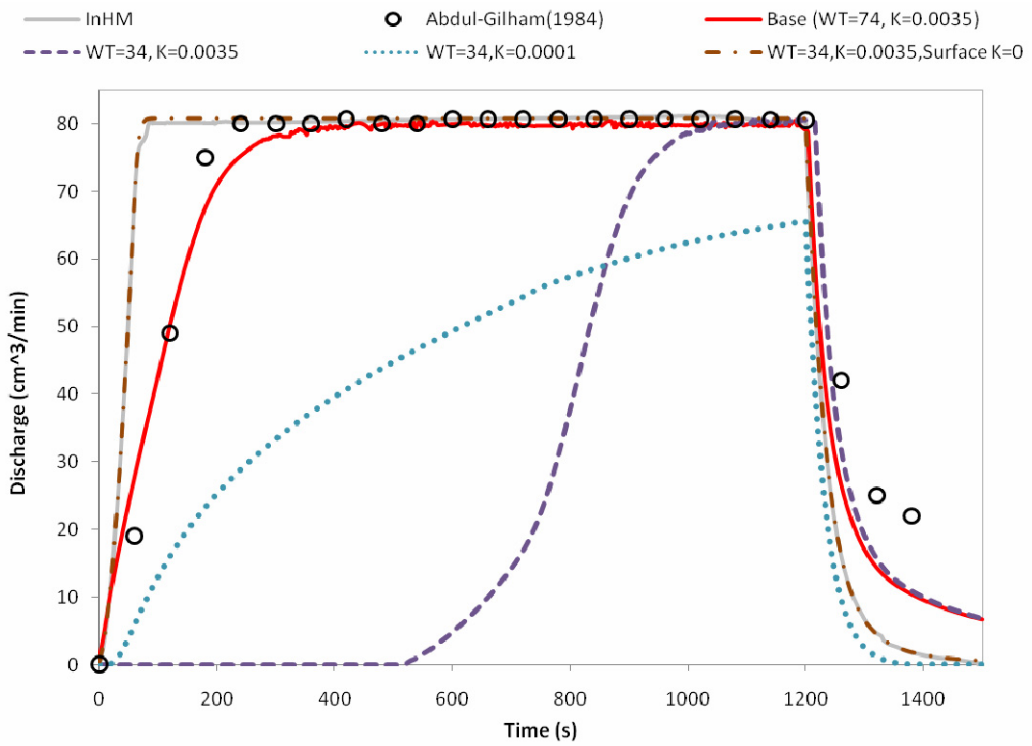

Figure 5.18 Streamflow hydrograph generated at the outlet of soil column in surface-subsurface coupling experiment by Abdul and Gilham (1984). Base case correspond to hydrograph simulated by FIHM (Case I) where initial water table was set at 74 cm. Three more experiments were conducted to study surface-subsurface coupling. In Case II, initial water table was set at 34 cm. Case III has the same settings as Case II with reduced conductivity of 0.0001 cm/s. Case IV has similar setting as Case II but the surface was made impermeable.

than InHM. Figure 5.19 and Figure 5.20 show that during the initial 1200 s of simulation (time for which water is applied on the surface), infiltration occurs on the upper portion of the hillslope at the same rate as precipitation. Concurrently, as the subsurface head builds up near the toe of the hillslope, groundwater exfiltrates and contributes to the surface flow hydrograph. The portion of the hillslope discharging groundwater to the surface increases from the lowest few cm initially, to approximately 45% of the total hillslope during peak outflow. Even in uphill areas where initial water table is deeper, quick groundwater response is observed due to the extended capillary fringe (almost 35 cm thick above the water table) which translates to an unsaturated zone with little storage capacity. We note that during the period of peak outflow, the exfiltration rate at the toe of the hillslope is higher than the infiltration rate anywhere on the surface. After the precipitation is stopped, the remaining overland flow on the hillslope drains down while

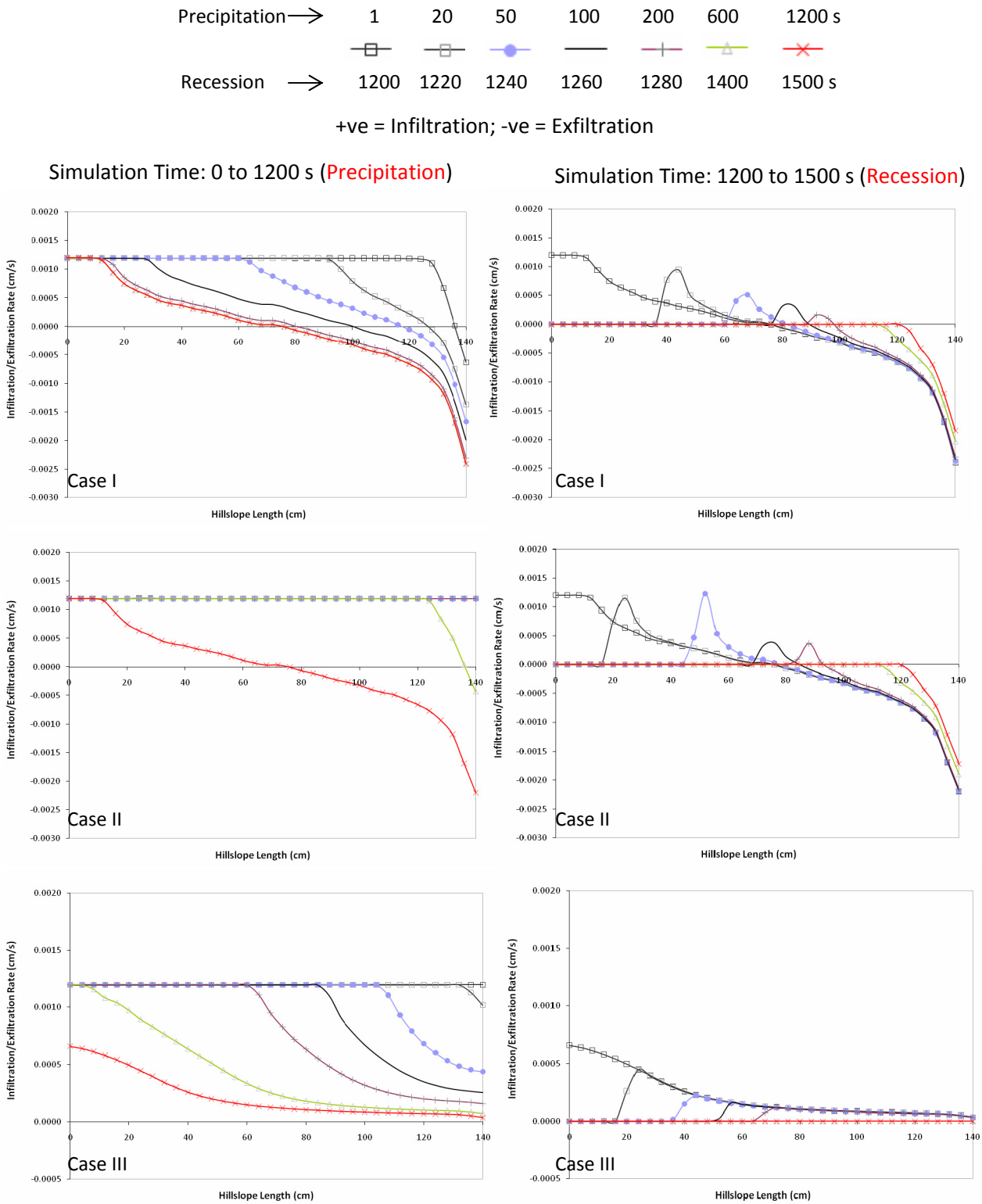

Figure 5.19 Infiltration/Exfiltration rate along the length of the hillslope. Four experiments each highlighting the influence of capillarity (Case I), initial water table height (Case II), conductivity and infiltration excess runoff (Case III and IV), along with topography were conducted to study the coupling between surface and subsurface processes. Case IV has zero infiltration/exfiltration rate at all times

the unsaturated zone desaturates. Infiltration ceases to occur on the upper portion of the hill, while exfiltration continues at the toe. The infiltration rate peaks at the junction between dry-overland and desaturated-subsurface, which shifts downhill as the recession proceeds. Region upslope of the infiltration peak is dry-overland, which results in zero infiltration rates. As we move downslope from the infiltration peak, both overland flow depth and potentiometric head in the underlying subsurface layer increases. However, the rate of increase of overland flow depth lags behind rate of increase of subsurface head. This leads to decrease in infiltration rate as we move down along the hillslope transect. The infiltration/exfiltration curve recedes towards a new equilibrium as the time progresses. We note that during recession (see Figure 5.20), hillslope area that exfiltrates exceeds that of infiltration.

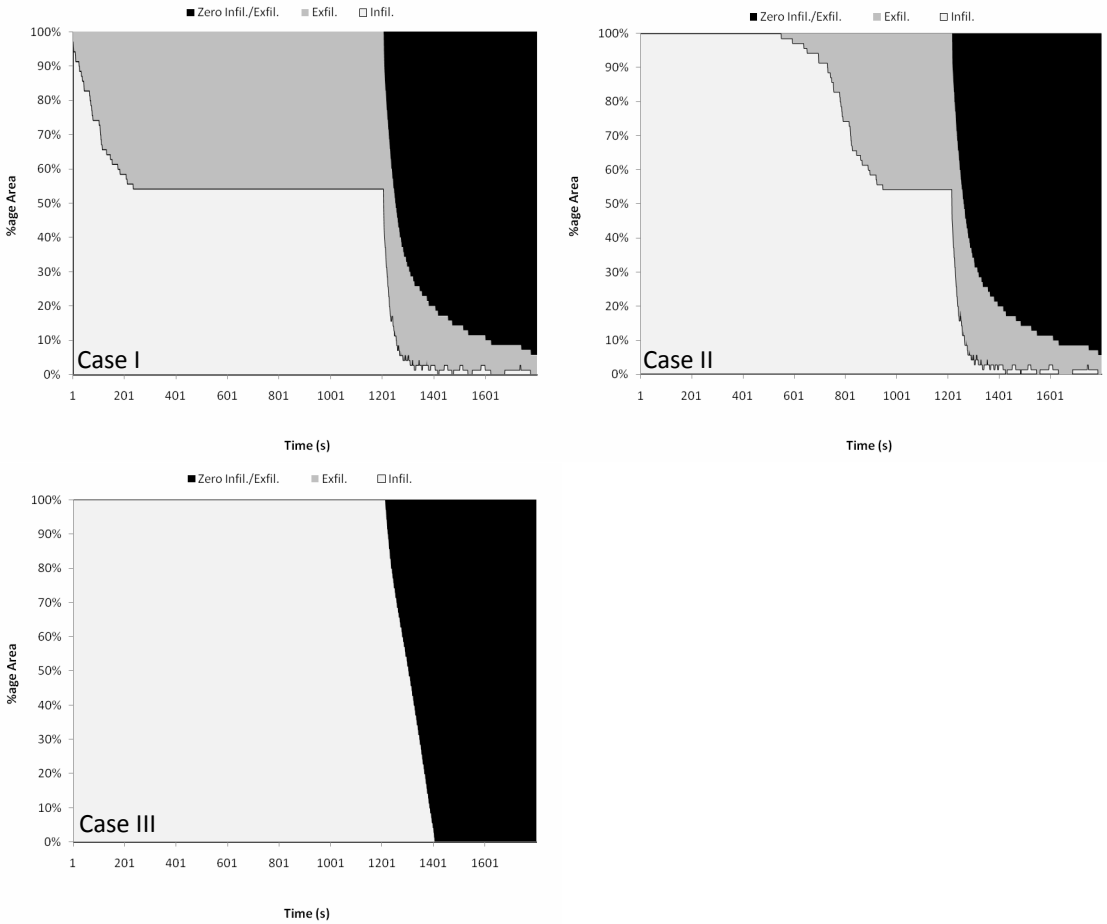

Figure 5.20 Temporal evolution of the percentage area of the hillslopes that contribute to infiltration and exfiltration for the three cases shown in Figure 5.19. Case IV has no area that infiltrates/exfiltrates during the simulation.

In order to explore the influence of initial water table (and hence the capillary zone that extends 35 cm above the water table) on runoff generation, we simulate the previous experiment (Case I) with a reduced initial water table height of 34 cm (40 cm lower than in last experiment, Case II). We note from the hydrograph in Figure 5.18 and from Figure 5.20, that for the initial 552 s, all the water applied to the hillslope infiltrates. Negligible infiltration-excess overland flow is produced and the infiltrated water contributes to increase in water table. Once the hillslope surface starts saturating, it results in generation of saturation-excess overland flow on the lower portion of the slope. Next we reduced the conductivity of the hillslope from 3.5×10^{-5} m/s to 1.0×10^{-7} m/s (Case III) in order to study the effect of physiographic properties on runoff generation. The reduced conductivity resulted in generation of infiltration-excess overland flow, right from the start of the simulation (see Figure 5.18). Because of the lower conductivity, the rate of water table increase is slower and so the surface of the hillslope never saturates. However, the persistent increase in subsurface saturation during this period (first 1200 s) still influences the infiltration rate. We observe from Figure 5.19 that infiltration rate decreases monotonically towards the toe of the hill slope where a higher subsurface saturation is expected. In the last experiment (Case IV), we used the experimental settings similar to Case II, with the only change being setting the top surface conductance to be equal to zero (impervious). As expected, the outflow produced in this case is entirely due to infiltration-excess runoff, as neither infiltration nor exfiltration can occur along the hillslope. The corresponding hydrograph is shown in Figure 5.18. This set of coupled surface-subsurface experiments show that vadose zone capillarity, initial position of groundwater table, soil properties and topography play important roles in the generation of surface runoff. The infiltration to the groundwater is observed to be equally dependent on these critical flow, material and topographic parameters.

5.5. Conclusions

A second-order accurate, finite volume framework to understand and predict coupled surface and subsurface flow is presented. The model simulates a full three dimensional solution for saturated–unsaturated flow in the subsurface and a two- dimensional solution

for overland runoff on the surface. Using a set of eight experiments we show the influence of soil heterogeneity, anisotropy and topography on the distribution of moisture above and below the ground surface. The capability of the integrated model to simulate flow behavior in heterogeneous, anisotropic materials showed the possible development of unique, local "flux rotation" phenomena. The experiments also underscore the degree to which detailed coupled surface-subsurface physics can be studied, such as where runoff generation and infiltration become closely coupled to underlying groundwater levels and adjacent surface water states. The model takes advantage of constrained Delaunay triangulation for domain decomposition, which is also supported by a "shared data model", leading to accurate representation of data and fast prototyping of model experiments. The test cases presented were chosen not only to compare individual model components against classical examples from the literature (e.g. 1-D unsaturated flow or 2-D surface flow), but to further examine the degree to which individual unsaturated-saturated zone flow or surface-subsurface processes are affected by each other. Representative experiments explored in detail the influence of drainage from unsaturated zone on delayed water table drawdown, the role of water table position on infiltration and surface runoff, and the interaction of overland flow-groundwater exchanges in relation to the dynamics of infiltrating/exfiltrating surfaces on the hillslopes. The authors intend to publish the details of all test cases with the journal article to provide a future resource for open-source community modeling and testing.

5.6. References

Abdul, A.S., and R.W. Gillham. 1984. Laboratory studies of the effects of the capillary fringe on streamflow generation. Water Resour. Res.;20(6):691–8.

Akindunni, F. F., and R. W. Gillham. 1992. Unsaturated and saturated flow in response to pumping of an unconfined aquifer: Numerical investigation of delayed drainage. Ground Water, 30(6), 873–884.

Barrash, W., and M.E. Dougherty. 1997. Modeling axially symmetric and nonsymmetric flow to a well with MODFLOW, and application to Goddard2 well test, Boise, Idaho. Ground Water; 35(4):602–11.

Bermúdez and Vázquez, 1994. Upwind methods for hyperbolic conservation laws with source terms, Comput. Fluids 23 (8), pp. 1049–1071.

Bertolazzi, E., and G. Manzini. 2004. A cell-centered second-order accurate finite volume method for convection–diffusion problems on unstructured meshes, Math. Mod. Meth. Appl. Sci. 8, 1235–1260.

Blazek, J., 2001, Computational Fluid Dynamics: Principles and Applications, Elsevier Science.

Brooks, R.H., and A.T. Corey. 1966. Properties of porous media affecting fluid flow. Journal of Irrigation Drainage Division, v. 92 (IR2), p. 61–88.

Clement, T. P., W. R. Wise, and F. J. Molz. 1994. A physically based, two-dimensional, finite-difference algorithm for modeling variably saturated flow. J. Hydrol., 161, 71–90.

Di Giammarco, P., E. Todini, P. Lamberti. 1996. A conservative finite elements approach to overland flow: the control volume finite element formulation. J Hydrol; 175(1–4):267–91.

Discacciati, E.M.M., and A. Quarteroni. 2002. Mathematical and numerical models for coupling surface and groundwater flows. Appl. Numer. Math. 43, 57–74

Fiedler, F.R., and J.A. Ramirez. 2000. A numerical method for simulating discontinuous shallow flow over an infiltrating surface, International Journal for Numerical Methods in Fluids, 32(1).

Frink, N. T. 1994.Recent progress towards a three-dimensional unstructured Navier–Stokes flow solver, AIAA Pap.94-0061.

Frink, N. T., and S. Z. Pirzadeh. 1998. Tetrahedral finite-volume solutions to the Navier–Stokes equations on complex configurations, in Proc. 10th International Conference on Finite Elements in Fluids, Tucson, AZ.

Gottardi, G., and M. Venutelli. 1993. A control-volume finite-element model for two-dimensional overland flow. Adv Water Resour ;16:277–84

Graham, D.N., and A. Refsgaard. 2001. MIKE SHE: a distributed, physically based modeling system for surface water/groundwater interactions. In: Seo, Poeter, Zheng, Poeter, editors. MODFLOW 2001 and Other Modeling Odysseys—Conference Proceedings, Golden, CO; p. 321–7

Haverkamp, R., R.M. Vauclin, J. Touma, P.J. Wierenga, and G. Vachaud. 1977. A comparison of numerical simulation models for one-dimensional infiltration: Journal of Soil Science Society of America, v. 41, p. 285–294.

Holmes, D. G., and S.D. Connell. 1989. Solution of the 2D Navier-Stokes equations on unstructured adaptive grids. Proc., AIAA 9th CFD Conf., AIAA Paper 89-1932.

Hubbard, M. E. 1999. Multidimensional slope limiters for MUSCL type finite volume schemes on unstructured grids. J. Comput. Phys., 155, 54–74.

Huyakorn, P.S., and G.F. Pinder. 1983. Computational Methods in Subsurface Flow. Academic Press.

Jawahar, P., and H. Kamath. 2000. A high-resolution procedure for Euler and Navier-Stokes computations on unstructured grids. J.Comput. Phys., 164, 165–203.

Kim, S.E., B. Makrov and D. Caraeni. 2003. A Multi-Dimensional Linear Reconstruction Scheme for Arbitrary Unstructured Grids, 16th AIAA Computational Fluid Dynamics Conference

Kollet, S.J., and R.M. Maxwell. 2006. Integrated surface-groundwater flow modeling: A free-surface overland flow boundary condition in a parallel groundwater flow model, Advances in Water Resources, (29)7, 945-958.

Kumar, M., G. Bhatt, and C. Duffy. 2009a. An efficient domain decomposition framework for accurate representation of geodata in distributed hydrologic models, International Journal of GIS, vol 23.

Kumar, M., G. Bhatt and C. Duffy. 2009b. The Role of Physical, Numerical and Data Coupling in a Mesoscale Watershed Model. Advances in Water Resources (In Review)

Kumar, M., G.Bhatt and C.Duffy, 2009c. An Object Oriented Shared Data Model for GIS and Distributed Hydrologic Models. International Journal of GIS, vol 23.

Kumar, M. 2009d. Towards a Hydrologic Modeling System. Doctoral Dissertation. Department of Civil and Environmental Engineering. The Pennsylvania State University.

Leake, S.A., and D.V. Claar. 1999. Procedures and computer programs for telescopic mesh refinement using MODFLOW. US Geological Survey Open-File Report 99-238.

Lin, G.F., J.S. Lai, and W.D. Guo. 2003. Finite-volume component-wise TVD schemes for 2D shallow water equations, Advances in Water Resources, 861-873

Lu, Q., M. Peszynska, and M.F. Wheeler. 2001. A parallel multi-block black-oil model in multi-model implementation. In: SPE 66359, 2001 SPE Reservoir Simulation Symposium, 2001, Society for Petroleum Engineers, Houston, 14–17

Manzini, G., and S. Ferraris. 2004. Mass-conservative finite volume methods on 2-D unstructured grids for the Richards equation, Advances in Water Resources, 27 1199–1215

Mehl, S., and M.C. Hill. 2004. Three-dimensional local grid refinement method for block-centered finite-difference groundwater models using iteratively coupled shared nodes: a new method of interpolation and analysis of errors. Adv Water Resour;27(9):899–912.

Mualem, Y., 1976, A new model for predicting the hydraulic conductivity of unsaturated porous media: Water Resources Research, v. 12, p. 513–522.

Nwankwor, G. I., J. I. Cherry, and R. W. Gillham. 1984. A comparative study of specific yield determinations for a shallow sand aquifer. Ground Water, 22, 764–772.

Nwankwor, G. I., R. W. Gillham, G. van der Kamp, and F.F. Akindunni. 1992. Unsaturated and saturated flow in response to pumping of an unconfined aquifer: Field evidence of delayed drainage. Ground Water, 30(5), 690–700

Ollivier-Gooch, C., and M. Van. Altena. 2002. A high-order-accurate unstructured mesh finite-volume scheme for the advection–diffusion equation, J. Comput. Phys. 181 (2) 729–752, ISSN 0021-9991.

Panday, S., and P.S. Huyakorn. 2004. A fully coupled physically-based spatially-distributed model for evaluating surface/subsurface flow. Adv Water Resour 27:361–382

Pasdunkorale, J.A., and I. W. Turner. 2003. A Second Order Finite Volume Technique for Simulating Transport in Anisotropic Media. The International Journal of Numerical Methods for Heat and Fluid Flow, Vol. 13(1), pp. 31-56

Qu, Y., and C.J. Duffy. 2007. A semi-discrete finite volume formulation for multi-process watershed simulation, Water Resourc. Res, 43, W08419

Shewchuk, J.R. 1996. Triangle: Engineering a 2D quality mesh generator and Delaunay triangulator. Applied Computational Geometry: Towards Geometric Engineering, v.1148 of Lecture Notes in Computer Science

Srivastava, R., and T. J. Yeh. 1991. Analytical solutions for onedimensional, transient infiltration toward the water table in homogeneous and layered soils. Water Resour. Res., 27(5), 753–762.

Turkel, E. 1985. Accuracy of schemes with nonuniform meshes for compressible fluid flows. Institute for Computer Applications in Science and Engineering Report No. 85-43, National Aeronautics Space Administration, VA.

US Environmental Protection Agency (USEPA), 1994. A technical guide to ground-water model selection at sites contaminated with radioactive substances. EPA/402/R-94/012, Office of Solid Waste and Emergency Response, US Environmental Protection Agency, Washington, DC.

VanderKwaak, J.E. 1999. Numerical simulation of flow and chemical transport in integrated surface–subsurface hydrologic systems, Doctorate Thesis, Department of Earth Sciences, University of Waterloo, Ontario, Canada.

van Genuchten, M. Th., 1980. A closed-form equation for predicting the hydraulic conductivity of unsaturated soils: Journal of Soil Science Society of America, v. 44, p. 892–898.

Vauclin, M., D. Khanji, and G. Vachaud. 1979. Experimental and numerical study of a transient, two-dimensional unsaturated-saturated water table recharge problem. Water Resour. Res., 15(5), 1089 –1101.

Weiyan, T. 1992. Shallow Water Hydrodynamics, Elsevier Oceanography Series, vol. 55. Elsevier, Amsterdam.

Winter, T., J. Harvey, O. Franke, and W. Alley. 1998. Ground water and surface water: A single resource. U.S. Geological Survey Circular 1139. United States Geological Survey, Denver.

Yeh, G. T., and J. R. Cheng. 1994. 3DFEMWATER user manual: A three-dimensional finite-element model of water flow through saturated-unsaturated media: Version 2.0. Pennsylvania State Univ., University Park, PA.

Yeh, G.T., and G.B. Huang. 2003. A Numerical Model to Simulate Water Flow in Watershed Systems of 1-D Stream-River Network, 2-D Overland Regime, and 3-D Subsurface Media (WASH123D: Version 1.5), Technical Report. Dept. of Civil and Environmental Engineering, University of Central Florida, Orlando, Florida.

5.7. Appendix

Normalized flux calculated in local coordinate system (x1, y1) that is oriented along the principal directions of anisotropy (see Figure 5.4). θ is the angle of orientation of ∇h to the global x-axis

$$\begin{aligned}
\vec{n}.\vec{F} &= (K_1 \nabla h_{x_1} \hat{i}_1 + K_2 \nabla h_{y_1} \hat{j}_1).\vec{n} \\
&= (K_1 \nabla h Cos(\theta - \beta)\hat{i}_1 + K_2 \nabla h Sin(\theta - \beta)\hat{j}_1).\vec{n} \\
&= (K_1 \nabla h Cos(\theta - \beta)Cos(\alpha - \beta) + K_2 \nabla h Sin(\theta - \beta)Sin(\alpha - \beta)) \\
&= (K_1 Cos(\theta - \beta)Cos(\alpha - \beta) + K_2 Sin(\theta - \beta)Sin(\alpha - \beta))\nabla h
\end{aligned} \tag{5.35}$$

Note the normalized lateral flux expression obtained in Eq. [5.30] and Eq. [5.35] is the same.

CHAPTER 6:

Domain Partitioning for Implementation of Large Scale Integrated Hydrologic Models on Parallel Processors

6.1. Introduction

Hydrologic models simulate hydrologic state variables in space and time while utilizing information regarding heterogeneity in climate, land use, topography and hydrogeology (Freeze and Harlan 1969). These models have inherent advantages over conventional lumped models due to incorporation of natural heterogeneities (Entekhabi and Eagleson, 1989, Pitman et al. 1990) leading to a more physically based simulation of hydrologic processes. But with increasing spatio-temporal resolution, number of physical processes incorporated in the model and the mathematical complexity of the physical equations and their approximations, the computational requirements of these models increases. This poses considerable challenge to the application of any distributed hydrologic model at fine spatio-temporal resolution. Just to give an idea about the scale of computation, Johnson (2000) took 20 hours of computing time to simulate 20 hours of event time using a two-dimensional numerical model CASC2D (Julien and Saghafian, 1991), a physics based diffusive wave model to simulate the rainfall runoff processes, in Buffalo Creek watershed at a resolution of 72 by 93 meters. Obviously significant advances in hardware speed and programming efficiency have been achieved since then. The advent of parallel processing architectures, due to their increased computing power and memory, and relatively cheap cost, furnishes an excellent opportunity to meet the computing challenges posed by distributed hydrologic models. Parallelized codes run concurrently on a network of large number of processors, thus reducing the time needed to obtain solution

Development of parallelized models is challenging. In addition to knowledge of numerical algorithms, it requires considerable understanding of hardware architecture, model data structure and interprocessor communications. The primary step in parallelizing a hydrologic model is to map out the problem on multi-processor environment. The speedup obtained from the parallel code strongly depends on how the mapping of the model domain is performed on different processors.

This paper introduces the crucial and unique factors that can potentially influence the efficiency of domain partitioning for a distributed hydrologic model. The paper suggests strategy to incorporate these factors in existing domain partitioning algorithms,

and studies and compares their effectiveness vis-à-vis PennState Integrated Hydrologic Model (PIHM). We begin by first introducing the hydrologic model structure of PIHM (in section 6.2), which will be used as a case study to test the partitioning algorithms on. Next we discuss some limited applications of domain partitioning in hydrology. We identify limitations of the previous attempts at partitioning for distributed hydrologic models (in section 6.3) and introduce a set of factors that need to be addressed for an efficient domain partitioning (section 6.4). Section 6.5 suggests ways to incorporate the factors which determine the efficiency of respective partitioning algorithms for hydrologic applications. Section 6.6 discusses several existing domain partitioning algorithms along with their strengths and weaknesses. Section 6.7 discusses the results of application of partitioning algorithms in Great Salt Lake River Basin (GSLB). We also discuss the limitations of the existing algorithms and will draw conclusions from the experiments presented in this paper. The paper synthesizes the existing knowledge in computer science community about domain partitioning with the unique issues posed by hydrologic model structure to obtain efficient distribute model partitions.

6.2. Pennstate Integrated Hydrologic Model (PIHM) structure

PIHM (Qu and Duffy, 2007; Kumar et. al., 2007a) solves coupled hydrologic process equations distributed over unstructured meshes. By applying divergence theorem over a control volume, governing partial differential equations (PDEs) defined on each discretized element is transformed to semi-discrete ODEs. The model is designed to capture "dynamics" in multiple processes while maintaining the conservation of mass at all cells, as guaranteed by the finite volume formulation. The "control-volume" used in PIHM is either a prismatic or linear physical element. Figure 4.2 shows a typical kernel defined on a triangular and a linear element (corresponding to river and sub-channel aquifer). The relevant ODEs defined on a kernel are shown in Table 4.1. The generic semi-discrete form of ODE that defines all the hydrologic processes incorporated in PIHM can be represented as

$$A_i \frac{d\overline{\psi}}{dt} = \sum_j N.\vec{G}A_{ij} + \sum_k N.\vec{F}A_{ik} + \overline{S}_\psi V_i \qquad (6.1)$$

where $\overline{\psi}$ (L) is the average volumetric conservative scalar per unit planimetric control volume area A_i, $\overline{S}_\psi$ is the average source/sink rate per unit control volume, $\vec{G}$ and $\vec{F}$ are vertical and lateral flux terms respectively and N is the normal vector to the surface j of the control volume i. Table 4.1 lists the vertical and horizontal flux terms associated with each state and identifies the coupled flux interactions between neighboring control volumes (both in vertical and in horizontal) through a process coupling function $f[]$. Individual vertical, horizontal and source/sink flux terms listed in Table 4.1 can be directly replaced in Eq. (6.1) to evaluate the respective state equations. The coupling function $f[]$ defined in Table 4.1 shows that the interaction between processes such as interception-snow, interception-unsaturated zone is "one-way" only, while interactions between unsaturated-saturated and river-saturated zone are "two-way". Explanations of the symbols not described in the text can be referred to in Appendix I (section 4.10). For more details about the individual process equations, readers are referred to Chapter 4. A stiff-ODE solver called CVODE (Cohen and Hindmarsh 1994) from Suite of Nonlinear and Differential/Algebraic equation Solvers (SUNDIALS, 1994), is used to solve the system of ODEs from across the model domain.

As is evident from the process equations listed in Table 4.1, the magnitude of the state variables on a kernel is dependent on those in the neighboring kernels and must be updated at each calculating time interval. On a serial computer this data transfer is accomplished by writing to and reading from memory. However when we map this computational grid to a parallel computer, two vertices joined by an edge and not owned by the same processor must communicate to exchange values. Since communication is more expensive than computation, a domain mapping strategy that minimizes it is desirable. In order to totally avoid communication overhead, an extreme strategy would be to assign the entire grid to a single processor and thus have no communication at all. But that wouldn't be an effective use of the parallel machines since one processor would do all the work while the others remained idle. We must therefore also observe the important constraint that each processor should be assigned about the same amount of work. This suggests that a classic domain-decomposition strategy as discussed in Gilbert et al. (1995) or Simon (1991) might fail to provide performance gains.

6.3. Domain Partitioning for Distributed Hydrologic Modeling: State of the Art

There have been a very limited number of studies that concern with domain partitioning for parallel distributed hydrologic modeling. Vivoni et al. (2005) presented a strategy for domain partitioning for parallelization of tRIBS (Ivanov et al., 2004) by dividing the domain based on subbasins. A similar exercise performed on GSLB (see Figure 6.1)

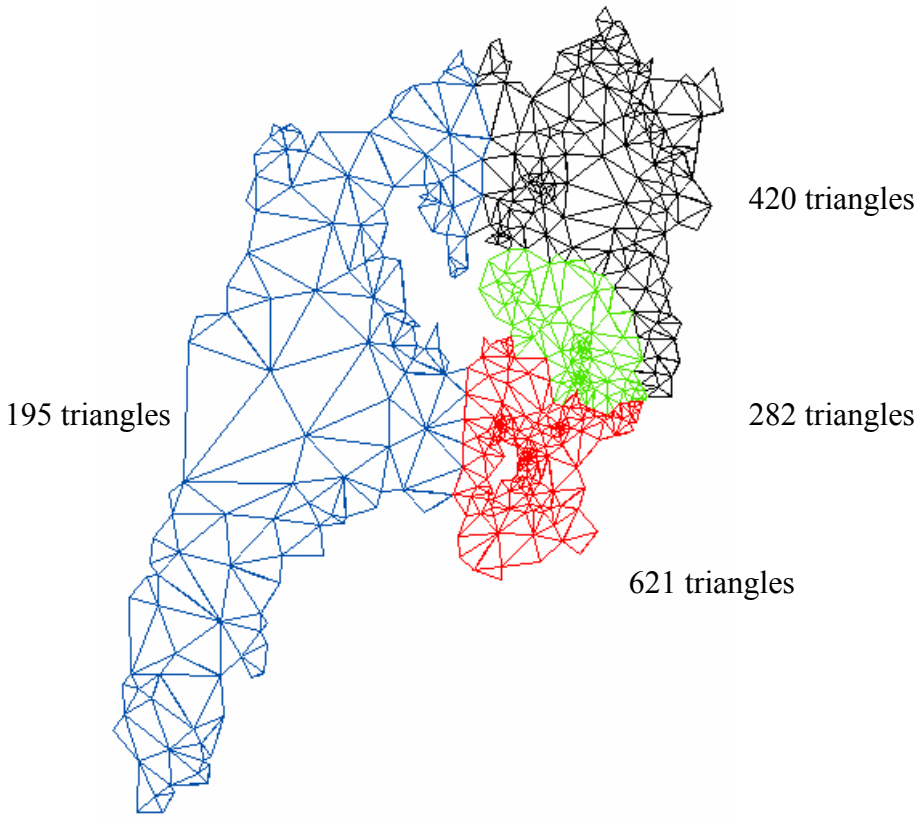

Figure 6.1 Domain partitioning of the model domain based on sub-watershed in GSLB. This leads to significant load imbalance. We note that very coarse mesh discretization is being used on purpose to simplify visual interpretation. Quality of meshes does not interfere with the inferences drawn in the paper

shows that this can lead to a disproportionate number of meshes getting generated within each sub-basin. This translates to different computation time on different processors thus resulting in reduced efficiency of parallelization. We note that different sub-basins can be forced to have the same number of meshes in them, however the modeler will lose the flexibility to control the resolution of meshes based on hydrologic constraints. Apostolopoulos and Georgakakos (1997) used uni-directional acyclic graphs to partition

rivers. Cui. et al. (2005) also partitioned the watershed into subbasins but tackled the problem of load imbalance by redistribution of load between processors using sending by pairs, sending circularly and sending by percentage methodology to send data from overloaded to underloaded processors in order to balance load among processors. The experiment is illuminating, however, the methodology involves large communication between processors which could have been completely avoided by partitioning the domain such that load is balanced. Also, both the applications assumed flow direction governed by topographic gradients only and were not generic enough to be used for fully distributed hydrologic models where direction of flow (on the surface and subsurface) are much more complex and can change directions based on head gradients.

6.4. Efficient Domain Partitioning: Goals and Controls

A generic and efficient domain partitioning algorithm must satisfy following two primary objectives:

a) Load Balancing: Load balancing means that the workload assigned to each processor is the same. Since the execution time for the program is crucially determined by the processors that take the longest to complete a job, load balancing ensures the most efficient use of all the processors and thus the minimum computation time.

b) Minimization of interprocessor communication: Even though the number of communication is lot less than the computations, since the cost of accessing memory on other processors is about 10 to 1000 times larger than that of accessing it locally, minimizing communication becomes crucial. The cost of communication among processors depends on the amount of data shared between them, the frequency at which they share the data, and latency and bandwidth of the interconnection network. Latency is the time it takes to set and prepare a complete communication for a message length of size zero, whereas bandwidth is the actual speed of transmission, or bits per unit time. This time must be minimized to get the best performance improvements from a parallel program. Next we discuss the factors affecting load balance and interprocessor communication.

6.4.1. Hydrologic Factors

6.4.1.1. Number of Hydrologic Processes

With increase in number of prognosticated variables, the amount of computation and also the data that needs to be shared with neighboring elements increases proportionally. This directly impacts computation time and interprocessor communication and accordingly needs to be accounted for in a partitioning algorithm

6.4.1.2. Spatial Coupling

Calculation of hydrologic states in a discretized element depends on its total head value in the adjacent elements. Distributed hydrologic models have varying degree of representation of process spatial coupling. For example, models such as HEC-HMS (http://www.hec.usace.army.mil/software/hec-hms/) and tRIBS (Ivanov et al., 2004) calculate overland flow flux based only on downstream head which lies in the direction of maximum elevation gradient. However, models such as ModHMS (Panday and Huyakorn 2004) and PIHM, account for head magnitudes in all the neighboring elements of a cell to calculate overland flow diffusive flux. So the degree of spatial coupling of hydrologic states in different models influences the amount of data that will be shared across neighbors if they are assigned to separate processors

6.4.1.3. Topology

The number of neighbors of a particular element is determined by the shape of unit elements and the topological relations between different feature types. The maximum number of communication interface for a grid will be equal to 4* (Number of state variable whose value depends on the states in neighboring cells) + River upstream-downstream topology dimension. For triangular unstructured grids, number of communicating interface between elements will be 3.

6.4.1.4. Heterogeneous Computational Load

Computing time on each processor depends on the evaluation of right hand side of ODEs (similar to one in Eq. 6.1). Depending on the dynamics of processes and the programmatical representation of ODEs on each processor, it can take significantly different time to finish the same job. For example, more computation can be expected in the part of model domain with significant rainfall in comparison to the domain which is dry. This means that in a distributed model, the heterogeneity in forcing and parameters will keep influencing the synchronicity between different processors. We note that the computational load will be varying spatio-temporally.

6.4.1.5. Heterogeneous Communication

The topological complexity and changes in spatial coupling within the model domain, because of the heterogeneity of hydrologic features, results in heterogeneous communication across processors. Table 6.1 shows that the amount of communication (in terms of variables shared across the edge) performed between neighboring elements in a simplified two layered (unsaturated and groundwater) conceptualization of PIHM. Similar heterogeneity in communication can be expected with other hydrologic models. Figure 6.2 represents the unit model element and the associated communicating processes

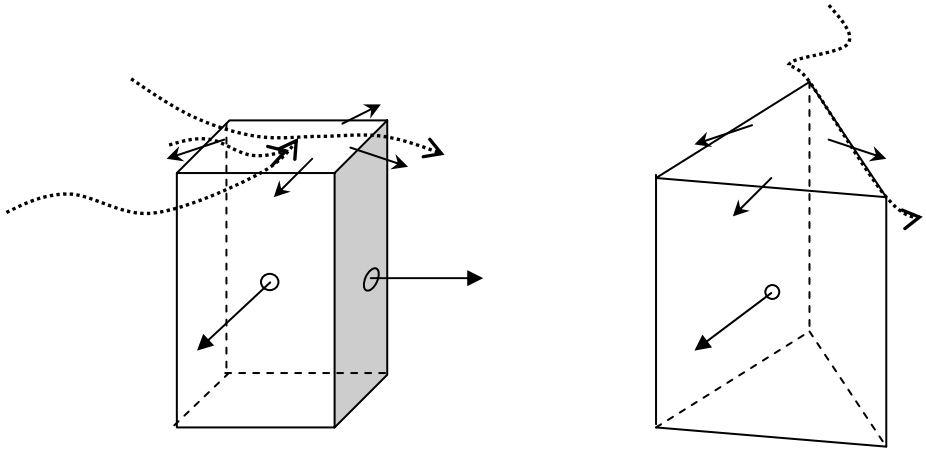

Figure 6.2 Model unit element for a) ModHMS and b) PIHM. Note that the maximum possible amount of communication across the edge face will be: (Number of River segments entering and going out through kernel face) + (NLayer for subsurface flow) + (1 units of Overland Flow communication) for ModHMS. For PIHM, maximum communication across as face will be: 1 (Overland flow) + 2 (Leakage/Baseflow to sub-channel aquifer element and the river)

across the edge for ModHMS (structured grid based model) and PIHM (unstructured grid based model). This heterogeneity in communication needs to be incorporated while partitioning the model domain. Also, the difference in timescale of various hydrologic processes like overland flow and groundwater flow can be used to our advantage in order to further improve the efficiency of the code by performing updates of groundwater variable on the boundary cells at relatively longer time intervals with respect to the model time interval. For example, if the overland flow model simulation is being carried out at time step *n*, groundwater flow across the subshed boundaries can be calculated at 5**n* only (say). The underlying assumption here would be that a change in the subsurface storage is very slow relative to the overland flow. Intervals of frequency can be determined through computational experiments by studying the tradeoff between the sharing frequency across edges and accuracy of the solution.

Table 6.1 Size of communication packet for different elements of the model domain

Elements	Shared Processes	Maximum Communication
Triangular Elements besides Subshed boundary	Sub-surface flow	1
Triangular Elements besides River	Subsurface flow between triangular elements and subchannel aquifer, Leakage/Base flow from/to between the river and triangular element, Overland flow to/from river	3
Generic Triangular elements	Overland flow, Sub-surface flow	2
River (and Sub-channel aquifer)	Flow from Upstream, Flow to downstream, Overland flow between triangular element and river, Base flow/Leakage between triangular element and river, Groundwater flow between triangular element and sub-channel aquifer	5

6.4.2. Architectural Factors

6.4.2.1. Interconnect Property and Type

The interconnection networks are wires and cables though which the multiple processors of a parallel computer are connected to each other and to the memory units. The communication time is dependent upon the specific type of the interconnection network and its properties like latency, bandwidth, diameter and degree. Latency is the delay on a network that occurs while a data packet is being stored and forwarded. Bandwidth determines the amount of data that can be sent through a network connection. Diameter is the distance between two processors that are farthest apart. Degree determines the number of communicating wires coming out of each processor. A smaller latency and diameter, and a larger bandwidth and degree are desired for shortest communication time.

Topology of the interconnection network also determines the chances of network congestion when a message is sent between distant processors. This is because while the interconnection is transferring messages, the wires are rendered unavailable to transmit other messages. Commonly used network topologies are Bus, Cross-bar switch and Hypercube. Bus based interconnections are more prone to have contention for access than cross-bar switch. The advantage with Hypercube interconnections is larger degree with increasing size of network. Hence when network congestion is important, weighting messages by the number of wires they use will lead to better domain mappings to distributed processors.

Many at times, the distributed processor are also connected heterogeneously, with communication occurring within a group and between groups of processors. The disparity between communication time between the local and remote connections needs to be incorporated in a domain partitioning strategy. Heterogeneity in data transfer can also be because of different network interfaces and protocols.

6.4.2.2. Heterogeneous Processor Speed

Heterogeneous clusters can have individual nodes with varying processor speeds. This is particularly likely for Beowulf cluster of PCs built with commodity-off-the-shelf equipment where faster machines with larger memories are continually added to the system or replaced for slower nodes. In order to minimize the idle processor time for

computing on heterogeneous clusters, the work over them should be so distributed such that no processor is waiting for the completion of another. Thus the partitioning algorithm for a heterogeneous processor configuration should be able to incorporate asymmetric load balancing.

6.5. Formulating Domain Partitioning Problem with Controls

Considering the architectural and hydrologic factors that influence load balance and communication between processors, the problem now is that of how to decompose the mesh into subdomains while incorporating the needs of an efficient parallel computation. This essentially translates to a set of minimization (or maximization) problem as discussed above, given an arbitrary number of balancing constraints like heterogeneous communication and processor speeds. Many of these partitioning problems can be formulated in terms of an undirected communication graph. The communication graph describes the relationship of computation on the mesh by connecting unit elements which share information between each other. If the numerical algorithm (finite difference, element or finite volume) has a node based data structure, meaning that the state variables e.g. hydraulic heads in a hydrologic model are defined on the mesh nodes and fluxes along the edges, then any updates of state variable over time will also require data from neighboring nodes. Therefore the communication graph in this case is essentially the computational mesh itself, with mesh nodes being the graph vertices and edges of the mesh being the edges of the graph. The other kind of data structure can be element based where the state variables are defined on the elements and fluxes are calculated across the interfaces of neighboring elements. In this case vertices of the communication graph are essentially the centroid of the elements, and the edge of the graph is the connecting segment joining two vertices lying in the neighboring elements that share a face with each other. Such a graph is called the *dual graph* of the mesh. This approach is explained in detail in Hu and Blake, 1999. Figure 6.3 shows the dual graph for unit elements for three different hydrologic models viz. ModHMS (Panday and Huyakorn, 2004), PIHM and ELCIRC (Zhang, et. al., 2004) respectively on an experimental rectangular model domain. We note that unit element shapes for each of these models is different viz.

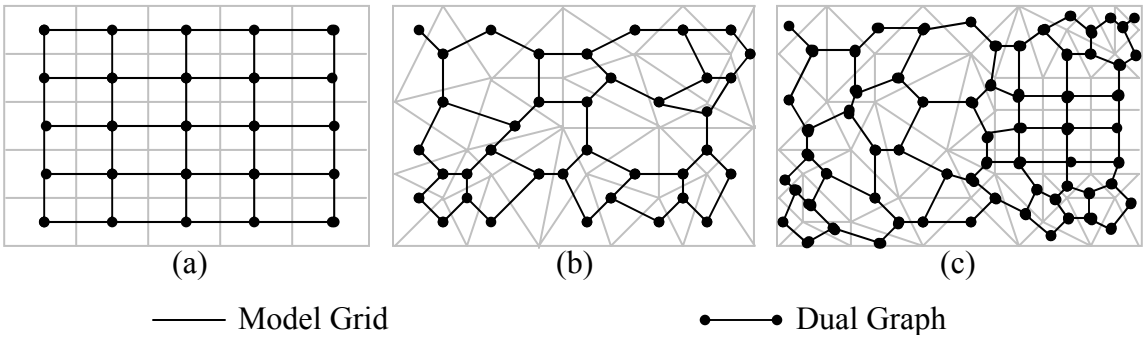

Figure 6.3 Dual graphs and the discretized model domain for a) ModHMS [solution strategy = finite difference] b) PIHM [solution strategy = finite volume] and c) ELCIRC [solution strategy = finite difference and volume]. Decomposed unit element shape in model (a) = Structured Grid, (b) = Unstructured Grid (Triangles) and (c) = Unstructured Grid (Triangles and Quadrilateral). Note that all of above three models are block centered

rectangular (structured mesh) for ModHMS, triangular (unstructured mesh) for PIHM and mixed mesh for ELCIRC.

The problem of efficient portioning can now be defined on the dual graphs. Given a dual graph G with n weighted vertices and m weighted edges, the objective is to divide the vertices into p partition sets in such a way that the sum of the vertex weights in each set is as close as possible and the sum of the weights of edges crossing between sets is minimized. The weights on the vertices and edges are generally proportional to the computation load on the elements and communication amount across the element face respectively. The posed problem is NP-complete and so it's hard to obtain the global optimum solutions. Therefore several near-optimal approximate, probabilistic and heuristic techniques have been explored to solve the problem (Walshaw and Cross, 1999; Hu and Blake, 1999; deCougny et. al., 1994; Simon, 1991).

6.6. Domain Partitioning Algorithms: Comparative Review

Some of the prominent heuristic methods and their characteristics are briefly discussed below. Many of these are bisection based which essentially means dividing the domain into two subdomains and to perform divisions recursively on the obtained subdomains.

a) Inertial Bisection: The recursive inertial bisection (RIB) algorithm (Hendrickson and Liland, 1994) is a coordinate based method which tries to find a principal axis hyperplane of the communication graph thus dividing it into two parts. The principal axis is the line from which the sum of the squares of distances of the mesh nodes is smallest. The method is rotationally invariant unlike other geometric bisection algorithms like recursive coordinate bisection algorithm (Williams, 1991). The algorithm has a low complexity of $O(n)$.

b) Greedy Method: This algorithm (Farhat, 1998) is one of the simplest and fastest graph based partitioning method. Assuming that desired number of partitions is *p* and the total number of nodes is *n*, first $\frac{n}{p}$ nodes are coded in a partition *i* by including all the neighbors of a node location with minimum number of neighbors and also the neighbor's neighbors. The process is repeated for rest of the domain until all the nodes have been assigned to a partition. The algorithm has a low complexity of $O(n)$.

c) Graph Bisection: The *recursive graph bisection* (RGB) algorithm (Williams, 1991) first finds a set of pseudo peripheral nodes (PPNs) which are basically the two vertices that are the furthest apart (their distance is called the diameter of the graph). Then, starting from either of the PPNs , half of the graph nodes that are closer to either of the PPNs are assigned to two separate partitions. This process is then recursively executed on each of the subdomains. The graph bisection algorithm has a complexity of $O(n)$.

d) Spectral Bisection: The *recursive spectral bisection* (RSB) algorithm (Pothen *et. al.*, 1990; Simon, 1991) is a discrete optimization method. By assigning each nodes of the graph with a value of either 1 or -1, and defining the edge-cut for the bisection by

$$\left|E_c\right| = \frac{1}{4} \sum_{i \leftrightarrow j,(i,j)\in V} (x_i - x_j)^2 \qquad (6.2a)$$

where $i \leftrightarrow j$ is an edge connecting the nodes i and j respectively in partition V, the communication can be minimized by minimizing E_c while ensuring

$$\sum_{i=1}^{n} x_i = 0 \tag{6.2b}$$

Also noting that all the nodes take the value of 1 or -1, the sum of the squares should be n, the number of nodes. This gives the extra constraint

$$\sum_{i=1}^{n} x_i^{\,2} = n \tag{6.2c}$$

Since

$$\sum (x_i - x_j)^2 = \sum (x_i^{\,2} + x_j^{\,2}) - \sum 2x_i x_j = x^T Dx - x^T Ax$$

where D and A are diagonal matrix, with degree of the nodes on the diagonal, and adjacency matrix respectively. Defining *Laplacian matrix* of the graph as $L = D - A$, the aforesaid optimization problem with constraints can be rephrased as

$$\left|E_c\right| = \frac{1}{4} x^T Lx \tag{6.3}$$

The eigenvector corresponding to second lowest eigenvalue of the matrix L, also called Fiedler vector, is used to divide the nodes into two halves. The procedure can then be repeated on each of the subdomains.

e) Multilevel partitioning: The spectral bisection method discussed above is very computationally intensive because of the eigenvector solution. Multilevel methods (Barnard and Simon, 1993) speeds up the computation of Fiedler vector still generating high quality partitions. The algorithm is based on the multilevel approach normally and consists of three phases viz.

i) coarsening phase: the original graph is reduced into a levels of successively coarser graphs

ii) partitioning phase: the coarsest graph is partitioned into p parts

iii) uncoarsening and refinement phase: the partitioning of the coarsest graph is interpolated to a finer level graph and refined. The process is repeated till refinement reaches the original graph level.

The coarsening is achieved by choosing the maximal independent set (MIS) as the vertices of the coarse graph. MIS is a set of vertices such that no two of them are connected by an edge and if the addition of even a single vertex will violate this criterion. The edges of the coarse graph are weighted to reflect the number of edges in the original graph. By using several levels of coarsening a much smaller graph can be obtained which can be easily and rapidly partitioned by other graph partitioning methods like graph or spectral bisection. Infact Karypis and Kumar, 1995 observed that the choice of partitioning algorithm applied at coarsest scale has almost no bearing on the final quality of partition because of refinement performed in uncoarsening phase. In uncoarsening and refinement phase, the partitioning information is transferred up through the levels to the original graph using methods like eigenvector interpolation.

f) K – L Algorithm: The K-L (Kernighnan-Lin) algorithm (Kernighan and Lin, 1970) is an iterative algorithm that tries to iteratively improve random load balanced partitions. The algorithm tries to exchange the vertices from one partition of the graph to the other in order to reduce the edge cut till all the nodes of the smaller partition have been swapped. The procedure is repeated even if there are no more improvements made and continues even when the highest gain may be negative thus enhancing its ability to climb out of local minima. The algorithm has a complexity of $O(|E|)$ where E is the number of edges. For large graphs, the algorithm is quite inefficient and so is now used for local refinement of partitions obtained by algorithms discussed above.

g) Hybrid Algorithms: These are basically combination of two or more algorithms, one suited for global partitioning and the other for local partitioning only due to its computational intensiveness, that work in unison to give better results. K-L algorithm has often been used as the local search algorithm to improve partitions generated by ML

algorithm (Karypis and Kumar, 1995), RSB and RGB algorithm (Fowler and Greenough, 1998).

e) Other partitioning algorithms: Many other geometric and graph partitioning methods exist like coordinate bisection method (Williams, 1991), linear method, simulated annealing (Mansour, 1992), generic algorithms (Bui and Moon, 1996) etc. While coordinate bisection method is anisotropic, simulated annealing and genetic algorithm based methods are computationally intensive though they also produce high quality partitions. Algorithms which take into account the physical equations for finite element based solution of PDEs (deCougny et al, 1994; Vanderstraeten and Keunings, 1995) have also been developed.

6.7. Analysis, Application and Results

All the above algorithms for domain partitioning are applied on unstructured domain decomposition of Great Salt Lake Basin. The mesh has been generated by using topographic and hydrologic features as internal boundary constraints. The topographic features such as subshed boundary essentially divides the basin in four subsheds viz. Weber River, Bear River, Utah Lake and Western Desert with corresponding areas varying from 6413 km^2 to 49117 km^2. The discretized domain is then partitioned in order to assign different computational model kernels to different processors. As is evident from the huge variation in area of the subshed, if the average resolution of unit elements within each subshed is same then the time of computation for each subshed will be vastly different. We note that the measure of amount of communication used in the following discussion is the cumulative weighted edge cut at each interface unless otherwise mentioned.

6.7.1. Homogeneous Communication

Figure 6.3 shows the partitioning of the decomposed domain using inertial, greedy, recursive graph bisection (RGB), recursive spectral bisection (RSB), random Kernighan-

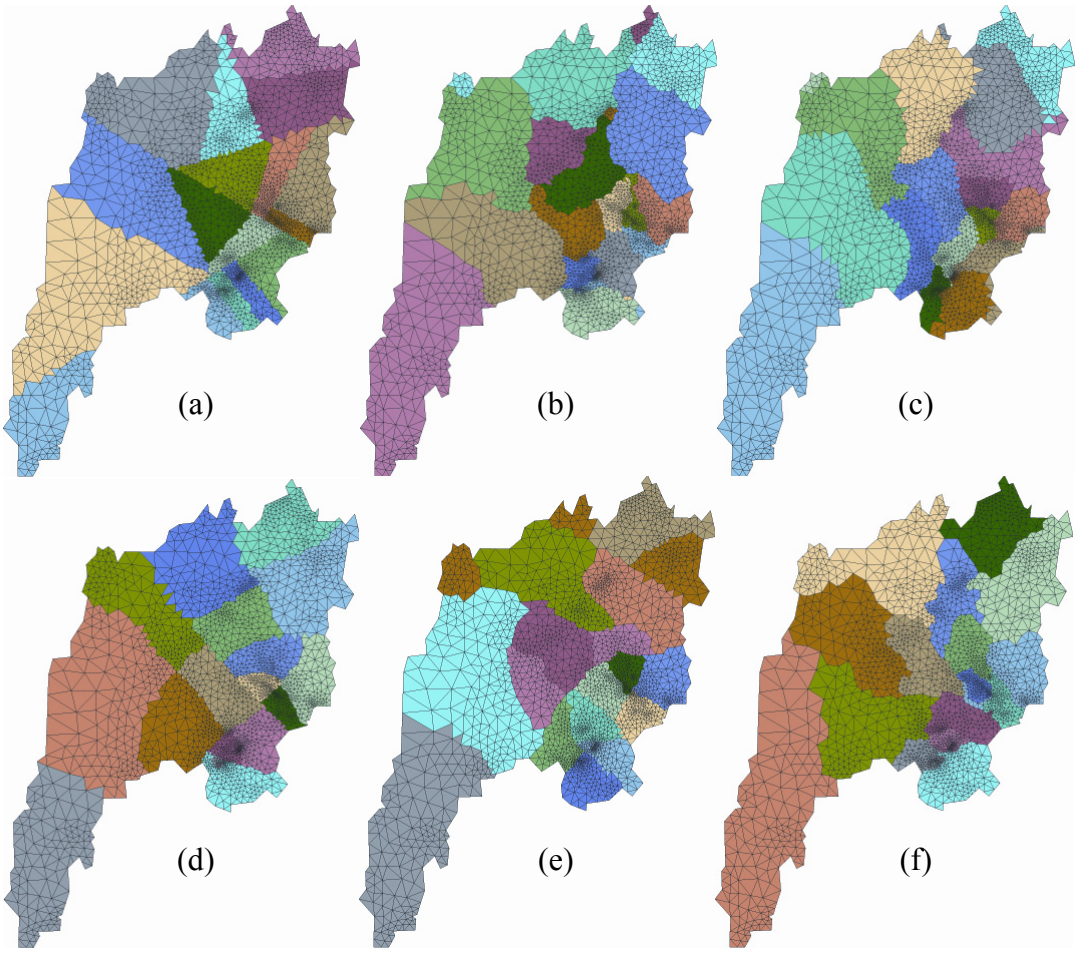

Figure 6.3 Partitioned domain for Great Salt Lake Basin (total number of unstructured grids = 4566) into 16 partitions. Algorithm used in partitioning is a) Inertial b) Greedy c) Recursive graph d) Recursive spectral e) Random KL and f) Multi-Level. Assumption: Homogeneous communication across the unstructured grid edges.

Lin (KL) method and Multi-Level (ML) method based on spectral algorithm. We observe that inertial bisection algorithm (Fig. 6.3a) generates disconnected and long partitions with large surface to volume ratio, which is not desirable. However, it also has a relatively smaller number of neighboring partitions which decreases the message startup time. Partitions produced by RGB (Fig. 6.3b) are found to be compact rough and disconnected. Similarly, partitioning based on Greedy and KL algorithms produce disconnected sets. On the other extreme, domains generated by both RSB and ML algorithms are smooth, compact and connected. As can be seen from the Figure 6.3, only RSB (Fig. 6.3d) and ML (Fig. 6.3f) generate all contiguous partitions. Other methods generate non-contiguous partitions, which suffer from message congestion as they will

have to generally travel longer distances and larger number of neighbors to fetch data. Quantitative comparison of the basic methods is shown in the Figure 6.4. We also show communication metrics for hybrid methods such as RGB_KL, RSB_KL and ML_KL. These methods use KL algorithm to refine their partition. Among the basic methods, KL algorithm outperforms other algorithms in minimizing interface communication whereas ML method based on spectral bisection algorithm outperforms the rest in minimizing congestion and message startup time which essentially depends on the average number of neighboring partitions. Ranking wise, RSB algorithm is found to perform best on an

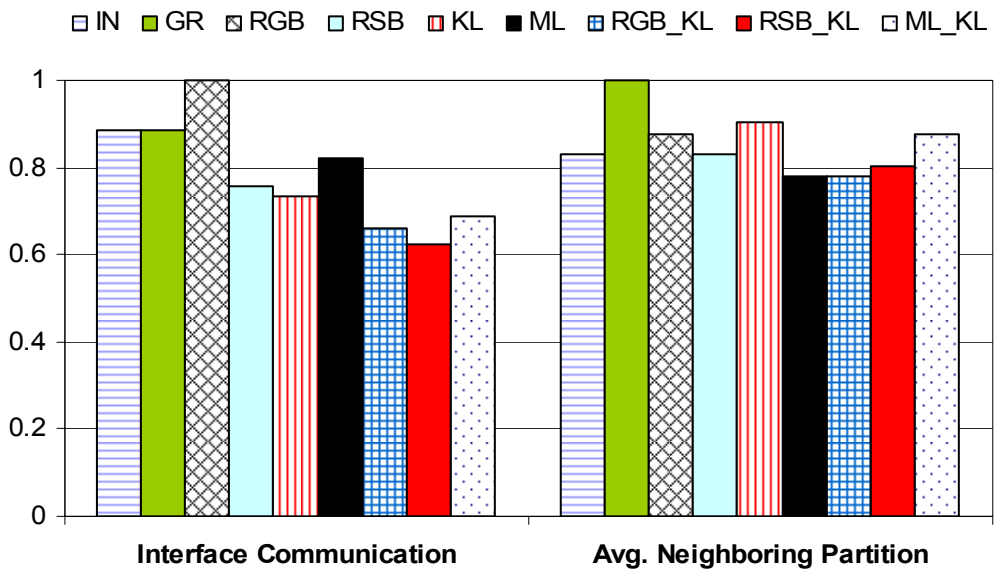

Figure 6.4 Relative values of communication and average number of neighboring partitions for different partitioning algorithms. IN is Inertial, GR is Greedy, RGB is Recursive Graph Bisection, RSB is Recursive Spectral Bisection, KL is Kernighan-Lin, ML is Multi Level (based on RSB) and RGB_KL, RSB_KL and ML_KL are hybrid methods with location refinement being performed using KL method. Hybrid methods perform best atleast in minimizing communication volume

average for both criteria. This is because the RSB algorithm captures the global property of the dual graph by calculating Fiedler vectors. The hybrid variant of RGB, RSB and ML algorithms with KL based refinement leads to improved performance in terms of decreased communication and number of neighboring partitions, except for ML_KL method where number of neighboring partition increases w.r.t. ML method. Depending on the relative time taken by the parallel hardware architecture in communication and startup, the number of times synchronization is forced between processors and new

communication is initiated (will also depend on the software coding strategy), and the length of the model simulation, decisions can be made by the user to give preference to a particular property and hence a particular algorithm. RSB_KL outperforms all the considered algorithms in minimizing communication volume. We note that KL refinement on RGB, RSB and ML increases the number of neighboring partitions. For larger domain size (number of graph nodes) ML algorithm is found to be computationally efficient than RSB based methods (Karypis and Kumar, 1995). So computation time saved due to less communication in RSB_KL algorithm can be offset by time it takes to derive the partition in the first place for very large graphs. This will particularly be crucial while performing spatio-temporal adaptive refinement/de-refinement of decomposed domain and during dynamic partitioning of the model domain due to spatio-temporal heterogeneity in computational load, as in these cases partitioning code has to be called numerous times.

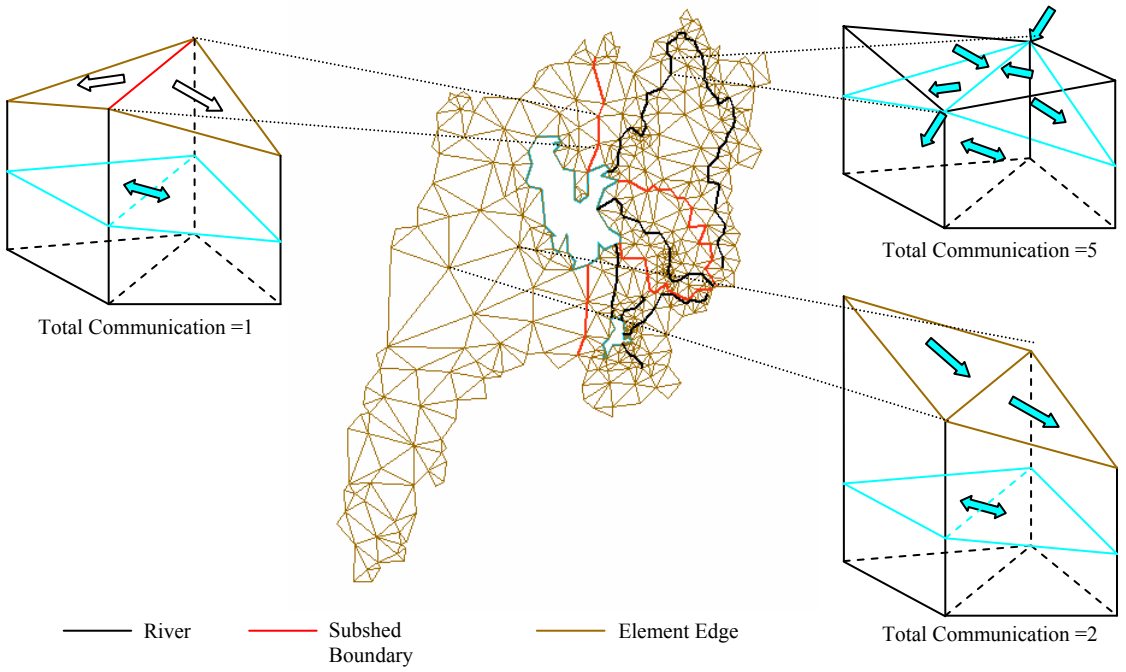

Figure 6.5 Heterogeneous communication exists in different parts of the model domain because of existence of disparate hydrologic features with different kinds of interacting processes

6.7.2. Heterogeneous Communication

In real hydrologic applications, the communication requirements across processors will be generally heterogeneous. As shown in Figure 6.5, the amount of communication between neighboring elements in different parts of the model domain is different. This heterogeneity can be incorporated in graph partitioning algorithms by assigning weights to the edges of dual graph proportional to the amount of communication. A detailed

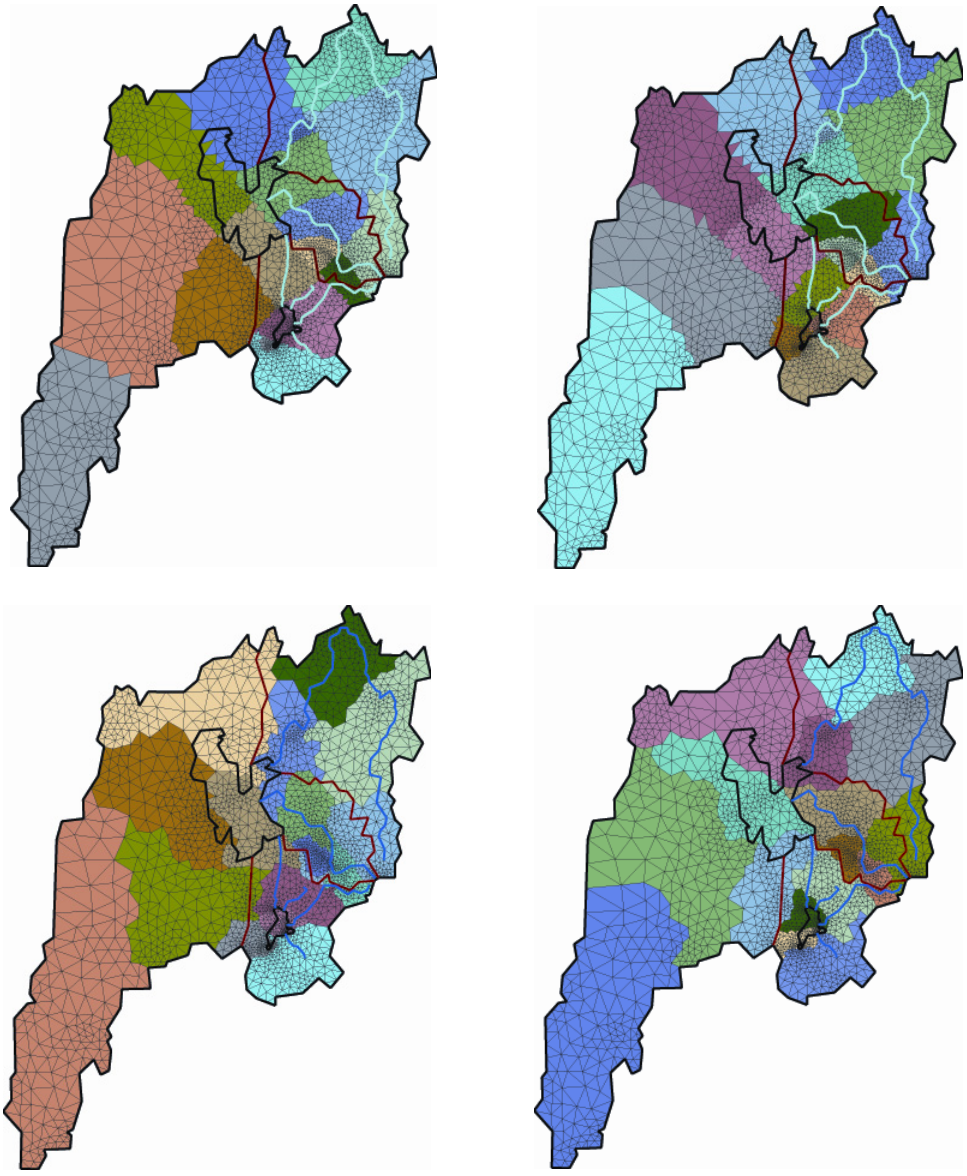

Figure 6.6a Mapping of GSLB into 16 partitions without (left) and with (right) heterogeneous communication taken into account using RSB_KL (top) and ML_KL (bottom) algorithm respectively. Note the alignment of partition boundary with sub-watershed boundary (particularly in bottom right figure) because of less communication across sub-watershed boundaries

discussion of RSB and ML algorithms where vertex and edge weights are modified to account for computational and communication heterogeneity is discussed in Hendrickson and Leland, 1995a,b respectively. Fig 6.6(a) shows the mapping of decomposed GSLB into 16 partitions using hybrid RSB_KL and ML_KL algorithms while considering heterogeneity in communication. The obtained partition has far less communication with respect to the case with no weights assigned to graph edges. Infact Figure 6.6(a) clearly shows the tendency of partition boundaries to align along the subshed boundaries because of relatively lower communication requirement across them. In order to study the effectiveness of the algorithm at various scales, the domain is decomposed into 979, 1295, 2232 and 4566 triangles respectively. Figure 6.6(b) shows the reduction in

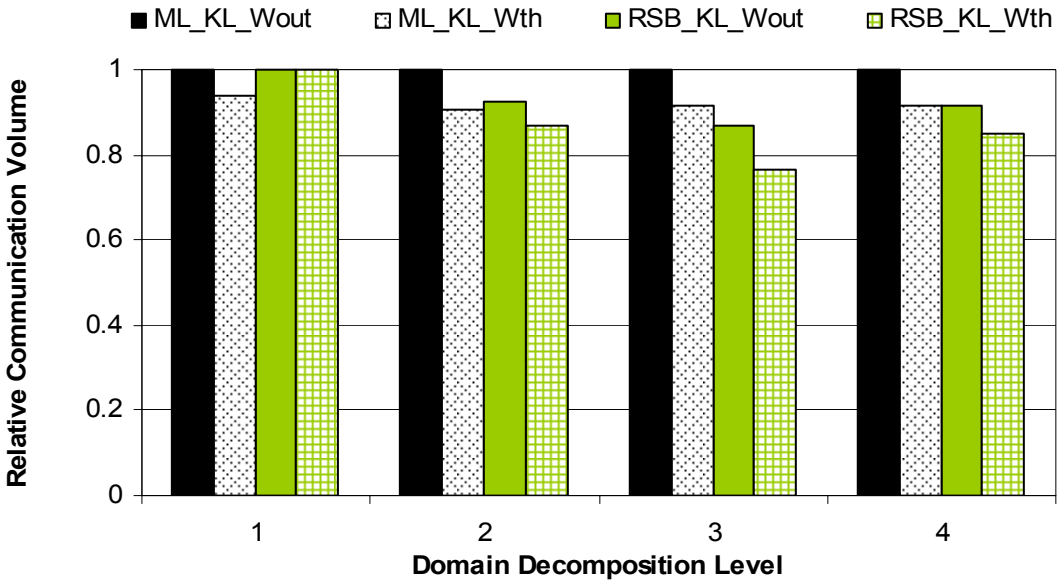

Figure 6.6b Relative communication volume for without and with heterogeneous communication taken into account in ML and RSB algorithm. Increasing decomposition level 1,2,3 and 4 denote higher level of discretization of the model domain with 979, 1295, 2232 and 4566 unit elements respectively. Wth and Wout stands for "With heterogeneity in communication consideration" and "Without heterogeneity in communication consideration" respectively

communication volume when heterogeneous communication weights are taken into account during partitioning. RSB_KL algorithm performs better than ML_KL at almost all scales. Weight assignments performed in Table 6.1 according to the process interaction that are shown in Figure 6.5 can be further made favorable by decreasing weights for groundwater flow particularly along the subshed boundaries, which are by-the-way often considered as groundwater divide also, to take advantage of the fact that

groundwater processes have relatively longer time scales at most of the places and can be considered to be non-dependent on the groundwater head of the neighboring element that lies across the watershed-divide. However, we note that such partitioning will introduce error in modeling and should be only implemented after studying the tradeoff between computational accuracy and load.

6.7.3. Heterogeneous Processors

If the processors used for computation have different speeds, then the load divided between them can be balanced by distributing the number of elements in proportion to processors speed. Figure 6.7 shows the partition of GSLB into 16 partitions using RSB algorithm on homogeneous and heterogeneous processors. The size of the partitions that are assigned to a faster processor increases in proportion to the processor speed.

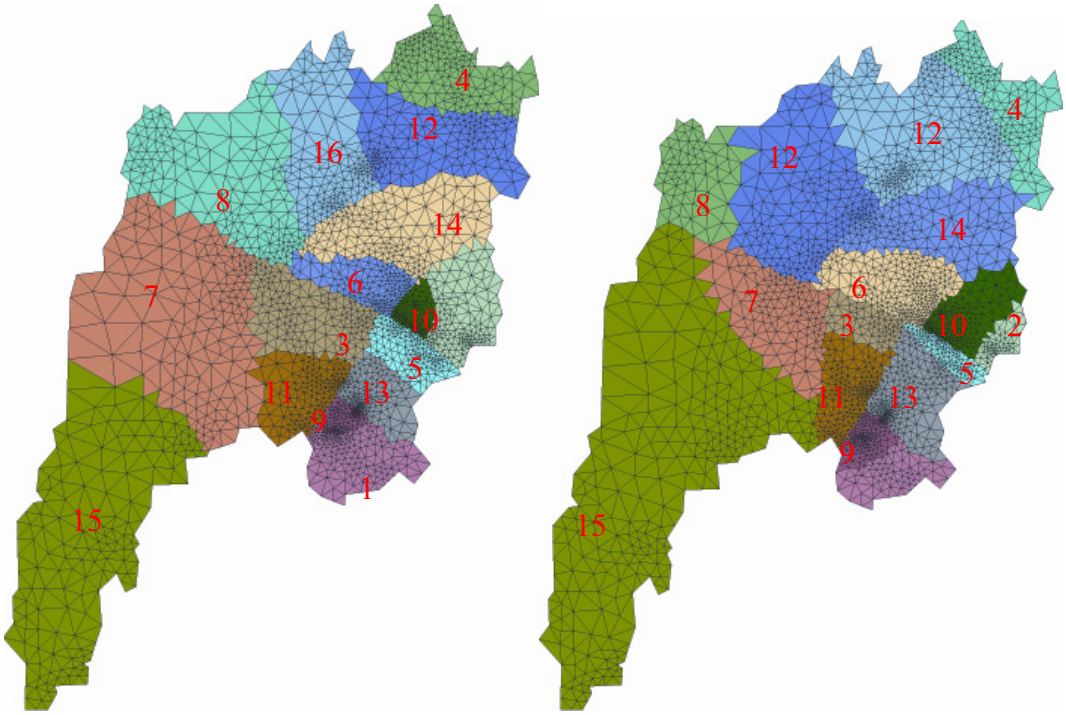

Figure 6.7 Partitioning of GSLB using RSB algorithm into 16 partitions. In the right figure, heterogeneous processor speeds have been considered with the relative speeds assigned as partNo(1,2,3,8) = procSpeed(1), partNo(4,5,7,14) = procSpeed(2), partNo(9,10,11,12) = procSpeed(3) and partNo(6,13,15,16) = procSpeed(4). Note the increase in size of partitions that are assigned to faster processors.

6.7.4. Message Congestion in Interconnect

Interconnection topology and sequence of assignment of partitions to processors significantly affect message contention costs. Since network contention renders the network unavailable to transmit any more messages, it should be minimized. Hendrickson et al., 1996 addressed this issue for ML and RSB algorithm using a method called terminal propagation which basically improves the data locality by including the processor location information in partitioning. The goal is to partition the domain such that processors sharing information are mapped closer together in the interconnect topology. This results in a message traveling between two processors to traverse least distance. Figure 6.8 shows the advantage of termination propagation in reducing the hop cost for spectral partitioning algorithm. However, this also results in increase in the number of edge costs and hence the communication volume. So depending on the relative time spent in starting send/receive operation and the time the message takes to traverse between processors, terminal propagation should be taken into account.

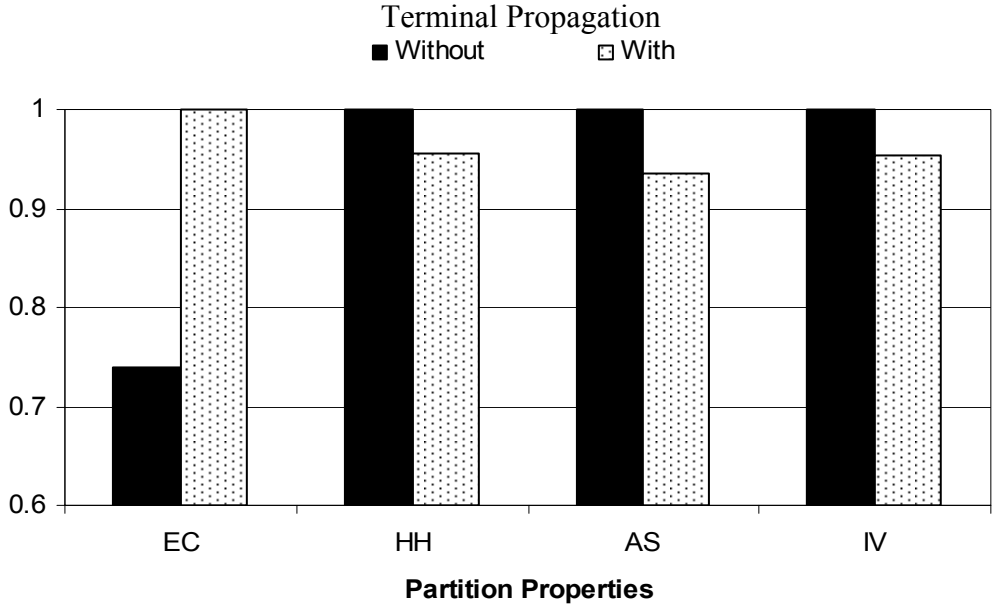

Figure 6.8 Terminal propagation reduces hypercube-hops. EC = Edge-Cuts, HH = Hypercube-Hops, AS = Average Adjacent Sets and IV = Internal Vertices. On the one hand accounting for terminal propagation in partitioning reduces HH, on the other it increases the EC. Tradeoffs have to be evaluated before a real model simulation

6.8. Limitations

Effectiveness of any of the partitioning algorithms can only be translated in real modeling application if the communication measure takes into account all the hydrologic and architectural factors discussed above. But first and foremost the basic assumption of the communication measure which have been implemented in most partitioning softwares i.e. use of weighted edge-cut needs to be representative. However, as pointed by Hendrickson and Kolda, 2000 existing measure to calculate communication volume using edge cuts can fail in certain situations. For example, sometimes edge cuts of the dual graph might correspond to transferring the same data from one partition to the other. This is generally the case with converging or diverging edges connecting nodes which belong to different partitions. The idea is shown in Figure 6.9 using a schematic two partition domain.

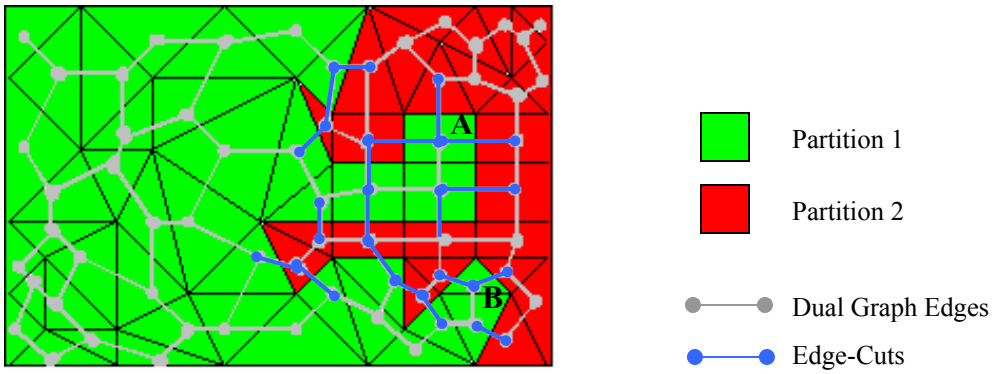

Figure 6.9 Partitioned domain for mixed unstructured grid (shown in Figure 6.2) into two partitions. Note that number of grids in green partition which share a face with red partition is 12, however number of edge cuts is 19.

Though grids A and B in Figure 6.9 need to send only one information each to the neighboring partition, the number of edge-cuts accounted for during partition is 3 and 2 respectively. Other limitations originate from how communications between different partitions are coded in the model. The communication measure to derive partitioning, and the data structure of the buffer that is actually used to perform communication through MPI should be consistent. Also as have been pointed out earlier, multiple objectives that will ultimately determine the performance of partitioning in a real application can not be satisfied all together. Single objective measures, such as “communication time” that uses the startup or latency time with communication volume can be derived (Fowler and Greenough, 1998). We note that even this measure doesn’t takes into account message

contention, multihop costs, message length dependent buffering and coding strategy. So domain partitioning is a multi-objective problem and the tradeoffs between objectives need to be considered for each application.

The partitions in this paper have been generated using codes from some of the state-of-the-art partitioning softwares like CHACO (http://www.cs.sandia.gov /CRF/chac_p2.html), JOSTLE (http://staffweb.cms.gre.ac.uk/~c.walshaw/jostle/), METIS (http://glaros.dtc.umn.edu/gkhome/views/metis/) and RALPAR (http://www.softeng.cse. clrc.ac.uk/ralpar/).

6.9. Conclusions

This paper examines the issues which impact efficient domain partitioning for a parallelized hydrologic model. These issues can be hydrologic such as time scale of hydrologic processes, the frequency of communication needed, number of interacting processes, coupling behavior, numerical solution strategy and unit element shapes of decomposed domain; or architectural such as heterogeneous processor speed and interconnect topology. Nine domain partitioning algorithm have been implemented on an unstructured grid decomposition of Great Salt Lake basin. Recursive spectral bisection algorithms refined by a KL algorithm are found to outperform the other algorithms in minimizing communication. The present best-partitioning measures are multi-objective in nature and the tradeoffs have to be accounted for between objectives before any particular partitioning can be applied in real hydrologic model simulation.

6.10. References

Arnold, J.G., Williams, J.R., Griggs, R.H., Sammons, N.B., 1991. A basin scale simulation model for soil and water resources management. Texas A&M Press, p. 255.

Barnard, S.T. and Simon, H.D., A fast multilevel implementation of recursive spectral bisection for partitioning unstructured problems", Proceedings of the 6th SIAM conf. on parallel processing for scientific computing, p711-718, 1993.

Band, L. E., Topographic partition of watersheds with digital elevation models, Water Resour. Res., 23(1), 15–24, 1986b.

Beven, K., Kirkby, M.J., 1979. A physically based, variable contributing area model of basin hydrology. Hydrol. Sci. Bull. 24, 43–69.

Beven, K.J., 1985, Distributed models, in M.G. Anderson and T.P. Burt (Eds) Hydrological forecasting, Wiley, Chichester.

Bui, T.N. AND B. R. Moon, Genetic algorithm and graph partitioning, IEEE Transactions on Computers, 45 (1996), pp. 841-855.

Cohen, S.D. and A.C. Hindmarsh, CVODE User Guide, Lawrence Livermore National Laboratory technical report UCRL-MA-118618, September 1994.

Cui. Z., B. E. Vieux, H. Neeman, and F. Moreda, Parallelization of Distributed Hydrologic Mode, International Journal of Computer Applications in Technology, 22, 1, 2005

DeCougny, H.L, K.D. Devine, J.E.Falherty, R.M. Loy, C. Ozturan and M.S.Shephard, Load balancing for parallel adaptive solution of partial differential equations, Applied Numerical Mathematics, 1994, pp. 157-182

Entekhabi, D., Eagleson, P.S., 1989. Land surface hydrology parameterization for atmospheric general circulation model including subgrid scale spatial variability. J. Climate 2, 816–831.

Farhat, C., A simple and efficient automatic FEM domain decomposer, Computer and Structures, 28 (1988), pp. 579-602

Fowler, R. F. and C. Greenough, RALPAR: RAL mesh partitioning program version 2.0, RAL Technical reports, RAL-TR-98-025, 1998.

Freeze, R.A., Harlan, R.L., 1969. Blueprint for a physically-based, digitally-simulated hydrologic response model. J. Hydrol. 105, 237–258.

Hammond, S., Mapping unstructured grid computations to massively parallel computers, PhD thesis, Rensselaer Polytechnique Institute, Dept. of Computer Science, Troy, NY, 1992

Hendrickson, B. and T. Kolda, Graph partitioning models for parallel computing, Parallel Computing, Vol. 26, 12, 2000

Hendrickson, B. and R. Leland, An empirical study of static load balancing algorithms, In Proceedings of the Scalable High Performance Computer Conference, pp. 682-685,IEEE, 1994

Hendrickson, B. and R. Leland, An improved spectral graph partitioning algorithm for mapping parallel communications, SIAM J. of Sci. Computation, 16, 1995a

Hendrickson, B. and R. Leland, A multilevel algorithm for partitioning graphs, Proc. ACM/IEEE conference on supercomputing, 1995b.

Hluchy, L., V. D. Tran, J. Astalos, M. Dobrucky, G. T. Nguyen, D. Froehlich: Parallel Flood Modeling Systems. International Conference on Computational Science ICCS'2002, pp. 543-551.

Hu, Y. and R. Blake. Load balancing for unstructured mesh applications. Parallel and Distributed Computing Practices, 2(3), 1999.

Ivanov, V.Y., Vivoni, E.R., Bras, R.L. and Entekhabi, D., 2004, The catchment hydrologic response with a fully-distributed triangulated irregular network model. Water Resources Research (In Press).

Johnson, B.E., Julien, P.Y., and Watson, C.C. (2000), Development of a Storm Event Based Two-Dimensional Upland Erosion Model (CASC2D-SED), American Water Resources Association (AWRA), February 2000

Julien, P. Y., and Saghafian, B. (1991). CASC2D user's manual - A two dimensional watershed rainfall-runoff model. Civil Eng. Report, CER90-91PYJ-BS-12, Colorado State University, Fort Collins, Fort Collins, CO

Karypis, G. and V. Kumar, A fast and high quality multilevel scheme for partitioning irregular graphs, Technical Report TR95-035, Department of Computer Science, University of Minnesota, 1995.

Kernighan, B. W., and S. Lin, An efficient heuristic procedure for partitioning graphs, Bell Systems Tech. J., 49 (1970), pp. 291-308.

Kumar, M., G. Bhatt and C.J. Duffy, 2009a, The Role of Physical, Numerical and Data Coupling in a MesoscaleWatershed Model, Advances in Water Resources, (In Review)

Kumar, M., G. Bhatt and C.J. Duffy, 2009b, An efficient domain decomposition framework for accurate representation of geodata in distributed hydrologic models, International Journal of GIS, v.23

Kumar, M and C. J. Duffy,2009c A large scale implementation of Parallelized Pennstate integrated hydrologic model. In preparation.

Lahmer, W.(1998). Macro- and Mesoscale Hydrological Modelling in the Elbe River Basin. In: Proceedings of the International Conference 'Catchment Hydrological and Biochemical Processes in Changing Environment' in Liblice, Czech Republic, September 22-24, 1998, p.57-61.

Leveque, R.J., 2002. Finite Volume methods for hyperbolic problems. Cambridge University Press.

Liang, X., Guo, J., Leung, L.R.,2004, Assessment of the effects of spatial resolutions on daily water flux simulations, Journal of Hydrology, 298, 287-310

Lin, H. C., D. R. Richards, G. T. Yeh, J. R. Cheng, H. P. Cheng, and N. L. Jones, FEMWATER: A three- dimensional finite element computer model for simulating density-dependent flow and transport in variably saturated media, Report CHL-97-12, U.S. Army Corps of Engineer, 3909 Halls Ferry Road, Vicksburg, MS 39180-6199, September, 1997

Macks,A.; Heterogeny in a Beowulf, High Performance Computing Systems and Applications, 2002. Proceedings. 16th Annual International Symposium on 16-19 June 2002 Page(s):42

Mansour, N., *Allocating data the multicomputer nodes by physical optimization algorithms for loosely synchronous computations*, Concurrency: Practice and Experience, 4 (1992), pp. 557-574.

Moore I. D. , E. M O'Loughlin, Burch. A., Contour-based topographic model for hydrological and ecological applications, Earth Surface Processes Landforms,13,305-320, 1988.

Namburu, R. R., D. Turner, and K. K. Tamma. An effective data parallel self-starting explicit methodology for computational structural dynamics on the Connection Machine CM-5. International Journal of Numerical Methods in Engineering, 38:3211-3226, 1995.

O'Neill, A. and Steenman-Clark, L. 2002. The computational challenges of Earth-system science. Philosophical Transactions of the Royal Society of London, Series A 360: 1267-1275.

Panday, S., and P.S. Huyakorn (2004). A fully coupled physically-based spatially-distributed model for evaluating surface/subsurface flow, *Advances in Water Resources*, *27*, 361-382.

Perkins, S.P. and A.D. Koussis, 1996, Stream–aquifer interaction model with diffusive wave routing. Journal of Hydraulic Engineering, American Society of Civil Engineers 122 (4), 210–218.

Pitman, A.J., Henderson-Sellers, A., Yang, Z.L., 1990. Sensitivity of regional climates to localised precipitation in global models. Nature 346, 734–737.

Pothen, A., D. H. Simon and K. P. Liou, Partitioning sparse matrices with eigenvectors of graphs, SIAM Journal of Matrix Analysis and Applications, 11 (1990), pp. 430-452.

Qu, Y., 2004, An integrated hydrologic model for multi-process simulation using semi-discrete finite volume approach., PhD Thesis, 2004, PSU

Rebaine, A., F. Fortin and A. Benmeddour, Parallelization of a Finite Volume CFD Code, ICPPW 04

Refsgaard, J. and B.Storm, 1996, MIKE SHE, pp 809-846 in Computer Models for Watershed Hydrology, Water Resource Public., Fort Collins, Colorado

Simon, H. D., Partitioning of unstructured problems for parallel processing, Computer Systems in Engineering, 2 (1991), pp. 135-148.

Tang, Y., P. Reed and T. Wagener, 2006, How effective and efficient are multiobjective evolutionary algorithms at hydrologic model calibration, HESS, 2, 2465-2520.

Vivoni E.R., V.Y.Ivanov, R.L. Bras, and D, Entekhabi (2004), Generation of triangulated irregular networks based on hydrological similarity, Journal of hydrologic engineering, *9*, 4. 288-302.

Vivoni., E.R., S. Mniszewski, P. Fasel, E.S. Springer, V. Y. Ivanov and R. L. Bras, Parallelization of fully distributed hydrologic model using Sub-Basin Partitioning, Fall AGU Annual Meeting, 2005.

Walshaw, C. and M. Cross. Parallel Mesh Partitioning on Distributed Memory Systems. In B. H. V. Topping, editor, Computational Mechanics Using High Performance Computing, pages 59-78.

Saxe-Coburg Publications, Stirling, 2002. (Invited Chapter, Proc. Parallel & Distributed Computing for Computational Mechanics, Weimar, Germany, 1999).

Williams, R. D., Performance of dynamic load balancing algorithms for unstructured mesh calculations, Concurrency: Practice and Experience, 3 (1991), pp. 457-481.

Zhang, Y.-L., Baptista, A.M. and Myers, E.P. (2004) A cross-scale model for 3D baroclinic circulation in estuary-plume-shelf systems: I. Formulation and skill assessment. Cont. Shelf Res. 24: 2187-2214.

Vanderstraeten, D. and R. Keunings, Optimized partitioning of unstructured finite element meshes, International Journal of Numerical Methods in Engineering, 38: 433-450, 1995

CHAPTER 7:

Parallelization of a fully-coupled hydrologic model on unstructured grid

7.1. Introduction

Physics-based distributed hydrologic models (DHMs) simulate multiple hydrologic states at numerous discretized locations within a watershed, in both space and time. With increase in spatio-temporal resolution of the model simulation and the number of predicted hydrologic states, these models become computationally intensive, rendering solution of large problems intractable or atleast not suitable for near real-time predictions on serial computers. The need to run DHMs at fine spatio-temporal resolution in large domains necessitates the use of high performance computing (HPC) systems. HPC systems are capable of solving problems at computational speeds unparalleled by the best workstations available while rationing large total memory, thus mediating the humongous amount of physical parameters describing heterogeneity in climate, land use, topography, vegetation and hydrogeology, all of which are necessary in DHMs.

Although growth in computing power and speed along with rapid decrease in hardware cost (Moore, 1965) facilitates the use of parallel computers for DHMs, efficient strategies for DHMs have not been common to date. One of the earlier implementations of a parallel DHM was performed by Morton et al. (1998) who developed a parallelized code for simulating hydrologic processes in Arctic regions, primarily on Cray architectures. Performance gains uptill 8 and 32 processors were obtained using MPI and CRAFT implementations respectively. Apostolopoulos and Georgakakos (1997) used ENCORE Parallel FORTRAN (EPF) for parallelization of a sub-basin based semi-distributed hydrologic model on 14 processors. EPF's like CRAFT and OpenMP (Chandra et al., 2001) are neither scalable, nor portable on distributed processors. Both these implementations performed partitioning on surface flow network only. Cui et al. (2005) parallelized a DHM by partitioning the watershed into sub-basins. All of the three studies a) have process-interaction representation that can at the most be considered as sequentially coupled (see definition in Langevin et al., 2005), b) do not consider lateral groundwater flow, and ignore flow interaction between aquifer and river element, and c) assume computational independence between sub-basins. Apart from the limitation that is inherent in these models due to sequential or weak coupling between processes, the flow topologies and process coupling representation in them are minimal (e.g. flow directions

determined by topographic gradient (one-way) rather than head gradient; one-way interaction between processes) and not be able to resolve dynamic fully-coupled behavior in real hydrologic systems.. A few parallelization studies on fully coupled DHMs have been tried. PARFLOW-Surface Flow (Kollet and Maxwell 2006) presented a parallelized, finite-difference based, fully coupled model by coupling overland flow with PARFLOW groundwater flow model (Ashby and Falgout 1996). Application of the parallelized coupled model on a 1D analytical setup to study surface-subsurface flow interactions recorded efficiency as high as 0.82 for 100 processors. The inherent simplicity of a structured grid in PARFLOW has the advantage of fast computations because of uniformity in the size of neighboring grids and the ease of determining grid's neighbors. Furthermore, the regularity of structured meshes makes the topology of the communication edges across different processors simpler. The computational advantage of modeling on structured grids is sometimes, however, offset by the need for very fine spatial discretization in order to capture local heterogeneities and boundary "edges". Limitations of structured mesh based computations because of its rigid structure are reviewed in detail in Kumar et al. (2009). Cheng et al. (2006) developed a parallelization code for fully coupled WASH123D model (called pWASH123D) which is based on unstructured grids. The model simulates flow system of one-dimensional (1-D) channel network, two-dimensional (2-D) overland regime, and three-dimensional (3-D) subsurface media. The advantage of an unstructured mesh is that it can provide an "optimal" representation of the domain with the least number of elements while still conforming to limited set of physical and geometric constraints. Also, it allows better representation of line-features such as the stream network, land-use/ land-cover boundaries and watershed boundaries (Kumar et al. 2009). pWASH123D partitioned the problem domain using PARMETIS (http://www-users.cs.umn.edu/ karypis/metis/parmetis/). The partitioning was however performed independently on 2D overland flow domain and 3D subsurface domain. No partitioning was performed on river and all the river segments were embedded on each overland and subsurface partition. For a watershed with large drainage density, this will add excessive computational load on individual processors. Application of the model on an experimental domain showed performance gains uptill 32 processors.

Here we present a parallelization strategy for unstructured grid based, fully-coupled DHM known as PIHM model (discussed in Chapter 4, Qu and Duffy 2007) on a cluster of 512 processors (maximum). The paper develops an application of graph theory based partitioning algorithms for assigning computational load on parallel processors. Unique hydrologic factors that influence the efficient partitioning for parallelized computation are highlighted and strategies to incorporate these factors in the partitioning algorithm are described. Numerical experiments exploring the scalability and speedup of the parallel code vis-à-vis the scale of problem, load balancing and interprocessor communication, in context of a real watershed with complex spatial parameter fields are presented.

7.2. Partitioning Strategy

Simply stated, the concept of designing parallelized solutions to system of partial differential equations is to divide the problem into discrete "chunks" that can be solved concurrently over multiple processors while sharing information with each other. There are two strategies of partitioning computational load among processors: Task partition and Data partition. In task parallelism, the code is split into independent pieces, often subroutines corresponding to different hydrologic processes, which are then assigned to different processors. In a fully-coupled hydrologic model, the processes interact closely at a variety of scales. This means that individual subroutines of land surface flow, subsurface and river flow interact with each other over a range of time scales resulting in frequent communication across processors. This quick interaction between processors essentially destroys the "coarse grain" parallel structure of task based partitions. Also, since the time scale of physical processes such as overland flow and groundwater flow are significantly distinct, time to compute each task on individual processors will be vastly different. In such situations, the performance of parallel code will be limited by the slowest processor, thus negatively impacting the time to complete a job. Task parallelism also limits the number of processors that can be utilized (because of the limited number of processes simulated in the hydrologic model) thus reducing the scalability of parallelization. On the other hand, in a data parallelization approach the same code

segment runs concurrently on each processor, but each processor is assigned its own part of the data (spatial domain in this case) to work on. Information is shared between neighboring elements of the domain which lie on different processors. Data parallelism strategy is scalable and can be used to run the parallel code on thousands of processors. However the efficiency of the parallel code crucially depends on how the partitioning of the model domain is performed on different processors. We explore this next.

7.3. Domain Partitioning: Issues posed by Hydrologic Models

The two objectives of domain partitioning are a) Load Balancing, and b) Minimization of interprocessor communication. The objective of load balancing is to ensure that computation on each processor finishes simultaneously during each time step, thus avoiding any idle-time delay incurred on processors which finish their jobs earlier than others. This leads to most efficient use of existing parallel computing resources. Communication of information between processors is time-expensive and it is crucial to minimize it as much as possible, less it can overwhelm the computation which is the primary objective of parallelization. The amount of computation and interprocessor communication is controlled by the hydrologic model structure, and the representation of processes and parameters and the mathematical form of coupling. Before we discuss the details of domain partitioning approach, we briefly review the model structure of PIHM.

7.3.1. PIHM model formulation

PIHM is a fully coupled, physically-based, spatially distributed hydrologic model. It simulates hydrologic states on an unstructured discretized domain using a semi-discrete, Finite-Volume approach. Unstructured meshes extend in vertical from the ground surface to the bedrock to form prismatic elements in 3D. Edges of the unstructured meshes form the river elements and are rectangular/trapezoidal in shape. The governing partial differential equations (PDEs) on each discretized element are locally reduced to ordinary differential equations (ODEs) by integration on a spatial unit element. The generic semi-discrete form of ODE that defines all the hydrologic processes incorporated in PIHM can be represented as

$$A_i \frac{d\overline{\psi}}{dt} = \sum_j N.\vec{G}A_{ij} + \sum_k N.\vec{F}A_{ik} + \overline{S}_\psi V_i \qquad (7.1)$$

where $\overline{\psi}$ (L) is the average volumetric conservative scalar per unit planimetric control volume area A_i, $\overline{S}_\psi$ is the average source/sink rate per unit control volume, $\vec{G}$ and $\vec{F}$ are vertical and lateral flux terms respectively and N is the normal vector to the surface j of the control volume i. Table 4.1 lists the vertical and horizontal flux terms associated with each state and identifies the coupled flux interactions between neighboring control volumes (both in vertical and in horizontal) through a process coupling function $f[]$. Individual vertical, horizontal and source/sink flux terms listed in Table 4.1 can be directly replaced in Eq. (7.1) to evaluate the respective state equations. The coupling function $f[]$ defined in Table 4.1 shows that the interaction between processes such as interception-snow, interception-unsaturated zone is "one-way" only, while interactions between unsaturated-saturated and river-saturated zone are "two-way". Explanations of the symbols can be referred to in Appendix I of Chapter 4. For more details about the individual process equations, readers are referred to Chapter 4.

7.3.2. Hydrologic Model Structure and Domain Partitioning Efficiency

The primary hydrologic factors that influence the computation and communication between processors and hence the efficiency of partitioning in a parallel code are:

a) Number of predicted hydrologic states and active hydrologic processes: With increasing number of prognostic hydrologic variables, the compute operations on each model grid also increases. As shown in Table 4.1, a total of five ODEs are defined on each unstructured grid in PIHM while two ODEs are defined on each linear element. This means the computational load is heterogeneously divided over the watershed. Heterogeneous computation also arises from transient activation of individual processes, such as macropore based stormflow or overland flow generation, in a localized part of the watershed (model domain). Such activations are time dependent and can only be addressed by a dynamic partitioning strategy. The "kernel flexibility" (see section 4.4.2) of PIHM also allows different representation of process equations for the same hydrologic state in different parts of the model domain. For example, we might use a relatively simple and computationally efficient, temperature-index based formulation for

snow-melt in a part of the model domain while a physics-based, multi-layer and computationally intensive energy-balance based formulation can be applied in rest of the domain. An efficient domain partitioning strategy should appropriately take account of heterogeneous computation arising due to any of the reasons documented above. More so, the partitioning strategy should be flexible enough to incorporate any number of process equations defined on each discretized element.

b) Discretization Strategy and Flow topology: The number of neighbors and hence the maximum number of possible interprocessor boundaries for a discretized element in the model is determined by the shape of unit elements and the topology of flow between adjacent elements. In PIHM, an unstructured element has three edge faces. As shown in Table 4.1, calculation of overland-flow depth and saturated zone depth depends on the corresponding hydrologic states in the adjacent triangles. This means that if an isolated triangular element is mapped to a particular processor while its neighbors are mapped to a different processor, it will be communicating a maximum of 3 edges x 2 hydrologic states = 6 units of data to neighboring processors. Similarly, any river element communicates a maximum of 6 units of data, 2 corresponding to flow between upstream/downstream elements plus 2 corresponding to overland flow to adjacent elements on either side of the river plus 2 corresponding to baseflow/recharge from/to the aquifer. This means that triangular edges which are also the river elements will have to communicate a larger amount of data than any other edge, thus resulting in a heterogeneous communication pattern in the watershed. The domain partitioning algorithm should take into account the heterogeneous communication between processors.

c) Order of Spatial accuracy: Higher spatial resolution and the order of the numerical approximation of the governing equations will increase the number of neighbor elements required to calculate a hydrologic state on any particular grid. For example, solutions on a grid cell for a first-order accurate hydrologic model such as PIHM requires knowledge of states on only three neighboring elements. For a second-order accurate hydrologic model such as FIHM (see Chapter 5), hydrologic states on all elements that share an edge or a vertex with the element under consideration needs to be known. This means that the amount of data communicated across processors in higher order number models is much larger.

7.4. Application of Partitioning Algorithms on PIHM unstructured mesh

The problem now is to obtain partitioning of the model domain that incorporates the challenges posed by hydrologic factors discussed in the previous section, while still satisfying its two primary objectives of minimizing interprocessor communication and ensuring load balance across processors. The partitioning problem can be formulated in terms of an undirected communication graph (Hu and Blake 1999) which is obtained by connecting unit elements which share information between each other. For a cell-centered based finite volume formulation, which is the case here, vertices of the communication graph are essentially the centroid of the elements, and the edge of the graph is the connecting segment joining the vertices. Edges connect the neighboring elements which share information with each other during a hydrologic state calculation. Such a graph is called the *dual graph* of the mesh. This approach is explained in detail in Hu and Blake, 1999. Figure 7.1 shows the dual graph for a representative domain discretization for PIHM. We note that the dual mesh obtained here is a bit different than traditionally obtained for unstructured grid based models. Specific communication connectivity (dual edges) is defined between river and watershed elements (triangles) and between river and upstream and downstream river elements (see Figure 7.1). Computation weights proportional to the number of ODEs solved on a particular element (5 for triangular elements and 2 for linear elements in PIHM) and communication weights proportional to the number of data units shared between neighboring elements (2 between triangle-triangle; 3 between river-triangle; 1 between river-river) are assigned to each vertex and edge of the dual graph respectively. Now we reformulate the partitioning problem on the dual graphs.

Given a dual graph (such as one shown in Figure 7.1), with n weighted vertices and m weighted edges, the objective is to divide the vertices into p partition sets in such a way that the sum of the vertex weights in each set is as close as possible and the sum of the weights of edges crossing between sets is minimized. The posed problem is NP-complete (Garey and Johnson 1979) and so it is hard to obtain the global optimum solutions. Several near-optimal techniques such as Recursive Inertial Bisection (Hendrickson and Liland 1994), Recursive Graph Bisection (RGB) (Williams 1991),

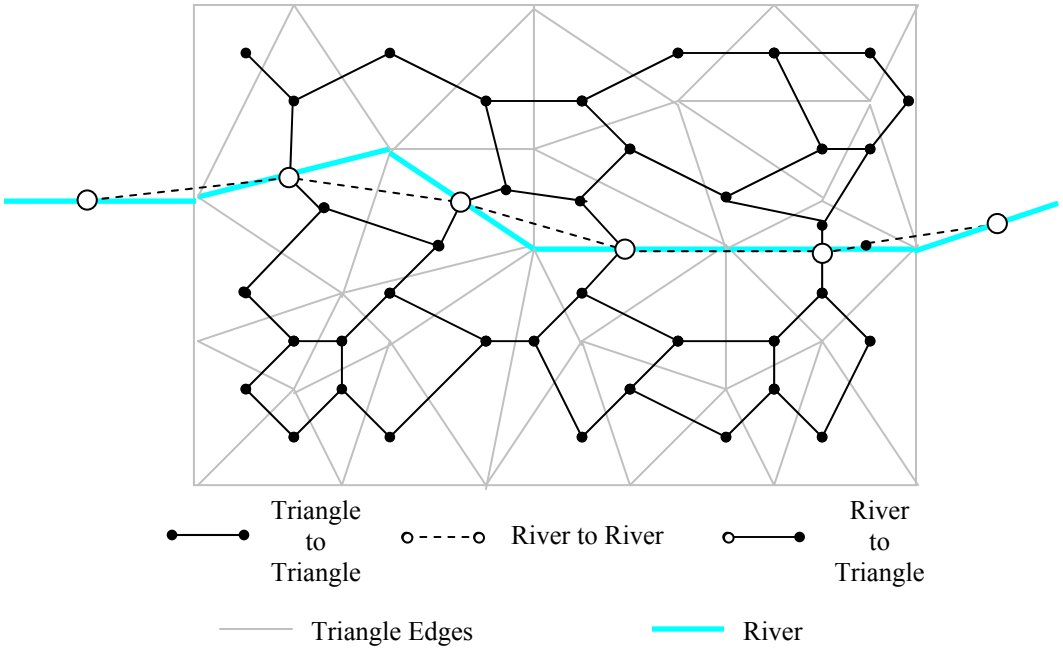

Figure 7.1 A representative dual graph for unstructured discretization of PIHM domain.

Recursive Spectral Bisection (RSB) (Pothen et al. 1990, Simon 1991), Multilevel partitioning (Barnard and Simon 1993) and Hybrid methods such as Multilevel-KL partitioning (Henderson and Liland 1995) exist for partitioning the dual graph. A review of partitioning algorithms and their comparative theoretical performance for hydrologic modeling is discussed in detail in Chapter 6. We use a slew of domain partitioning tools such as CHACO (http://www.cs.sandia.gov/CRF/chac_p2.html), JOSTLE (http://staffweb.cms.gre.ac.uk/~c.walshaw/jostle/) and METIS (http://glaros.dtc.umn.edu/gkhome/views/metis/) to partition the model domain using all the above methods. The best partition (in terms of theoretical metrics of communication of load) is used to carry out numerical simulation.

7.5. Code parallelization

The governing ODEs for the physical process (shown in Table 4.1) are solved using an implicit Newton-Krylov based solver called CVODE (Cohen and Hindmarsh, 1996). Within each integrator time step, the right hand side of ODEs that lie on each partition (and hence on separate processors) are evaluated. The message passing interface system

(MPI) (Gropp et al. 1999) is used to perform parallel communications between partitions at synchronization points, thus ensuring that data from other processes are available locally when needed. Extra care was taken to avoid the communication deadlocks. MPI global reduction operations such as dot products, weighted root-mean-square norms and linear sums are launched at each convergence iteration steps, based on the absolute and relative tolerance metric criteria (discussed in Brown et al. 1989). This location acts as the synchronization point, thus ensuring that all ODE evaluations are performed simultaneously with each processor while working on its local partition. The portability of the solver has already been successfully tested on IBM SP2, a Cray- T3D and Cray-T3E, and a cluster of Sun work stations (Wittman 1996). In this work, the developed parallelized code is run on IBM x3450 1U Rackmount Server with 64 GB of ECC RAM and Dual 3.0 GHz Intel Xeon E5472 (Woodcrest) Quad-Core Processors.

7.6. Experiments and Results

To demonstrate the effectiveness of the parallel model and the domain partitioning methodology, we implemented the model for the Little Juniata River Watershed, located in south central Pennsylvania. The watershed size is 845.6 sq. km. The watershed is characterized by significant complexity of the bedrock geology and physiography. Topography ranges from 204 to 800m above sea level, with the slope ranging from 0 to 55 degrees. The geology of the Little Juniata watershed consists of carbonate and siliclastic mix of around ten bedrock strata. Figure 4.7 shows the the spatial distribution of geology, soil, land cover, precipitation and elevation. We note that All types of physiographic, geologic and climate forcing distributed data and other topological relations are appropriately mapped to the model unstructured grid and discretized linear river elements in an automated way using PIHMgis (Bhatt et al. 2008).

7.6.1. Domain Decomposition

For grid generation, we use a constrained Delaunay triangulation based strategy (Kumar et al. 2009) to decompose the domain at four different spatial resolution scales. The

average spatial resolutions for the four discretizations are 412, 243, 169 and 99 m (square root of area). The discretizations were generated with increasing number of hydrographic and thematic constraints. Table 7.1 shows the details of the four discretization levels. The

Table 7.1 Details for four levels of discretizations of Little Juniata Watershed. VIPs stand for Very Important Points (Chen and Guevara 1987)

Discretization	Number of triangular elements (NTE)	Number of river elements (NRE)	Total number of ODEs (= 5* NTE +2*NRE)	Minimum, Maximum, Mean Area of Triangular Element (sq. m)	Minimum, Maximum, Mean Length of River Element (m)	Constraints
Case I	5065	1088	27501	1163, 1323137, 169607	38, 1725, 549	VIPs+Sub-watershed Bdd. +Rivers
Case II	14553	1751	76267	5.4, 149872, 59029	2.7, 926, 341	VIPs+Sub-watershed Bdd. +Rivers + Land Cover
Case III	30155	2608	155991	0.03, 59985, 28488	0.3, 564, 229	VIPs+Sub-watershed Bdd. +Rivers + Land Cover + Soil
Case IV	87645	4089	446403	0.03, 15999, 9801	0.3, 328, 146	VIPs+Sub-watershed Bdd. +Rivers + Land Cover + Soil

unique advantage of using these constraints in decomposition is that the resulting model grid accurately conforms to the boundaries. The use of thematic classes such as land cover or soil boundaries ensures a single class within each grid thus leading to non-introduction of any additional data uncertainty arising from subgrid variability of themes within a model grid (Kumar et al. 2009).

7.6.2. Domain Partitioning and Parallel Model Efficiency

The decomposed domain is partitioned using the algorithms discussed in section 4. The partitioning algorithms take into account the hydrologic factors while still ensuring load balance and minimization of interprocessor communication. The parallel model run is performed (for a maximum of 24 hrs.) to simulate hydrologic states for a period of year ranging from Nov, 1, 1983 to Oct, 31, 1985. More details regarding the simulation

settings are in section 4.5. The model is run at the four discretization scales to test the scalability and efficiency of the model. Before we delve into the individual experiments, we explain the parallel efficiency metrics which will be used for comparative analysis of the experiments.

The efficiency of a parallel simulation is quantified as the ratio of Speedup to the number of processors. Speedup, S_{N_p}, is defined as the ratio of wall-clock time for a serial program to the time for a parallel version of the same program. Assuming the total wall clock time for the serial code to be T_1, it can be broken into a parallelizable part and a nonparallelizable part as

$$T_1 = T_{ser} + T_{par} \tag{7.2}$$

where T_{par} is the time for the parallelizable part and T_{ser} is for the serial part. If the same program is run on N_p processors, the total wall clock time, T_{N_p}, can then be written as

$$T_{N_p} = T_{ser} + \frac{T_{par}}{N_p} + T_{comm} \tag{7.3}$$

where T_{comm} is the interprocessor communication time. The efficiency of the parallel program then can be calculated as (Amdahl, 1967)

$$E = \frac{S_{N_p}}{N_p} = \frac{T_1 / T_{N_p}}{N_p} = \frac{T_{ser} + T_{par}}{N_p (T_{ser} + \frac{T_{par}}{N_p} + T_{comm})} \tag{7.4}$$

In our case $T_{ser} << T_{par}$, which results in the parallel efficiency to be approximated as

$$E = \frac{T_{par}}{T_{par} + N_p T_{comm}} \tag{7.5}$$

This means that a maximum efficiency of 1 can be obtained. Scalability refers to a parallel implementation's capability to demonstrate a proportionate increase in parallel speedup with additional processors.

7.6.2.1. Experiment 1: Domain Partitioning with Load Balance and Minimum Communication

The partitionings for 2, 4, 8, 16, 32, 64, 128, 256 and 512 processors for all the four

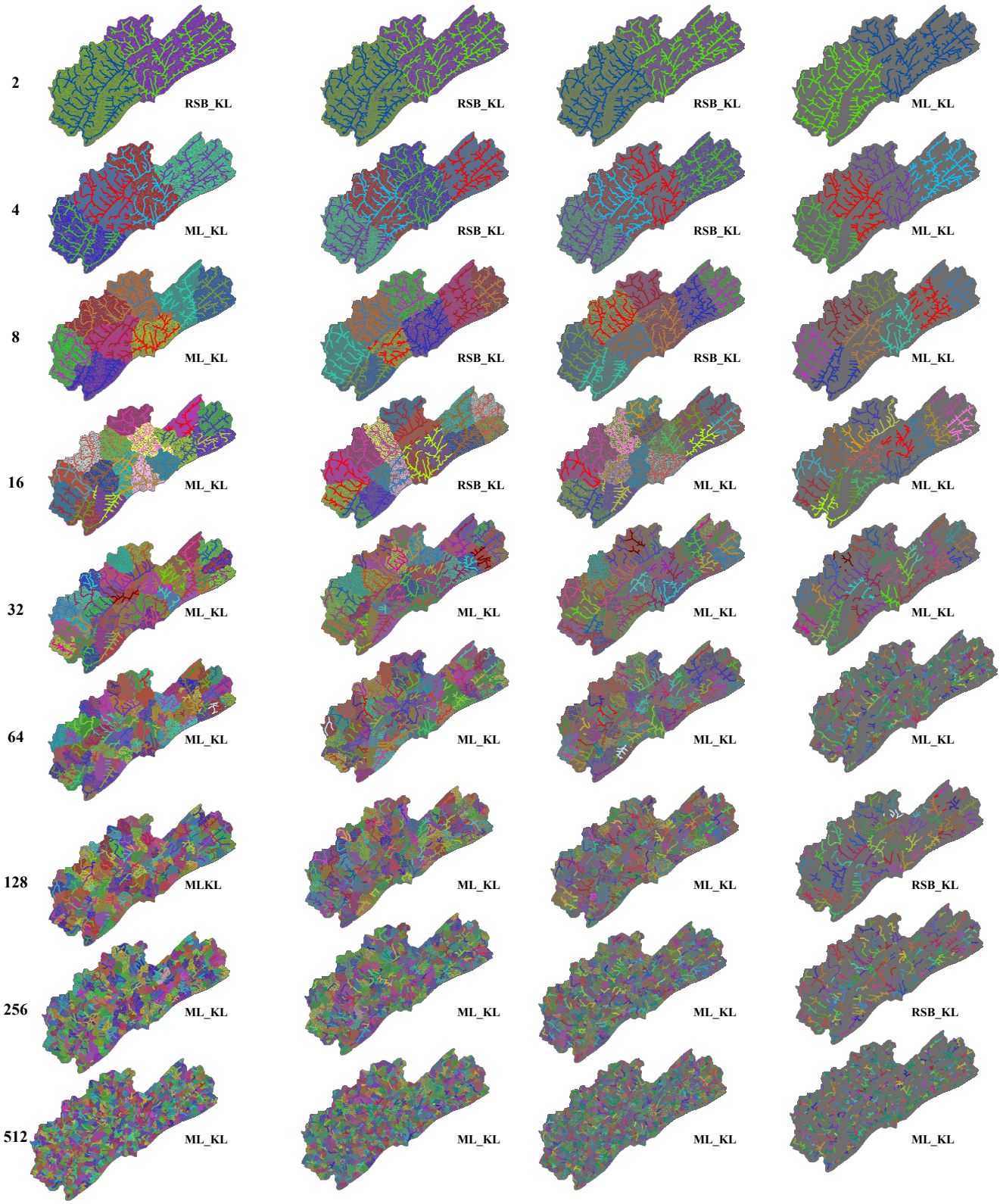

Figure 7.2 Domain partitioning results for the Little Juniata watershed on 2, 4, 8, 16, 32, 64, 128, 256 and 512 processors (top to bottom) and for four discretization levels listed in Table 7.1. The partitioning algorithm used for each partition is also shown. RSB_KL ≡ Recursive Spectral Bisection Method with Kernighan-Lin Refinement. ML_KL ≡ Multi-Level Method with Kernighan-Lin Refinement

discretization levels listed in Table 7.1 are shown in Figure 7.2. Fig 7.3 shows the efficiency of the parallel code for simulation on corresponding partitions. We note with increasing size of the number of processors for the same level of discretization, efficiency

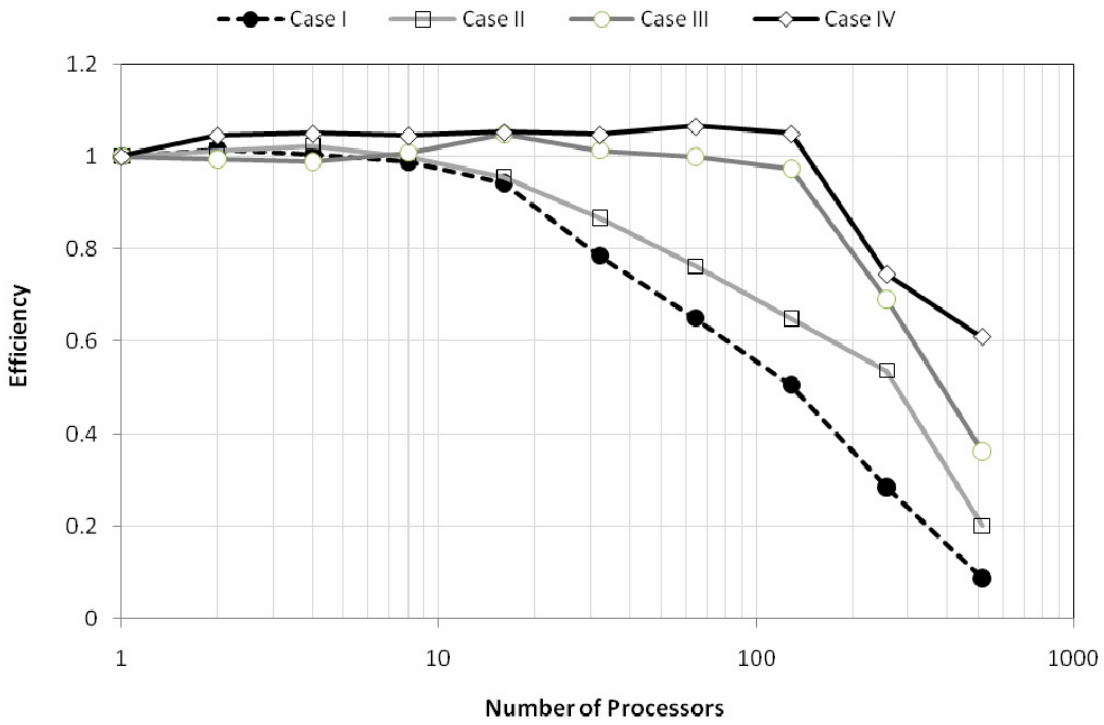

Figure 7.3 Efficiency of parallellized PIHM model at four discretization levels for processors 1,2,4,8,16,32,64,128,256 and 512 processors. Configuration details of each case is listed in Table 7.1.

of the code decreases. This is because of the increase in communication between processors while the amount of total computation remains same. We also observe that as the size of the problem (or number of meshes) increases, a higher efficiency is sustained to a greater degree even for larger number of processors. For example, parallel efficiency in Case IV remains (greater than or) equal to one for 128 processors and it decreases only to 0.6 for 512 processors. Comparatively for Case I simulation where the size of the problem is much smaller, the parallel efficiency reduces to around 0.63 for 64 processors. The results can be explained based on equation 7.5 which can be rewritten as

$$E = \frac{1}{1 + N_p \dfrac{T_{comm}}{T_{par}}} = \frac{1}{1 + N_p R} \tag{7.6}$$

where R is communication to computation ratio. R is directly proportional to $\frac{E_c}{N_{ODEs}}$

where, E_c is the number of edge cuts in the dual graph i.e. the number of edges that connect vertices assigned to different partitions and N_{ODEs} is the number of ODEs being solved. R for all the processors and the discretization levels is plotted in Figure 7.4. We note (from Eq. 7.6) that larger is the R, smaller will be the efficiency. From Figure 7.4, for large problems R is much smaller than for the smaller problems (coarser discretizations) thus resulting in sustained efficiency even for larger number of processors. This experiment shows that a higher efficiency can be expected for larger number of processors as the size of the problem increases.

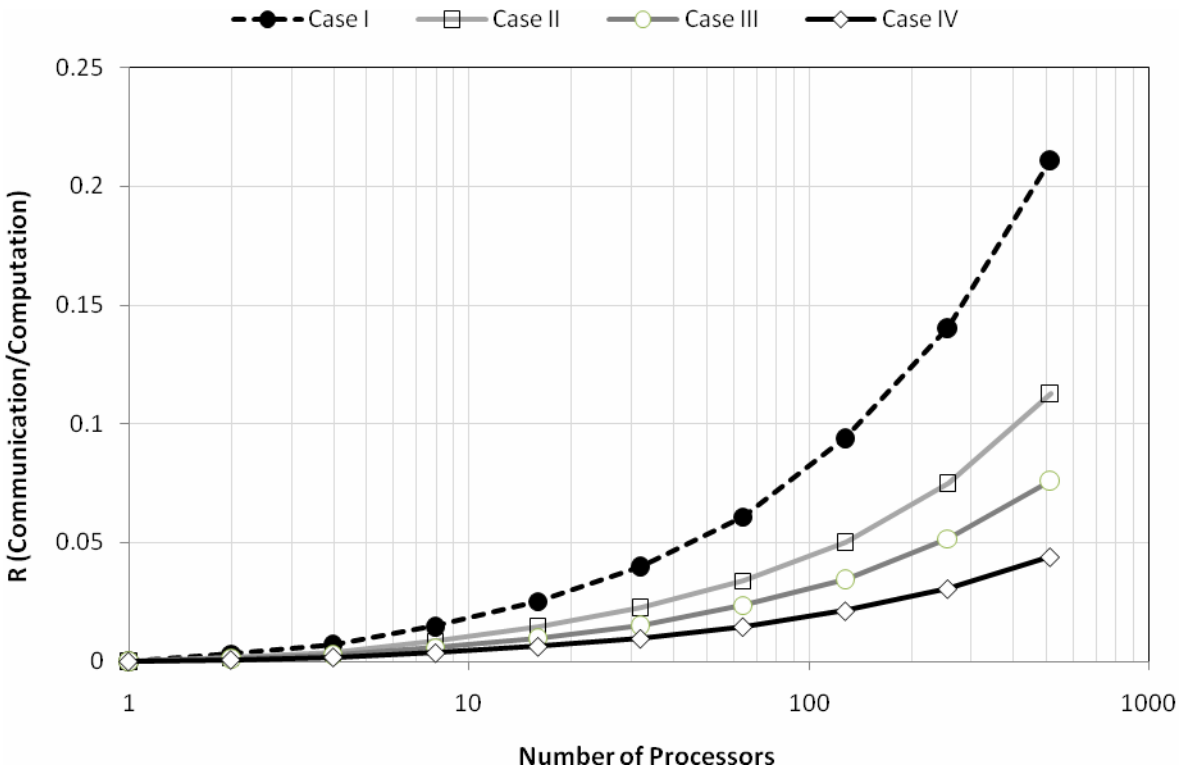

Figure 7.4 Communication to computation ratio for all four discretization levels for processors 1,2,4,8,16,32,64,128,256 and 512 processors. Note that for larger size problems (finer discretizations), the ratio is small. Configuration details of each case is listed in Table 7.1.

7.6.2.2. Experiment 2: Domain Partitioning with Load Balance and Minimum Communication

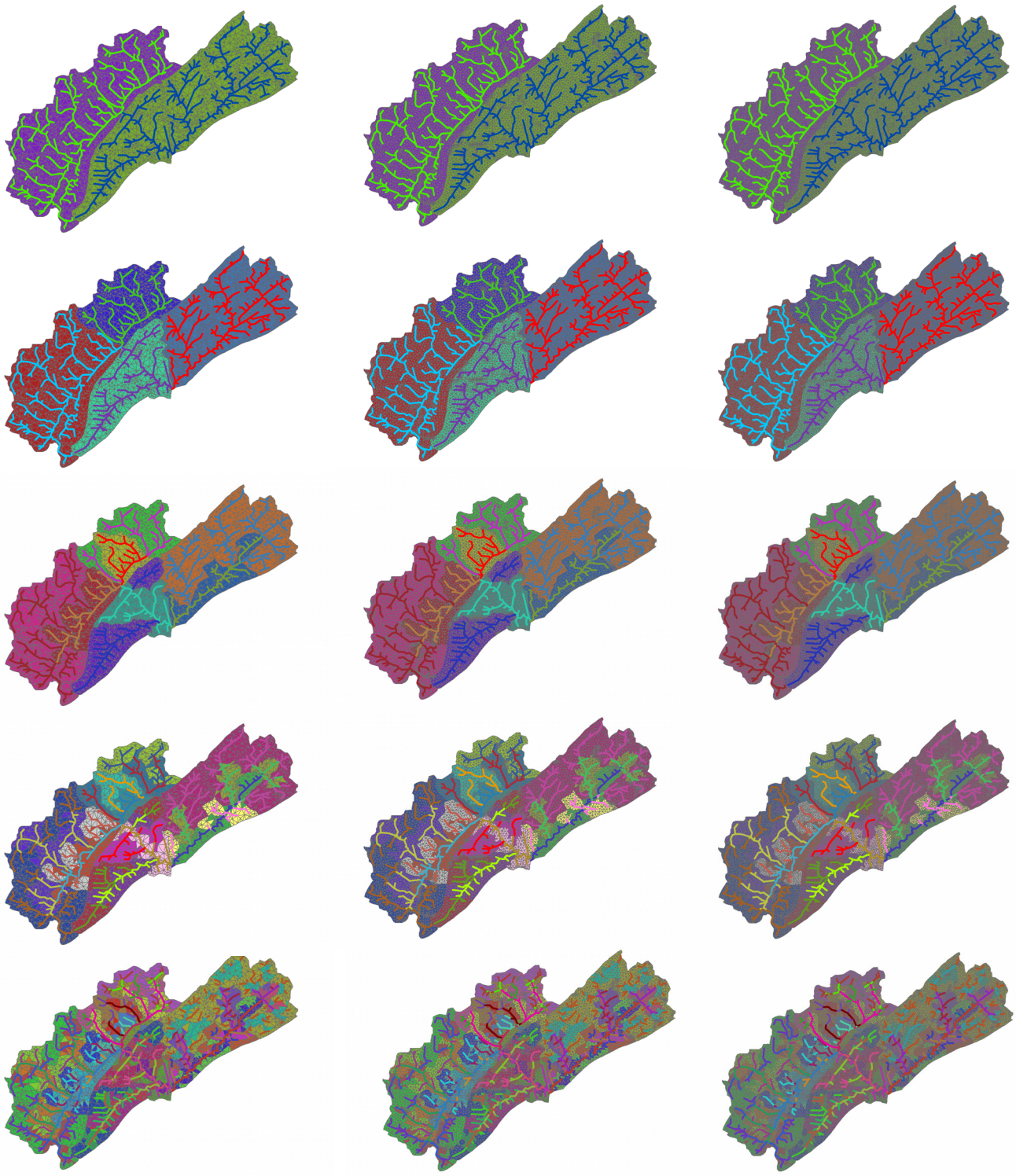

Figure 7.5 Partitioning of the domain based on sub-watersheds for 2, 4, 8, 16 and 32 processors.

The effectiveness of the proposed domain partitioning algorithms w.r.t traditional strategy of partitioning watersheds based on sub-watersheds (such as in Cui et al. 2005, Vivoni et al. 2005) is explored. We partitioned discretization cases I, II and III with upto

32 processors based on sub-watersheds (see Figure 7.5). Sub-watersheds contributing to same Strahler order stream (Strahler 1952) were classified into identical partitions. Figure 7.6 show the parallel efficiency of the code for sub-watershed based partitioning. The efficiency, even for the largest problem (case III) in this case, for 32 processors is only 0.19. Comparatively, parallel efficiency using the proposed partitioning strategy is 1 for 32 processors. The reduced efficiency is because of the load imbalance and large communication across sub-watershed boundaries. We note that in this experiment, communication between processors for groundwater flow, overland flow and river has been considered.

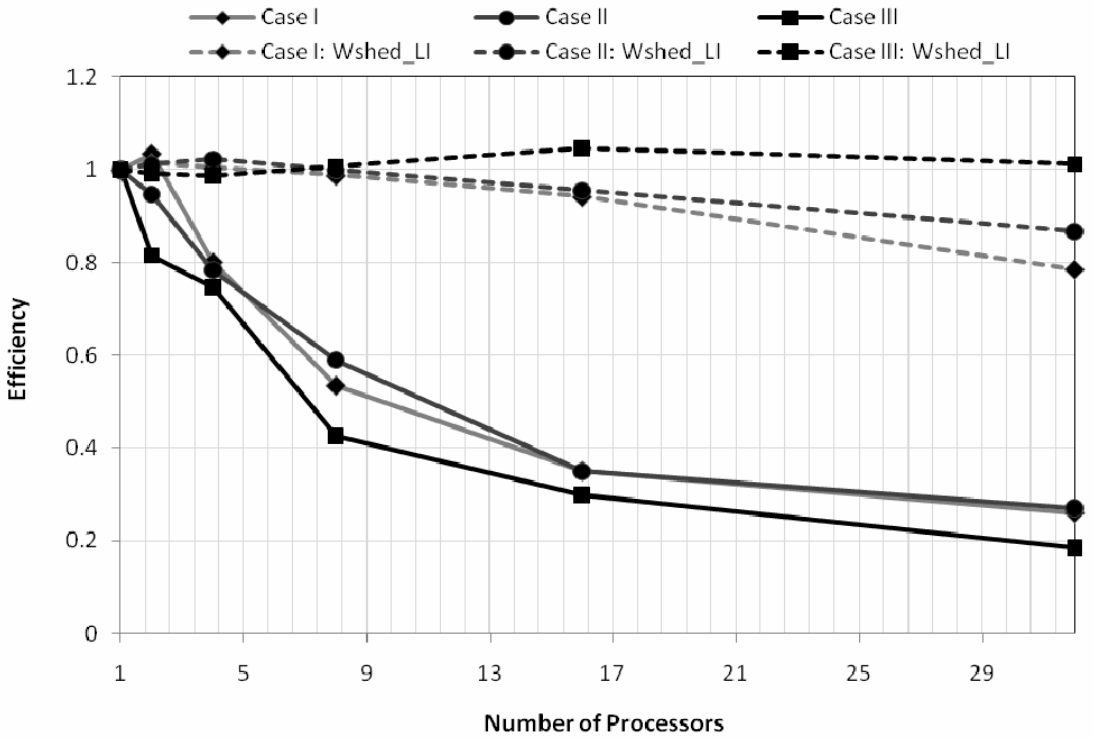

Figure 7.6 Parallel efficiencies for (load balance + minimum communication) based partitioning and for load imbalanced, sub-watershed (Wshed_LI) based partitioning at three discretization levels (details in Table 7.1). Sub-watershed based parallelization performs poorly w.r.t to simulation on optimal partitions.

7.6.2.3. Experiment 3: Impact of Load Imbalance and Communication Minimization on Parallel Efficiency

Next we explore the impact of load imbalance on parallel efficiency. Starting with the Case II discretization and a partitioning-set for 16 processors, reassignment of cells

between two partitions were performed to create load imbalance while still minimizing the interprocessor communication (see Figure 7.7). Load balance ratio was quantified by

$$\text{Load Balance Ratio} = \frac{\sum_{i}^{N_p} N_{E_i}}{N_p \max(N_{E_i})} \text{ x } 100 \qquad (7.7)$$

where N_{E_i} is the number of element in i^{th} partition. For a perfectly balanced partition set, load balance ratio is equal to 100. As the load imbalance increases, the ratio becomes smaller. Figure 7.8 shows the total wall-clock time taken by 16 processors to simulate of 125 days. We note that with increasing load imbalance (decreasing load balance ratio), the time taken by 16 processors to simulate same number of days increases as one might expect.

In this last experiment we quantify the impact of minimization of communication in domain proposed partitioning. Using the Case I discretization of the domain, we

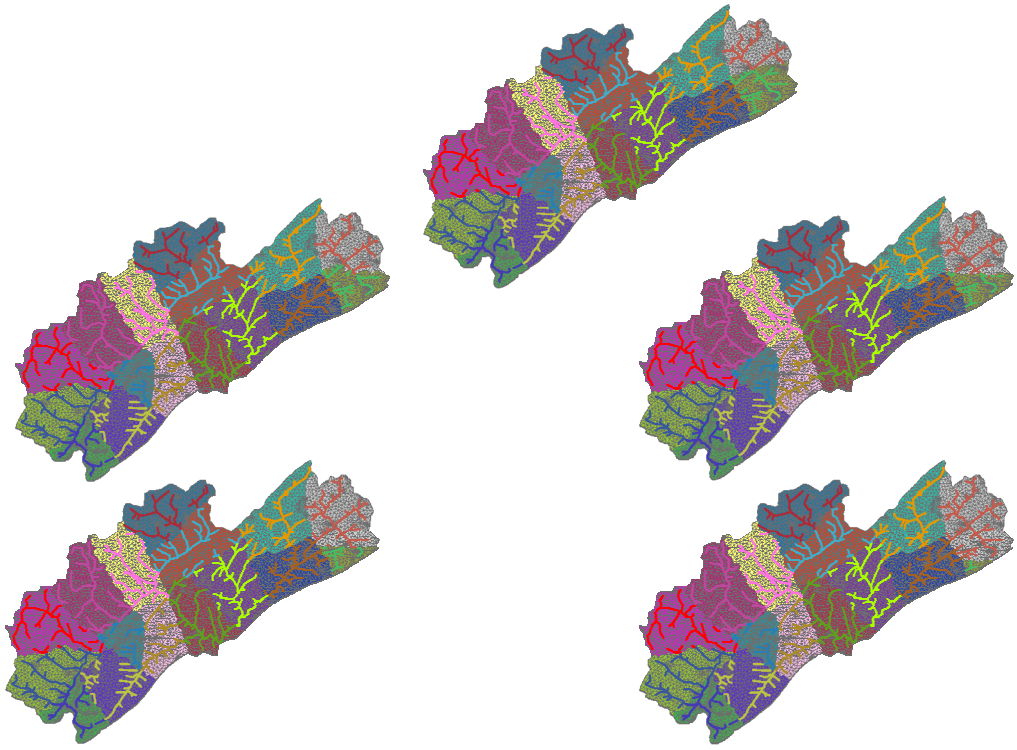

Figure 7.7 Repartitioning of Case II discretization (see Table 7.1) to generate load imbalance between processors. The partitioning is performed using RSB_KL (Recursive Spectral Bisection + Kernighan refinement) algorithm

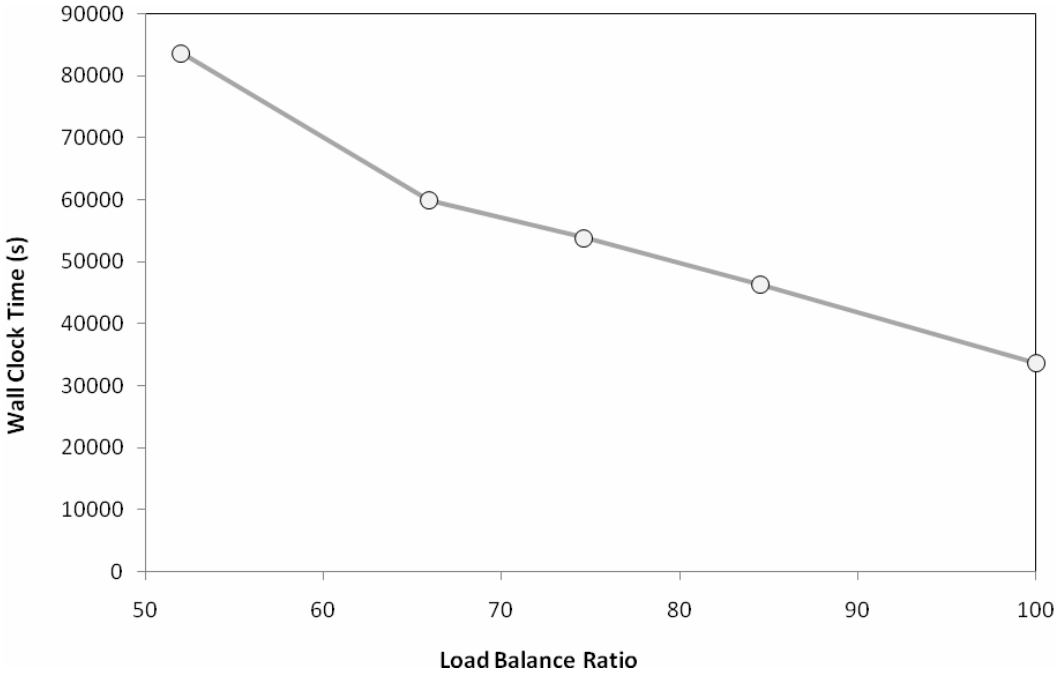

Figure 7.8 Wall clock time to solve the same problem increases with decrease in load balance.

partitioned the domain in such a way that load balance between processors is ensured. However the minimization in communication was not enforced (referred to as unconstrained case). This results in the number of edge-cuts (and hence the communication) for the unconstrained case to be an order of magnitude higher than in constrained case. For partitions of 2, 4, 8, 16, 32 and 64, the number of edge-cuts for constrained and unconstrained cases are (82, 5690), (196, 8354), (406, 10688), (682, 11634), (1082, 12318) and (1654, 13102) respectively. The new partitions are shown in Figure 7.9. Comparing the parallel efficiency for the two cases in Fig. 7.10, we see that efficiency for partitions with minimized communication is consistently larger for all processors. These experiments underscore the importance of load balance and minimization of communication for efficient parallel hydrologic model simulations.

7.7. Conclusion

A parallelized, fully coupled distributed hydrologic model (pPIHM) for simulation of

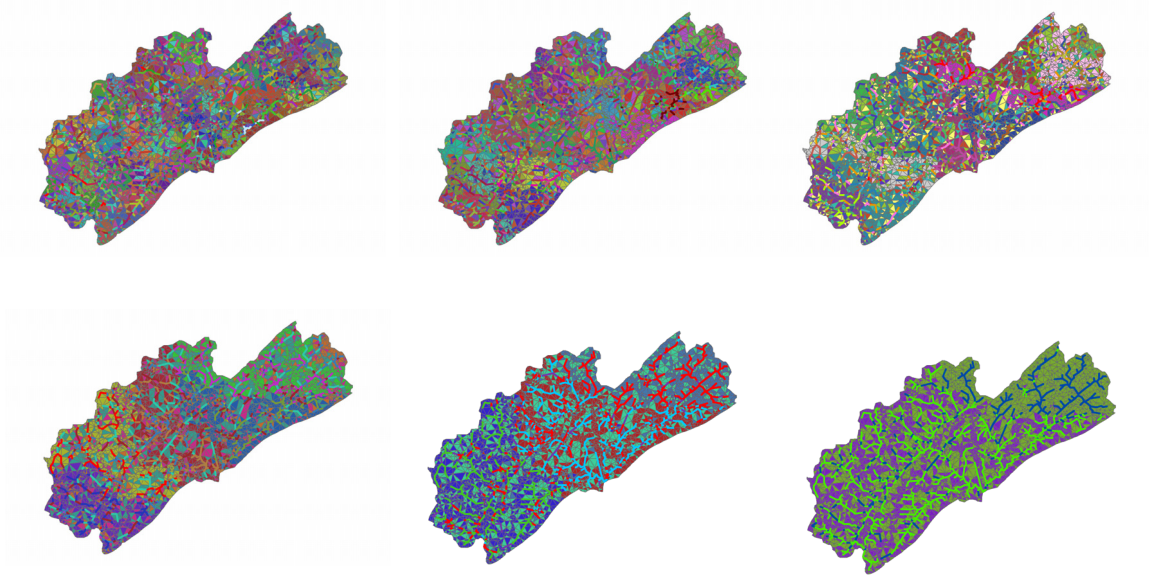

Figure 7.9 Partitioning of Case I discretization (see Table 7.1) while ensuring load balance but no minimization of interprocessor communication

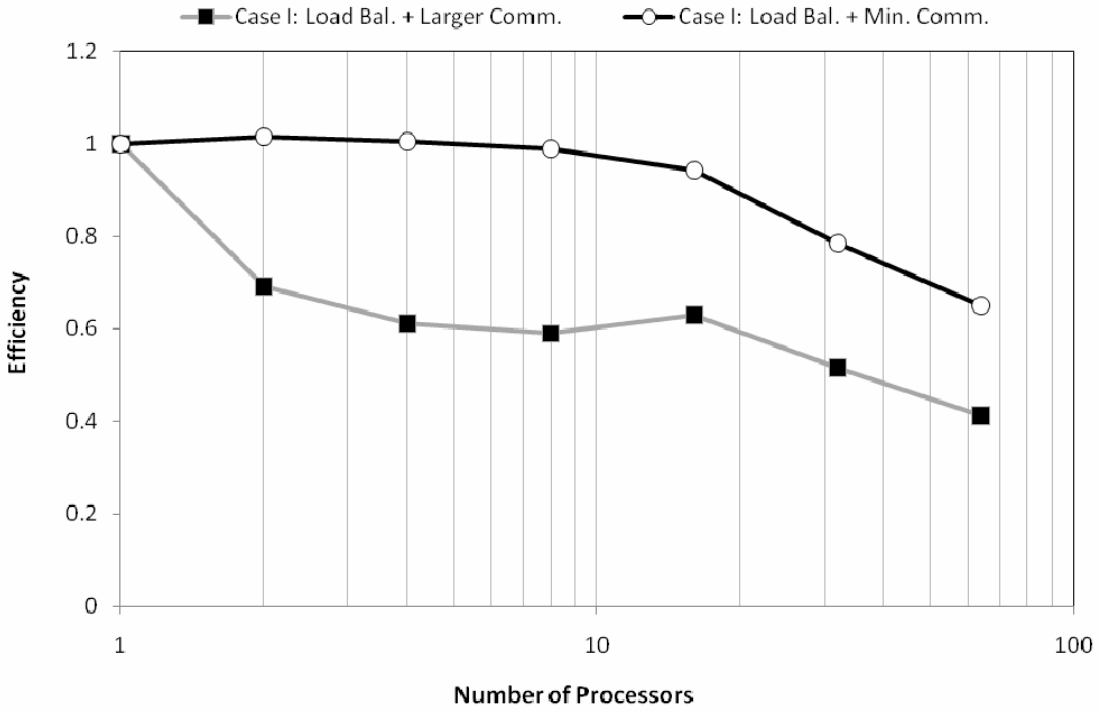

Figure 7.10 Comparison of parallel efficiency for upto 64 processors with the case for minimized communication to where no such condition for communication minimization is ensured

hydrologic states on large parallel processors is presented. We show the importance of optimal domain partitioning for efficient parallelization of a hydrologic model. In concept, the partitioning strategy is generic and coupled be applied to other fully

distributed hydrologic models. Using the simulation results for the four constrained discretizations, we intend to study the changes in the hydrologic states at multiple scales and parameter resolutions. Of future interest to us are the changes at the transition boundaries of land-cover and soil classes and study how a constrained based, single-class discretization impacts the hydrologic state simulation.

7.8. References

Anderson, J.D., 1995. Computational Fluid Dynamics, The Basics with Applications, McGraw Hill.

Apostolopoulos, T.K., and K.P. Georgakakos, 1997. Parallel computation for streamflow prediction with distributed hydrologic models, Journal of Hydrology, 197, 1-24.

Ashby., S.F, Falgout., R.D, 1996. A parallel multigrid preconditioned conjugate gradient algorithm for groundwater flow simulations. Nucl. Sci. Eng.;124(1):145–59;

Barnard, S.T. and Simon, H.D., 1993. A fast multilevel implementation of recursive spectral bisection for partitioning unstructured problems, Proceedings of the 6th SIAM conf. on parallel processing for scientific computing", p711-718

Bradford, S.F. and Sanders, B. F. (2002),Finite-Volume Model for Shallow-Water Flooding of Arbitrary Topography, Journal of Hydraulic Engineering, 128(3), pp. 289-298.

Brown, P. N., G. D. Byrne, and A. C. Hindmarsh. 1989. VODE, a variable- coefficient ODE solver. SIAM J. Sci. Stat. Comput. 10 (5): 1038- 51.

Byrne, G. D., and A. C. Hind marsh. 1998. User documentation for PVODE, an ODE solver for parallel computers. Technical report UCRL- ID- 130884, Lawrence Livermore National Laboratory.

Chen and Guevara, 1987 Z.-T. Chen and J.A. Guevara, Systematic selection of very important points (VIP) from digital terrain model for constructing triangular irregular networks. In: N. Chrisman, Editor, Proceedings of Auto-Carto 8 (Eighth International Symposium on Computer-Assisted Cartography), American Congress of Surveying and Mapping, Gaithersburg, MD (1987), pp. 50–56.

Cai, X., 2003. Overlapping domain decomposition methods, Advanced Topics in Computational Partial Differential Equations – Numerical Methods and Diffpack Programming, H. P. Langtangen and A. Tveito editors, Springer.

Chandra, R., Dagum, L., Kohr, D., Maydan, D., McDonald, J. and Menon, R. (2001) Parallel Programming in OpenMP, Morgan Kaufmann Publishers Inc., San Francisco, CA.

Cheng, J.-R. C., R. M. Hunter, H.-P. Cheng, H.-C. J. Lin, and D. R. Richards: May 15-19, 2005, 'Parallelization of the WASH123D code—Phase II: coupled two-dimensional overland and three-dimensional subsurface flows'. In: World Water & Environmental Resources Congress. Anchorage, Alaska, USA, EWRI CD-ROM

Cohen, S. D., and A. C. Hindmarsh. 1994. CVODE user guide. Technical report UCRL-MA- 118618, Lawrence Livermore National Laboratory.

Cohen, S. D., and A. C. Hindmarsh. 1996. CVODE, a stiff/non-stiff ODE solver in C. Computers in Phys ics 10 (2): 138- 43.

Cui. Z., B. E. Vieux, H. Neeman, and F. Moreda, 2005. Parallelization of Distributed Hydrologic Mode, International Journal of Computer Applications in Technology, 22, 1.

Garey, M.R.; Johnson, D.S., 1979. Computers and Intractability: A Guide to the Theory of NP-Completeness. New York: W.H. Freeman.

Gropp, W., Lusk, E. and Skjellum, A., 1999. Using MPI: Portable Parallel Programming with the Message-Passing Interface, 2nd ed., MIT Press, Cambridge, MA.

B. Henderson and R. Leland, 1995. A multilevel algorithm for partitioning graphs, in Proceeding of Supercomputing '95, ACM.

Hendrickson, B. and R. Leland, 1994. An empirical study of static load balancing algorithms, In Proceedings of the Scalable High Performance Computer Conference, pp. 682-685,IEEE

Hu, Y. and R. Blake, 1999.Load balancing for unstructured mesh applications. Parallel and Distributed Computing Practices, 2(3)

Kollet S.J, Maxwell R.M, 2006. Integrated surface-groundwater flow modeling: A free-surface overland flow boundary condition in a parallel groundwater flow model, Advances in Water Resources, (29)7, 945-958

Kumar M, Bhatt G, Duffy C.J., 2009 An efficient domain decomposition framework for accurate representation of geodata in distributed hydrologic models, International Journal of GIS; vol 33.

Langevin C, Swain E, Wolfert M., 2005. Simulation of Integrated Surface-Water/Ground-Water Flow and Salinity for a Coastal Wetland and Adjacent Estuary. Journal of Hydrology 314 (1-4), 212-234

D. J. Morton , Z. Zhang , L. D. Hinzman , S. O'Connor, 1998. The parallelization of a physically based, spatially distributed hydrologic code for arctic regions, Proceedings of the 1998 ACM symposium on Applied Computing, p.684-689, February 27-March 01, 1998, Atlanta, Georgia, United States

Moore, G.E., 1965. Cramming more components onto integrated circuits, Electronics, Vol. 38, No. 8, pp.114–117.

Pacheco, P.S., 1997, Parallel Programming with MPI, Morgan Kaufmann.

Pothen, A., D. H. Simon and K. P. Liou, Partitioning sparse matrices with eigenvectors of graphs, SIAM Journal of Matrix Analysis and Applications, 11 (1990), pp. 430-452

Qu Y, Duffy CJ. 2007. A semi-discrete finite volume formulation for multi-process watershed simulatioin, Water Resourc. Res

Simon, H. D., 1991. Partitioning of unstructured problems for parallel processing, Computer Systems in Engineering, 2, pp. 135-148

B. Smith, P. Bjorstad and W. Gropp, 1996. DomainDecomposition, Cambridge University Press, Cambridge, UK.

M. Snir, S. Otto, S. Huss-Lederman, D. Walker and J. Dongarra, 1998. MPI – The Complete Reference, Volume 1, The MPI Core, The MIT Press, Massachusetts, USA.

Strahler, A. N., 1952. Dynamic basis of geomorphology. Geological Society of America Bulletin, 63, 923-938.

Vivoni, E. R.; Mniszewski, S.; Fasel, P.; Springer, E.; Ivanov and V. Y.; Bras, R. L. 2005, Parallelization of a Fully-Distributed Hydrologic Model using Sub-basin Partitioning, AGU Fall Meeting, San Francisco

Williams, R. D., 1991. Performance of dynamic load balancing algorithms for unstructured mesh calculations, Concurrency: Practice and Experience, 3, pp. 457-481

Wittman, M. R. 1996. Testing of PVODE, a par allel ODE solver. Technical report UCRL- ID- 125562, Law rence Livermore National Laboratory.

Zhou, J.G., Causon, D.M., Mingham, C.G., and Ingram, D.M., 2001. The Surface Gradient Method for the Treatment of Source Terms in the Shallow-Water Equations, Journal of Computational Physics, 168, 1-25.

CHAPTER 8:

Synthesis

8.1. Summary of Scientific Contributions

This dissertation comprehensively addresses a set of challenges posed by large scale, physics based, distributed hydrologic modeling. The work builds on the earlier work of Qu (2004) who developed the first generation version of PIHM for unstructured grids and his efforts recognizing the linkage between the physical model and data. The present study addresses a range of challenges that include: accurate and efficient representation of data in models; seamless transfer of data between modeling, management and visualization components; physics-based representation and numerical solution of processes; and finally integrating data, processes and numerics for large scale simulation.

Chapter 2 presented a flexible domain decomposition strategy for efficient and accurate integration of the physiographic, climatic and hydrographic watershed features. The approach took advantage of different GIS feature types while generating high-quality unstructured grids with user-specified geometrical and physical constraints. The proposed decomposition framework is a critical step in implementing high quality, multiscale, multiresolution, temporally adaptive and nested grids with least computational burden. The framework is generic and can be used in other finite element/volume based hydrologic models. It outperforms structured grids and traditional unstructured meshes (and TINs) based representations in terms of accurate representation of raster and vector layers.

Chapter 3 presented the design and details of a shared data model which can support coupling of GIS with a hydrologic model. The developed data model is rich yet flexible in terms of its extensibility and simplicity. The data model incorporates representation of wide range of data types varying from static and floating points to 3D feature line and volume objects. The conceptualization and characterization of this coupling strategy can be used with other physically distributed models and can be extended to management, visualization and decision support tools (e.g. ecological models). The object oriented strategy streamlines the design of the data model and clarifies the relationships between classes. The shared data model concept creates a process for modeling that improves data flow, model parameter development, parameter steering, efficient grid design and allows real time visualization and decision support.

Based on the shared data model paradigm and with the flexible domain decomposition strategy (developed in chapter 2), an open-source GIS (http://sourceforge.net/projects/pihmgis/) have been developed.

Chapter 4 presented coupling of physical processes, natural numerical coupling, and parsimonious but accurate data coupling for efficient and accurate simulation of distributed hydrologic states in watersheds. Data-coupling is aided by the use of constrained unstructured meshes (developed in Chapter 2), and a flexible data model (developed in Chapter 3) incorporated within an open-source GIS tool (PIHMgis). The spatial adaptivity of the mesh elements and temporal adaptivity of the numerical solver facilitates capture of multiple spatio-temporal scales, allowing important insight into hydrologic process interactions. The fully-coupled model unfolds a range of multiscale/multiprocess interactions including: 1) an apparent inverse relationship between fraction of total evapotranspiration rate due to transpiration and interception loss, 2) the role of forcing (precipitation, temperature and radiation), soil moisture and overland flow on evaporation-transpiration partitioning, 3) the importance of water table depth on evaporation-transpiration, 4) the influence of local upland topography and stream morphology on spatially distributed, asymmetric right-left bank river-aquifer interactions, and, 5) the role of macropore and topography on ground water recharge magnitude, time scale and spatial distribution. New predictions in terms of distributed spatio-temporal stream-aquifer interaction (gaining/loosing streams) maps, groundwater recharge maps, distributed stream flow maps and process separation at multiple scales is obtained. We attempt to make a case for the importance of an integrated modeling framework, which in the future will also require a new kind of observing system that can resolve and test the coupled dynamic predictions beyond the a-priori data used here. The integrated theory and shared data-model provides a new way to "explore" hydrologic states and can be used to develop scenarios of change for parameters, forcing data sets, and new descriptions of the physical processes. The success of this fully-coupled model in predicting the stream flow hydrographs at the outlet and internal points in a basin of this size (~900 sq. km) while also capturing process interactions within in the watershed at adaptively fine time scales lends credence to the potential of using fully coupled distributed hydrologic models for operational forecasting, water management, as well as

a research and analysis tool to answer and unravel science questions. The developed model is available open-source at http://sourceforge.net/projects/pihmmodel/.

Chapter 5 presented a physically distributed, fully coupled, second order accurate, upwind cell-centered, constrained unstructured mesh based Finite-Volume modeling framework (FIHM) that simultaneously solves unsteady overland and subsurface flow equations in heterogeneous, anisotropic domains. The model simulates a full three dimensional solution for saturated–unsaturated flow in the subsurface and a two-dimensional solution for overland runoff on the surface. Using a set of eight experiments we show the influence of soil heterogeneity, anisotropy and topography on the distribution of moisture above and below the ground surface. The capability of the integrated model to simulate flow behavior in heterogeneous, anisotropic materials showed the possible development of unique, local "flux rotation" phenomena. The experiments also underscore the degree to which detailed coupled surface-subsurface physics can be studied, such as where runoff generation and infiltration become closely coupled to underlying groundwater levels and adjacent surface water states. The model took advantage of constrained Delaunay triangulation for domain decomposition (developed in Chapter 2), which is also supported by a "shared data model" (developed in Chapter 3), leading to accurate representation of data and fast prototyping of model experiments. The test cases presented were chosen not only to compare individual model components against classical examples from the literature (e.g. 1-D unsaturated flow or 2-D surface flow), but to further examine the degree to which individual unsaturated-saturated zone flow or surface-subsurface processes are affected by each other. Representative experiments explored in detail the influence of drainage from unsaturated zone on delayed water table drawdown, the role of water table position on infiltration and surface runoff, and the interaction of overland flow-groundwater exchanges in relation to the dynamics of infiltrating/exfiltrating surfaces on the hillslopes. The experiments presented showed a) the influence of initial moisture conditions, soil properties, anisotropy and heterogeneity in determining the pressure head distributions in the vadose and saturated zones, b) the existence of localized "flux rotation" phenomenon due to heterogeneous anisotropy, leading to creation of convergence-divergence zones, c) the influence of vertical drainage from unsaturated zone on the response of an unconfined

aquifer to pumping, and d) the effects of capillarity, saturation excess, infiltration excess, and initial water table location on determining the overland flow generation.

In order to perform high temporal and spatial resolution simulations of fully-coupled hydrologic models (developed in Chapter 4 and 5) in a large problem domain in feasible time, parallelization of the model needs to be performed. An efficient parallelization of a fully-coupled hydrologic model requires optimal partitioning of the model domain. Chapter 6 examines the issues which impact efficient domain partitioning for a parallelized hydrologic model. In particular, we identify the hydrologic issues such as time scale of hydrologic processes, the frequency of communication, number of interacting processes, coupling behavior, numerical solution strategy and unit element shapes of decomposed domain, which impact the efficiency of parallelization. We show the strategy to incorporate hydrologic factors in existing domain partitioning algorithms and compare their efficiency in a) minimizing interprocessor communication, b) load balancing, c) adaptability to constraints, and d) capture of actual communication volume. The experiments show that hybrid algorithms are most effective in minimizing communication volume. We also highlight the conflicting criteria that impacts total communication time and limit the effectiveness of theoretical communication metrics in modeling actual communication time on distributed processors.

Using the partitions and the hydrologic factors studied in Chapter 6, Chapter 7 presented the development and implementation of Parallelized Pennstate Integrated Hydrologic Model (pPIHM). The efficiency of the model simulation is achieved by utilization of optimal domain partitioning algorithm. The efficiency and scalability of the parallel code is successfully tested at multiple scales within the Little Juniata Watershed (845 sq. m) by running the parallel code upto 512 processors. The computational experiments showed a significant advantage of the parallelization strategy vis-à-vis load balancing and minimization of communication, with respect to sub-watershed based partitioning methods.

The novel algorithms, paradigms and numerical models for performing large scale simulations, which has been presented in this dissertation, provide a framework to perform multi-scale distributed modeling in watersheds with varying climate, hydrogeologic and physiographic regimes. The integrated framework facilitates fast

prototyping of simulations in new settings and scenarios. The modeling system also acts as a "virtual watershed" to experiment and understand the process interactions at multiple scales. The modeling framework and the test cases developed in this dissertation will act as a future resource for open-source community modeling and testing.

8.2. Recommendations for future work

Recommendations of future work are identified for each section of the work presented in this dissertation.

In Chapter 1, we showed the potential of performing temporally adaptive discretization of the problem domain. In order to successfully use temporally adaptive spatial grids in a real model application, a) strategies for fast remapping of data in the refined domain, b) identification (derivation) of error metrics to perform and control the frequency of (de)refinement, and c) solution methodology of variable system of ODEs, have to be explored. It would also be important to perform numerical experiments to study the computational advantages of temporally adaptive grids w.r.t to static grids vis-à-vis the process dynamics. In Chapter 1, we also showed that generating grids based on constraints lead to assignment of single class within each discretized element. However, sometimes the tradeoff of doing that is generation of meshes with very small triangles. An algorithm to generate quality meshes based on constraints, while still ensuring a minimum triangle size needs to be developed.

Chapter 2 lays the groundwork for integration of data management, model and visualization systems. Using the developed shared data-model, new visualization, analysis and decision support systems that can dynamically interact with the observed and modeled data sets, and with the numerical model needs to be developed. The framework will allow resource-managers, researchers and policy-makers to explore alternatives and tradeoffs for sociological, economic and environmental vulnerabilities thus facilitating better policy and decision making. The hydrologic modeling system can be extended further for simultaneous multi-environment, multi-user steering by taking advantage of grid-computing and multi-threaded architecture.

The application of PIHM and FIHM models (as discussed in Chapter 4 and 5 respectively) has been performed at different spatial scales. It is important to comparatively study the accuracy of predicted states simulated by both models. In particular, it is important to asses the vertical recharge flux and the distribution of soil moisture prognosticated by both models. The study can be used to derive process equations relevant to different spatial and temporal distribution of parameters, topography and climate forcings. Continuing on the work on the development of coupled models, incremental enrichment of existing model with new physical processes to answer new science questions in newer settings has to be followed. For example, coupling of energy-based snow models to FIHM will help understanding and prediction of the ongoing and potential future changes in hydrologic regimes due to earlier melting of the snowpack. Similarly, the impact of depletion in groundwater table or of land use/cover change on weather and climate at local and global scales can be studied by coupling of climate models with FIHM. Other processes that should be coupled with the hydrologic model are heat and contaminant/sediment transport and this work is underway by my colleague G. Bhatt who is working on a coupled hydrologic and solute transport model and Dr. Shuangcai Li who recently completed his PhD work on development of sediment transport coupled to PIHM. Verification experiments discussed in Chapter 5 were not adequate to study the impacts of arbitrarily oriented anisotropy of surface (roughness) and subsurface (conductivity) properties. So was the case to study surface-subsurface coupling. V-shaped catchment experiment to simulate overland flow is observed to give decent results for a variety of overland flow assumptions. Mindful of the fact that "stress-test" verification of processes in a hydrologic model is essential for forecasting, new protocols and verification experiments for each model component need to be developed. To increase the speed of the model code, pre-conditioners for Newton iteration based Krylov solvers need to be implemented.

pPIHM model (discussed in Chapter 7) uses static partitioning of model domain to perform simulation on distributed processors. However for processes, such as snow-melt which are temporally varying and exist generally in part of the model domain (higher elevations) only, the computational load can be expected to be vastly varying, thus contributing to heterogeneous load across processors. Effectiveness of dynamic

partitioning algorithms needs to be explored in heterogeneous temporally varying computational load settings. The model codes also have to be modified to take advantage of hybrid processor environment.

Vita

Mukesh Kumar

Education

- 2003-2009, PhD, Civil and Environmental Engineering, Pennstate University
- 1998-2002, B.Tech, Civil and Environmental Engineering, Indian Institute of Technology, Kanpur

Internships

- Summer 2001, Princeton University and USDA-ARS Maryland.
- Winter 2000, Indian Institute of Remote Sensing (IIRS)

Awards and Honors

- CUASHI-CMWR Fellow, 2008
- Outstanding Student Paper Award at AGU Spring Meeting, 2006

Selected Publications

- M. Kumar, G. Bhatt and C. Duffy, An efficient domain decomposition framework for accurate representation of geodata in distributed hydrologic models, *International Journal of GIS*, v.23, 2009
- M. Kumar, G. Bhatt and C. Duffy, An Object Oriented Shared Data Model for GIS and Distributed Hydrologic Models, *International Journal of GIS*, v.23, 2009
- M. Kumar and C.J. Duffy, Detecting Hydroclimatic Change in Colorado River Basin, *Journal of Hydrology*, 2009
- M. Kumar and D.A. Miller, A Non-Parametric Classification Strategy for Remotely Sensed Images Using Both Spectral and Textural Information, *Signal Processing and Pattern Recognition Applications (SPPRA-IASTED)*
- M. Kumar, G. Bhatt and C.J. Duffy, The Role of Physical, Numerical and Data Coupling in a Mesoscale Watershed Model, *Advances in Water Resources*, 2009 (In Review)
- M. Kumar and C.J. Duffy, Domain Partitioning for Implementation of Large Scale Integrated Hydrologic Models on Parallel Processors, *Computers and Geosciences*, 2009 (In Review).
- M. Kumar, C.J. Duffy and K. Salvage, A Second Order Approach for Coupled Vadose-Zone Surface-Flow simulation in Heterogeneous Anisotropic Media, *Vadose Zone Journal*, 2009 (In Review)
- M. Kumar and C.J. Duffy, Shared Data Model to Support Environment Sensor Network Data in Hydrologic Models, *iEMSs*, 2008
- G. Bhatt, M. Kumar and C. J. Duffy, Bridging gap between geohydrologic data and Integrated Hydrologic Model: PIHMgis, *iEMSs*, 2008